Faculdade de Engenharia da Universidade do Porto

Influence of process parameters on the properties of 3D printed components and predictive model

João Araújo Afonso



Mestrado Integrado em Engenharia Mecânica

Orientador: Professor Doutor Jorge Lino
Co-orientador: Professor Doutor Jorge Belinha

June 2019

"And once the storm is over, you won't remember how you made it through, how you managed to survive. You won't even be sure, whether the storm is really over. But one thing is certain. When you come out of the storm, you won't be the same person who walked in. That's what this storm's all about."

Haruki Murakami

Abstract

The following master's dissertation integrates the SIMUL3F pilot project, which is focused around the development of simulation *software* for fused-filament fabrication (FFF) additive manufacturing processes. In this case, the content was organised in a way that allowed for deep process knowledge and understanding of process parameter influence in poly-lactide (PLA) components to be obtained, followed by the creation of predictive models as feedback for said simulation *software*.

Due to the wide variety of process parameters, the incorrect value selection and understanding of their influence on the characteristics of the produced components leads to the invalidation of these parts for the desired purposes, constituting an increase in waste production. As such, there is a need for comprehensive research on process parameter influence, as well as for the possibility to simulate the characteristics resulting from different combinations, which is why the predictive models are required.

Additionally, this works focuses solely on the printing of components made from poly-lactide acid due to the fact that this is one of the most utilised materials for this method and there is yet a wide range of information regarding this material that needs further consolidation.

Subsequentially, two different stages can be distinguished in this dissertation. First, there is a contextualisation stage focused on obtaining vast amounts of information regarding the process and process parameter influence, followed by an experimental stage consisting of the variation of print speed and extruder temperature in the production of compressive, tensile and flexural test specimens. The latter stage is concluded with an analysis of the results and predictive model generation.

As for the obtained conclusions, it was observed that both parameters exert meaningful influence on the amount of extruded material (reflecting directly on the mass of the components). The mechanical properties, namely tensile resistance, were mainly influenced by extruder temperature, with print speed becoming less significant.

Keywords: FFF, PLA, print speed, extruder temperature.

Resumo

Esta dissertação de mestrado surge como integrante do projeto SIMUL3F, focado no desenvolvimento de um *software* de simulação de processos de fabrico aditivo de filamento extrudido (FFF). Neste caso, o presente conteúdo incide sobre a obtenção de conhecimento aprofundado acerca da influência dos parâmetros de processo e na criação de modelos de previsão para fornecimento à estrutura do dito *software*, desenvolvido paralelamente por outros membros integrantes do projeto.

Devido à grande variedade de parâmetros que compõem este processo de fabrico, a incorreta seleção de valores e fraco entendimento acerca da influência que cada um dos parâmetros exerce nas características dos componentes finais origina a inviabilização destes mesmos e um consequente aumento de desperdícios. De tal modo, surge a necessidade de um estudo aprofundado acerca dos parâmetros e a possibilidade de simular as características resultantes de diferentes combinações, sendo que, para tal, é também necessária a criação de modelos preditivos.

Adicionalmente, o presente trabalho foca-se apenas na impressão de peças em ácido poli-láctico (PLA), por se tratar de um dos materiais mais utilizados neste método de fabrico e por existir ainda uma vasta gama de informação por consolidar relativamente a este material.

Consequentemente, o trabalho encontra-se dividido em duas fases distintas. Inicia-se com uma fase de contextualização onde é possível adquirir uma vasta quantidade de informação sobre o método de fabrico, assim como das diferentes influências dos parâmetros de processo. Em seguida, uma fase experimental onde se fazem variar dois dos parâmetros (velocidade de impressão e temperatura de extrusão) na impressão de provetes de compressão, tração e flexão, concluindo-se com a análise de resultados e criação dos modelos preditivos.

No que toca aos resultados, observou-se que ambos os parâmetros exercem uma influência significativa na quantidade de material extrudido, refletindo-se diretamente na massa dos provetes. Relativamente às propriedades mecânicas, ainda que se tenha tratado de pequenas variações, apenas a temperatura de extrusão exerceu influência significativa, nomeadamente na resistência à tração.

Palavras-chave: FFF, PLA, velocidade de impressão, temperatura de extrusão.

Acknowledgments

Em primeiro lugar quero deixar um agradecimento ao Professor Jorge Lino por ter feito sempre o máximo para que não me faltassem os recursos necessários e por tentar valorizar ao máximo o trabalho efetuado. Igualmente, deixo também a minha gratidão ao Professor Jorge Belinha que se mostrou sempre disponível para rever o progresso feito e sugerir melhorias essenciais à qualidade do trabalho final.

Em seguida, agradeço aos meus pais, Isabel e Jorge, por me terem dado a oportunidade de entrar no ensino superior e de fornecerem todo o seu apoio durante estes 5 anos. Obrigado por também terem feito o máximo possível para que nenhuma adversidade prejudicasse o meu percurso académico, assim como pessoal.

Igualmente importante, quero agradecer à minha irmã por participar no meu percurso e por me fazer passar bons momentos. Agradeço também ao Hugo por ser o melhor amigo que tive neste percurso.

Com um lugar especial, quero agradecer à Ana por, em 5 anos, ter sido um dos meus pilares, por me fazer querer melhorar no dia a dia e por me acompanhar em todos os meus bons e maus momentos, estando lá para disfrutar dos bons comigo e para me tirar dos maus.

Em seguida quero deixar o meu apreço pelos Clitos, amigos e companheiros para todos os momentos.

Dentro daqueles que me receberam em Macau e fizeram com que fosse a experiência mais entusiasmante e positiva que tive até aqui, quero destacar o Diamantino e a São, sem o apoio dos quais não teria sido metade da experiência que foi. Quero também agradecer ao João, ao Louis, ao Rui e ao Simão por todas as experiências que tivemos em Macau, no Japão e em tantos outros países que visitamos juntos.

Quero também deixar uma palavra ao Moura, ao Zé, ao Manel e ao Hugo Franco, por ao fim de tantos anos continuarem a ser parte do meu círculo de verdadeiros amigos e por se preocuparem comigo.

Institutional acknowledgments

The authors truly acknowledge the funding provided by Ministério da Ciência, Tecnologia e Ensino Superior - Fundação para a Ciência e a Tecnologia (Portugal) by project funding MIT-EXPL/ISF/0084/2017. Additionally, the authors acknowledge the funding of Project NORTE-01-0145-FEDER-000022 - SciTech - Science and Technology for Competitive and Sustainable Industries, co-financed by Programa Operacional Regional do Norte (NORTE2020), through Fundo Europeu de Desenvolvimento Regional (FEDER).

Table of contents

1. Introduction 2
1.1 Contextualization 2
1.2 Objectives 2
1.3 Methodology 2
2. Additive Manufacturing 4
2.1 Definition and classes 4
2.2 Generic Additive Manufacturing process 6
2.3 Material extrusion technologies 7
2.4 Fused Filament Fabrication 9
2.4.1 Materials 10
2.4.2 Polylactide Acid – PLA 10
2.4.3 Main printer models 12
2.5 Process parameters and influencing factors 16
2.5.1 Layer Thickness 20
2.5.2 Contours 22
2.5.3 Raster Angle 22
2.5.4 Raster Width 24
2.5.5 Infill percentage 25
2.5.6 Infill Pattern 26
2.5.7 Air gap 27
2.5.8 Build Orientation 29
2.5.9 Printing speed 30
2.5.10 Extruder temperature 31
2.5.11 Build surface temperature 32
2.5.12 Slicing software 33
2.6 Summarization 35
3. Experimental stage - materials and methods 36
3.1 Software 37
3.2 FormFutura PLA 38
3.3 Printing devices 39
3.3.1 Extrusion calibration 41
3.3.2 Dimensional calibration 42
3.3.3 Assessment 43
3.4 Instrumentation and upgrading 44
3.4.1 Temperature Measurement 44
3.4.2 Enclosure 46
3.5 Experiment design - Printing and testing the components 48
3.5.1 First Stage – Raster orientation variation 49
3.5.2 Second Stage – Speed and Temperature variation 51
3.5.2.1 Other parameters 52
3.5.2.2 Methodology for testing 52
3.5.2.3 Methodology for analysis 57
4. Analysis and comparison of the results 58
4.1 Mass 58
4.1.1 Short compression test specimens 58
4.1.2 Long Compression test specimens 62
4.1.3 Tensile test specimens 66

4.1.4 Flexural test specimens 69
4.1.5 Generic predictive model 73
4.2 Dimension 74
4.3 Mechanical properties 78
4.3.1 Compression 78
4.3.2 Tensile 87
4.3.3 Flexural 94
5. Conclusions 97
5.1 Future works 102
6. References 104
7. Appendix 112

Terminology

- ABS – Acrylonitrile Butadiene Styrene
- BOM – Bill of materials
- DIY – Do it yourself / Build it Yourself
- FDM – *Fused Deposition Modelling*
- FFF – Fused Filament Fabrication
- LDPS – Laboratório de Desenvolvimento de Produtos e Serviços
- PA – *Polyamide*
- PC – *Polycarbonate*
- PLA – *Polylactide Acid*
- PEI - *Polyetherimide*
- SEM –Scanning Electron Microscopy
- STL – *Stereolitography file*

Figures

Figure 1 – Target industries of AM producers (left) and percentage of components produced for different sectors of the industry. Adapted from Wohlers et al. (2019). 4
Figure 2 - Sales growth for Industrial grade printers (left) and Desktop grade printers (right) (Wohlers et al. 2019). 5
Figure 3 - Percentage that each type of feedstock material represents on the AM material market. (Wohlers et al. 2019). 5
Figure 4 - Schematization of the essential steps in the production of AM components. Adapted from DeloitteUniversityPress (2018). 6
Figure 5 – Generalized process planning flows for AM and machining, reflecting the decision-making and manpower aspects. Taken from Urbanic and Saqib (2019). 6
Figure 6 - Schematization of the working principle in material extrusion technologies applied to AM. 7
Figure 7 - Different types of axial movement rigs that most material extrusion devices present: a) robotic arm; b) polar coordinates; c) cartesian coordinates (combination between build plate and extruder); cartesian coordinates (delta printers, fixed build plate). Adapated from 3DNatives (2017). 8
Figure 8 - Most common types of mechanisms used to feed material through the nozzle. Taken from Gleadall et al. (2018). 8
Figure 9 - First working model of the RepRap 3D printer Project (Jones et al. 2011). 9
Figure 10 - Schematic representation of a generic FFF system. Obtained from Górski et al. (2015b). 9
Figure 11 - Prusa i3 MK3 model. Obtained from "Prusa Research Original Prusa i3 MK3" 2017) 12
Figure 12 - DIY project being carried out at LDPS, based off blueprints obtained at RepRap. 13
Figure 13 - Ender 3 by Creality (unaltered) used at LDPS. 14
Figure 14 - Model of the Ultimaker 3, taken from Ultimaker (2016). 14
Figure 15 - Schematization of a layer produced by FFF with some of the process parameters represented. Taken from Shojib Hossain et al. (2014). 16
Figure 16 - Example of different build orientations possible. Taken from Shojib Hossain et al. (2014). 17
Figure 17 - Influence of the layer height in the shape of the deposited filament. Adapted from Akhoundi, Behravesh and Bagheri Saed (2019). 20
Figure 18 - Representation of the staircase effect in FDM produced componentes (Jamalabad et al. 1996) 20
Figure 19 - Influence of layer height in the air gap and bonding area dimensions. Adapted from Rankouhi et al. (2016) 21
Figure 20 - Influence of layer height in the tensile strength of 3D printed components (Rajpurohit and Dave 2018). 21
Figure 21 - Different number of contours that can be used to produce the same geometry, with three contours on the left and only one on the right. Adapted from Jamalabad et al. (1996) 22
Figure 22 - Graphical definition of raster angle. Taken from Wu et al. (2015). 22

Figure 23 - Imperfections and lack of filament deposition in curved geometries due to raster angle. Adapted from Rankouhi et al. (2016).....23
Figure 24 – Comparison of fractures modes between different raster angles (Ziemian, Sharma and Ziemian 2012).....23
Figure 25 - SEM analysis of fracture surfaces in a) 0° b) 90° c)±45° and d)45° test specimens (Ziemian, Sharma and Ziemian 2012).....24
Figure 26 - Raster width (w) of the deposited filament. Adapted from Akhoundi, Behravesh and Bagheri Saed (2019).....24
Figure 27 - Stress - Strain curves for tensile trials with different raster widths (Rajpurohit and Dave 2018).....25
Figure 28 - Differences in air gap between fibres and the width of the fibres them selves, as a result of the smaller infill percentage (35%), on the left, and 100% infill percentage (on the right). Adapted from Torres et al. (2016).....25
Figure 29 - Examples of the infill patterns commonly used and studied by Alafaghani and Qattawi (2018).....26
Figure 30 - Various types of infill patterns that are typically used. Taken from Akhoundi and Behravesh (2019).....27
Figure 31 - Photograph of the gyroid model already being used for infill patterns (Gonick 2018).....27
Figure 32 - Different types of air gaps. From left to right: positive, null and negative. (Akhoundi, Behravesh and Bagheri Saed 2019).....28
Figure 33 – Comparison between the dimension of injection moulded (a), negative air gap (b) and positive air gap (c). Taken from Dawoud, Taha and Ebeid (2016).....28
Figure 34 - Example of the various typical build orientations that different test specimens can be printed at. Taken from Torres et al. (2016).....29
Figure 35 - Discrepancies in extruded fiber width and predicted fiber width. Adapted from Coogan and Kazmer (2017).....30
Figure 36 - Typical consequences of dimensional and geometrical error caused by the use of higher than reccomended extruder temperature.....31
Figure 37 - Creation of an STL file (right) by inputing a 3D CAD model (left).....33
Figure 38 - Portion of a G-Code file (left) and its graphical representation of the slicing software (right).....33
Figure 39 - Discrepancies between different slicers when building the same geometries. Taken from Baumann et al. (2016).....34
Figure 40 - Adopted methodology for the experimental stage.....36
Figure 41 - Example of Simplify3D's interface for the imput of process, material and machine parameters.....37
Figure 42 - Spool of Premium PLA by FormFutura.....38
Figure 43 - Components and assemblies for the construction of the printer.....39
Figure 44 - Extruder tensioner applied to the geared system arm.....40
Figure 45 - Filament guide instaled on the alluminium frame.....40
Figure 46 - Fan guard installed on top of the motherboard cover.....40
Figure 47 - Simplify 3D's terminal feature and input window.....41
Figure 48 - Cubes that were utilized for axis calibration purposes. Model taken from MakerBot Industries (2019).....42
Figure 49 - Component used to assess the calibration of the printer. Taken fromMakerBot Industries (2019).....43

Figure 50 - Heating block and Pt100 temperature sensor, side by side (left) and assembled (right). 44
Figure 51 - Data logger and final setup of the temperature measurement device. 45
Figure 52 - Example of the time-temperature output resulting from the utilisation of the data logger and Pt100 sensor. Temperature measurement of the compression test specimens at 30mm/s and various temperatures. 45
Figure 53 - Upper corner piece (left) and lower corner piece (right) being prepared for printing in Simplify3D. 46
Figure 54 - Assembled enclosure. 47
Figure 55 - Adopted methodology for the experimental stage. 48
Figure 56 - Example of the printed test specimens. Tensile (top), large compression, flexural and short compression (bottom, left to right). 49
Figure 57 - Sutures present at the surface and, presumably, at each layer, caused by reminiscing filament deposited during nozzle movements. 50
Figure 58 - Stress – Strain graphs for tensile and flexural trials. 50
Figure 59 - Stress - Strain graphs for compression trials. 50
Figure 60 - Dimension of the test specimens according to the standard ISO 527. 53
Figure 61 - Dimension of the test specimens according to the standard ISO 178. 54
Figure 62 - Dimension of the test specimens according to the standard ISO 604, type A to the right and type B to the left. 55
Figure 63 - Instron 5966 UTS device utilized for the compressive test specimens. 56
Figure 64 - Typical stress-strain curve for a compressive test according to the standard ISO 604. 56
Figure 65 - Example of the records that were kept for each of the test specimens, in this case the ones regarding the flexural analysis. 57
Figure 66 - Scale utilised to record the mass of the test specimens. 57
Figure 67 - Surface representation of the influence that Extruder temperature and Print Speed have in terms of the mass for short compression test specimens. 59
Figure 68 – Short Compression -Tukey Pairwise comparisons on the influence of Print speed (left) and Extruder temperature (right) with 95% Confidence. 59
Figure 69 – Short Compression - Graphical representation for the difference of means for different print speeds (left) and extruder temperatures (right). 60
Figure 70 – Short Compression - Plotting of the means and standard error for the mass according to the different levels of extruder temperature (left) and printing speed (right). 60
Figure 71 – Short Compression - Predictive model for the mass with print speed and extruder temperature as inputs. Based of exponential regressions obtained through experimental results. 61
Figure 72 – Short Compression - Subtraction of the experimental and the predictive model. 62
Figure 73 - Influence of the Extruder temperature and Print speed in the mass of long compression test specimens. 63
Figure 74 - Long Compression test specimens -Tukey Pairwise comparisons on the influence of Print speed (left) and Extruder temperature (right) with 95% Confidence. 63

Figure 75 - Long Compression test specimens - Graphical representation for the difference of means for different print speeds (left) and extruder temperatures (right).....64
Figure 76 - Long Compression - Plotting of the means and standard error for the mass according to the different levels of extruder temperature (left) and printing speed (right).....64
Figure 77 - Long Compression - Predictive model for the mass with print speed and extruder temperature as inputs. Based of exponential regressions obtained through experimental results.....65
Figure 78 - Long Compression - Subtraction of the experimental and the predictive model.....65
Figure 79 - Influence of the Extruder temperature and Print speed in the mass of tensile test specimens.....66
Figure 80 - Tukey Pairwise comparisons on the influence of Print speed (left) and Extruder temperature (right) with 95% confidence.....67
Figure 81 - Tensile test specimens - Plotting of the means and standard error for the mass according to the different levels of extruder temperature (left) and printing speed (right).....68
Figure 82 - Tensile - Predictive model for the mass with print speed and extruder temperature as inputs. Based off exponential regressions obtained through experimental results.....68
Figure 83 - Tensile - Subtraction of the experimental and the predictive model. 69
Figure 84 - Influence of the Extruder temperature and Print speed in the mass of flexural test specimens. 70
Figure 85 - Flexural - Tukey Pairwise comparisons on the influence of Print speed (left) and Extruder temperature (right) with 95% confidence.....70
Figure 86 - Flexural test specimens - Plotting of the means and standard error for the mass according to the different levels of extruder temperature (left) and printing speed (right).....71
Figure 87 - Flexural - Predictive model for the mass with print speed and extruder temperature as inputs. Based off exponential regressions obtained through experimental results.....72
Figure 88 - Flexural - Subtraction of the experimental and the predictive model. 72
Figure 89 - Technical drawings of the test specimens according to the specified standards, with the dimensions under study (yy and zz) identified at the respective places.....74
Figure 90 - Tuckey pairwise comparison regarding the yy dimension. 75
Figure 91 - Tuckey pairwise comparison regarding the zz dimension.....76
Figure 92 - Plotting of the means and standard error for the yy (left) and zz (right) according to the different levels. 77
Figure 93 - Representation of the non-linear region (Hookean behaviour) in AC, and the corresponding linear aproximation in EF. Adapted from ASTM D 638-03. 78
Figure 94 - Type B (Short compression test specimen) with the imperfections that caused the non-linear behaviour during the initial instances of the test specimen.....78
Figure 95 - Misalignment phenomenons that occured during the trials of the type A test specimens, causing for reproducibility issues. 79

Figure 96 - Influence of print speed and extruder temperature on the compressive modulus (left), yield stress (right) and strain (bottom). 81
Figure 97 - Tuckey pairwise comparison regarding the compressive modulus....82
Figure 98 - Plotting of the means and standard error for the compressive modulus according to the different levels. 82
Figure 99 - Tuckey pairwise comparison regarding the compressive yield stress. 83
Figure 100 - Plotting of the means and standard error for the compressive yield stress according to the different levels. 83
Figure 101 - Tuckey pairwise comparison regarding the compressive yield strain. 84
Figure 102 - Plotting of the means and standard error for the compressive yield strain according to the different levels. 84
Figure 103 - Predictive model for the compressive modulus (left), yield strength (right) and strain (bottom) with print speed and extruder temperature as inputs. Based off exponential regressions obtained through experimental results. 85
Figure 104 - Subtraction of the experimental and the predictive models for the compressive modulus (left), yield strenght (right) and strain (bottom). 86
Figure 105 - Influence of print speed and extruder temperature on the tensile modulus (left), yield stress (right) and yield strain (bottom). 88
Figure 106 - Test specimens with print speeds of 75mm/s and extruder temperatures from 190-230°C. 89
Figure 107 - Plotting of the means for the tensile modulus, yield stress and strain. 90
Figure 108 - Predictive model for the tensile modulus (left), yield stress (right) and strain (bottom) with print speed and extruder temperature as inputs. Based off exponential regressions obtained through experimental results. 91
Figure 109 - Subtraction of the experimental and the predictive models for the tensile modulus (left), yield stress (right) and strain (bottom). 92
Figure 110 - Plotting of the means for the maximum flexural stress according to the different levels of print speed and extruder temperature. 95
Figure 111 - Influence of print speed and extruder temperature on the flexural modulus (left), maximum stress (right) and maximum strain (bottom). 95
Figure 112 - Plotting of the means for the flexural modulus and maximum flexural strain. 96
Figure 113 - Predictive model for the flexural modulus (left), maximum flexural stress (right) and maximum flexural strain (bottom) with print speed and extruder temperature as inputs. Based off exponential regressions obtained through experimental results. 97
Figure 114 - Subtraction of the experimental and the predictive models for the flexural modulus (left), maximum flexural stress (right) and maximum flexural strain (bottom) 98

Tables

Table 1 - Different categories of additive manufacturing according to ISO/ASTM 52900. 4
Table 2 - Common designations for the two types of AM printers. 5
Table 3 - Different types of material and some examples. 10
Table 4 - Some of the properties observed in general-use PLA compared to general-use ABS (CESEduPack 2019). 11
Table 5 - Comparison between the referenced models in terms of price, build volume, materials, among other parameters. Table built by the author. 15
Table 6 - List of process parameters, relevant concepts and their description. 16
Table 7 - Summary of relevant recent studies on the influence of various processing parameters in AM PLA components. Adapted from Popescu et al. (2018). 18
Table 8 - Summary of relevant studies on the influence of various processing parameters in AM ABS components. Adapted from Popescu et al. (2018) 19
Table 9 - General properties of FormFutura's Premium PLA. 38
Table 10 - Iterations used to calibrate the extruder motors. 41
Table 11 - Iterations ran to calibrate the movement stepper motors. 42
Table 12 - Levels of V_{print} used during the experimental phase. 51
Table 13 - Levels of T_{print} used during the experimental phase. 51
Table 14 - Parameters not subject to alterations during the experimental phase. 52
Table 15 – Short Compression -Mean values of the mass of the test specimens for each of the used conditions. 58
Table 16 – Long Compression - Mean values of the mass of the test specimens for each of the used conditions. 62
Table 17 – Tensile test specimens -Mean values of the mass of the test specimens for each of the used conditions. 66
Table 18 - Flexural test specimens -Mean values of the mass of the test specimens for each of the used conditions. 69
Table 19 - Estimated errors for each of the components using coefficients from different models. (LC - Long Compression; F - Flexural; T - Tensile). 73
Table 20 - Influencing factors under study and their different levels. 75
Table 21 - Summary of the average compressive mechanical properties. 80
Table 22 - Summary of the average tensile mechanical properties 87
Table 23 - Summary of the average flexural mechanical properties. 94

Influence of process parameters on the properties of 3D printed components and predictive model

1. Introduction

1.1 Contextualization

Over the past few years a wide variety of readily available open-source fused filament fabrication (FFF) printers have been made available to all (Wohlers et al. 2019), with the main characteristic being their noticeably low price (with a sound baseline starting at 150€) for the number of features and printing capabilities they can present. These devices can either be built from scratch while following pre-established blueprints and guides, or bought pre-assembled, later being upgraded by implementing new components.

As such, the fact that modules like these can be obtained for such a low price point implies that some compromises are made in terms of the components and, consequentially, the printing quality. In addition, the strong dependency on the various process parameters increases the probability of failed prints occurring, as well as producing components with insufficient mechanical properties.

This inconsistency of results leaves a gap for the development of simulation software to predict the behaviour of components produced in devices like these using polylactide acid (PLA) and thus reducing waste of resources before producing final versions of the desired components. In order to do so, these program's outputs have to be based off of real experimental results represented by empirical models, which is where this study plays its role.

1.2 Objectives

- Establish the current baseline for low-cost FFF printers (the most common, degree of reliability and upgradability) and the most relevant printing parameters;
- Integration of in-situ monitoring systems during the printing of test specimens under different printing conditions;
- Perform a series of mechanical trials to the printed test specimens;
- Observe the influence of the variation of process parameters in the components' mass, dimensions and mechanical properties;
- Output predictive models for the mass and mechanical properties of the components.

1.3 Methodology

In order to carry out the proposed work, an initial research was made in order to obtain relevant information regarding FFF technologies, commonly used devices and the many studies regarding the influence of process parameters on the properties of 3D printed components.

After this, a base design for the printers was selected and the devices were constructed, followed by the fine tuning and implementation of monitoring systems.

Then, after an exploratory stage where further practical knowledge on the particularities of 3D printing was obtained, the printing and mechanical trialling of test specimens was carried out, along with an analysis of the obtained results and the generation of predictive models.

2. Additive Manufacturing

With this chapter the intention is to provide an insight into the most relevant aspects of the universe of additive manufacturing, namely fused filament fabrication using PLA.

2.1 Definition and classes

Additive manufacturing, commonly shortened to AM and also named as 3D Printing, derives from what was previously called as Rapid Prototyping. It consists of a range of technologies able of reproducing physical models and components by successive layer deposition of certain materials, by using print heads, nozzles and similar technologies, as opposed to traditional methods, where subtractive and formative techniques are used (Gibson, Rosen and Stucker 2009). The terminology Rapid Prototyping was deterred in favour of AM due to the fact that, by the current methods and capabilities of additive manufacture methods, it was already possible to produce functional components and not only prototypes.

According to ISO/ASTM 52900, this type of manufacturing technique has many variants which can be divided into the categories presented in Table 1.

Table 1 - Different categories of additive manufacturing according to ISO/ASTM 52900.

Category	Description
Material Extrusion	Process where the material is extruded through a fixed diameter orifice, commonly designated as nozzle, as long as it is presented in a semi-fluid state.
Material Jetting	Process where small particles of construction material coupled with support material are deposited in specific areas of a build plate.
Binder Jetting	Process where a mixture of granulate and binding materials are selectively deposited to form a solid structure.
Sheet Lamination	Process where there is successive deposition and bonding of sheets of material with defined sections.
VAT Photopolymerization	Process where there is a cure phenomenon (photopolymerization) of photocurable resins by resorting to fixed wavelength radiation exposure.
Powder Bed Fusion	Process with build surface filled with powdered material that is fused together by resorting to thermal energy.
Directed Energy Deposition	Process where materials are gradually deposited and then fused together by focused thermal energy.

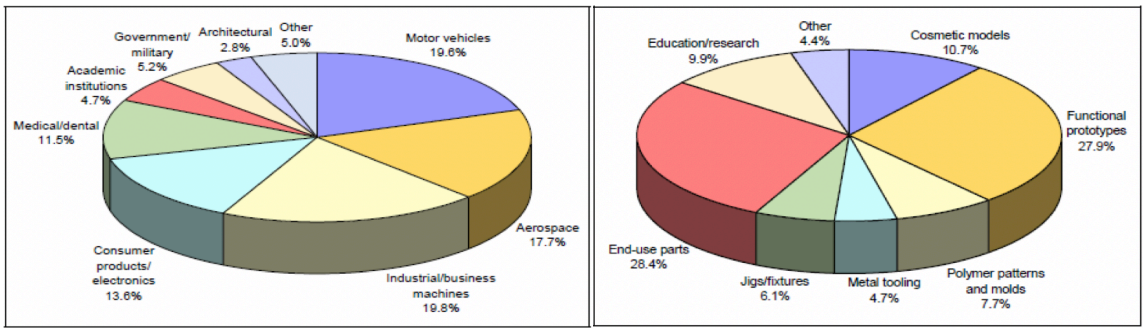


Figure 1 – Target industries of AM producers (left) and percentage of components produced for different sectors of the industry. Adapted from Wohlers et al. (2019).

A testimony to the current reality of the additive manufacturing industry is the growth it has experienced over the past few years, with a 26,9% average annual growth in the past 30 years and a presence in a wide range of industries and applications (Wohlers et al. 2019), as it can be seen in Figure 1.

As part of the growth in interest in these technologies, an increase in the sales of devices for this purpose was observed, devices which can be divided into two separate classes, visible in Table 2.

Table 2 - Common designations for the two types of AM printers.

Class	Description
Industrial grade AM printers	High grade devices sold for a value upwards of 5000$, capable of extreme precisions and dealing with high grade materials typically used with proprietary *firmware*.
Desktop grade AM printers	Devices sold below 5000$, typically present lower dimensional accuracy, work with a more limited array of materials and are largely used with *open-source firmware*.

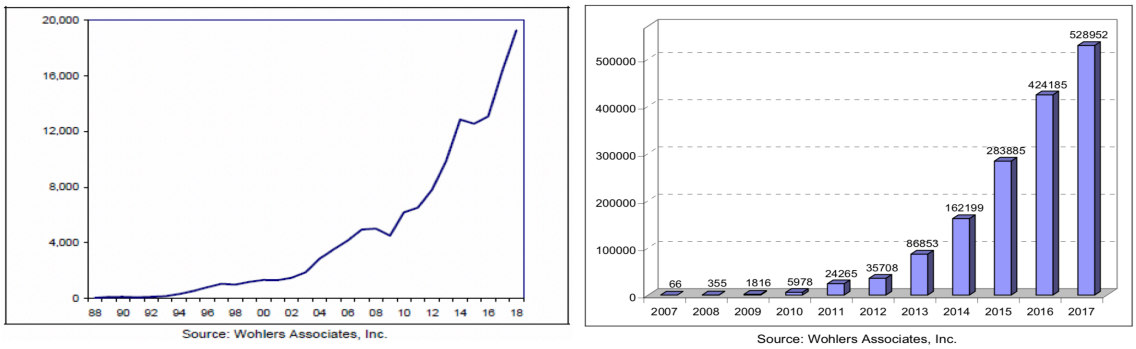


Figure 2 - Sales growth for Industrial grade printers (left) and Desktop grade printers (right) (Wohlers et al. 2019).

Both Industrial and *Desktop* grade AM printers have shown an increase in sales, visible in Figure 2, with a growth of 17,8% in 2018 for the first kind and 24,7% in 2017 for the latter, which respectively amounts to a total of 19285 and 528952 sold printers with an average selling price of 85837.36€.

Typically utilized materials vary depending on the purposed variant of AM category, ranging from thermoplastic and elastomer filaments, to powdered metals or polymers, photopolymers and other materials such as ceramics and lamination sheets, as it can be observed in Figure 3.

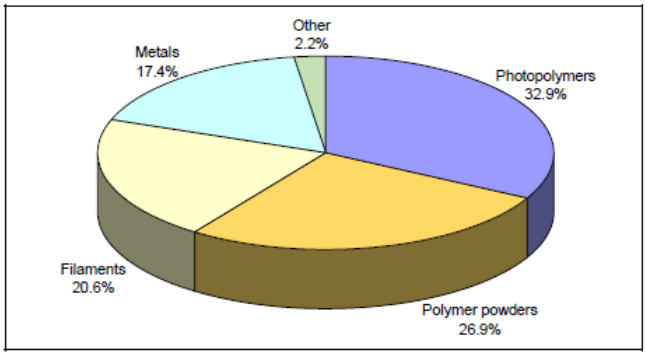


Figure 3 - Percentage that each type of feedstock material represents on the AM material market. (Wohlers et al. 2019).

2.2 Generic Additive Manufacturing process

In order to produce components with resource to these technologies, there are some crucial steps, visible in Figure 4 and Figure 5, that are common to almost all variants of AM techniques. According to Volpato et al. (2017), these can be described as:

- Modelling of the component in a CAD *software*;
- Conversion of the CAD file into a superficial mesh file, typically in STL or AMF formats (STereoLitography and Additive Manufacturing Format, respectively);
- Definition of the process parameters and production planning. This step is commonly named the *Slicing* stage (see chapter 2.5.12);
- Production of the component with the desired AM technique;
- Post-processing.

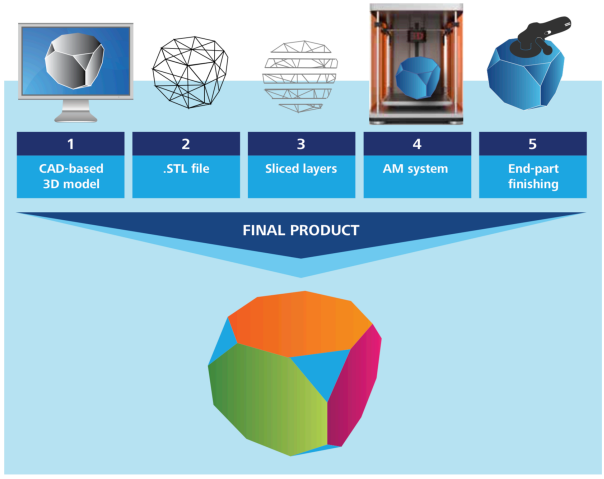


Figure 4 - Schematization of the essential steps in the production of AM components. Adapted from DeloitteUniversityPress (2018).

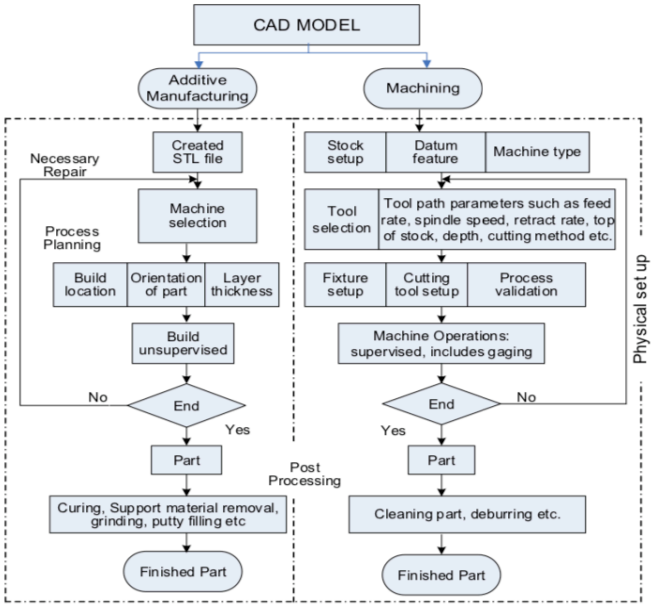


Figure 5 – Generalized process planning flows for AM and machining, reflecting the decision-making and manpower aspects. Taken from Urbanic and Saqib (2019).

2.3 Material extrusion technologies

Despite each of the different categories for AM methods presenting a series of advantages and disadvantages when compared to each other, material extrusion technologies have had a surge in interest over the past few years due to the original patents for Fused Deposition Modelling (FDM), the first commercialized extrusion technology and patented by Crump in 1992, having fallen in 2009. This led to the appearance of the open-source movement, where highly capable machines working with the same principle were built and commercialized with significant cost reductions in comparison the original devices (Lanzotti et al. 2015), thus making them accessible to a larger crowd and experiencing a large growth in terms of the devices' capabilities.

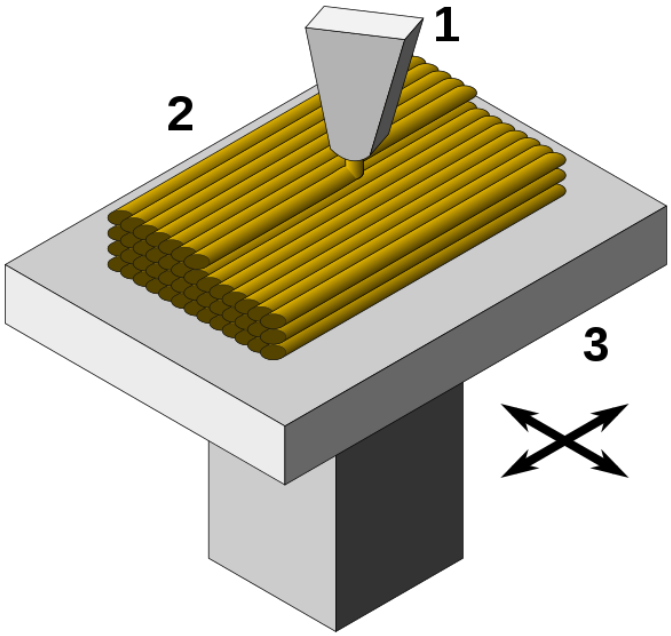


Figure 6 - Schematization of the working principle in material extrusion technologies applied to AM.

Material extrusion technologies base their functioning principles around the extrusion of material in the shape of a thin filament through a small and fixed diameter nozzle, with the feedstock material being any material that is in a semi-fluid state, be it a molten thermoplastic, slurries or pastes, considering it can return to the solid state either by cooling or chemical processing. For the majority of cases, the deposition of the filament can be divided into two separate operations:

- X and Y-axis movement, responsible for allowing movements of the nozzle (1 in Figure 6) and/or the build plate (3 in Figure 6). These movements are responsible for obtaining the geometry for each of the layers;
- Z-axis movement, responsible for allowing movements of the nozzle in the vertical direction. These movements are, usually, done separately from the other axial movements and correspond to the respective height of each layer of filament (2 in Figure 6).

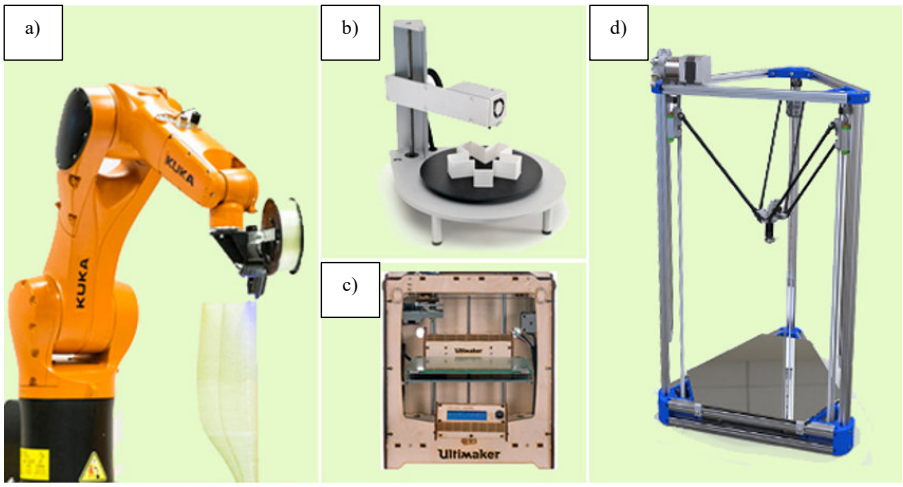


Figure 7 - Different types of axial movement rigs that most material extrusion devices present: a) robotic arm; b) polar coordinates; c) cartesian coordinates (combination between build plate and extruder); cartesian coordinates (delta printers, fixed build plate). Adapated from 3DNatives (2017).

The aforementioned movement description is not the only way that extrusion systems work, as that is respecting to a cartesian printer and there are variants that work with different adaptations to cartesian coordinates, polar coordinates or even by resorting to robotic arms, as it can be seen in Figure 7.

Aside from the differences in the way that the axial movement is performed, there can also be more than one variant as to the way the feedstock material is passed until the nozzle. The most conventional method consists of using a fixed diameter filament (usually 1,75mm or 2,85mm) that is pushed by means of rollers or geared crowns into a melting chamber and then into the nozzle (these two components can be coupled together), where the filament itself will exert enough pressure for a continuous and constant strand of filament to be extruded. Other methods consist of using extruding screws, where the feedstock material is in the form of either a granulate or a paste, or by the use of plungers (mechanic or pneumatic), as is shown in Figure 8.

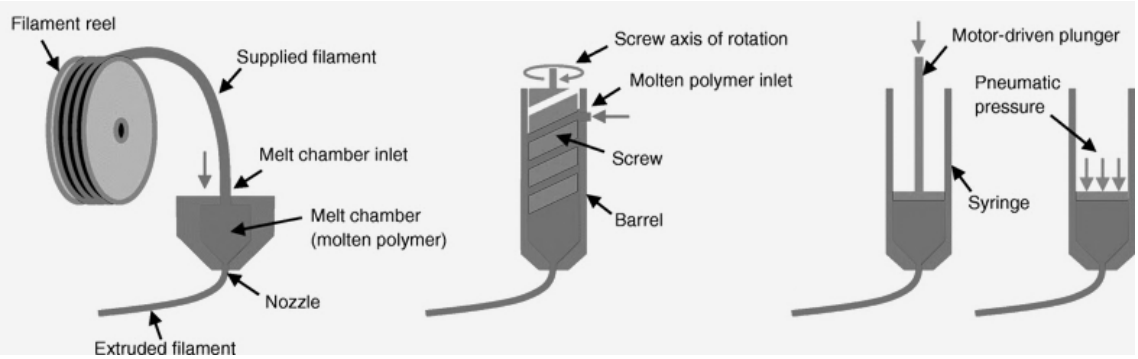


Figure 8 - Most common types of mechanisms used to feed material through the nozzle. Taken from Gleadall et al. (2018).

2.4 Fused Filament Fabrication

As it was mentioned in chapter 2.3, after the expiration of the patent for FDM, extremely similar technologies started appearing, along with a revamping movement for the accessibility to these devices due to the decrease in total cost and ease of use, as is the well-known example of projects such as RepRap, by Dr Adrian Bowyer from the University of Bath, that created a machine (Figure 9) working with the material extrusion principle by resorting to filament feedstock material and made the project available to the open public for future developments, marking the definition and importance of the *open-source movement (Jones et al. 2011)*.

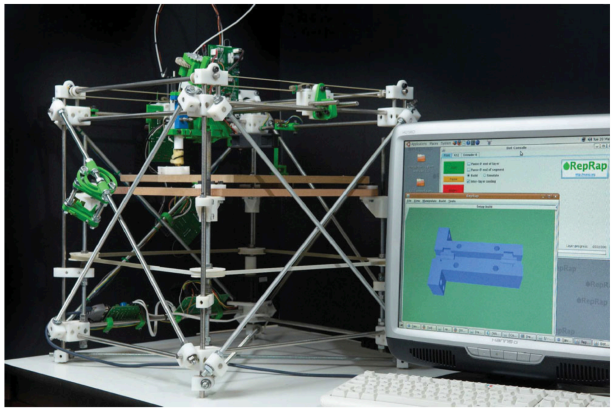


Figure 9 - First working model of the RepRap 3D printer Project (Jones et al. 2011).

Due to the legal restrictions associated with the term FDM, the creators of the RepRap project coined the term Fused Filament Fabrication (FFF) and made it free for general use, despite having the same working principles as the original material extrusion method (Volpato et al. 2017).

Attempting to define this technology leads to say that Fused Filament Fabrication (FFF) consists of a method where a part is built layer by layer using filament in a semi-molten state that is extruded through a nozzle of known diameter (using a CAD model in STL format as a reference) (Gibson, Rosen and Stucker 2009). A schematic of a generalized FFF device is shown in Figure 10.

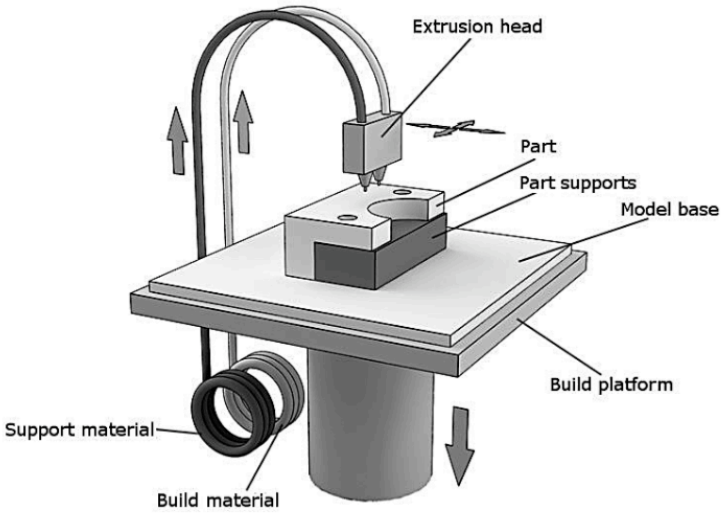


Figure 10 - Schematic representation of a generic FFF system. Obtained from Górski et al. (2015b).

2.4.1 Materials

Although not all FFF devices are capable of simultaneously using more than one material due to having only one extruder (the scheme in Figure 9 presents two nozzles for this purpose), typically, utilised materials are comprised into two categories, as is shown in Table 3.

Table 3 - Different types of material and some examples.

Class	Description
Construction material	Material utilised to produce the geometries in each layer that comprise the desired component's structure. The most used materials are PLA, ABS, PETG, PC, PA, PP and PEI (thermoplastics) and TPU (elastomer).
Support Material	Material utilised to produce geometries destined to provide support to certain structural features of the desired component during the printing stage, after which they are entirely removed and classified as waste material. Dual-extruder devices typically utilize soluble material such as PVA and single-extruder machines use the same material as for the component.

The intent of this work is to evaluate the properties of *polylactide acid,* PLA, components built using desktop printers, as it will be discussed further ahead in chapter 2.4.2. However, different materials can be utilised depending on the demands for each of the components, allocated budget and machine limitations.

- Applications for simple devices with fewer restrictions on the required mechanical resistance of the components are typically built with PLA, *acrylonitrile butadiene styrene* (ABS) or *polyethylene terephthalate glycol* (PETG). Costs are usually around 26€ per reel of 1kg of filament;
- Applications were mechanical properties are extremely relevant for the end-use are typically built with *polycarbonate* (PC), *polyamide* (PA), *polyetherimide* (PEI) or *polyether ether ketone* (PEEK). Extremely demanding materials, destined for engineering applications and highly capable printers, with costs ranging from 26-200€ per reel with 1kg of filament.

Aside from these materials, some manufacturers such as Makerbot (2015) have also issued out variants of PLA as a composite filled with steel, bronze, wood or marble, allowing for interesting looks and even different properties from the non-composite variants (Volpato et al. 2017).

2.4.2 Polylactide Acid – PLA

Inserted into the category of biodegradable thermoplastics, *polylactide acid*, typically known as PLA, is steadily becoming one of the most commonly used filaments for *desktop* 3D printers due to its eco-friendly origins relatively close properties to the other most common filament, *acrylonitrile butadiene styrene* – ABS ("Material Profiles" 2014). Typically used for packaging, disposable recipients,

casings, clothing, medical implants and homeware, this material derives from natural lactic acid obtained from maize or milk and its main characteristics when applied to FFF production methods are, according to Relvas (2018):

- High processability with low glass transition and melting point temperatures;
- High rigidity and low ductility;
- Reduced impact strength;
- Reduced volumetric contraction;
- Reduced cost;
- Absence of odours while printing.

It is possible to observe some of the physical, economical, mechanical and thermal properties of PLA compared to ABS in Table 4.

Table 4 - Some of the properties observed in general-use PLA compared to general-use ABS (CESEduPack 2019).

	PLA	ABS
Density [kg.m^{-3}]	1240 – 1270	1020 – 1080
Price [€.kg^{-1}]	~26	~20
Young's Modulus [GPa]	3 – 3,6	2 – 2,9
Yield Strength (σ_r) [MPa]	55 – 72	29,6 – 44,1
Tensile Strength ($\sigma_{0,2}$) [MPa]	40-70	30 – 50
Compressive module [GPa]	3,3 – 3,6	1,03 – 2,68
Flexural module [GPa]	3,1 – 3,6	1,2 – 2,8
Hardness [HV]	17 – 22	9 – 13
Impact strength [kJ.m^{-2}]	1,3 – 2,8	7,9 – 63
Melting point [°C]	145 – 175	---
Glass transition [°C]	50 – 60	88 – 120
Thermal expansion coefficient [µstrain/°C]	126 – 145	108 – 234

The information above, however, is derived from monolithic test specimens and, as it was mentioned in Chapter 2.4's introduction, Górski et al. (2015b) state that due to volumetric errors such as air gaps between layers and rasters the mechanical properties of AM components are almost always significantly lower than their monolithic counterparts obtained through injection moulding.

In order to better understand this phenomenon, research has been done by comparing test specimens built by injection moulding and the FFF method in ABS, as is the case of Ahn et al. (2002) who built the FFF test specimens and then created a granulate material from the filaments used in the additive manufacturing method to build the injection mould test specimens with the exact same material. Their results showed that the components displayed around 73% of their monolithic counterparts' tensile strength. Posteriorly, Dawoud, Taha and Ebeid (2016) showed, using a similar approach, also for ABS, that tensile and flexural properties of FFF components could reach as far as 93% and 86% respectively when compared to injection mould components. Lastly, Netto et al. (2017) demonstrated that in a similar study but focused on PLA, it was possible to obtain tensile strength of around 86% of the value from injected components.

2.4.3 Main printer models

As previously mentioned in 2.1, the definition of *desktop printer* is commonly directed towards equipment that is sold for less than 4300€, being commercially available to any entity. However, due to the price range varying from as low as 130$ to 4300€, the quality may vary largely.

In order to better understand the current panorama of *desktop* FFF printers a market study was performed. During this stage it was taken into consideration the importance of not only components and quality of production, but brand-recognition, community support and customisability of the equipment as well.

As such, with these setpoints in mind, the following models were shortlisted, and summarised. No distinction between *do-it-yourself* (DIY) projects and kits[1] was made at this stage.

- **Prusa i3 MK3**

Visible in Figure 11, this model comes across as one of the most revered and commonly used printers inside the category of low-cost printers. Due to its popularity large community support groups exist and are focused on providing support for recurrent troubleshooting, as well as for upgrading existent components, seen as though this is an open-source device (which means that the manufacturers allow for the community to tinker with the devices' *firmware* and implement new modifications, in order to improve their products along with the community).



Figure 11 - Prusa i3 MK3 model. Obtained from "Prusa Research Original Prusa i3 MK3" 2017)

[1] Manufacturers such as the one referenced in Figure 11 sell custom made models that come partially pre-assembled. Although components are not assembled, the BOM for these devices are all standard.

- **DIY devices**

Unlike partially pre-assembled printers, these are totally dependent on what the person building it chooses to incorporate into its structure. As a consequence, the quality and investment required can vary largely, as visible on the summary Table 5. The fact that these types of devices have a large community base to provide support, as well as a steep learning curve, make it extremely interesting for a project that is focused on implementing multiple sensors and different upgrades to produce test specimens. An example of a device of this nature can be observed in Figure 12.

Generally these devices are built by following blueprints based on existing printers, such as the popular Prusa mentioned in this same chapter, and purchasing the required components from the BOM's referring to a specific model (RepRap 2018).

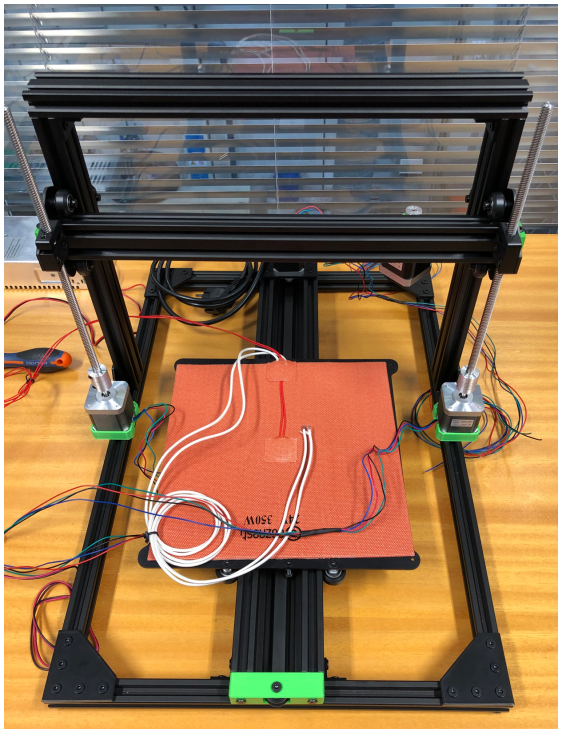


Figure 12 - DIY project being carried out at LDPS, based off blueprints obtained at RepRap.

- **Creality Ender 3**

By analysing its components and price point, this device, Figure 13, inserted itself at the very start of the category of low-cost printers. However, due to its reliability in terms of print quality and, overall, ease of use, it has amassed a large user base over the course of only a few months after its release in 2017.

Additionally, the fact that it is also an open-source device increases its overall interest towards a project such as the one proposed in this document, making it possible to implement new components down the line.

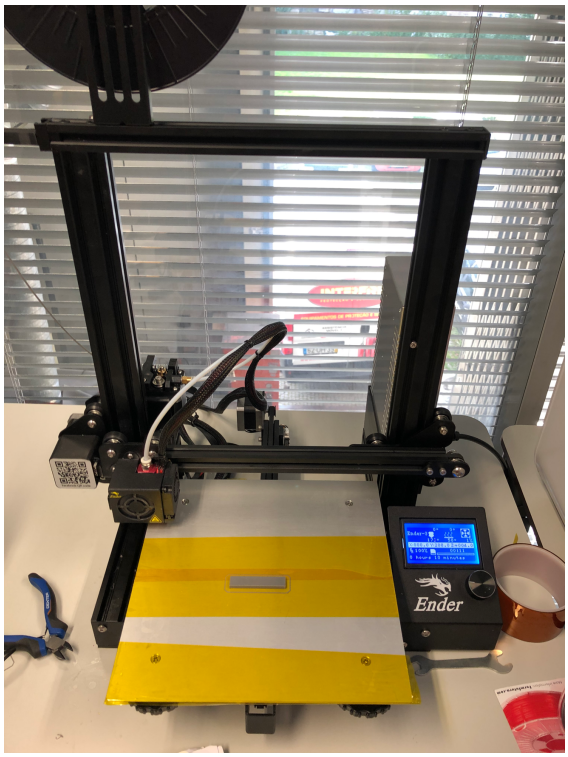


Figure 13 - Ender 3 by Creality (unaltered) used at LDPS.

- **Ultimaker 3**

During the research on the upper tiers of desktop printers, typical results pointed towards the Ultimaker FFF printers as being one of the most referenced devices. According to the manufacturer, devices such as the Ultimaker 3, visible in Figure 14, are used by Vokswagen to produce tools, jigs and fixtures, thus avoiding having to resort to external manufacturers (Vries 2017).

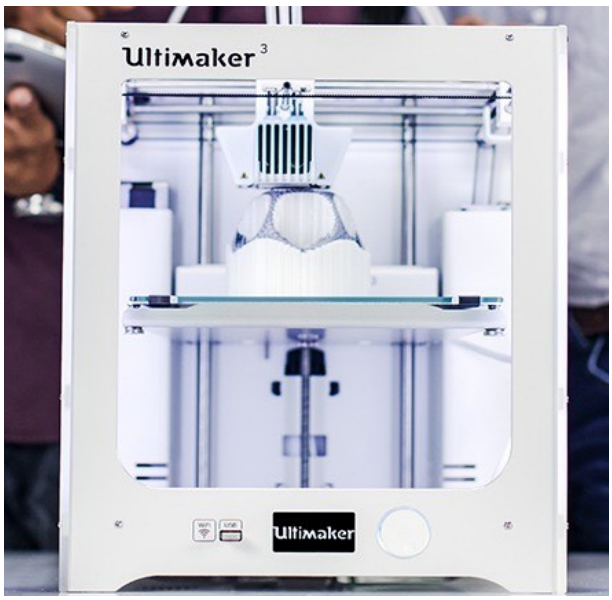


Figure 14 - Model of the Ultimaker 3, taken from Ultimaker (2016).

Focusing on the Ultimaker 3, still characterized as a desktop printer, this device is described as having a good build quality, reliable printing characteristics and a large range of materials available for printing. However, these devices are refrained to only being able to use proprietary components from Ultimaker.

- **Summary**

The previously presented devices all vary between themselves in terms of build volume, price-range and build quality, among other parameters. Below it is possible to observe a comparison between the devices.

Table 5 - Comparison between the referenced models in terms of price, build volume, materials, among other parameters. Table built by the author.

	Prusa i3 MK3	DIY Project	Ender 3	Ultimaker 3
Brand	Prusa	---	Creality	Ultimaker
Price	769€	1000€	170€	2995€
Build Volume	250x210x210 mm	250x210x210 mm	220x220x250 mm	215x215x200 mm
Min. layer height	50 µm	Varies	0,1mm	20 µm
Extruders	2	Varies	1	2
Materials	PLA, PETG, ABS, PP, TPU, others	PLA, PETG, ABS, TPU	PLA, PETG, ABS	PLA, PETG, ABS, PC, TPU, PVA, PP, CPE
Type	Open-source	Open-source	Open-source	Proprietary firmware
State of Assembly	Partially pre-assembled	Unassembled separate components	Partially pre-assembled	Pre-assembled

As it can be observed, Table 5 contains data gathered from manufacturers, retail sellers and annual reports. In 2018 the average price for desktop printers was estimated around 1000€, according to Wohlers et al. (2019). However, this value can largely oscillate depending on the number of features, frame materials and electronics used to build the device. As for DIY projects, the build volume and minimum layer height also may vary but are usually similar to the Prusa models, seen as though a vast majority are based off of them. As a matter of fact, the main characteristic of the DIY projects is that their feature range depends mostly on what the entity building them decides to implement, thus implying that parameters such as the number of extruders, work temperatures and viable materials can vary largely from printer to printer.

As for the printer with the widest range of workable materials, the Ultimaker stands out, being well suited to print (as provided) and maintain the higher temperatures required to print materials such as ABS, PC or other more demanding substances.

Out of all the mentioned printers, only the Ultimaker 3 runs solely on proprietary firmware, whereas the remaining devices are all considered as open-source printers and can suffer the implementation of desired modifications, such as the implementation of additional sensors, new components and respective *firmware* alterations.

2.5 Process parameters and influencing factors

Due to its additive nature, FFF allows for the possibility to produce extremely complicate designs with internal features that would be otherwise impossible to produce with traditional manufacturing methods. However, as stated by Górski et al. (2015b), this technology produces non-monolithic components that, combined with the weak bond between adjacent layers, are substantially weaker when compared to their injected counterparts, as well as presenting dimensional and geometrical inaccuracies.

In fact, in order to mitigate this effect, many studies have focused on determining the main influencing factors on the quality of the produced components and how to improve them, having found that chemical treatments, heat treatments, machining and the optimization of processing parameters all play a significant role, as summarized by Alafaghani et al. (2017).

Evidently, out of all the aforementioned information, the processing parameters stand out as being the only ones directly related to the printing process itself, whereas the remaining are all considered as post-processing appliances. In Table 6, along with Figure 15 and Figure 16, it is possible to observe a summary of the main parameters in an FFF process along with a description for each one of them.

Table 6 - List of process parameters, relevant concepts and their description.

Nr	Parameter	Description
1	Slice/Layer thickness	Thickness of the deposited layers according to the vertical axis.
2	Contours	Deposited filament that composes the outer shape of the component.
3	Raster	Deposited filament that composes the interior infill of the component.
4	Number of contours	Number of contours that compose the outer shape.
5	Raster width	Width of the raster.
6	Infill percentage	The infill percentage directly affects the gap between raster, being that the bigger the percentage, smaller are the gaps. This dictates the density of the component.
7	Raster angle/ Infill Orientation	Angle between the raster and the positive X axis direction from the build plate.
8	Build orientation	Orientation of the component in regard to the build plate's X, Y and Z axis.
9	Printing Speed	Speed at which the extruding end is moved during material extrusion.

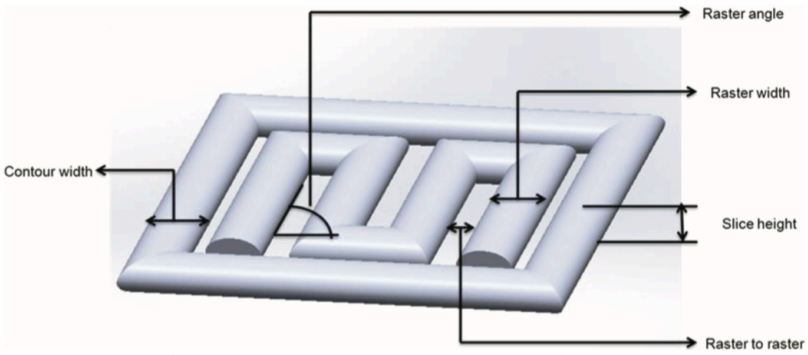


Figure 15 - Schematization of a layer produced by FFF with some of the process parameters represented. Taken from Shojib Hossain et al. (2014).

The parameters in Table 6 are all referring to the process itself and, evidently, it has to be considered that there are other extremely relevant parameters. According to Jamalabad et al. (1996), various parameter categories exist, such as process, machine, material and specific geometry, with the above-mentioned parameters all falling under the category of process specific. However, it is important to refer that they are also dependent on other material and machine specific parameters such as viscosity, thermal conductivity or nozzle diameter, filament diameter and extruder speed.

The way that these parameters influence the produced components can vary depending on whether it is only one parameter being altered or more, as well as in the scale that the alterations are done, as seen in Thrimurthulu, Pandey and Venkata Reddy (2004); Onwubolu and Rayegani (2014); Nancharaiah (2011), where the parameters under analysis were build orientation alone, build orientation coupled with layer thickness, raster angle, width and infill, or layer thickness, raster angle and infill, respectively.

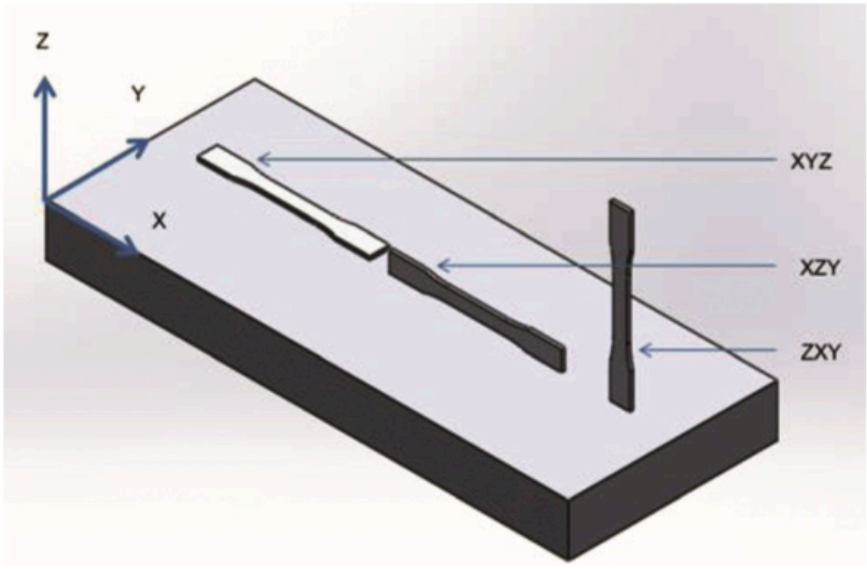


Figure 16 - Example of different build orientations possible. Taken from Shojib Hossain et al. (2014).

Lastly, it is pointed out the discrepancy in the amount of research being done at the moment for different materials, mainly when comparing the two most commonly used thermoplastics in *desktop* FFF printers: ABS and PLA. In Table 7 it is possible to observe the scarce amount of relevant research focused on AM PLA components, when compared to the extensive studies performed for their ABS counterparts, visible in Table 8. This fact further justifies one of the propositions of this work, which is the need for research on this topic.

Table 7 - Summary of relevant recent studies on the influence of various processing parameters in AM PLA components. Adapted from Popescu et al. (2018).

Study	Variable parameters	Analysis
Tymrak, Kreiger and Pearce (2014)	Variations of layer thickness and raster orientations	Tensile strength, elastic modulus
Ebel and Sinnemann (2014)	Infill pattern and percentage	Tensile strength
Wittbrodt and Pearce (2015)	Different coloration of the filament	Tensile strength
Lanzotti et al. (2015)	Layer thickness, print orientation, infill percentage	Tensile strength, elastic modulus
Torres et al. (2015)	Layer thickness, infill density, post processing heat-treatments at 100°C	Shear stress
Li et al. (2018)	Layer thickness, print speed, infill percentage	Tensile strength
Torres et al. (2016)	Temperature, infill direction, infill percentage, layer thickness	Tensile strength
Liu et al. (2017)	Deposition orientation, layer thickness, deposition style, raster variation, air gap	Tensile strength, flexural strength, impact strength
Santana, Lino Alves and da Costa Sabino Netto (2017)	Layer height, infill percentage, print speed, contours, extruder temperature, extrusion multiplier	Dimensional accuracy
Chacón et al. (2017)	Building orientation, layer thickness, feed rate	Tensile strength, flexural strength
Santana et al. (2018)	Building orientation, raster angle, raster pattern	Thermal, chemical, tensile strength

Table 8 - Summary of relevant studies on the influence of various processing parameters in AM ABS components. Adapted from Popescu et al. (2018)

Study	Variable parameters	Analysis
Bertoldi et al. (1998)	Building orientation, raster orientation	Tensile strength, yield strength, elongation, elastic modulus
Rodríguez, Thomas and Renaud (2001)	Air gap and flow rate	Stress-strain behaviour
Ahn et al. (2002)	Raster orientation, air gap, raster width, colour, temperature	Tensile strength, compressive strength, comparison with injection moulding
Lee, Abdullah and Khan (2005)	Raster, air gap, raster width, layer thickness	Application to a practical model
Sun et al. (2008)	Temperature profiles	Flexural strength, thermal analysis
Sood, Ohdar and Mahapatra (2010)	Layer thickness, orientation, raster angle, raster width, air gap	Tensile, flexural and impact strength, development of empirical models
Fatimatuzahraa, Farahaina and Yusoff (2011)	Raster orientation	Tensile strength, flexural strength, impact strength
Sood, 2012 Sood, Ohdar and Mahapatra (2012)	Layer thickness, building orientation, raster angle, raster width, air gap	Compressive strength (analytical and experimental)
Croccolo, De Agostinis and Olmi (2013)	Raster pattern, raster angle, building orientation	Tensile strength, stiffness
Durgun and Ertan (2014)	Raster angle, building orientation	Tensile strength, flexural strength
Gorski (2014)	Build orientation	Impact strength
Baich and Manogharan (2015)	Infill percentage	Tensile strength, compression strength and flexural strength
Górski et al. (2015a)	Build orientation	Tensile strength
Ziemian, Sharma and Ziemian (2012)	Raster orientation	Tensile, compressive, flexural and fatigue strength
Onwubolu and Rayegani (2014)	Layer thickness, part orientation, raster angle, raster width, air gap	Tensile strength
Tymrak, Kreiger and Pearce (2014)	Layer thickness, raster orientation	Tensile strength, elastic modulus
Ebel and Sinnemann (2014)	Infill pattern, infill percentage	Tensile strength
Rankouhi et al. (2016)	Layer thickness, raster orientation	Tensile strength
Letcher, Rankouhi and Javadpour (2015)	Layer height, raster orientation	Tensile strength, Elastic modulus, elongation at break
Fernandez-Vincente, 2016 Miguel et al. (2016)	Infill percentage, infill pattern	Tensile strength

2.5.1 Layer Thickness

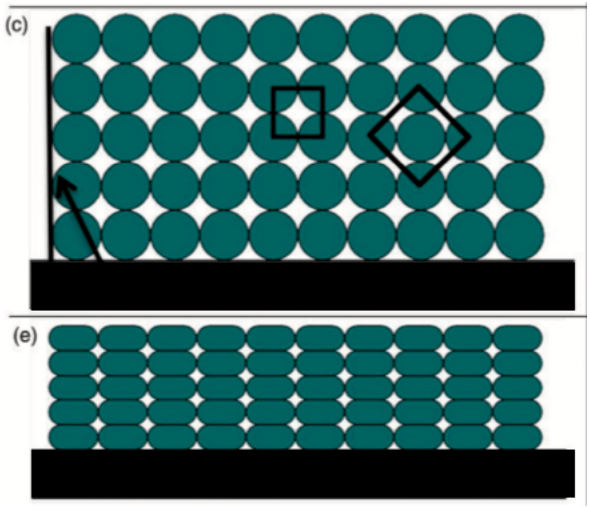


Figure 17 - Influence of the layer height in the shape of the deposited filament. Adapted from Akhoundi, Behravesh and Bagheri Saed (2019).

As previously mentioned, layer thickness consists of the height each layer of the component has, with typical values usually ranging from approximately 0,1mm to 0,3mm, depending on the size of the nozzle. The layer thickness is directly correlated with the shape of the deposited filaments, given that the closer it gets to the value of the nozzle diameter, the rounder it will get, and as it gets smaller the raster become similar to a round-cornered rectangle (Akhoundi and Behravesh 2019), as it can be visible in Figure 17.

In fact, the most evident effect caused by using increasingly higher layer thicknesses is the *staircase effect*, which is the result of the successive deposition of bi-dimensional layers with different sections to form a three-dimensional component (Jamalabad et al. 1996) and can be observed in Figure 18. This side-effect has been shown to directly influence the superficial roughness of the components, being that the less prominent this effect becomes by using smaller layer thicknesses, the better the obtained surface finishes are, despite increasing build time. Udroiu, Braga and Nedelcu (2019) inclusively state that this parameter is the most influent one regarding surface finish in AM components.

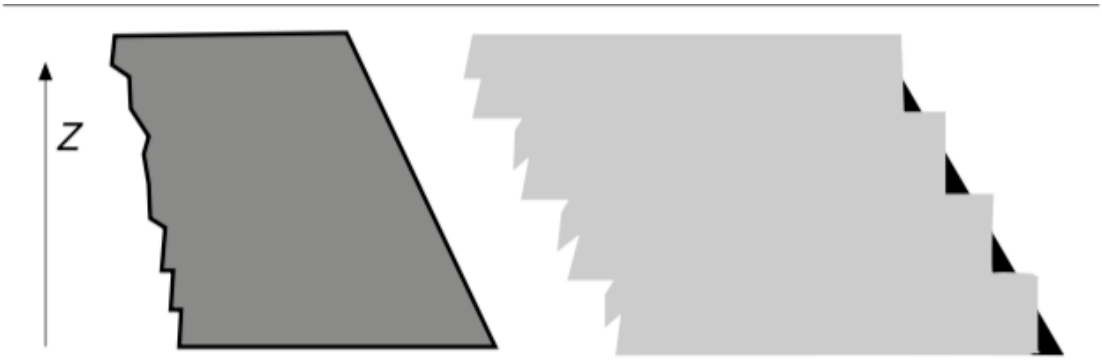


Figure 18 - Representation of the staircase effect in FDM produced componentes (Jamalabad et al. 1996).

Additionally, Alafaghani et al. (2017) also denoted the importance of layer height regarding dimensional accuracy for produced components in two ways: smaller layer heights tend to yield lower error values and the error tends to increase if component is not an integer multiple of the defined layer height.

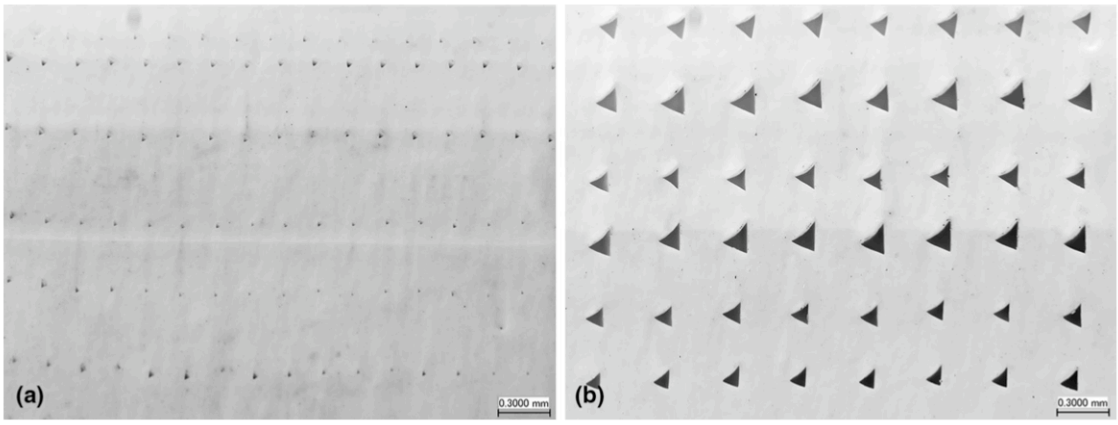


Figure 19 - Influence of layer height in the air gap and bonding area dimensions. Adapted from Rankouhi et al. (2016).

Regarding the effects on mechanical properties, Onwubolu and Rayegani (2014) first stated that for minimum layer heights it was possible to obtain higher tensile strength, which was later reinforced by others, such as Lanzotti et al. (2015), and Chacón et al. (2017), who also state that the tensile strength of produced components was found to be maximum at lower value of layer thickness along with their ductility, as well as the fact that ductility is decreased with increment in layer thickness. According to Rankouhi et al. (2016), an explanation for this phenomenon is the fact that with lower layer heights, the air gaps between layers becomes smaller, as well as the fact that bonding areas between layers become larger, as it can be observed in Figure 19. Later works have confirmed these claims, providing more evidence, such as Figure 20, that layer height indeed influences the tensile properties of test specimens in such a way. However, Torres et al. (2016) provide interesting research information that as the relative density of the components decreases, smaller layer heights actually contribute to decrease tensile strength, mostly due to the fact that more flaws tend to appear, as will be further discussed in 2.5.5.

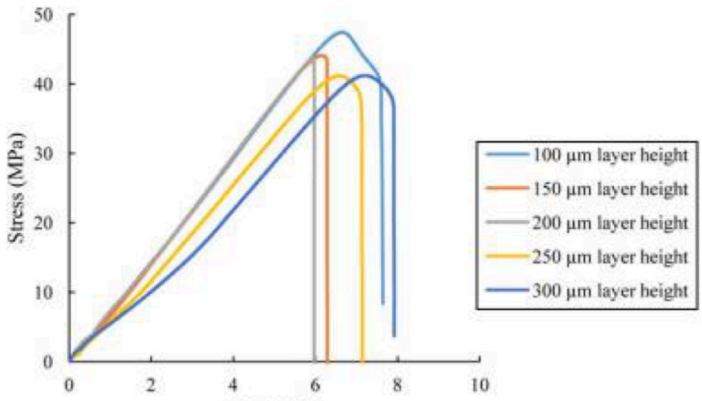


Figure 20 - Influence of layer height in the tensile strength of 3D printed components (Rajpurohit and Dave 2018).

2.5.2 Contours

The contour consists of a pre-defined number of rasters that are deposited along the edges of the component, basically dictating its geometry, and can vary in number, with at least one being typically used and no limitation to the maximum number of contours (aside from the dimension of the component itself) (Volpato et al. 2017), as it can be seen in Figure 21.

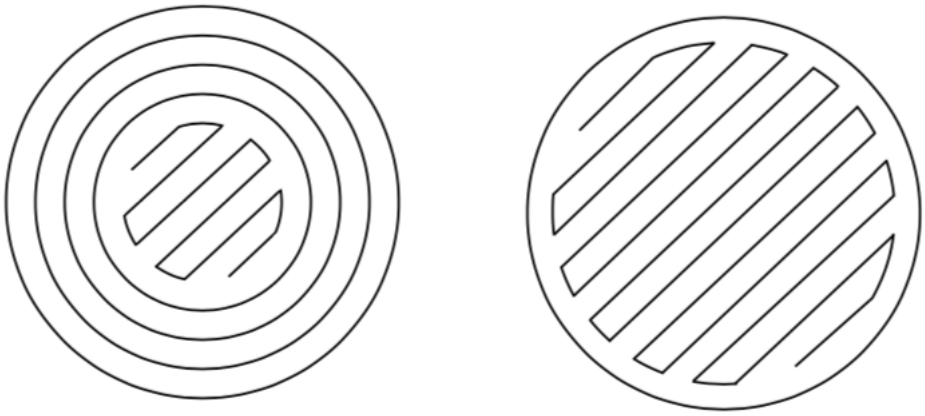


Figure 21 - Different number of contours that can be used to produce the same geometry, with three contours on the left and only one on the right. Adapted from Jamalabad et al. (1996)

The number of contours, also known as perimeters, is directly related to the resistance of AM produced test specimens, seen as though they are deposited along their longitudinal direction, which coincides with the axial load, thus contributing to resist solicitations. As such, the higher the number of contours is, the larger the tensile load resistance becomes, due to the higher number of fibres displayed along the solicitation direction (Lanzotti et al. 2015). This effect tends to decrease with the decrease in raster angle, becoming almost statistically irrelevant for raster angles of 0°.

2.5.3 Raster Angle

Raster angle, also called infill orientation, consists of the degree that the raster is deposited in regard to the X axis as it can be seen in Figure 22, typically assuming values in the order of 0°, 45°, ±45° and 90°.

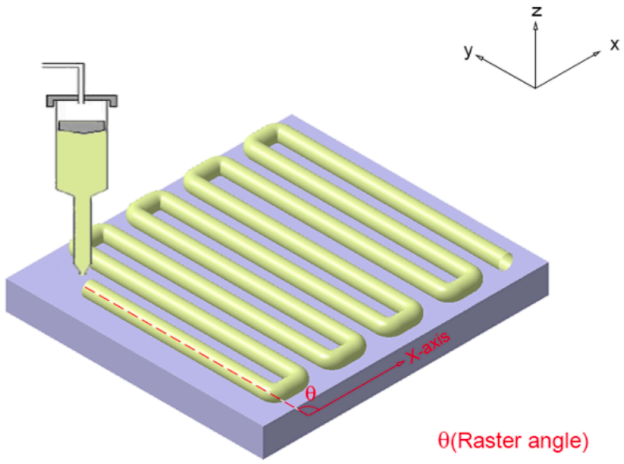


Figure 22 - Graphical definition of raster angle. Taken from Wu et al. (2015).

This parameter has been shown to influence certain aspects of AM components, such as the creation of defects and insufficient material deposition in certain geometries. Tymrak, Kreiger and Pearce (2014) showed that for certain curved edges, such as the one shown in Figure 23, it is not possible to fully deposit material in the entire section of the component, which leads to early fracture and fracture outside of the minimum section zone in tensile test specimens and complicates the analysis of mechanical trials.

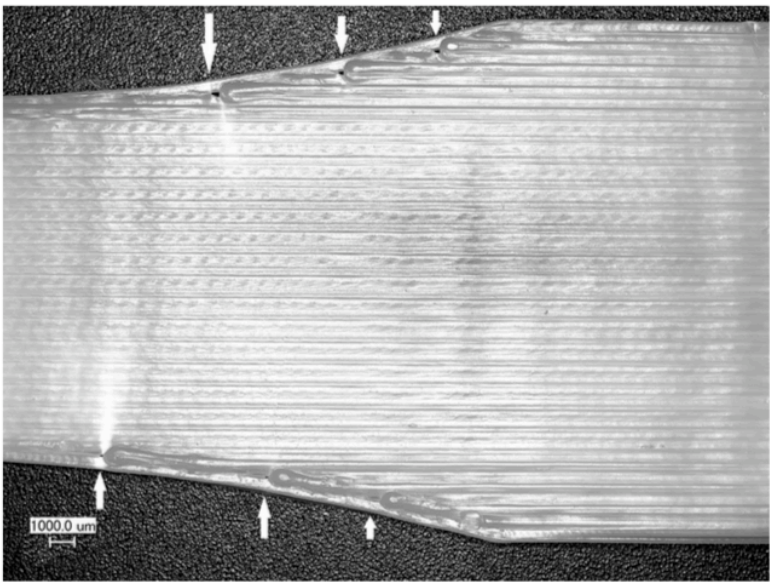


Figure 23 - Imperfections and lack of filament deposition in curved geometries due to raster angle. Adapted from Rankouhi et al. (2016).

However, in cases where such defects are absent it has been shown that the tensile strength of components is actually increased by using smaller raster angles such as 0° and ±45°, when in comparison to 90°, due to the increasingly bigger orientation towards the solicitation direction. Additionally, the fracture mode also varies depending on the raster angle that is used, as it can be seen in Figure 24, where tensile test specimens are displayed with different raster angles used in their construction and compared side by side.

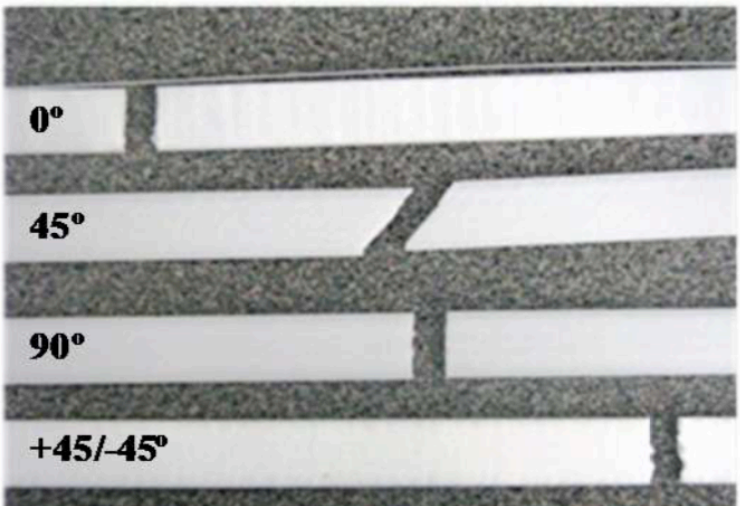


Figure 24 – Comparison of fractures modes between different raster angles (Ziemian, Sharma and Ziemian 2012).

As visible in Figure 25a), for test specimens with 0° the fracture occurs in a transverse path with some delamination and fibre pull-out, with some plastic deformation in whiter areas, whereas for test specimens with 90° raster angle the fracture occurs along the interface between two separate filaments, which can be explained due to the weaker bonds that exist in these interfaces. For test specimens with 45° there is an evident path of 45° across the width of the fracture zone, whereas in the ±45° the fracture occurs at the intersection of 45° and -45° degrees (Ziemian, Sharma and Ziemian 2012).

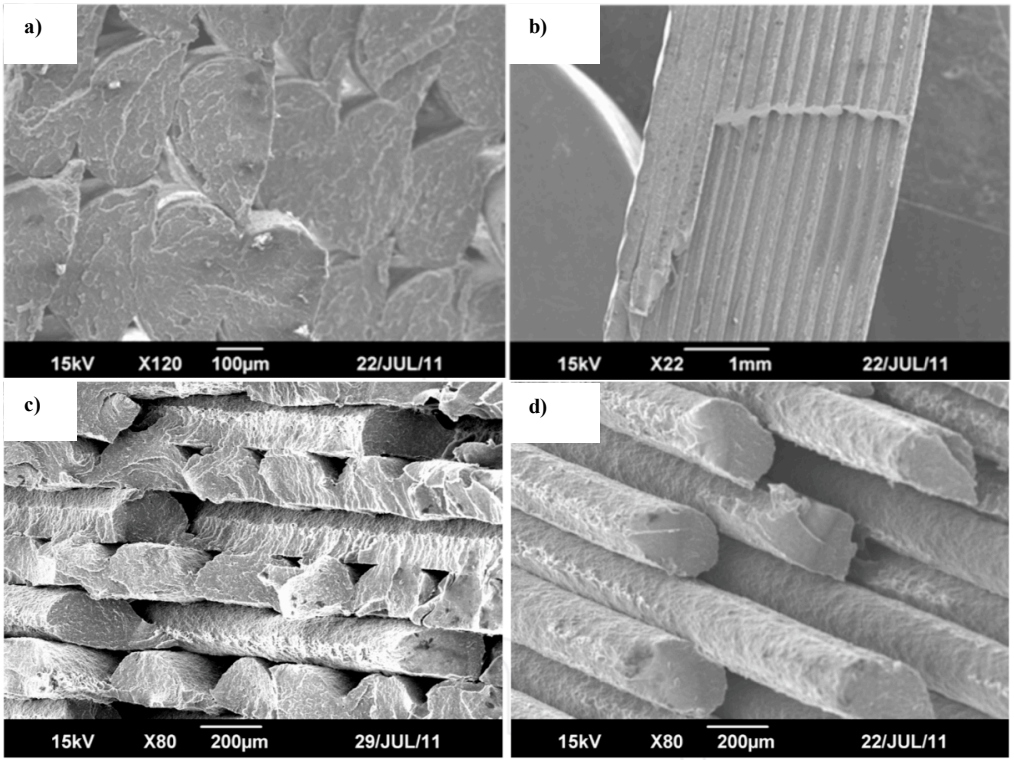


Figure 25 - SEM analysis of fracture surfaces in a) 0° b) 90° c)±45° and d)45° test specimens (Ziemian, Sharma and Ziemian 2012).

2.5.4 Raster Width

Raster width is, as the name implies, the width of the deposited filament as shown in Figure 26.

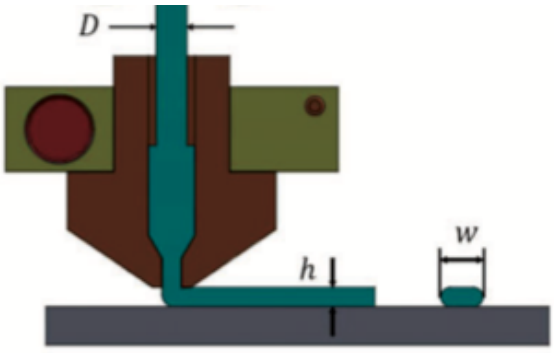


Figure 26 - Raster width (w) of the deposited filament. Adapted from Akhoundi, Behravesh and Bagheri Saed (2019).

This is a parameter that, at the moment, does not yet have as many studies focused on its influence in the properties of FFF components. However, some publications have enabled to draw interesting conclusions, such as the fact that for small raster widths, the higher this value becomes, the higher the bond strength is. This is due to the fact that there is more thermal mass, which causes the raster to cool down slower and remain at glass transition temperature for longer stays, thus improving the bonding between adjacent raster (Coogan and Kazmer 2017). Additionally, the higher raster width also means a higher contact area in-between layers that increases bond strength in the components. However, Rajpurohit and Dave (2018) discovered that for bigger raster widths (above 600µm), the tensile strength becomes gradually smaller (shown in Figure 27, mostly due to the fact that the void between layers becomes larger as well, which leads to crack initiation and lower tensile strength.

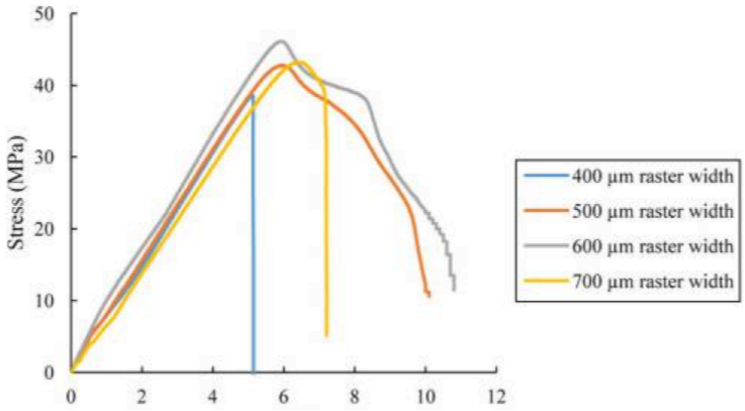


Figure 27 - Stress - Strain curves for tensile trials with different raster widths (Rajpurohit and Dave 2018).

2.5.5 Infill percentage

It is common practise in the FFF method to construct components with only a fraction of their bulk actually being solid, in order to decrease the weight of the components as well as reduce the amount of material and cost for each component. This technique consists of altering what is called as the infill percentage, which basically increases the amount of void areas in each layer. This value is either a percentage of the total inner volume or a distance between two consecutive rasters in each layer, always taking into consideration the defined raster angle. While

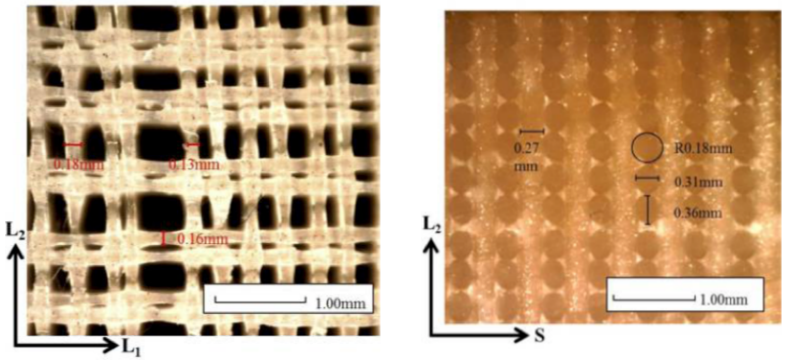


Figure 28 - Differences in air gap between fibres and the width of the fibres them selves, as a result of the smaller infill percentage (35%), on the left, and 100% infill percentage (on the right). Adapted from Torres et al. (2016).

defining this parameter usually a pattern for the way the filament is to be deposited is defined as well, in itself an important process parameter that will be further discussed.

As for the influence of the infill percentage, Torres et al. (2016) showed that using infill percentages smaller than 100% tends to originate a larger number of flaws in the weaving of the fibre patterns, shown in Figure 28, due to the fact that there is less control of the way the filament is deposited, as well as its width, because of large gaps between fibres.

2.5.6 Infill Pattern

The infill pattern relates to the geometry/structure that the inner parts of a partially solid AM component possesses, and it can assume different shapes, capable of conferring properties to that same component. In fact, the ability to produce components with intricate infills is one of the most interesting characteristics of AM processes when in comparison to traditional manufacturing methods, seen as though some geometries are either extremely difficult and expensive to obtain or even impossible by these methods (Compton and Lewis 2014).

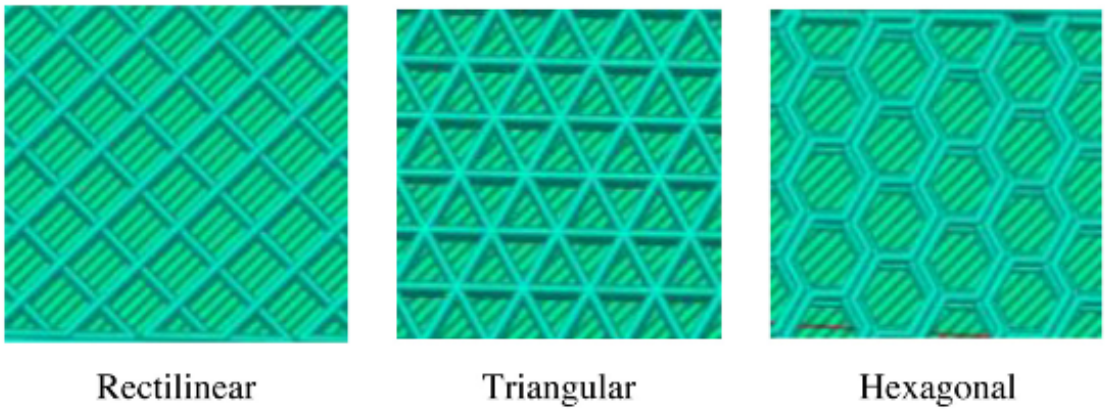


Figure 29 - Examples of the infill patterns commonly used and studied by Alafaghani and Qattawi (2018).

Alafaghani and Qattawi (2018) found that certain patterns such as a hexagonal one, shown in Figure 29, commonly named as a *honeycomb structure*, produces components with the highest stiffness and strength but with low ductility, whereas triangular and rectilinear patterns produce components with high ductility. As for the influence on dimensional accuracy, it was noted that rectilinear infill patterns often yield smaller errors when compared to triangular and *honeycombed* patterns. Additionally, in terms of influence on the mass of the components, patterns such as the triangular one led to the increase of mass when in comparison to rectilinear and *honeycombed* structures.

According to Lubombo and Huneault (2018), the disposition of the infill pattern has similar influence to the one contours have in terms of uniaxial tensile strength, declaring that for infill patterns that allow higher cross-sectional area in the direction of the solicitation, the value of this mechanical property is enhanced. The authors also stated the interesting effect that hexagonal patterns, typically named *honeycomb-structures*, can have in terms of lightweight energy absorption due to their long plateau regimes.

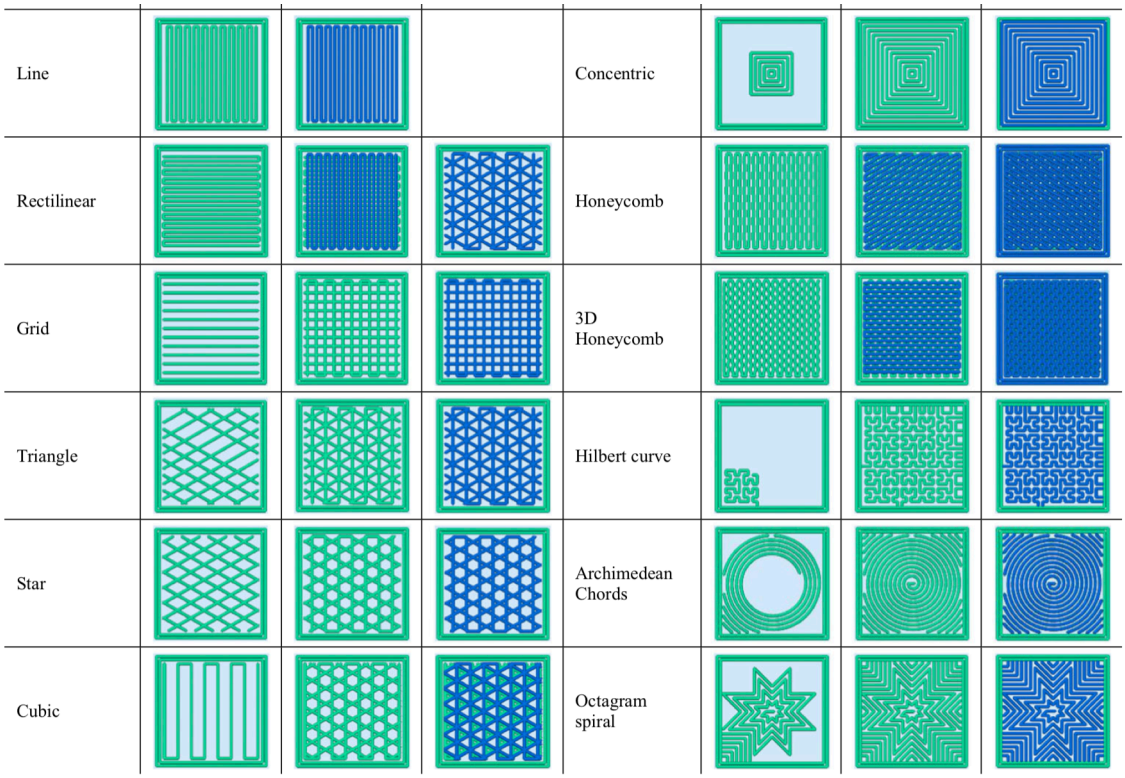


Figure 30 - Various types of infill patterns that are typically used. Taken from Akhoundi and Behravesh (2019).

In addition to the more typical patterns shown in Figure 30, recently there has also been a surge in the interest of using cellular structures with organic and repetitive patterns for sandwich structures and composites, as well as the implementation of mathematical models, as is the case of the gyroid infill visible in Figure 31 and recently investigated by the MIT due to its interesting mechanical and isotropic properties when produced by AM methods.

Clearly there is yet a small amount of research available for the influence of infill patterns in the mechanical and dimensional properties of AM components, which leads to the necessity of further investigation on these aspects.

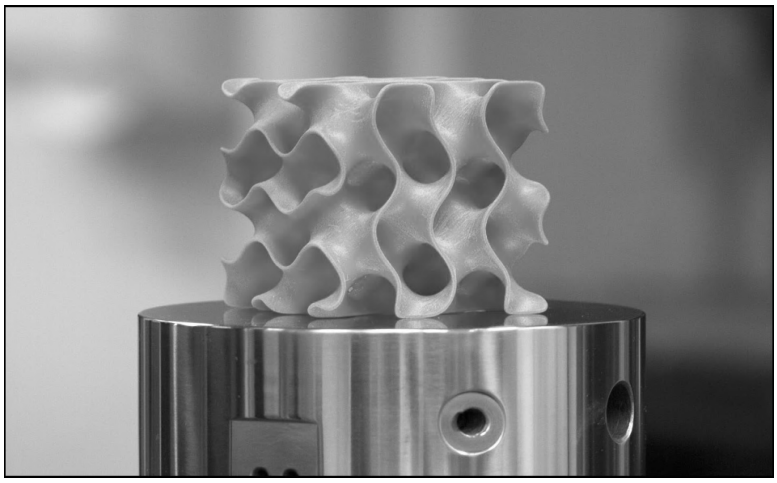


Figure 31 - Photograph of the gyroid model already being used for infill patterns (Gonick 2018).

2.5.7 Air gap

Raster air gap consists of the distance at which each raster is deposited from its adjacent fibres and, as such, it can either be a positive, null or negative value as it is shown in Figure 32.



Figure 32 - Different types of air gaps. From left to right: positive, null and negative. (Akhoundi, Behravesh and Bagheri Saed 2019).

Although this parameter is affected when the infill percentage is altered (Volpato et al. 2017), it is important to still distinguish one another, seen as though, even for 100% infill, it is possible to alter the value of the air gap, with significant consequences to the components' mechanical properties. Typically, this parameter is set to positive if the intent is to minimize the production times and, according to Rayegani and Onwubolu (2014), it should be set for negative for better tensile properties to be obtained, while respecting a ratio between air gap to raster width so as to avoid over-filling phenomena. This further helped complement what was stated by Sood, Ohdar and Mahapatra (2010) in regard to the fragilization of components with excessively negative air gap, where heat dissipation was restricted and caused stress accumulation. The fact that negative air gaps tend to yield better mechanical properties overall is due to the larger proximity the components have to their injection moulded counterparts in terms of density, being able to reach as much as 98% of the bulk volume. Conversely, the bigger the air gap becomes, the smaller the contact surface between adjacent rasters becomes, leading to weaker bonding (Dawoud, Taha and Ebeid 2016), as it can be observed in Figure 33.

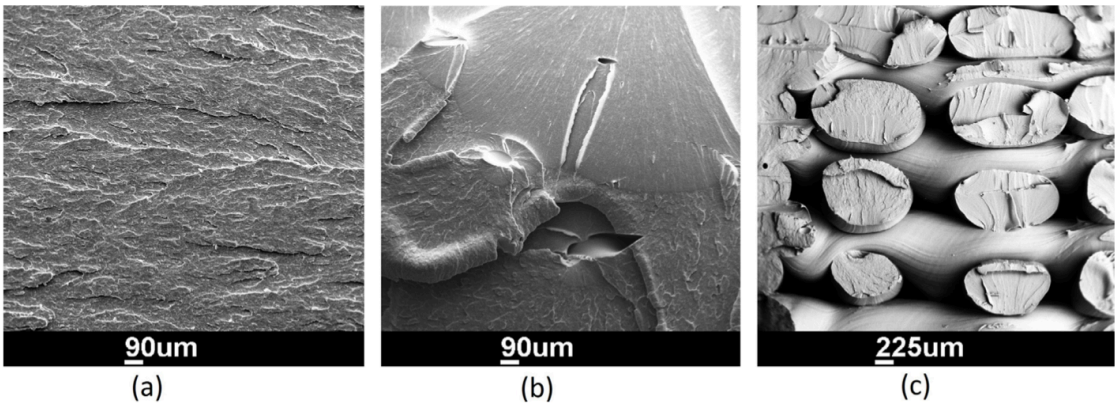


Figure 33 – Comparison between the dimension of injection moulded (a), negative air gap (b) and positive air gap (c). Taken from Dawoud, Taha and Ebeid (2016).

However, Ahn et al. (2002) did state that negative air gaps, although capable of yielding better mechanical properties to the components, can produce zones with excess of material and degraded surface quality, as well as poor dimensional tolerances. This is due to the constant overlapping of deposited rasters and should be taken into consideration when building components for applications where surface finish and dimensional precision are relevant factors.

2.5.8 Build Orientation

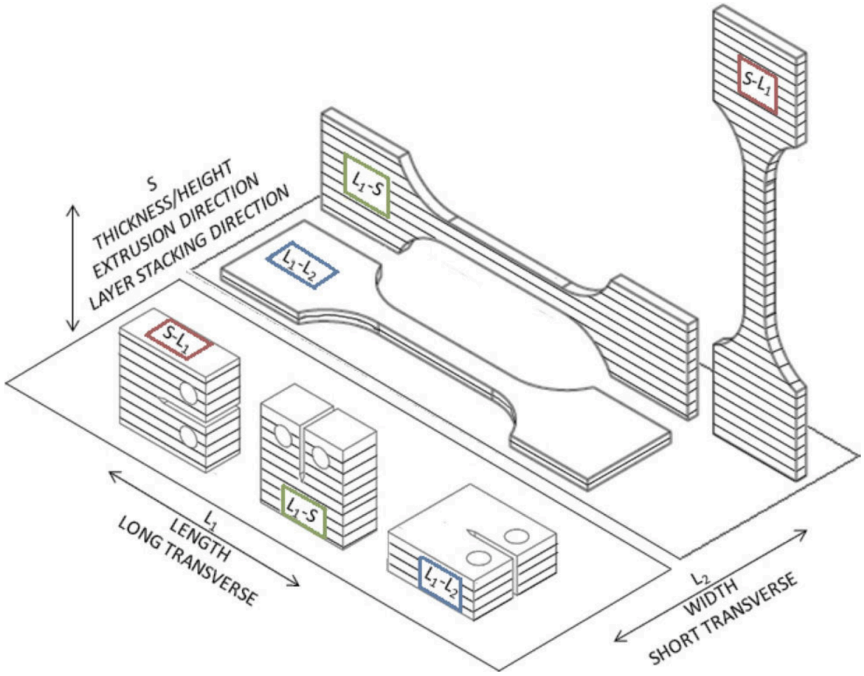


Figure 34 - Example of the various typical build orientations that different test specimens can be printed at. Taken from Torres et al. (2016).

As it can be observed in Figure 34, the build orientation can assume a wide range of settings, as well as confer different characteristics to the components depending on the solicitations they'll be subjected to. By changing this parameter, the user will be displaying the component under a certain rotation angle for each of one of the separate axis, X, Y and Z. Shojib Hossain et al. (2014) showed that orientations XZY, XYZ and ZXY (reference to Figure 16) yielded significantly different values for tensile strength due to the way the components were built, with the XZY orientation yielding the highest values, followed by XYZ and, significantly lower, ZXY. This was due to the fact that for the ZXY orientation, all the deposited layers were perpendicular to the solicitation direction, whereas in the XZY direction, all the layers were oriented in the same direction as the load during the test trials.

Later, Torres et al. (2016) generalized that the optimal direction for a certain component is the one that allows for the placement of the fibres in way that the largest cross-sectional area per printed layer is oriented in the same way as the solicitations applied to it.

However, the build orientation is also extremely relevant in terms of surface roughness and geometrical accuracy. Seen as though the process consists of consecutive deposition of bidimensional layers, certain geometries like curved surfaces or overhangs tend to present a challenge for certain building orientations. As an example, taking the test specimens from Shojib Hossain et al. (2014), in cases where tensile strength was the most important aspect, then the XZY orientation would be the optimum solution. However, if geometrical accuracy and material waste were factors to be considered, then this orientation should be deterred in favour of the XYZ orientation, due the fact that in that case, there would be overhangs with support material and the fillets would have *staircase-effect* replicas.

2.5.9 Printing speed

Printing speed consists of the speed at which a raster is effectively deposited throughout a layer, a process parameter which comes across as highly influential in regard to the build time, seen as though the higher speeds of deposition mean that each layer is completed in shorter amounts of time.

Christiyan, Chandrasekhar and Venkateswarlu (2016), Ning et al. (2017) and Chacón et al. (2017) provide statistical data for analysis regarding the influence on the mechanical properties of components, showing that the increase in speed rate may lead to a small decrease in tensile and flexural resistance of AM components, proving justification in the fact that with the increase in infill speed, the rasters became sparser and porosity increased due to shorter deposition times translated into weaker bonding between adjacent rasters.

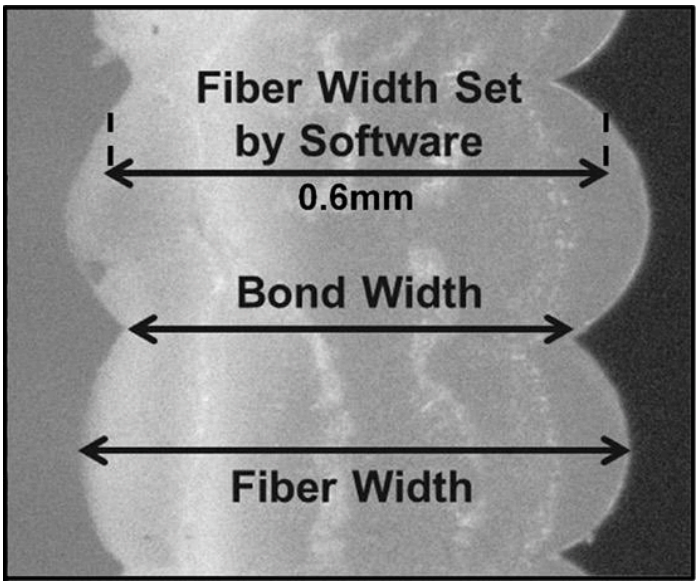


Figure 35 - Discrepancies in extruded fiber width and predicted fiber width. Adapted from Coogan and Kazmer (2017).

However, information has also been published by others such as Pan et al. (2016) or Coogan and Kazmer (2017), who provide statistical evidence that higher printing speeds can indeed produce components with stronger bond strength, usually linked to better mechanical properties. A common justification for this is the fact that with higher interface temperatures in an already deposited layer at the start of the deposition of the adjacent layer, the diffusion rate increases and benefits the bonding strength between the two of them.

Additionally, Coogan and Kazmer (2017) call out to the importance of print speed in terms of raster width and refer that at higher printing speeds, raster width is not always according to what is specified in the *slicing* software, as it can be seen in Figure 35. This can lead to insufficient wetting between fibres and the formation of void structures, harmful to the mechanical properties of the produced components. It is also relevant to consider that this phenomenon might have occurred either due to the used motor not having enough torque to push out the required amount of filament, or the need to use higher processing temperatures in order to increase fluidity of the material.

Due to the discrepancies in obtained results by different works in the past, it became clear that there is yet room for more research when it comes to the influence

of printing speed on the mechanical properties of AM components, specifically made of PLA. Thus, this parameter is to be considered as one of the factors for the experimental phases. Furthermore, it would also be quite interesting to study the influence this parameter might have on the dimensional accuracy of the FFF method.

2.5.10 Extruder temperature

Taking into consideration that the principle of the FFF method is the extrusion of a semi-fluid material through a fixed diameter nozzle, it becomes evident that the temperature at this component, responsible for maintaining the filament in a state with low enough viscosity to be extruded at a constant rate, is of extreme relevance and, as such, gathering knowledge regarding this process parameter becomes extremely important.

According to Torres et al. (2016), extruder temperature is a highly influential parameter in terms of mechanical properties of the AM components in a manner that higher temperatures are usually favoured. In order to understand this, it is convenient to understand the way how extruder temperature is measured, explained in 3.4.1. Considering the small size of the extrusion nozzle, it is nearly impossible for *desktop* FFF devices to get a measure that comes from the component itself and, as such, the extruder temperature is actually approximated by the temperature of the heating block, as close to the nozzle as possible, not considering eventual heat dissipation phenomena. Consequentially, the temperature at which the filament is actually extruded may be, depending on the structure of the device being used to print out the components, lower than what is specified in the *slicing software*. Taking this into consideration and depending on the processing window of the material being used, the temperature at which the filament is extruded may not favour adhesion between layers due to the smaller amount of thermal energy being exchanged.

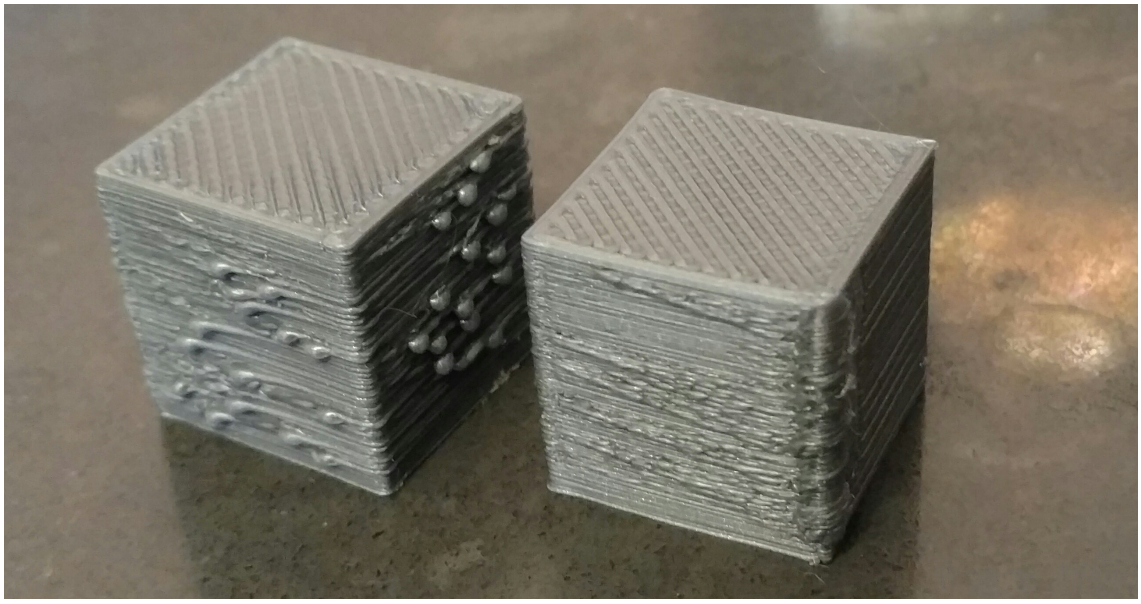


Figure 36 - Typical consequences of dimensional and geometrical error caused by the use of higher than reccomended extruder temperature.

However, operating with temperatures higher than recommended by producers and/or the adequate processing window for a specific type of material, can also cause problems such as over-extrusion and improper cooling. As the printing occurs, thermal gradients from top to bottom of the component become larger as total height is increased Sood, Ohdar and Mahapatra (2010) state that these thermal gradients lead to the accumulation of inner stresses in the fibres and posterior formation of cracks, de-lamination, both factors which compromise the components' strength and even dimensional/geometrical aspects, as it can be seen in Figure 36, mostly on the left cube.

Due to the importance of this aspect and the somewhat scarce information regarding its influence on the mechanical and dimensional properties of PLA AM components, it would be extremely relevant to further investigate on this topic as part of the experimental stage.

2.5.11 Build surface temperature

A typical component for almost any 3D printer is a heated bed, which basically consists of a build surface that can be heated and maintained at a certain temperature during the printing stage. This is done so that the adhesion between the component's first layer and the build surface is enough to withstand the thermal contraction that occurs as the layers are successively deposited, thus avoiding the appearance of deformations or invalidation of the component. However, excessive temperatures can lead to over adhesion to the build surface and consequent damaging of the component during its extraction. Aside from the temperature itself, some common recommendations to increase adhesion are the proper cleaning of the surface area, maintaining it properly levelled, use of polymeric films, water-soluble glues or hair-sprays and utilizing surfaces with the same material as the one being used to construct the component.

According to Spoerk et al. (2018) the optimum relation between build surface and adhesion can be obtained for temperature values of slightly above the glass transition temperature of the polymer being used. In the case of PLA, with a glass transition of around 60°C, when the build surface was kept at this temperature the adhesion forces (measured with a device specifically for that purpose) where substantially increased in comparison to situations where the temperature was below 60°C. According to Jabbari and Peppas (1994), when a polymer is at its glass transition temperature, the segmental mobility of macromolecules is the highest it can be, which is a condition that allows for polymer segments to be diffused into the surface and adhere better to this component. On the other end, if the temperature is raised further than the 70°C, then warping phenomena occur and the adhesion forces are decreased (Kim, Heo and Kim 2010).

2.5.12 Slicing software

Slicing software is responsible for providing the required input to actually enable a 3D printer to build the desired components. These types of software do so by creating a command file, typically G-Code in the case of *desktop* FFF printers, that acts as a script and contains all the information regarding:

- Build area dimensions;
- Machine specifications;
- Trajectories required to build the component;
- Filament Diameter;
- Amount of extruded filament;
- Layer height;
- Temperatures;
- Speeds;
- Other relevant process parameters.

Considering that this type *software* is responsible for dictating how the components are built, it is relevant to understand the differences between different *slicers* and how they actually work.

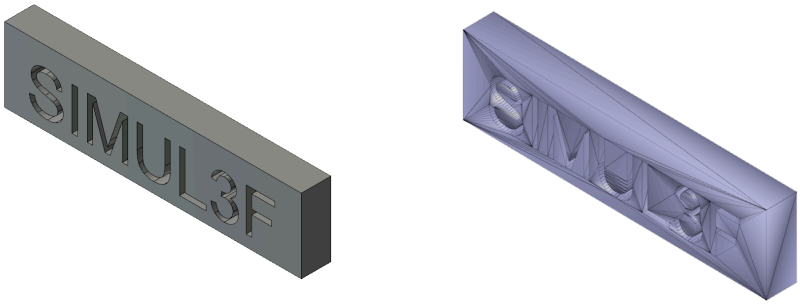


Figure 37 - Creation of an STL file (right) by inputing a 3D CAD model (left).

Basically, what *slicing* software does is split an STL file as the one shown in Figure 37 into an integer number of bi-dimensional layers that represent consecutive cross-sections of the STL file. The geometry for each layer and the amount of material to be deposited is calculated by a set of algorithms, all of which can vary depending on the *slicing software* that is being used, hence the influence that using different *slicers* can have in AM components properties (Gibson, Rosen and Stucker 2009). After the geometries for each layer are all defined, an output like the one shown in Figure 38 is given by the software and transferred to the machine.

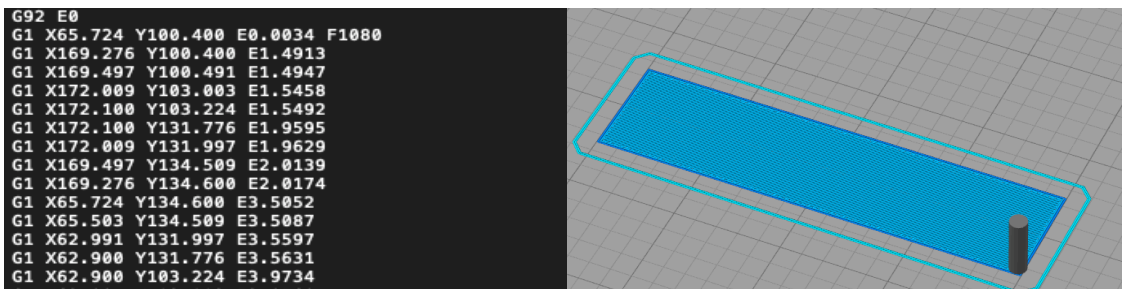


Figure 38 - Portion of a G-Code file (left) and its graphical representation of the slicing software (right).

Some examples of situations where using the same process parameters to build the same components, but using different *slicers* are the one that Santana, Lino Alves and da Costa Sabino Netto (2017) report, where dimensional errors were mostly due to the way the *slicing software* calculated the amounts of material to be extruded, causing the dimensions and mass to be different than the expected. A graphical example of this was also shown by Baumann et al. (2016) when he paired different *slicers* against each other to build the same geometries and analysed the output, as seen in Figure 39.



Figure 39 - Discrepancies between different slicers when building the same geometries. Taken from Baumann et al. (2016).

2.6 Summarization

At this stage, after having processed the information regarding the process parameters and other influencing factors, it was possible to outline some relevant points.

First off, it was noted that different process parameters such as layer height, build orientation, raster angle, air gap or even the infill pattern that is used exert influence on the outcome of the components' mechanical properties, mass, dimensional and geometric features.

The most typically studied parameters have been layer height, build orientation and air gap, mostly due to their large influence on the resulting tensile properties and surface finishes. Additionally, a large sum of the revised studies focused solely on the optimization of the process parameter selection as a mean to improve tensile resistance, with the outcome being a range of optimum values for different combinations of these parameters.

Secondly, it was observed that parameters such as print speed, extruder temperature and nozzle diameter do not yet have a significant amount of conclusive research regarding the mechanical and dimensional properties of the produced components. Ultimately, the amount of conclusive research that is lacking for print speed influence, as well as the contradictory information found regarding this process parameter, coupled with the importance of extruder temperature for the proper functioning of this manufacturing method, led to the decision to choose both of these parameters as the ones to be variated in the experimental stage.

In addition, it was noted that the amount of studies focused on obtaining simple empirical models, which could be used in later stages, was also lacking in terms of quantity. This was, in part, due to the fact that the use of design of experiments (DOE) techniques such as the Taguchi Method (which was used in a large part of literature that was revised) did not allow for large amounts data to be outputted, due to the omission of some of the combinations resulting from the studies at hand.

Considering this, the opportunity to analyse the influence of print speed and extruder temperature arose, recurring to a full-factorial DOE. This would, in turn, allow for the output of enough data to create phenomenological curves and smoother predictive models.

3. Experimental stage - materials and methods

At this stage, the experimental work was initiated, with the flowchart from Figure 40 showing the main procedures that were outlined as necessary for the realisation of this work.

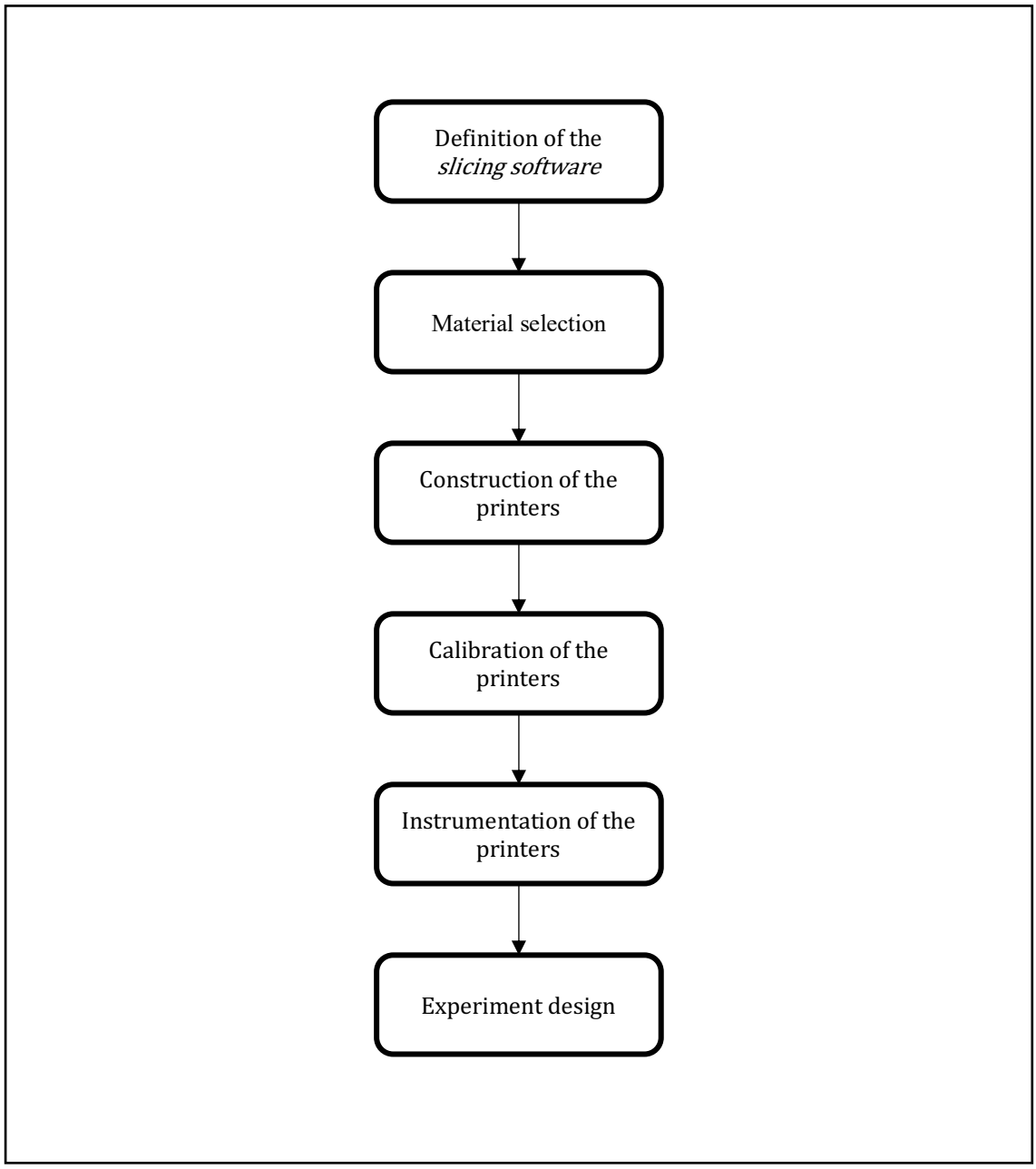


Figure 40 - Adopted methodology for the experimental stage.

3.1 Software

In order to prepare the required files, printing profiles for the production of the test specimens and to calibrate the used devices, Simplify3D® was used. This *slicing* software allows for the importation and reparation of STL files, along with the choice of parameters regarding the process itself, the components and the material being used. This *slicer* already had pre-set profiles for commonly used devices, which helped establish a base for some of the parameters, as well as a fairly user-friendly interface, shown in Figure 41, that allowed for the manipulation of a wide range of specifications. These considerations helped decide which *slicer* to use from a range of similarly capable *software* such as Slic3r, Slic3r PE or Cura.

Another extremely relevant aspect of this *software* was the ability to save various profiles with the different alterations required for each of the printing conditions, easily alternating between them and ensuring a good workflow during the preparation of the test specimens' G-Code files.

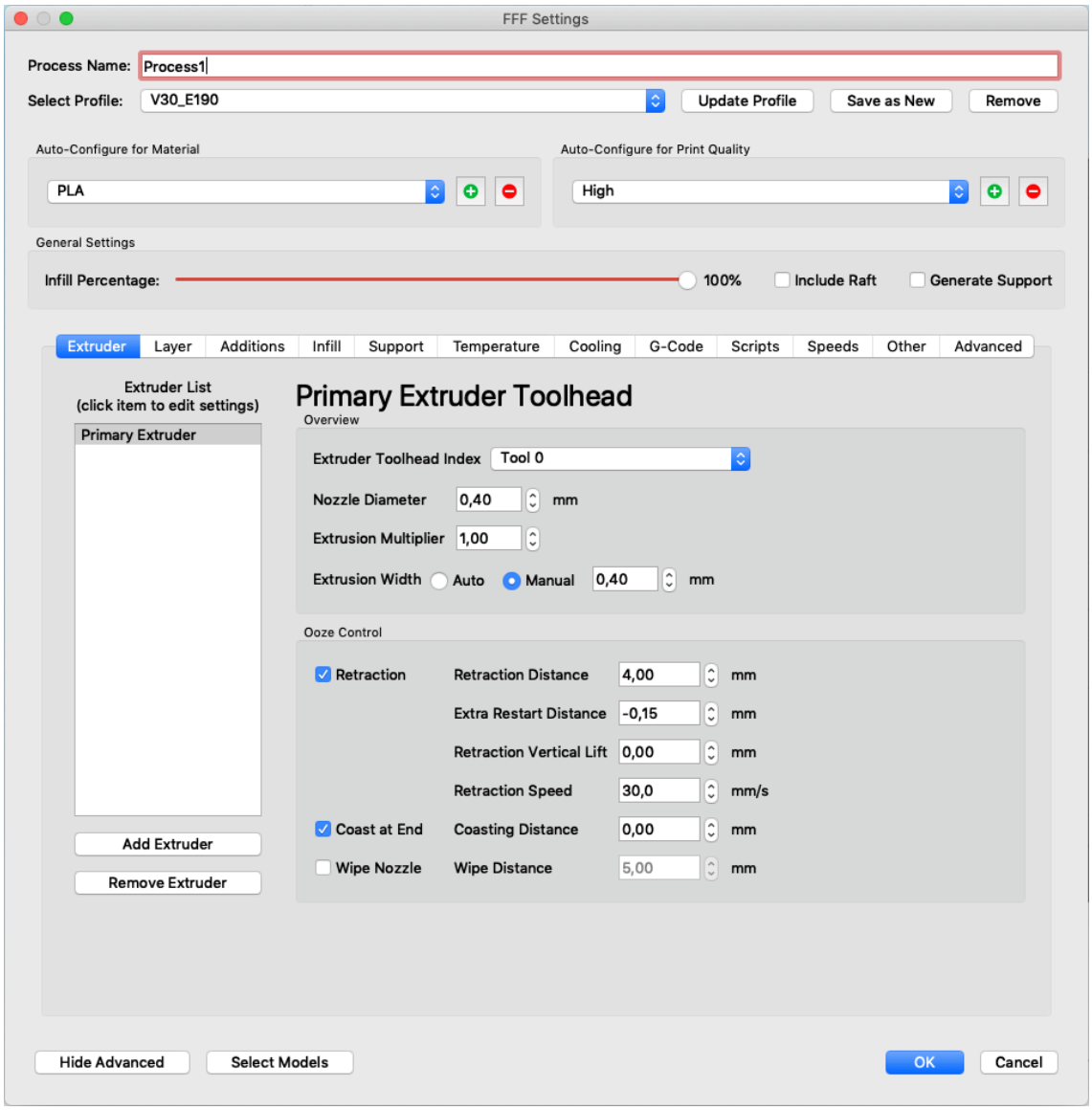


Figure 41 - Example of Simplify3D's interface for the imput of process, material and machine parameters.

As it can be seen in Figure 41, there are different tabs, each with a respective category of parameters that can be altered, which conveys the user a large degree of freedom in terms of how the different printing profiles would be defined. Additionally, Simplify3D also provided a terminal feature that allowed for direct connectivity with the printer for calibration stages, as will be shown in 3.3.

3.2 FormFutura PLA

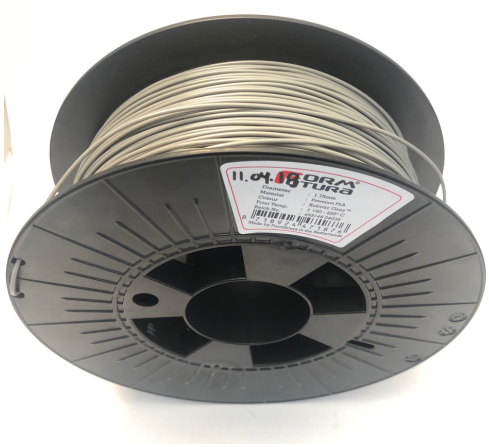


Figure 42 - Spool of Premium PLA by FormFutura.

Taking into consideration the wide range of varieties that PLA can be found in, as well as the different mechanical properties certain applications might demand, it was decided that PLA in filament format with as least alterations to its composition as possible would be used. After some market research, the filament from Form Futura, classified as Premium PLA and visible in Figure 42, was decided to be used. This was due to the claim of it being a fairly unaltered PLA filament with good mechanical properties. Some of this filament's properties are shown in Table 9 and the full specification sheet is available in Appendix C.

Table 9 - General properties of FormFutura's Premium PLA.

PLA	
Density	1240 $kg.m^{-3}$
Price	26 €.kg^{-1}
Young's Modulus (E)	3.15 GPa
Tensile Strength ($\sigma_{0,2}$)	105 MPa
Flexural module (E_f)	2.36 GPa
Flexural Strength	54.4 MPa
Melting point	210 $\pm$ 10 °C
Print Temperature	190 – 225 °C

3.3 Printing devices

After having gathered knowledge on the most dominant devices and projects regarding desktop FFF printers, the decision of building two devices similar to the Ender 3 Model by Creality3D was made.

Considering that the proposed study was to analyse the influence of process parameters and creating predictive models based on the output of the experimental stage, variation of the machine's conditions throughout the whole experiment would have to be as least as possible. As such, the sturdy design of the device came across as more than adequate. In addition, the fact that it was an open-source printer would make it easier for different upgrades to be implemented during the construction of the device.

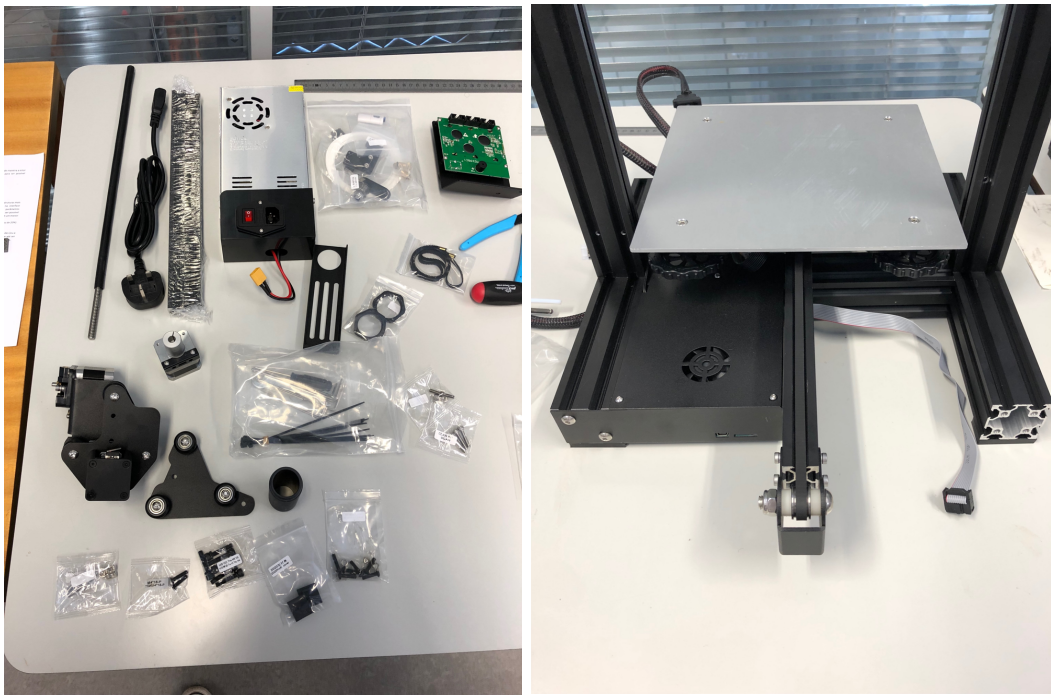


Figure 43 - Components and assemblies for the construction of the printer.

The components shown in Figure 43 were acquired (left) and assembled (right), with the outcome being two identical printers. After having built the devices, the following steps consisted of three stages:

- Extrusion calibration;
- Dimensional calibration;
- Assessment.

Aside from the components that were bought, some parts were printed as gradual upgrades, such as an extruder tensioner to ensure that the filament was properly fed by the geared system (Figure 44), a filament guide to ensure that the entry degree of the filament on the geared system was not steep, so as to not damage it and create posterior extrusion problems (Figure 45) and a fan cover that prevented the aspiration of filaments, strands and other debris into the *mainboard*, which could prevent this component from properly working (Figure 46).

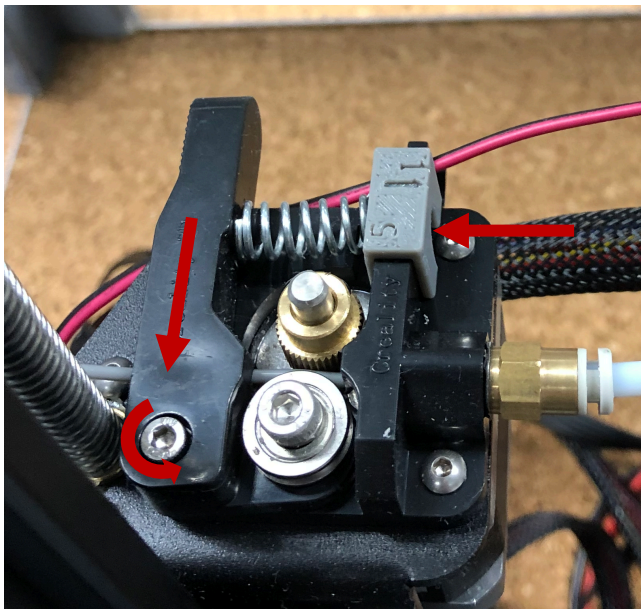


Figure 44 - Extruder tensioner applied to the geared system arm.

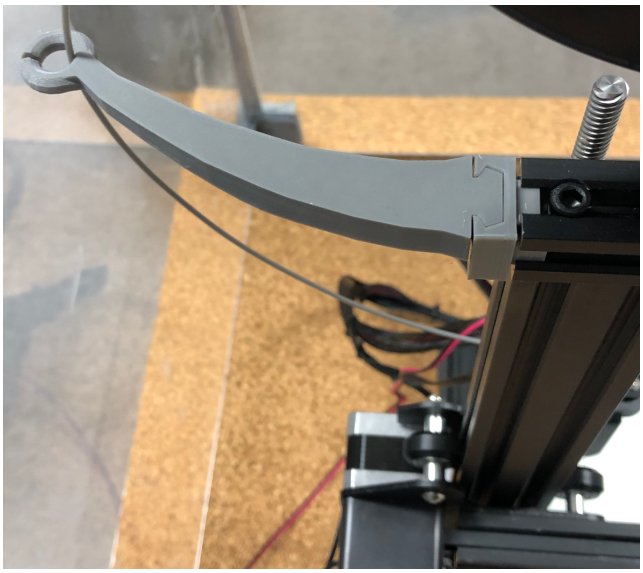


Figure 45 - Filament guide instaled on the alluminium frame.

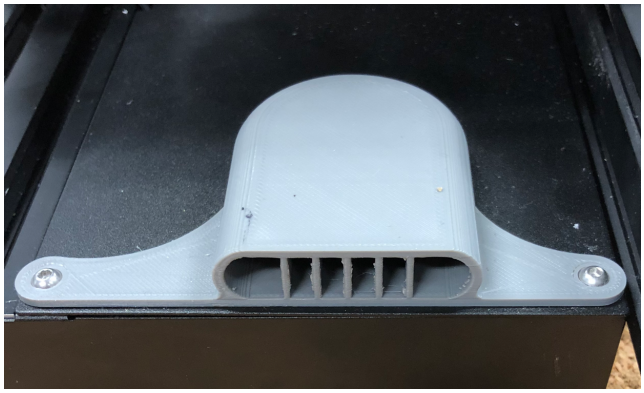


Figure 46 - Fan guard installed on top of the motherboard cover.

3.3.1 Extrusion calibration

The extrusion calibration consisted of an iterative process where the printer was commanded, via terminal, to extrude a known length of material, followed by a measurement and calculation of the new number of steps that the extruder motor had to take per *mm* of extruded filament.

In order to execute this, Simplify 3D's terminal feature, visible in Figure 47, was used to set the extruder temperature up to 200°C and to issue the command for linear movement of the extruder motor.

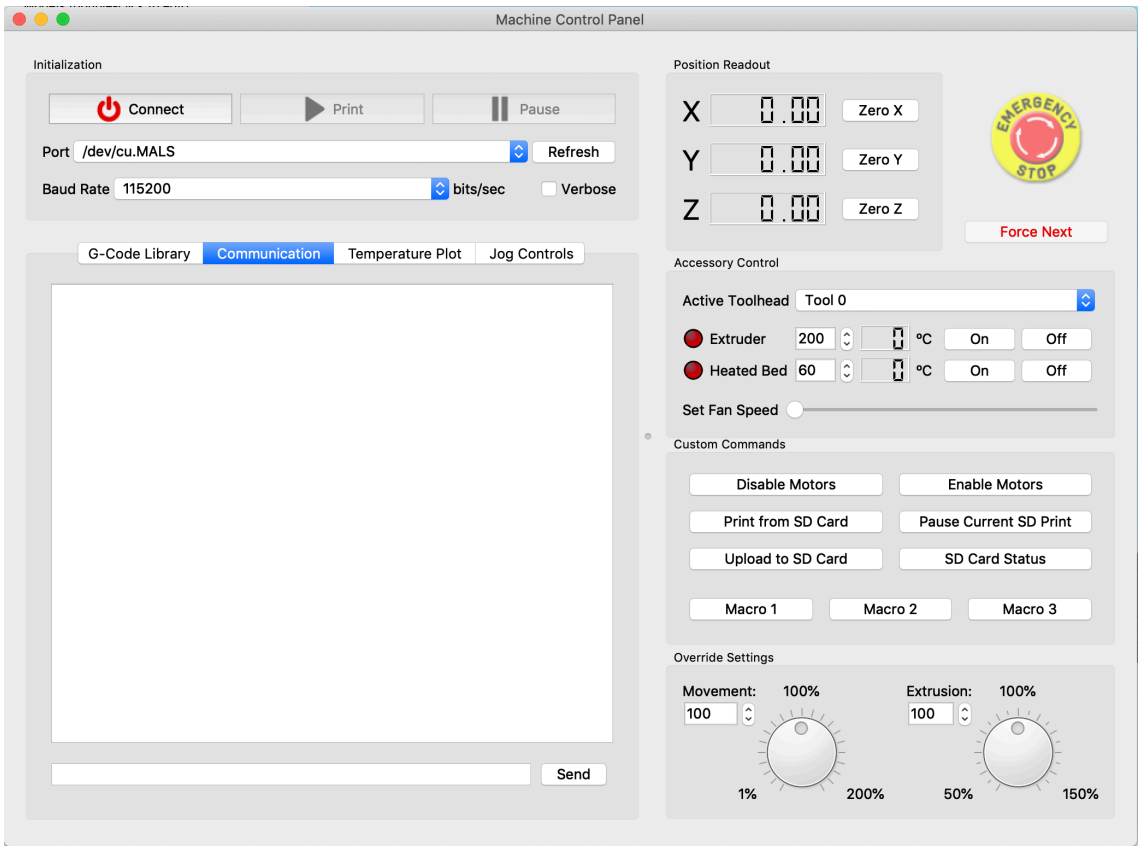


Figure 47 - Simplify 3D's terminal feature and input window.

The command for extrusion was G1 E100 F100, which translates into a linear movement of 100mm of the extruder motor at 100mm/min. Before actually issuing the command, the filament was marked at 120mm, so as to have a measurable point to calculate how much filament was extruded.

The new *steps per mm* were calculated in the following manner:

$$Steps\ per\ mm_i = \frac{100}{120 - Measured\ distance\ [mm]} \times Steps\ per\ mm_{i-1} \quad (3.1)$$

Table 10 - Iterations used to calibrate the extruder motors.

Measured distance [mm]	Steps per mm
20.05	98.76

After having found the value of steps per mm, shown in Table 10, that allowed for free extrusion of 100mm of filament, the command M500 was issued to permanently replace the value on the machine's firmware.

3.3.2 Dimensional calibration

This stage was done in the same fashion as the calibration of the extruder motors, with the outcome being a new value for the number of steps each motor (X, Y and Z-axis) had to take per each mm to be reflected on the print, dimension-wise. In this case, a cube with known dimensions of 20x20x20mm in X, Y and Z (shown in Figure 48) was used as a reference and measured after the print was done. Afterwards, recurring to the equation shown below, the new value of steps per mm was calculated for each of the axis.

$$Steps\ per\ mm_i = \frac{20}{Measured\ distance\ [mm]} \times Steps\ per\ mm_{i-1} \tag{3.2}$$

The procedure was the same for each of the different axis motors, with the final values being shown in Table 11.

Table 11 - Iterations ran to calibrate the movement stepper motors.

Measured distance [mm]			Steps per mm		
X	Y	Z	X	Y	Z
20.05	19.95	20.00	79.86	79.91	400

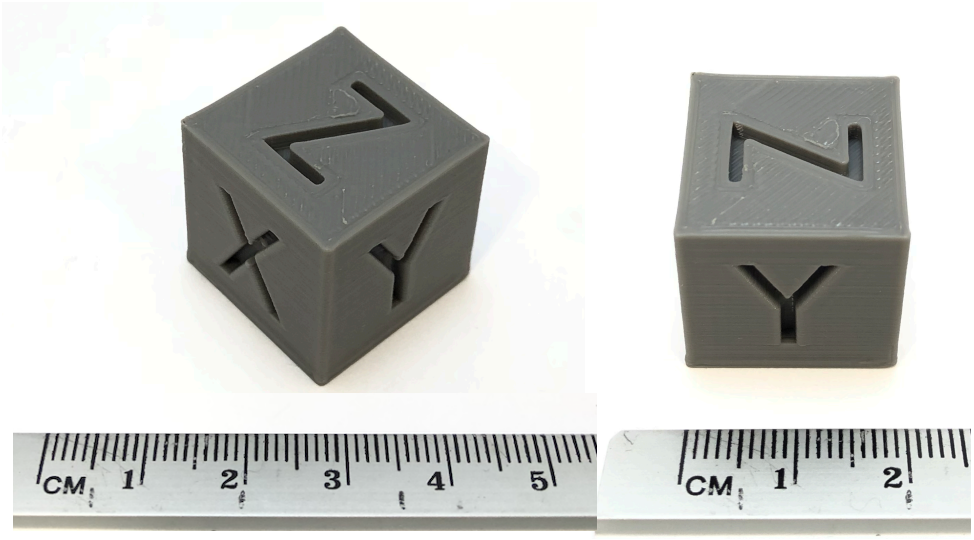


Figure 48 - Cubes that were utilized for axis calibration purposes. Model taken from MakerBot Industries (2019).

3.3.3 Assessment

After having calibrated the main aspects of the machine, an optical assessment was made by printing components with a wide range of commonly troublesome features for FFF printing such as bridging[2], retraction tests [3], thin walls and overhangs.

In Figure 49, a component with fine details, retraction sets and overhangs was printed. Retraction issues were not observed and there were no extrusion or bridging issues, with overhangs being built without issue up until 60°, value after which overhanging issues such as deformation started occurring, as it can be observed on the right in Figure 49. As for the surface temperature that was used, 60°C allowed for proper bed adhesion without any damaging of the components during the extraction procedure (as stated in 2.5.11).

At this stage it was possible to establish a base for some of the parameters that would not be altered throughout the experiment while at the same time providing good printing outcomes. Some examples of these parameters are raster width (0.4mm), layer height (0.2mm), retraction settings (4mm at 30mm/s), surface temperature (60°C) and travel speeds (100mm/s).

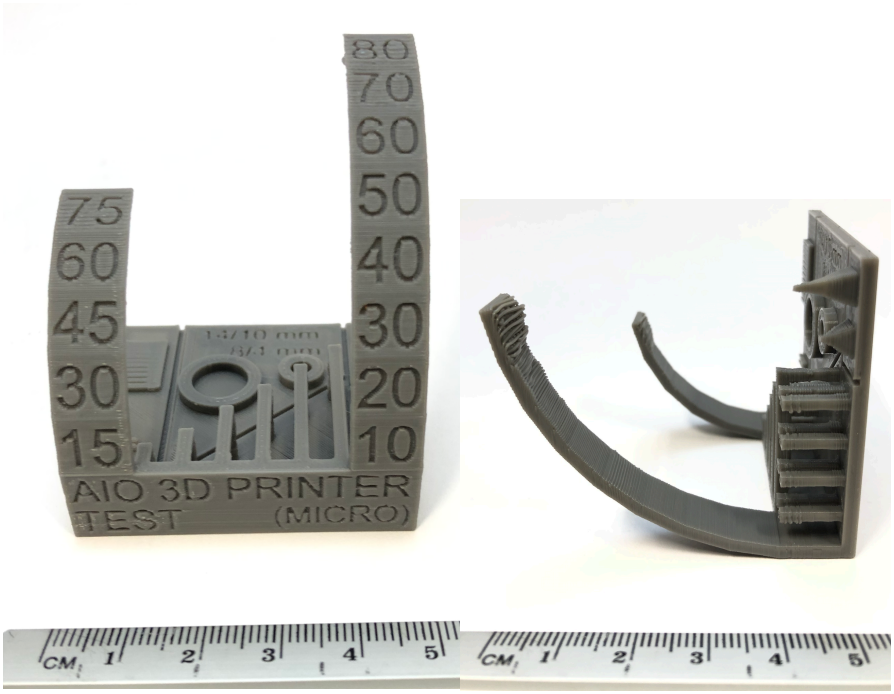


Figure 49 - Component used to assess the calibration of the printer. Taken fromMakerBot Industries (2019)

[2] Bridging phenomena occurs when long horizontal paths of unsupported material deposited with no material to support their base. The principle is the same for the occurrence of deformations in overhangs.
[3] A retraction test evaluates the optimum amount of filament that should be pulled back by the extruder when this component is moving from one point to another in areas where it is not supposed to exist deposited material.

3.4 Instrumentation and upgrading

Seen as though one of the main purposes of this work was to evaluate the influence of process parameters in desktop printers, the need to ensure stable ambient conditions were maintained, as well as the ability to obtain relevant measurements during the printing process was identified

As such, considering what was observed in 2.5 regarding the influence of process parameters, namely the fact that FFF methods strongly rely on heating the material to a stage where it is extrudable, it was decided that an additional means of measuring nozzle temperature would be implemented, in order to both ascertain fluctuations in temperature and obtain thermal profiles during the printing of each test specimen.

Additionally, during the assembly and calibration stages of the printers, it was noticed that the work environment temperature presented fluctuations between 21°C and 29°C throughout the day. As such, in order to guarantee a controlled work environment, an enclosure for the printers was also built.

3.4.1 Temperature Measurement

As previously mentioned, an additional way of measuring the temperature at the extruder was required. For this purpose, it is relevant to mention that the sensor used in the built devices was a Type K thermocouple that was integrated into the *firmware*, which sent a signal to heat the extruder block until a certain temperature is reached and then maintained by PID control. A thermocouple allows for temperature measurement due to the *Seebeck effect*, where a potential difference is created when there is a temperature difference at the junction of two different materials (Bentley 1998).

Different types of thermocouples can have wide temperature ranges for optimum usage, and, in this, a type-K thermocouple was used. According to Åström and Hägglund (1995), seen as though the temperature control is done by a PID process, temperature fluctuations may occur and, coupling this to the resolution of a Type-K thermocouple, temperature readings may be more inaccurate than shown on the device output. Consequentially, the objective was to resort to an RTD temperature sensor that both presented a better resolution in terms of temperature readings and allowed for continuous monitorisation of the temperature on the heating block, which could be later used during the data analysis phase.

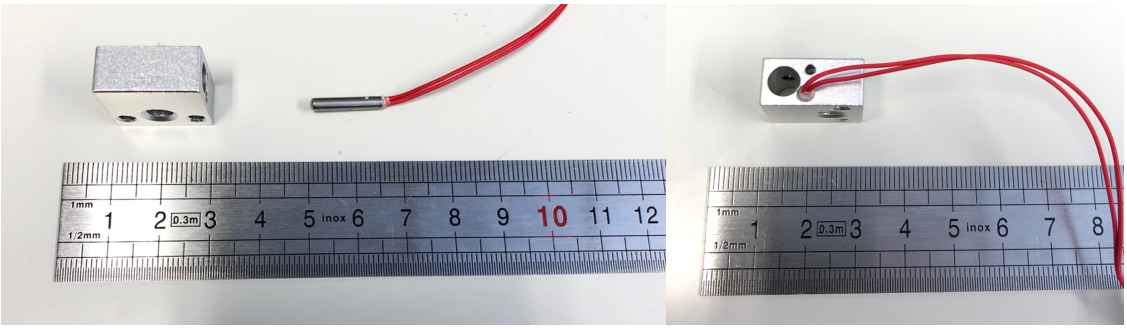


Figure 50 - Heating block and Pt100 temperature sensor, side by side (left) and assembled (right).

As such, due to the temperatures at stake (spanning a range of 190 to 230 °C) and the small size of the heating block, the selected sensor was a 100Ω platinum resistance temperature detector with a diameter of ⌀=3mm and a length of l=15mm, as seen in Figure 50.

As for the data collection, a continuous monitoring data logger was used to log data from the before-mentioned sensor. The output from this combination is a temperature-time chart, as well as the numerical values of temperature measured over fixed time intervals, as shown in Figure 51 and Figure 52.

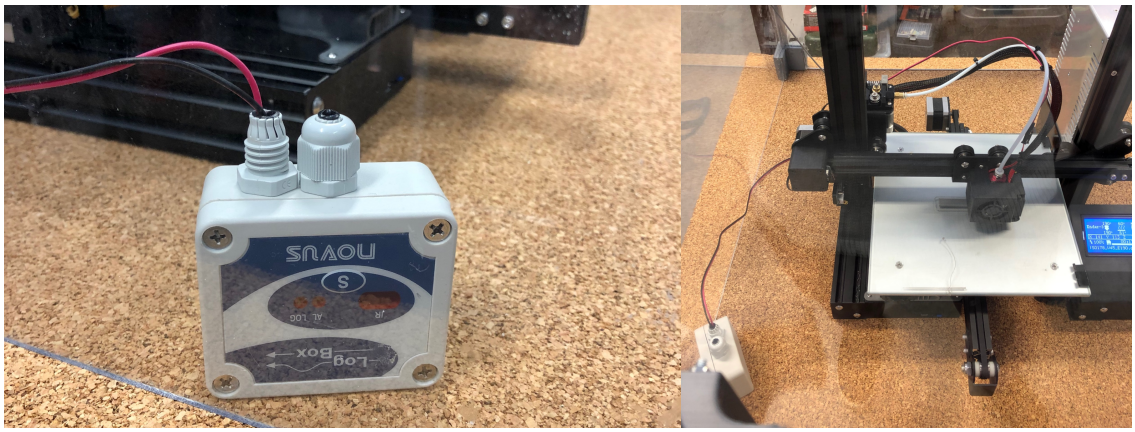


Figure 51 - Data logger and final setup of the temperature measurement device.

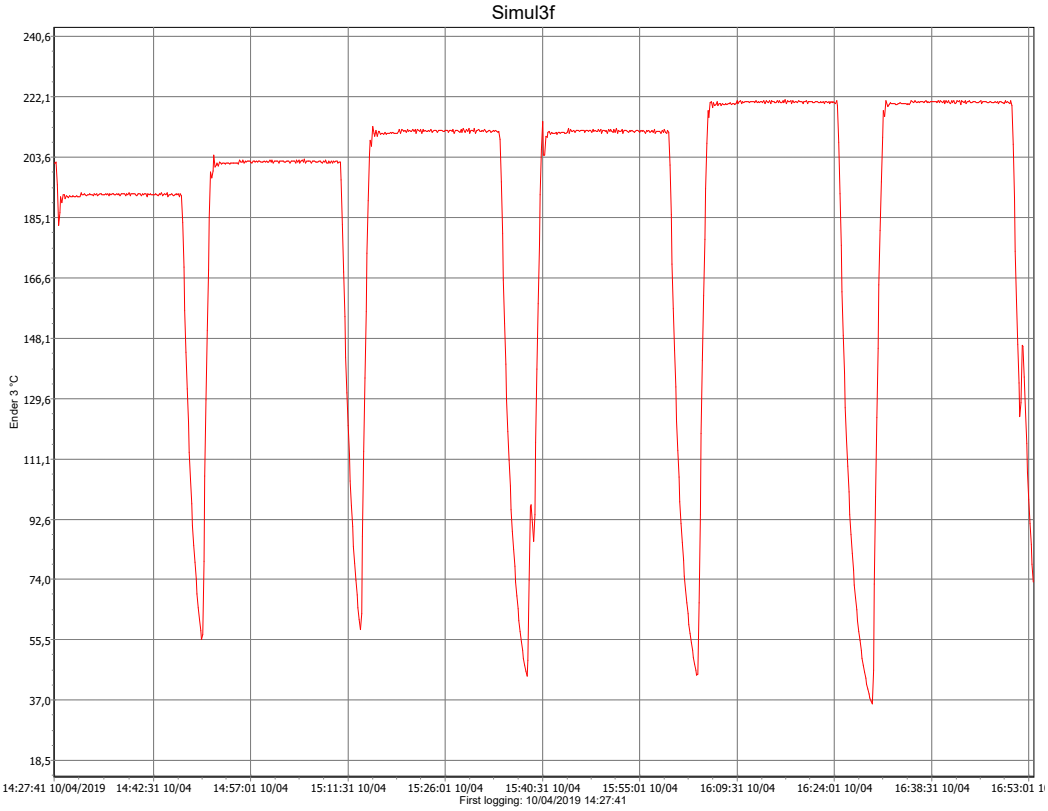


Figure 52 - Example of the time-temperature output resulting from the utilisation of the data logger and Pt100 sensor. Temperature measurement of the compression test specimens at 30mm/s and various temperatures.

3.4.2 Enclosure

The enclosure of the devices was built with the intent of mitigating the temperature changes that occurred around the build plate of the machines, thus consisting of a set of acrylic boards around the device with a door installed for removal of the test specimens and any other calibrations that were necessary.

The first step was to measure the devices, design and project the case using CAD *software*, followed by printing and obtaining the required components and finish by proceeding to the building stage. It is possible to observe the technical drawings for enclosure in Appendix A.

In terms of materials for the construction, the following were used:

- Two 2000x1000[mm] acrylic panels;
- Four upper corner pieces;
- Four lower corner pieces;
- Two 800x800x10[mm] cork panels;
- Silicone paste.

The acrylic panels were cut using an electric saw and put together afterwards by using eight total corner pieces and silicone paste. The corner pieces, visible in Figure 53, were modelled as well and printed using one printer for the purpose.

Afterwards, using the corner pieces together with the silicone paste, the enclosure was built together and allocated over the printers, using the two cork panels as a base to minimize vibrations, as shown in Figure 54.

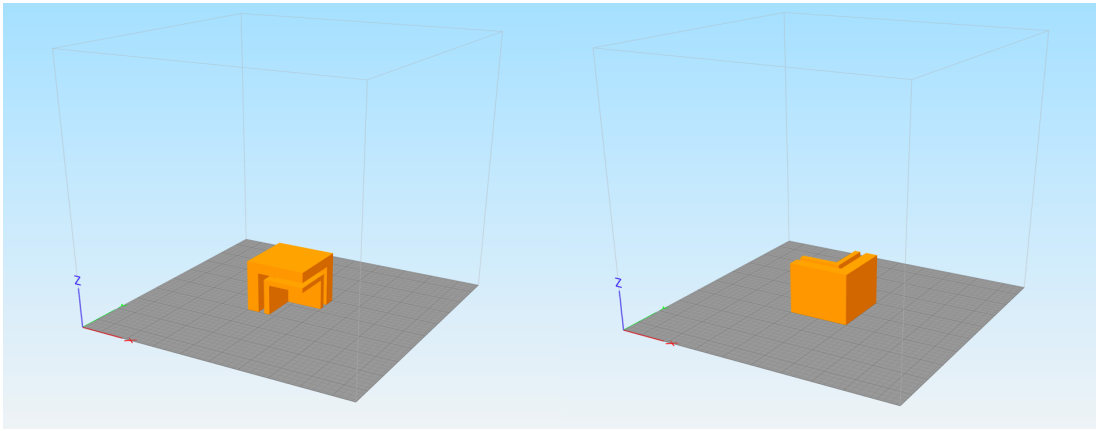


Figure 53 - Upper corner piece (left) and lower corner piece (right) being prepared for printing in Simplify3D.

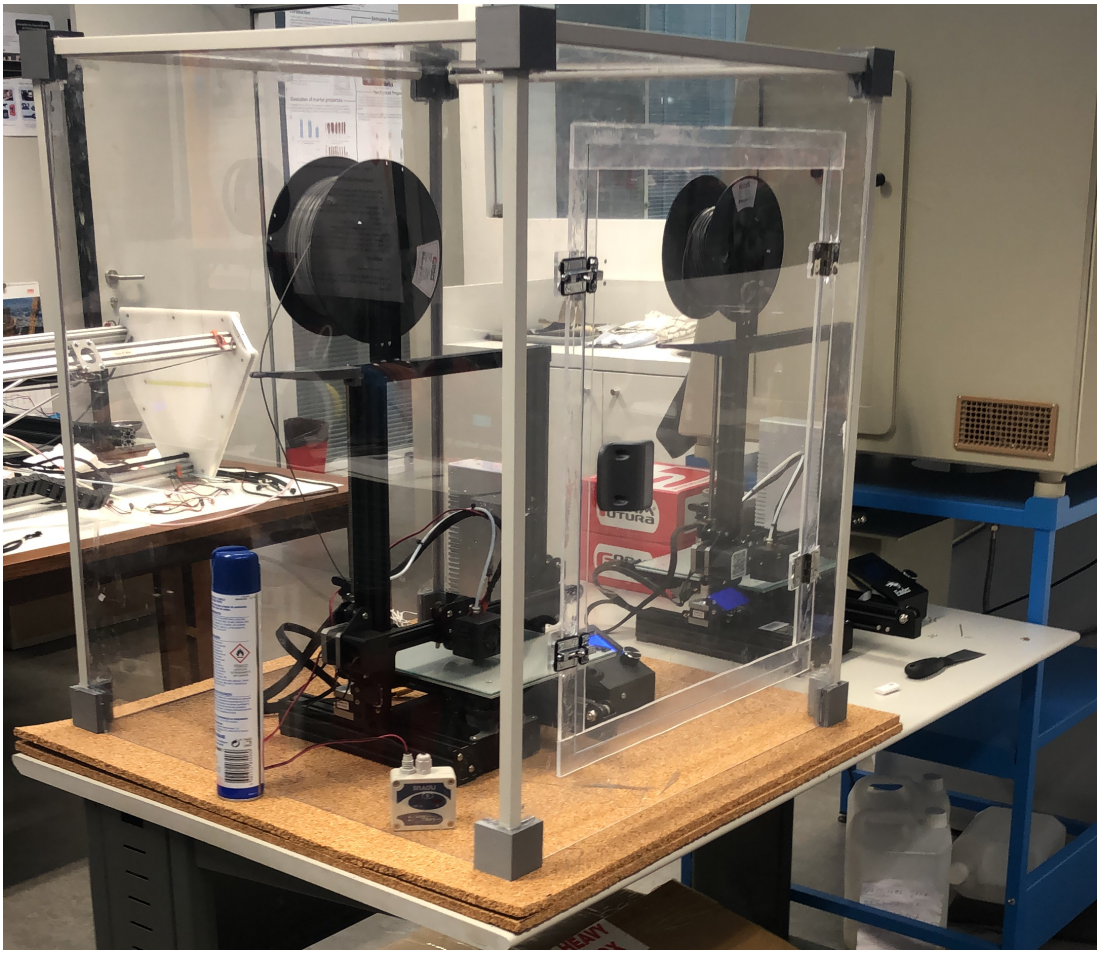


Figure 54 - Assembled enclosure.

3.5 Experiment design - Printing and testing the components

Taking into consideration the purposes of this study, to evaluate the influence of the process parameters in desktop FFF printers and to create predictive models for the mechanical properties and mass, there was a need to test out various parameter alterations. In order to do so, the experiment was divided into different stages where gradual variations to the parameters were introduced, so as to define optimum parameter values (for the conditions at which they were printed) before moving to posterior experiment stages. The adopted methodology can be observed in Figure 55.

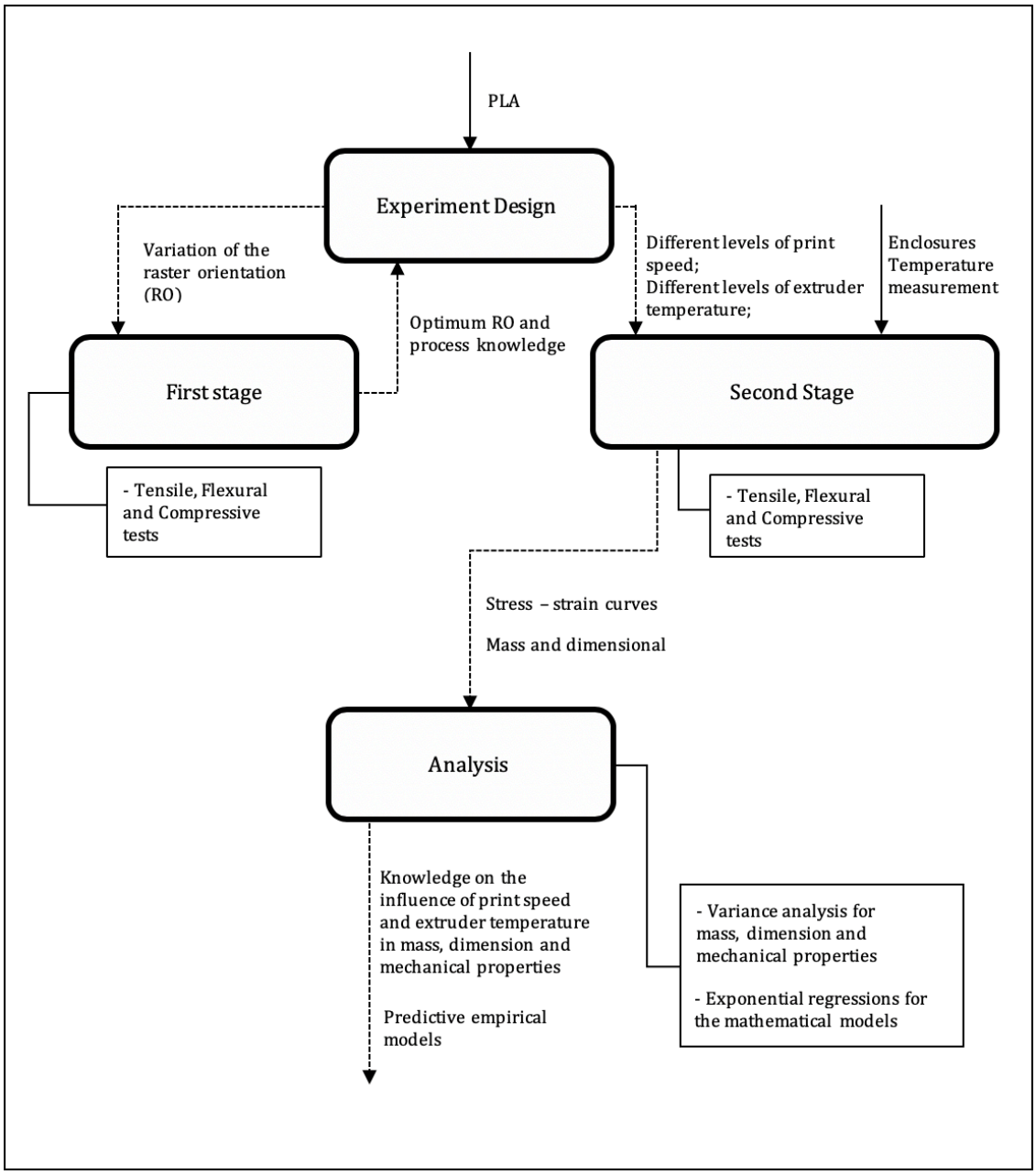


Figure 55 - Adopted methodology for the experimental stage.

3.5.1 First Stage – Raster orientation variation

Initially, both to obtain further knowledge on the process parameters and understand which orientation for the raster would allow for a more homogeneous behaviour under tensile, flexural and compressive solicitations, the test specimens from Figure 56 were produced with different raster orientations: 0°, 90°, 45° and ±45°.

It is possible to analyse the outcome of these tests in the charts from Figure 58 and Figure 59, obtained from Silva (2019), and verify the following:

- Test specimens with raster orientation of 0° presented the highest tensile resistance, as expected according to what was stated in 2.5.3. However, they all fractured in areas were reminiscing filament intersects the raster, as seen in Figure 57. This type of raster orientation, although very resistant in the direction of the solicitations, become inefficient when solicited in different orientations due to the interfaces between deposited filaments;
- Test specimens with raster orientation of 90° presented the lowest tensile resistance and suffered fracture at the raster interface. In the same fashion as 0° raster orientation, these test specimens are also frail when submitted to orientations perpendicular to the raster orientation;
- Test specimens with raster orientation of ±45° and 45 present similar tensile strength and plastic behaviour, albeit fairly insignificant. Although these behaved similarly, the ones with ±45° presented a more homogeneous behaviour than the ones with 45°, due to the crossing of raster orientations, which helped decide which raster orientation to use for the following stages of the experiment.

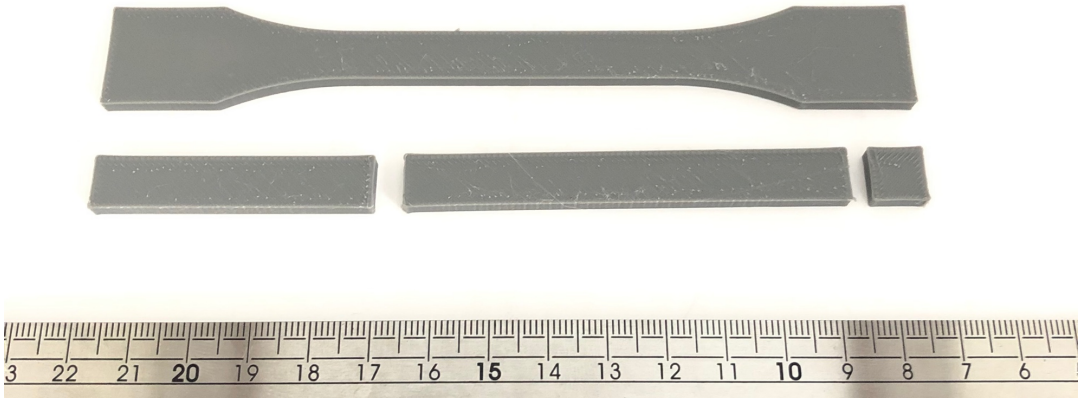


Figure 56 - Example of the printed test specimens. Tensile (top), large compression, flexural and short compression (bottom, left to right).

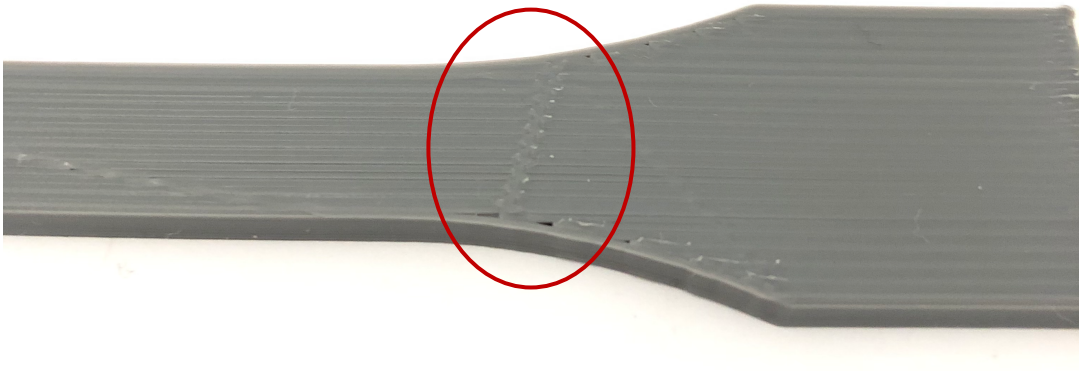


Figure 57 - Sutures present at the surface and, presumably, at each layer, caused by reminiscing filament deposited during nozzle movements.

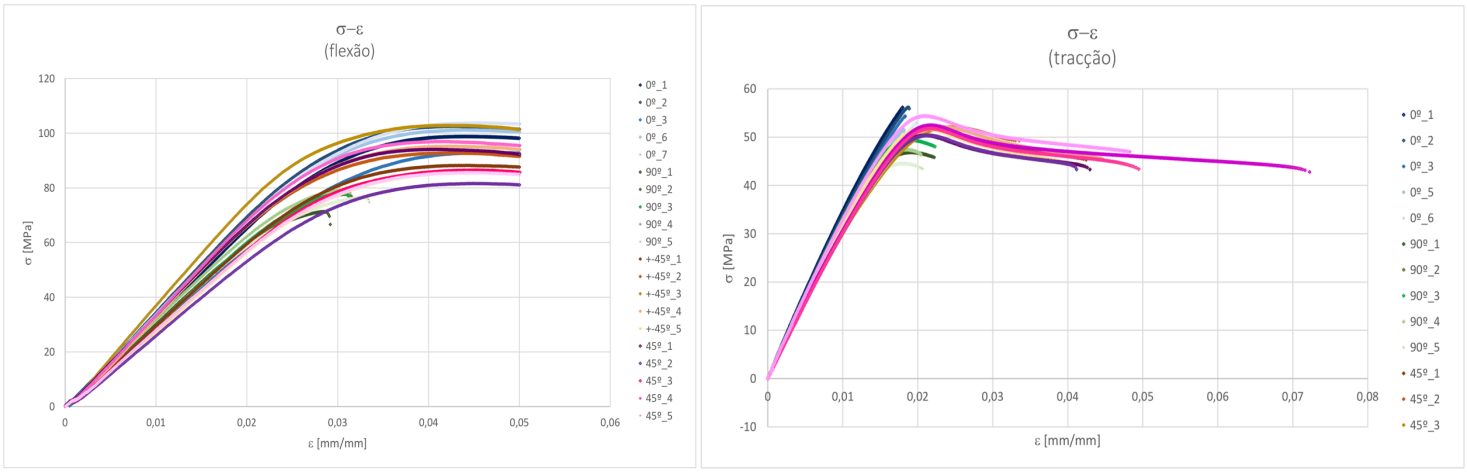


Figure 58 - Stress – Strain graphs for tensile and flexural trials.

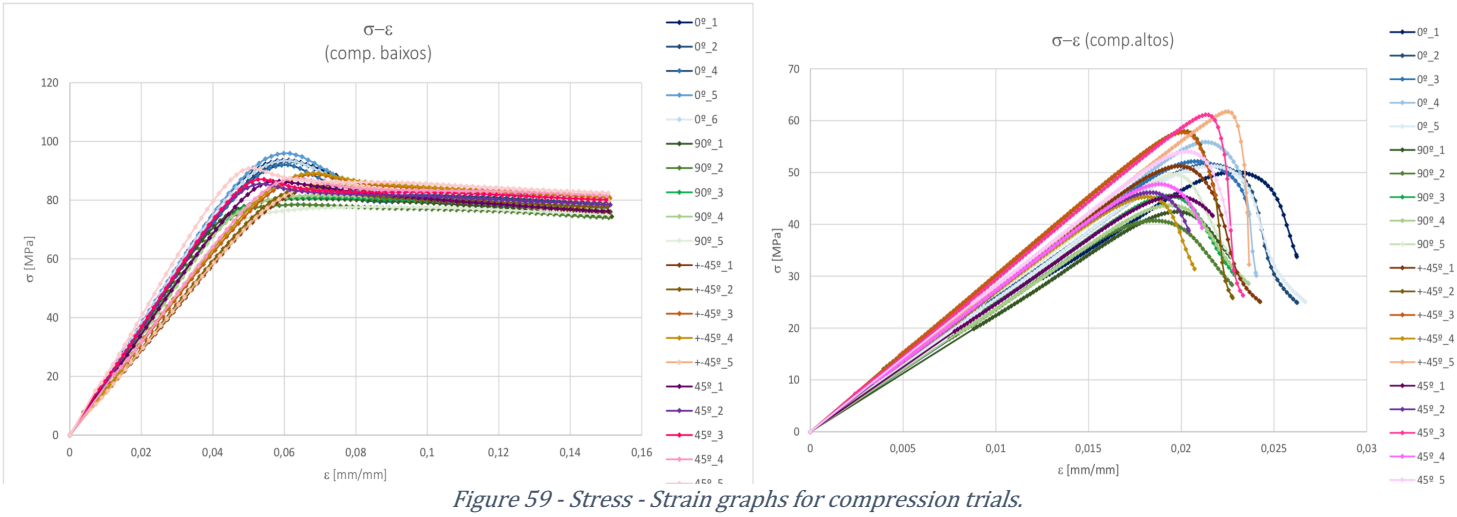


Figure 59 - Stress - Strain graphs for compression trials.

3.5.2 Second Stage – Speed and Temperature variation

The first stage consisted of introducing parameter variation in terms of printing speed (V_{print}) and printing temperature (T_{print}).

As such, the following printing speeds where established:

Table 12 - Levels of V_{print} used during the experimental phase.

V_{print}	Value
Level 1	30 mm/s
Level 2	45 mm/s
Level 3	60 mm/s
Level 4	75 mm/s
Level 5	90 mm/s

At this stage, it was decided that all of the test specimens' layers (*infill* and *contours*) would be printed at the same speed in order to obtain test specimens as homogeneous as possible, aside from the first layer. In this case the speed was reduced to 30% in order to ensure proper adhesion of the test specimens base, thus avoiding warping and the prints coming loose for higher print speeds, according to Devicharan and Garg (2019).

As for the printing temperature, the decision on which temperatures to be used was made according to the specifications of the manufacturer, as stated in 3.2, also introducing a temperature above the recommended by the manufacturer to understand the behaviour of the filament under said conditions. The following temperatures were used:

Table 13 - Levels of T_{print} used during the experimental phase.

T_{print}	Value
Level 1	190°C
Level 2	200°C
Level 3	210°C
Level 4	220°C
Level 5	230°C

All portions of the test specimens were printed at the same temperature so as to ensure homogeneity throughout their composition.

With this stage of the experiment the intention was to obtain information regarding the following aspects:

- Influence of print speed and extruder temperature on the mass and dimensions of the test specimens;
- Influence of print speed and extruder temperature on the mechanical properties of the test specimens;
- Stress-Strain graphs regarding tensile, flexural and compressive trials;
- Establish an optimum relation between print speed and extruder temperature for the considered conditions.

3.5.2.1 Other parameters

As for the remaining conditions and parameters, the following were defined as fixed:

Table 14 - Parameters not subject to alterations during the experimental phase.

Parameter	Value
Nozzle diameter ($\varnothing_{nozzle}$)	0.4mm
Layer height (H_{layer})	0.2mm
Extrusion width ($W_{extrusion}$)	0.4mm
Number of perimeters	1
Number of top/bottom layers	0
First layer height ($H_{firstlayer}$)	0.2mm
First layer width ($W_{firstlayer}$)	0.4mm
Raster pattern and orientation	Linear with $\pm$45°
Printing surface temperature ($T_{surface}$)	60°C

Taking into consideration what was mentioned in 2.5.2, only 1 perimeter was implemented, so as to minimize contributions in terms of load resistance for tensile and compressive test specimens. In addition, the printing surface temperature was defined at $T_{surface} = 60°C$ in order to ensure that adhesion was proper but not excessive so as not to damage the test specimens during their extraction, as per what was stated in 2.5.11.

During the printing stage of the test specimens, the thermal profiles mentioned in 3.4.1 and available in Appendix B were used for monitoring, with no anomalies or temperature fluctuations having been detected.

3.5.2.2 Methodology for testing

All of the test trials were carried out according to the respective standards, ISO 527 for the tensile tests, ISO 178 for the flexural tests and ISO 604 for the compression tests using an Instron 5960 UTS with axial clip-on extensometers 2630-111 and transverse clip-on extensometer W-E404-E. All the used standards are briefly explained here.

ISO 527 – Tensile test specimens

The evaluation of the type 1B test specimens resulting from tensile tests according to this standard, visible in Figure 60, was expected to yield the following data:

- Tensile stress at yield (σ_y), which is the maximum tensile stress the test specimen can withstand in the elastic domain, expressed in MPa;
- Tensile stress at break (σ_B), which is the maximum tensile stress the test specimen can withstand before rupturing, expressed in MPa;
- Tensile strength (σ_M), which is the maximum tensile stress sustained by the test specimen during the tensile test, expressed in MPa;
- Tensile strain at yield (ε_y), which is the tensile strain at the moment the yield stress is obtained, expressed in percentage (%) or mm/mm;
- Tensile strain at break (ε_B), which is the tensile strain at the moment the stress at break is obtained, expressed in percentage (%) or mm/mm;

- Tensile strain at tensile strength (ε_M), which is the tensile strain at the moment the tensile stress is obtained, expressed in percentage (%) or mm/mm.

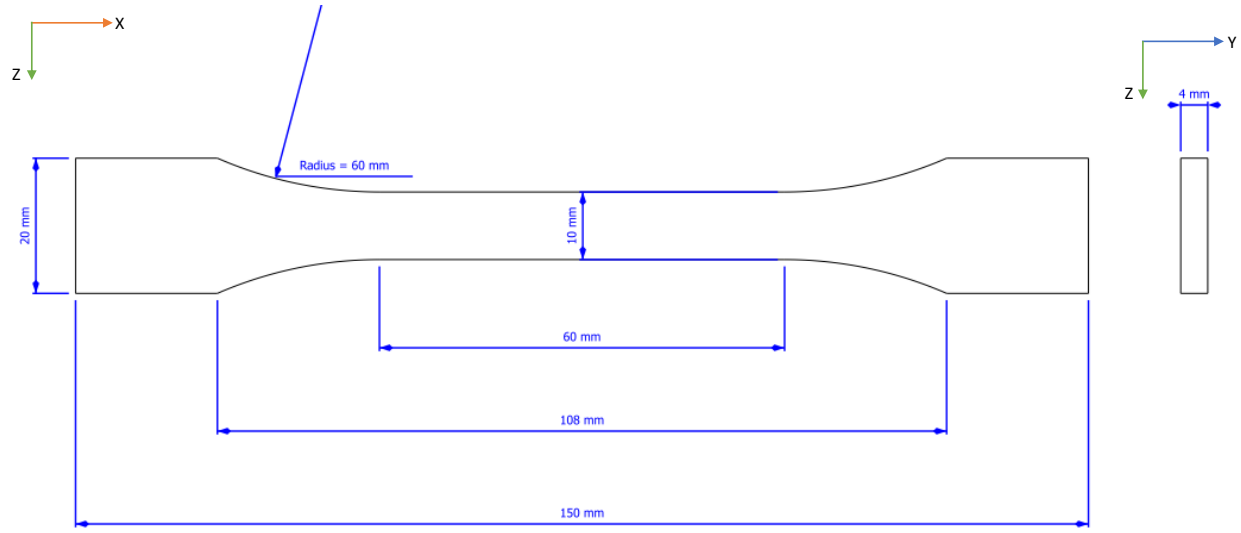


Figure 60 - Dimension of the test specimens according to the standard ISO 527.

As for the calculations that derived from this test trial, the following were outlined:

- Stress, σ, calculated by a ratio between the exerted force, F [N], and the initial cross section area, A [mm²]: $\sigma = \frac{F}{A}$ [MPa];
- Strain, ε, ratio between the increase in the specimen length between the gauge marks, ΔL_0 [mm], and the initial gauge length, L_0 [mm]: $\varepsilon = \frac{\Delta L0}{L0}$;
- Young Modulus, E, ratio between the stress difference and respective strain difference: $E = \frac{\sigma_2 - \sigma_1}{\varepsilon_2 - \varepsilon_1}$ [GPa] considering that $\varepsilon_2 = 0{,}0025$ and $\varepsilon_1 = 0{,}005$;
- Poisson ratio, ν, ratio between transverse direction strain, ε_n, and the longitudinal direction strain, ε: $\nu = -\frac{\varepsilon_n}{\varepsilon}$.

All trials were performed at 1mm/min in an Instron 5966 UTS machine, with a load cell of 10kN.

ISO 178 – Flexural test specimens

The evaluation of the test specimens resulting from three-point flexural loading tests according to this standard, with the test specimen visible in Figure 61, was expected to yield the following data:

- Flexural stress at break(σ_{fB}), which is the nominal stress of the outer surface of the test specimen at midspan during the time of breakage, expressed in MPa;
- Flexural strength (σ_{fM}), which is the maximum flexural stress sustained by the test specimen during a bending test, expressed in MPa;
- Flexural stress at conventional deflection (σ_{fC}), which is the flexural stress at the time of deflection, expressed in MPa;
- Deflection (s), which is the distance over which the top or bottom surface of the test specimen at midspan deviates from its original position during flexure, expressed in mm;
- Conventional deflection (s_C), which is the deflection equal to 1,5 times the thickness of the test specimen's height (h), expressed in mm;
- Flexural strain at break (ε_{fB}), which is the flexural strain at the moment of the breakage, expressed in percentage (%) or mm/mm;
- Flexural strain at flexural strength (ε_{fM}), which is the flexural strain at a maximum flexural stress, expressed in percentage (%) or mm/mm.

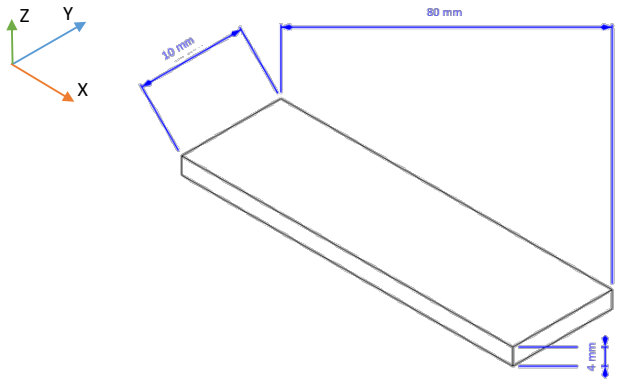


Figure 61 - Dimension of the test specimens according to the standard ISO 178.

The following calculations were outlined:

- Flexural stress, σ_f, is determined by $\sigma_f = \frac{3FL}{2bh^2}$ [MPa];
- Flexural strain, ε_f, is determined by $\varepsilon_f = \frac{6sh}{L^2} * 100$ [%];
- Flexural modulus, E_f, is determined by $\begin{cases} E_f = \frac{\sigma_{f_2} - \sigma_{f_1}}{\varepsilon_{f_2} - \varepsilon_{f_1}} \\ \varepsilon_i = \frac{s_{f_i} 6h}{L^2} \end{cases}$, expressed in MPa.

All test specimens were trialled at 2mm/min in an Instron 5966 UTS and with a load cell of 10kN.

ISO 604 – compression test specimens

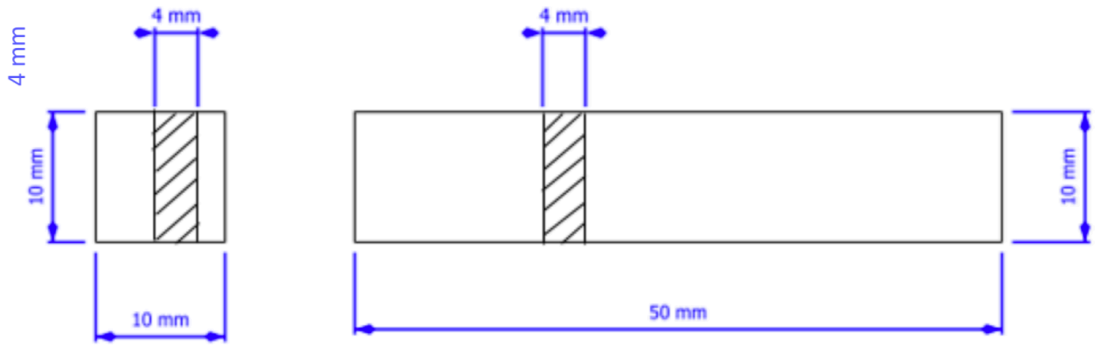


Figure 62 - Dimension of the test specimens according to the standard ISO 604, type A to the right and type B to the left.

The evaluation of the test specimens, resulting from compressive loading along the major axis of both the type A (Figure 62 on the right) and type B test specimens (Figure 62 on the left), consisted of evaluating the following data:

- Compressive stress at yield (σ_y), which is the maximum compressive stress the test specimen can withstand before an increase in strain occurs, expressed in MPa;
- Compressive stress at break (σ_B), which is the maximum compressive stress the test specimen can withstand before rupturing, expressed in MPa;
- Compressive strength (σ_M), which is the maximum compressive stress sustained by the test specimen during the test, expressed in MPa and obtained by the type B test specimens;
- Compressive strain at yield (ε_{cy}), which is the compressive strain at the moment the yield stress is obtained, expressed in percentage (%) or mm/mm;
- Compressive strain at break (ε_{cB}), which is the compressive strain at the moment the stress at break is obtained, expressed in percentage (%) or mm/mm;
- Compressive strain at tensile strength (ε_{cM}), which is the compressive strain at the moment the tensile stress is obtained, expressed in percentage (%) or mm/mm.

The following calculations were outlined:

- Compressive Modulus, E_c, ratio between the stress difference and respective strain difference: $E = \frac{\sigma_2 - \sigma_1}{\varepsilon_2 - \varepsilon_1}$ [GPa], considering that $\varepsilon_2 = 0{,}0025$ and $\varepsilon_1 = 0{,}005$ and this value was calculated with the Type A test specimens;

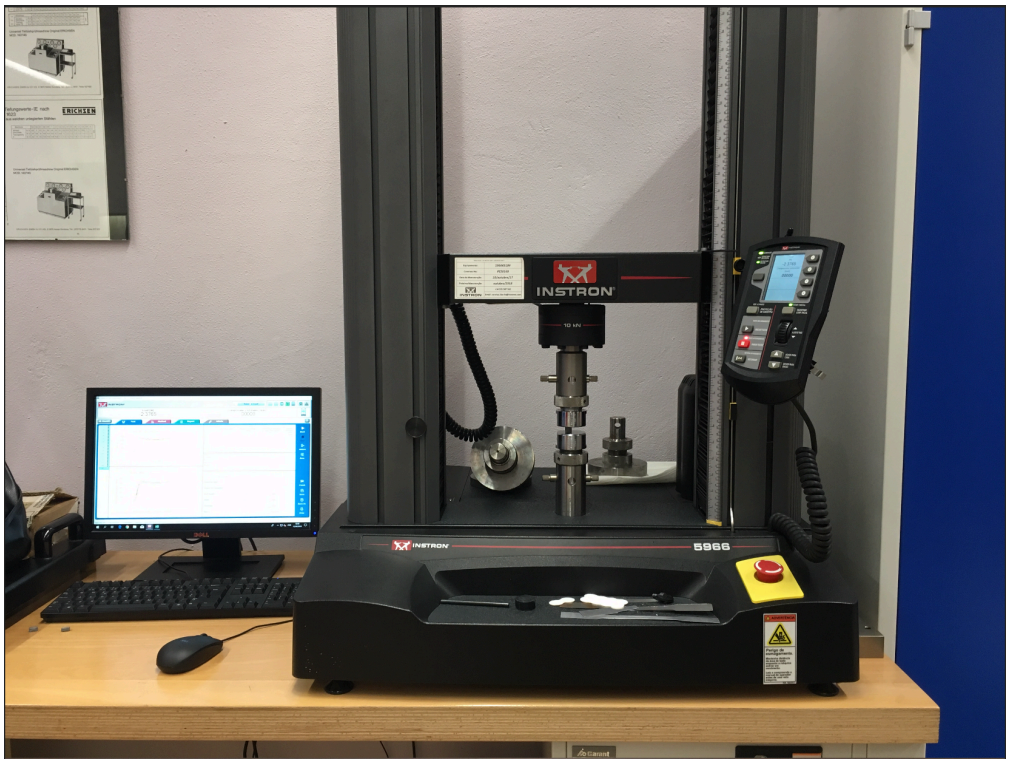


Figure 63 - Instron 5966 UTS device utilized for the compressive test specimens.

All test specimens were trialled at 5mm/min in an Instron 5960 UTS using a load cell of 10kN, as shown in Figure 63.

Typical stress-strain curves for these type of test trials can be observed in Figure 64, where different examples are shown.

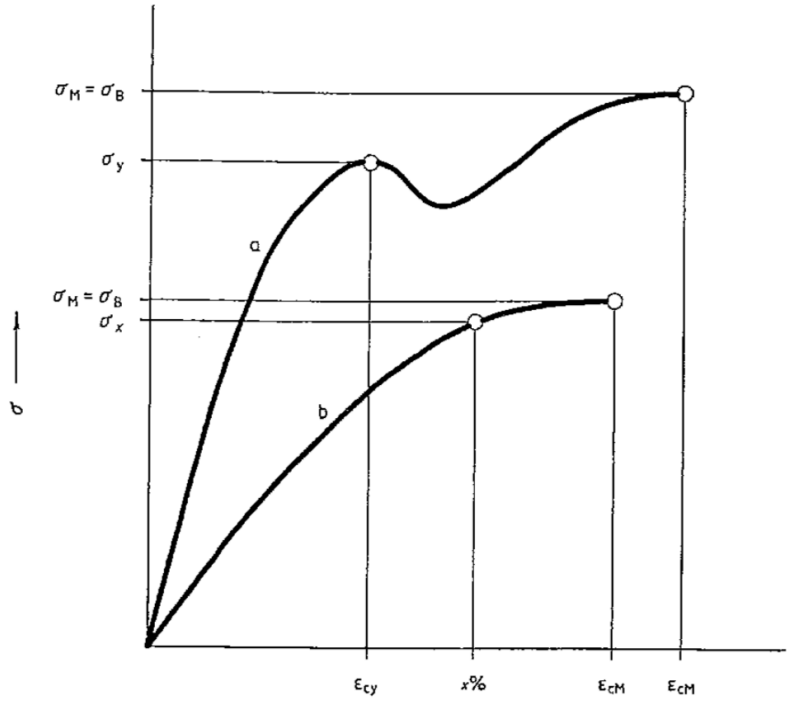


Figure 64 - Typical stress-strain curve for a compressive test according to the standard ISO 604.

3.5.2.3 Methodology for analysis

In order to ensure a structured methodology, some guidelines for this stage were outlined regarding the way the analysis of the influence of the process parameters will be done. The focus points were:

- Mass;
- Dimensions;
- Mechanical Properties.

The analysis was focused on each one of the above-mentioned aspects and consisted of a variance analysis, afterwards transforming the output into the form of graphs, tables and three-dimensional representations of the correlations between the process parameters, in order to better understand their influence.

The data acquisition for the analysis of the mass and the dimensional aspects was recorded in tables such as the one shown in Figure 65, using a HLD300 digital scale from ScaleHouse® with a resolution of ±0.005g (visible in Figure 66) and a steel calliper with a resolution of ±0.05mm.

				ISO 178						
				Temperatura [°C]				Dimension (±0,05 mm)		
Number	øNozzle [mm]	H_layer [mm]	P_speed [mm/s]	T_print	Environment	Weight [g]	Duration [min]	A	B	C
1	0,4	0,2	30	190,0	22,7	3,985	22,0	79,90	10,00	4,25
2	0,4	0,2	30	190,0	22,6	3,915	22,0	79,85	10,00	4,25
3	0,4	0,2	30	190,0	26,0	3,865	22,0	79,80	10,00	4,10
16	0,4	0,2	30	200,0	22,1	3,940	22,0	79,80	10,00	4,25
17	0,4	0,2	30	200,0	22,1	4,050	22,0	79,90	10,00	4,20
18	0,4	0,2	30	200,0	31,3	3,900	22,0	79,95	9,95	4,15
31	0,4	0,2	30	210,0	22,2	3,960	22,0	79,85	10,05	4,25
32	0,4	0,2	30	210,0	22,2	3,985	22,0	79,80	10,10	4,20
33	0,4	0,2	30	210,0	32,4	3,935	22,0	79,95	9,90	4,15
46	0,4	0,2	30	220,0	22,6	4,055	22,0	79,85	10,10	4,30
47	0,4	0,2	30	220,0	22,6	4,065	22,0	79,90	10,15	4,25
48	0,4	0,2	30	220,0	30,1	3,985	22,0	79,95	10,00	4,25
61	0,4	0,2	30	230,0	22,3	4,080	22,0	79,90	10,10	4,30
62	0,4	0,2	30	230,0	22,4	4,085	22,0	79,80	10,15	4,25
63	0,4	0,2	30	230,0	29,3	4,035	22,0	79,85	10,00	4,20

Figure 65 - Example of the records that were kept for each of the test specimens, in this case the ones regarding the flexural analysis.



Figure 66 - Scale utilised to record the mass of the test specimens.

Additionally, in order the fulfil the remaining goals of this work, an attempt to provide empirical models able of emulating the experimental results for the mass and some of the mechanical properties was done, so as to provide phenomenological curves to the simulation *software*.

4. Analysis and comparison of the results

For analysis purpose and the creation of the predictive models, Minitab 2018® and MATLab2018 were used.

4.1 Mass

Some important considerations for the proper analysis of the influence in the mass:

- Due to the four different kind of test specimens (tensile, flexural, short and long compression), the mass analysis and comparison can only be done between each trial;
- Although calibration of both the machines was performed, given the fact that they are, for all effects, *desktop-printers* with simplistic features, some discrepancies may exist between test specimens printed out in different devices.

4.1.1 Short compression test specimens

In Table 15 it is possible to observe the records of the mass for each of the different conditions (properly identified in the table), knowing that the presented value of the mass is a mean of the tree test specimens for each condition.

Table 15 – Short Compression -Mean values of the mass of the test specimens for each of the used conditions.

Condition	V_{print} [mm/s]	T_{print} [°C]	Mass [g]	± S.Dev [g]
CV1_T1	30	190	0.482	0.008
CV1_T2	30	200	0.505	0.009
CV1_T3	30	210	0.513	0.003
CV1_T4	30	220	0.513	0.003
CV1_T5	30	230	0.518	0.003
CV2_T1	45	190	0.498	0.003
CV2_T2	45	200	0.515	0.005
CV2_T3	45	210	0.518	0.003
CV2_T4	45	220	0.517	0.008
CV2_T5	45	230	0.525	0.000
CV3_T1	60	190	0.510	0.005
CV3_T2	60	200	0.523	0.003
CV3_T3	60	210	0.515	0.005
CV3_T4	60	220	0.523	0.003
CV3_T5	60	230	0.527	0.006
CV4_T1	75	190	0.515	0.010
CV4_T2	75	200	0.518	0.003
CV4_T3	75	210	0.523	0.003
CV4_T4	75	220	0.522	0.003
CV4_T5	75	230	0.523	0.003
CV5_T1	90	190	0.510	0.005
CV5_T2	90	200	0.510	0.003
CV5_T3	90	210	0.518	0.005
CV5_T4	90	220	0.515	0.003
CV5_T5	90	230	0.523	0.003

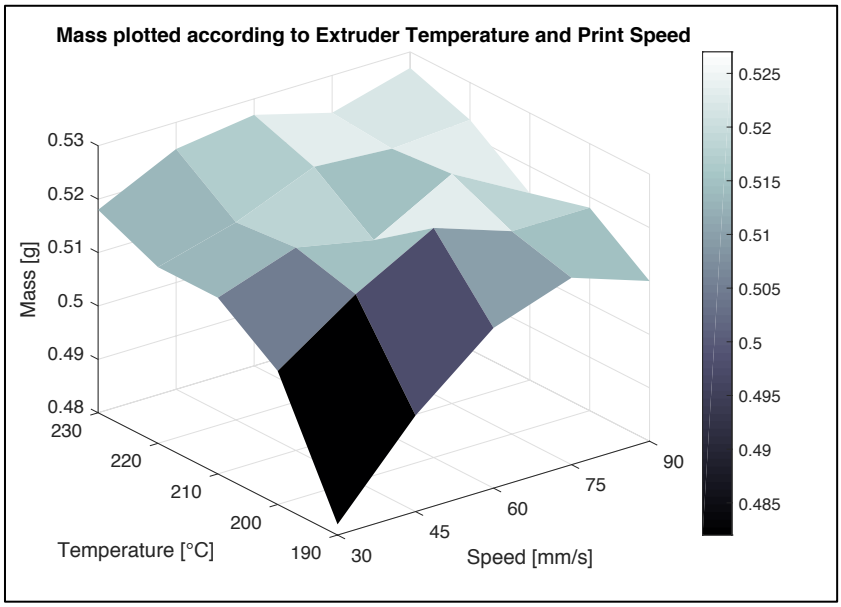


Figure 67 - Surface representation of the influence that Extruder temperature and Print Speed have in terms of the mass for short compression test specimens.

By passing the information from the table into a graphical surface representations such as the one in Figure 67, it was possible to observe that there was a tendency to increase the mass as both the print speed and the temperature were increased, being that the highest value of 0.527g was obtained for the conditions CV3_T5 and CV5_T5. Both of these consist of the highest extruder temperature, 230°C, which might imply phenomena related to over extrusion of material. However, the fact that higher print speeds presented higher mass was somewhat incoherent to the literature, given that higher speeds have been shown to present smaller material deposition (Ning et al. 2017). Taking into consideration what was said in 2.5.9 about printing speed influencing material deposition due to, in some cases, the stepper-motors not having enough torque to either extrude enough material or move accordingly to the set speeds, it should be considered that these effects influenced the results, coupled with the inertial effects on the extruder module and the small dimension of these specific test specimens.

By the surface in Figure 67 it is not exactly clear how these parameters influenced the mass of the components, other than that they made it increase. As such, resorting to an ANOVA variance analysis, it was possible to obtain more insight on this regard. According to the results, both of the process parameters, extruder temperature and printing speed, are highly influential (*p-value* smaller than 0.05) and, pairing this with a Tukey analysis, it is possible to further infer on how the different levels of each factor influenced the mass of the components.

Print speed [mm/s]	N	Mean	Grouping
75	15	0,520333	A
60	15	0,519667	A
90	15	0,518667	A
45	15	0,514667	A
30	15	0,506333	B

Extruder Temperature	N	Mean	Grouping	
230	15	0,524000	A	
220	15	0,519667	A	B
210	15	0,517000		B
200	15	0,516000		B
190	15	0,503000		C

Figure 68 – Short Compression -Tukey Pairwise comparisons on the influence of Print speed (left) and Extruder temperature (right) with 95% Confidence.

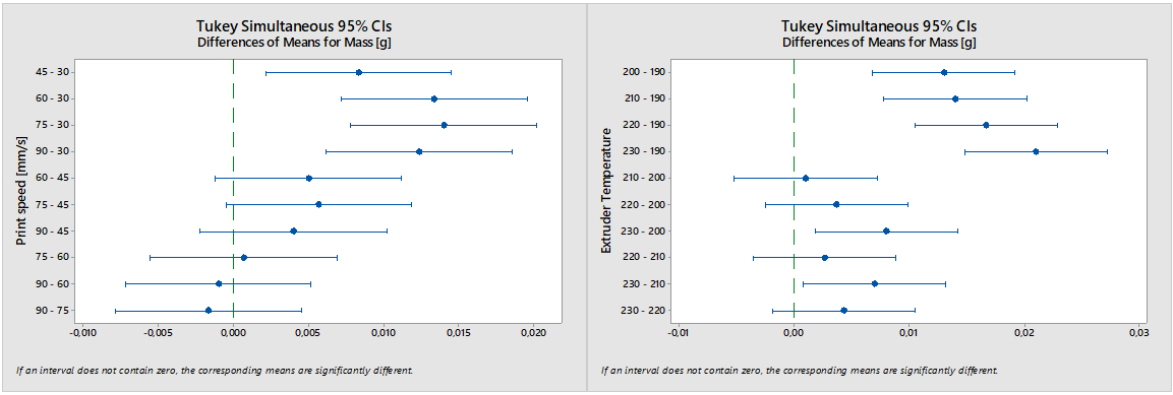
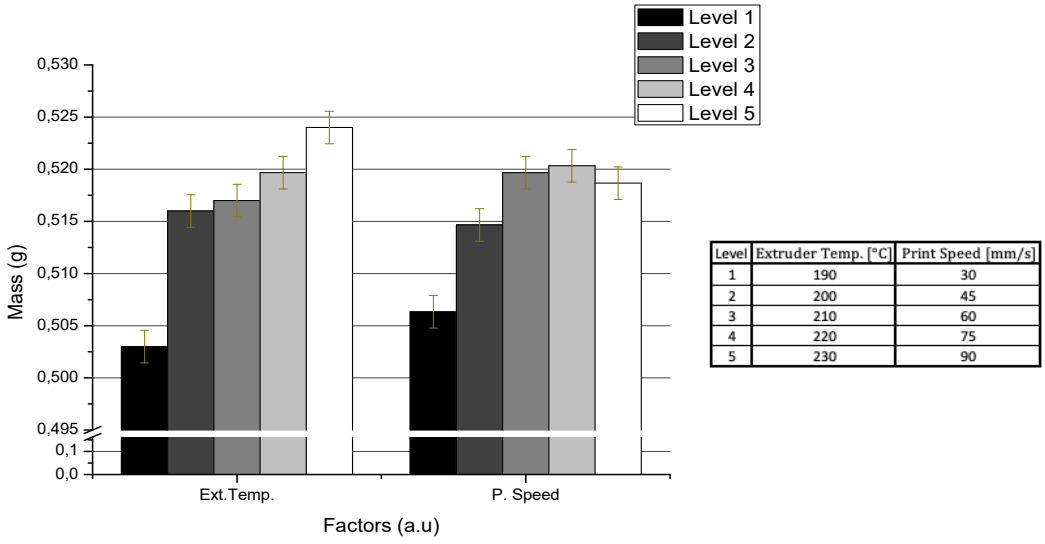


Figure 69 – Short Compression - Graphical representation for the difference of means for different print speeds (left) and extruder temperatures (right).

By analysing Figure 68 and Figure 69, it was noted that the different levels of print speed had two distinct types of influence on the mass of the short compression test specimens, with the lowest print speed (30 mm/s) being statistically different to the higher print speeds. However, the range of speeds from 45 – 90 mm/s was statistically classified as being similar in all values. Further analysis by graphical input for the means and standard error, visible in Figure 70, helped understand this similarity and state that there was a tendency to increase the mass from 30 mm/s until 75 mm/s, afterwards presenting a tendency to decrease as the speed was increased until 90 mm/s, although the values from 60-75mm/s were similar between themselves.



Level	Extruder Temp. [°C]	Print Speed [mm/s]
1	190	30
2	200	45
3	210	60
4	220	75
5	230	90

Figure 70 – Short Compression - Plotting of the means and standard error for the mass according to the different levels of extruder temperature (left) and printing speed (right).

As for the influence of the extruder temperature, it was noted that as the temperature was increased so was the resulting mass, with the temperature of 190°C yielding significantly lower mass than the groups of 200-220°C and 230°C. This behaviour went accordingly to what was reported in 2.5.10 and, interestingly, the temperatures from 200-220°C, which are indicated as the optimum processing

temperature interval as per the manufacturer, yielded statistically similar results between themselves.

Afterwards, in an attempt to provide the phenomenological curves, an exponential regression was applied to the dot plots of Mass – Printing speed and Mass- Extruder temperature, so as to obtain the following formulas, that depicted mass as a function of print speed and extruder temperature respectively:

$$v - print\ speed;\ T - extruder\ temperature$$

$$m_{SC}(v) = \alpha * v^{\beta} = 0.4686 * v^{0.0239} \quad (4.1)$$

$$m_{SC}(T) = \gamma * T^{\xi} = 0.1878 * T^{0.1891} \quad (4.2)$$

In order to be able to obtain a surface model that simulated the one from Figure 67, it was necessary to create equation 4.3, that was a result from the multiplication of equations 4.1 and 4.2.

$$m_{SC}(v,t) = \left[\alpha * v^{\beta}\right] * \left[\gamma * T^{\xi}\right] \quad (4.3)$$

Taking into consideration that the values from $m_{sc}(v,t)$ had a difference to the ones from the surface on Figure 67 of $\sqrt{m}$, it was necessary to add a correction factor μ, thus originating equation 4.4:

$$m_{SC}(v,t) = \mu * \left[\alpha * v^{\beta}\right] * \left[\gamma * T^{\xi}\right] = 1.95 * \left[\alpha * v^{\beta}\right] * \left[\gamma * T^{\xi}\right] \quad (4.4)$$

Of course, the value of μ had to be obtained by an iterative method, seen as though it was a function of mass itself, which was the desired output. For the values shown before, it was possible to obtain the predictive model shown in Figure 71.

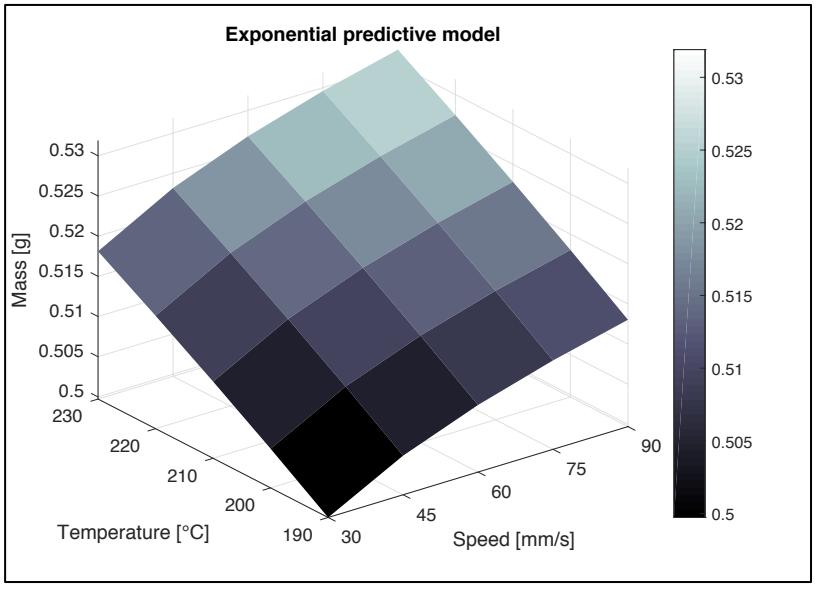


Figure 71 – Short Compression - Predictive model for the mass with print speed and extruder temperature as inputs. Based of exponential regressions obtained through experimental results.

This model allowed for an estimate of the test specimen to be made by knowing the temperature and the print speed and providing them as an input. A subtraction of the surfaces was a good measure of how far from the actual values of

the mass the model is. As it can be seen in Figure 72, the model can be considered as fit, with an average calculated error of around 0.76%. The way that the associated error was calculated was by subtraction of the mass matrixes (experimental and modelled), dividing each of the resulting values by the corresponding experimental value, as shown in equation 4.5.

$$Error_{ij} = \frac{|Mass_{experimental_{ij}} - Mass_{exponential_{ij}}|}{Mass_{experimental_{ij}}} * 100 \quad (4.5)$$

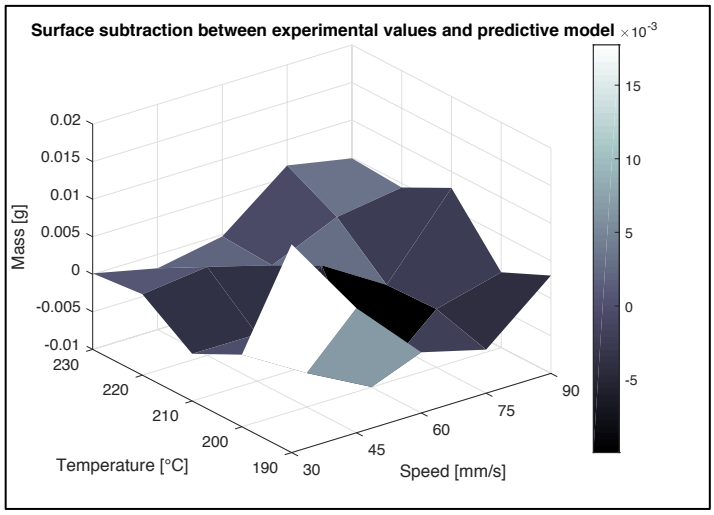


Figure 72 – Short Compression - Subtraction of the experimental and the predictive model.

4.1.2 Long Compression test specimens

Table 16 – Long Compression - Mean values of the mass of the test specimens for each of the used conditions.

Condition	V_{print} [mm/s]	T_{print} [°C]	Mass [g]	± S.Dev [g]
CV1_T1	30	190	2.493	0.020
CV1_T2	30	200	2.513	0.008
CV1_T3	30	210	2.535	0.026
CV1_T4	30	220	2.555	0.022
CV1_T5	30	230	2.542	0.010
CV2_T1	45	190	2.442	0.010
CV2_T2	45	200	2.477	0.014
CV2_T3	45	210	2.495	0.017
CV2_T4	45	220	2.515	0.005
CV2_T5	45	230	2.527	0.008
CV3_T1	60	190	2.418	0.025
CV3_T2	60	200	2.453	0.016
CV3_T3	60	210	2.485	0.013
CV3_T4	60	220	2.520	0.015
CV3_T5	60	230	2.542	0.019
CV4_T1	75	190	2.423	0.031
CV4_T2	75	200	2.465	0.026
CV4_T3	75	210	2.488	0.025
CV4_T4	75	220	2.520	0.040
CV4_T5	75	230	2.542	0.049
CV5_T1	90	190	2.415	0.048
CV5_T2	90	200	2.458	0.051
CV5_T3	90	210	2.487	0.036
CV5_T4	90	220	2.537	0.013
CV5_T5	90	230	2.532	0.050

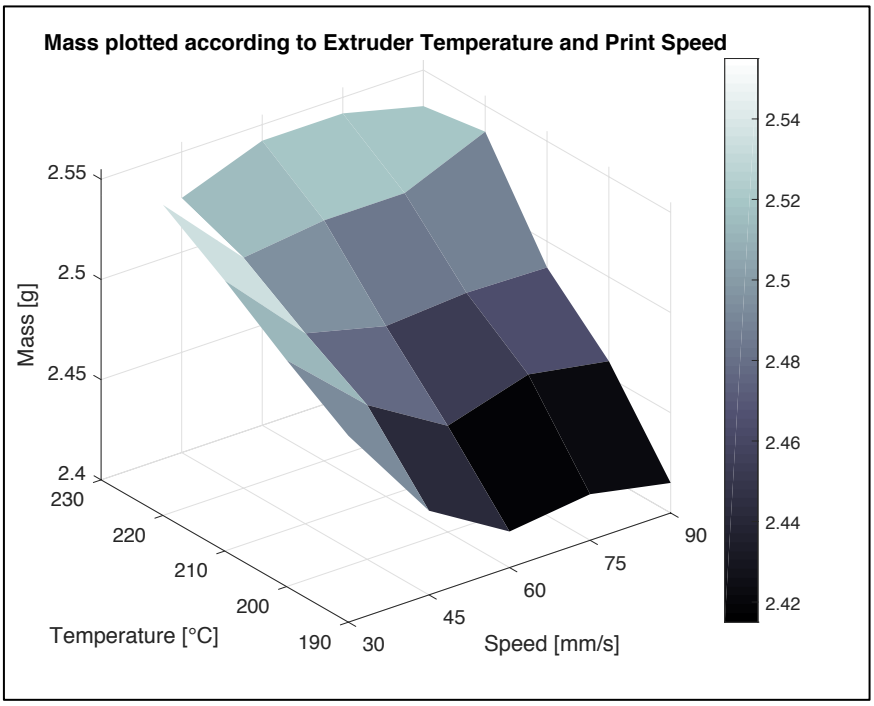


Figure 73 - Influence of the Extruder temperature and Print speed in the mass of long compression test specimens.

The values in Table 16 were obtained in the same fashion as the ones from Table 15, with an average of the three replicas made for each condition. Passing these values into the form of a surface such as the one in Figure 73 it was possible to observe that, similarly to the first case, the mass increased as the extruder temperature was increased as well. However, for these test specimens it was observed that, as the printing speed was increased, the mass showed a tendency to decrease, opposite to what was observed for the short compression test specimens and more according to the literature. The highest mass values of 2,555g and 2,542g were obtained for the conditions CV1_T4 and CV1_T5 respectively.

By then resorting to an ANOVA analysis it was possible to confirm that both of these parameters were influencing the mass of the test specimens, as expected, and, with the Tukey analysis output, visible in Figure 74 and Figure 75, it was possible to observe similar patterns to what was observed for the short compression test specimens in the way that the print speed of 30 mm/s is significantly different than the remaining set values (despite the influence on the mass for this case being the opposite), as well as the fact that there were three distinct groups of temperature ranges with different influences, them being 190°C, 200-210°C, and 220-230°C.

Print Speed [mm/s]	N	Mean	Grouping
30	15	2,52767	A
45	15	2,49100	B
75	15	2,48767	B
90	15	2,48567	B
60	15	2,48367	B

Means that do not share a letter are significantly different.

Extruder Temperature [°C]	N	Mean	Grouping
230	15	2,53667	A
220	15	2,52933	A
210	15	2,49800	B
200	15	2,47333	B
190	15	2,43833	C

Means that do not share a letter are significantly different.

Figure 74 - Long Compression test specimens -Tukey Pairwise comparisons on the influence of Print speed (left) and Extruder temperature (right) with 95% Confidence.

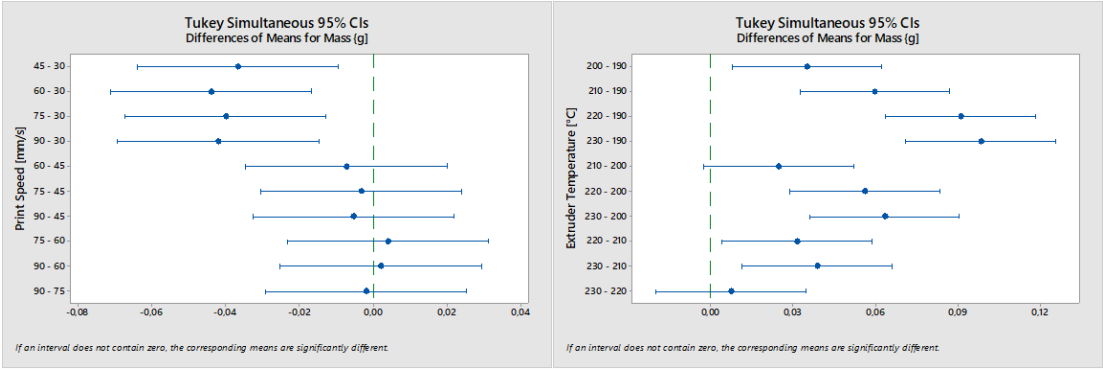
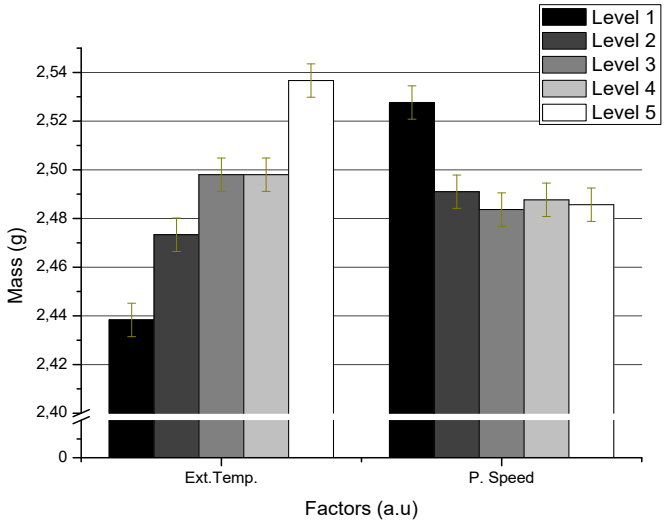


Figure 75 - Long Compression test specimens - Graphical representation for the difference of means for different print speeds (left) and extruder temperatures (right).

Straight away, it could be observed that the temperatures corresponding to the optimum processing windows as per the manufacturer yielded, again, relatively similar mass values between themselves, helping understand the importance of using the recommended temperatures for each filament. This phenomenon was further evidenced by the graph in Figure 76, where for the values of 210 – 220°C the masses were again very similar to each other, despite the small variance overall. It was additionally denoted that, although the printing temperature was defined as an influencing parameter, the differences it made were more reflected when altering from 30mm/s to 45mm/s, being relatively insignificant for the remaining values up to 90 mm/s.



Level	Extruder Temp. [°C]	Print Speed [mm/s]
1	190	30
2	200	45
3	210	60
4	220	75
5	230	90

Figure 76 - Long Compression - Plotting of the means and standard error for the mass according to the different levels of extruder temperature (left) and printing speed (right).

Afterwards, employing the same procedure as for the short compression test specimens to obtain a predictive model for the mass of the long compressive test specimens, the following expressions were obtained:

$$m_{LC}(v) = \alpha * v^{\beta} = 2.6439 * v^{-0.014} \quad (4.6)$$

$$m_{LC}(T) = \gamma * T^{\xi} = 0.7962 * T^{0.2137} \quad (4.7)$$

$$m_{LC}(v,t) = \mu * [\alpha * v^{\beta}] * [\gamma * T^{\xi}] = 0.4 * [\alpha * v^{\beta}] * [\gamma * T^{\xi}] \quad (4.8)$$

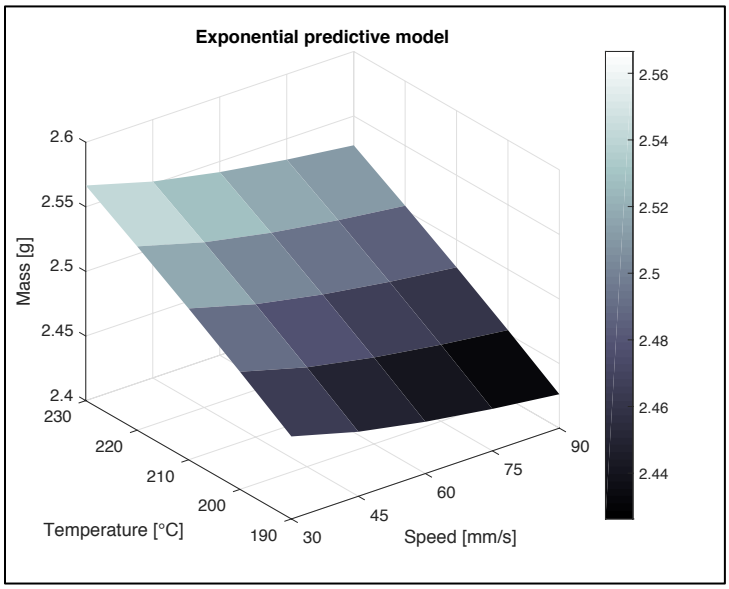


Figure 77 - Long Compression - Predictive model for the mass with print speed and extruder temperature as inputs. Based of exponential regressions obtained through experimental results.

The resulting predictive model is shown in Figure 77 and, in the same fashion as the one resulting from equation 4.4, it outputs an estimate for the mass of the long compression test specimens by providing a value for the mass and the print speed. In order to ascertain the validity of this model, the subtraction of both surfaces was performed, and the result is shown in Figure 78. As it can be seen, the associated error was low, around 0.49%, which helped validate the model.

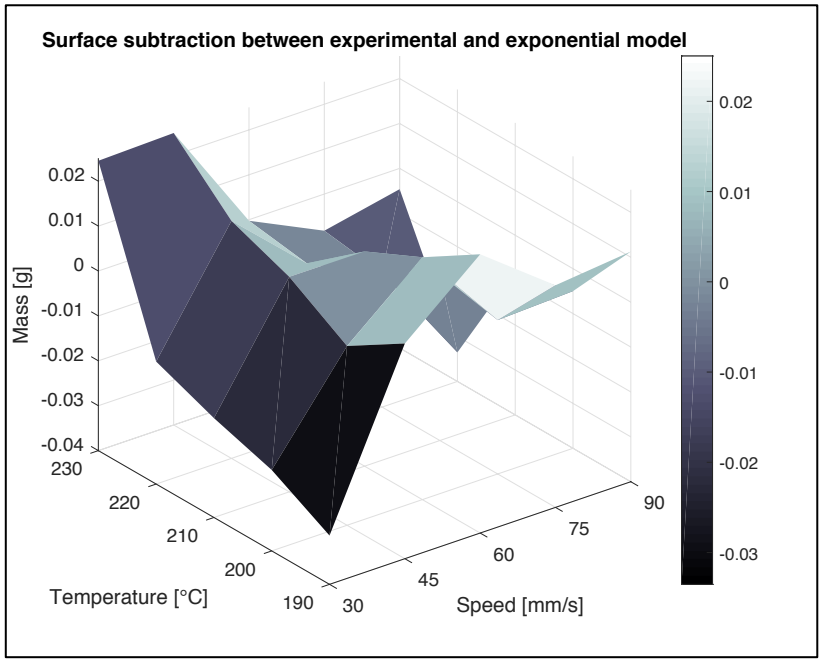


Figure 78 - Long Compression - Subtraction of the experimental and the predictive model.

4.1.3 Tensile test specimens

Table 17 – Tensile test specimens -Mean values of the mass of the test specimens for each of the used conditions.

Condition	V_{print} [mm/s]	T_{print} [°C]	Mass [g]	± S.Dev [g]
CV1_T1	30	190	10.033	0.042
CV1_T2	30	200	10.348	0.180
CV1_T3	30	210	10.493	0.175
CV1_T4	30	220	10.485	0.160
CV1_T5	30	230	10.580	0.161
CV2_T1	45	190	10.100	0.126
CV2_T2	45	200	10.200	0.173
CV2_T3	45	210	10.355	0.266
CV2_T4	45	220	10.247	0.129
CV2_T5	45	230	10.315	0.190
CV3_T1	60	190	9.9550	0.013
CV3_T2	60	200	1.1530	0.155
CV3_T3	60	210	1.1930	0.134
CV3_T4	60	220	1.2600	0.069
CV3_T5	60	230	10.358	0.052
CV4_T1	75	190	10.023	0.172
CV4_T2	75	200	10.160	0.179
CV4_T3	75	210	10.200	0.079
CV4_T4	75	220	10.313	0.120
CV4_T5	75	230	10.372	0.085
CV5_T1	90	190	9.9430	0.144
CV5_T2	90	200	10.052	0.110
CV5_T3	90	210	10.093	0.101
CV5_T4	90	220	10.152	0.054
CV5_T5	90	230	10.293	0.136

In Table 17 are shown the recorded values of the mass as an average of the three replicas for each condition of the tensile test specimens. After passing the information into a three-dimensional format, the output was as follows in Figure 79.

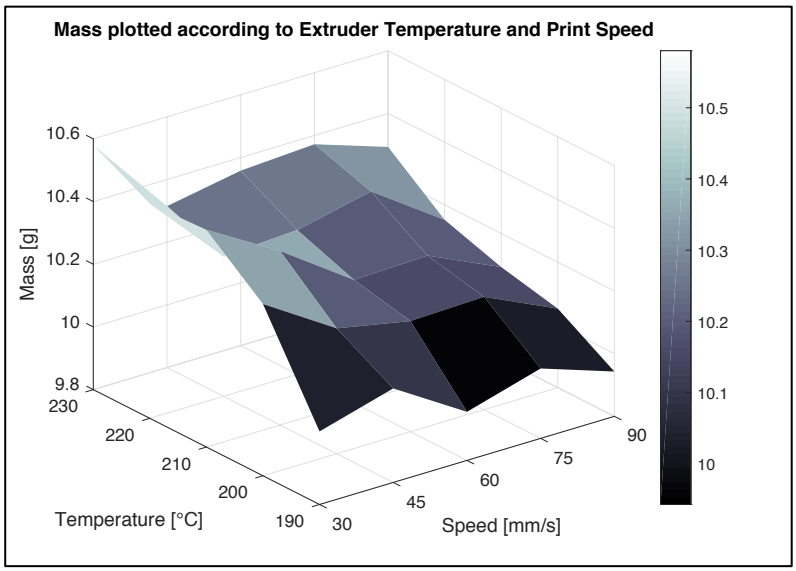


Figure 79 - Influence of the Extruder temperature and Print speed in the mass of tensile test specimens.

At this stage, a similar pattern to the one observed in 4.1.2 for the long compression test specimens was observed, with the mass being consequentially larger as the extruder temperature was increased, and becoming lower as the print speeds were increased. The highest recorded mass occurred for the condition CV1_T5, which corresponded to the lowest print speed coupled with the highest extruding temperature, similar to what occurred for the long compression test specimens.

The influence of these parameters was later verified with an ANOVA variance analysis and a Tukey analysis, shown in Figure 80, where it was observed that, for print speed, the slowest speed of 30 mm/s was significantly distinct from speeds from 45-90 mm/s, with the particularity that at this stage the largest speed of 90mm/s was significantly different from the 45 mm/s, making it more and more plausible to assume that in previous cases the set speed was not obtained due to inertial effects coupled with the small dimensions of the test specimens, as opposed to the tensile test specimens were, due to the larger dimensions, higher speeds were obtained. As for the influence of extruder temperature, again, the higher temperatures (210-230°C) yielded significantly different mass values than the smaller ones (190-200°C). Additionally, the range of optimum use provided very similar results, as it can be verified in Figure 81.

Print Speed [mm/s]	N	Mean	Grouping
30	15	10,3880	A
45	15	10,2433	B
75	15	10,2137	B C
60	15	10,1840	B C
90	15	10,1067	C

Means that do not share a letter are significantly different.

Extruder Temperature [°C]	N	Mean	Grouping
230	15	10,3837	A
220	15	10,2913	A B
210	15	10,2670	A B
200	15	10,1827	B
190	15	10,0110	C

Means that do not share a letter are significantly different.

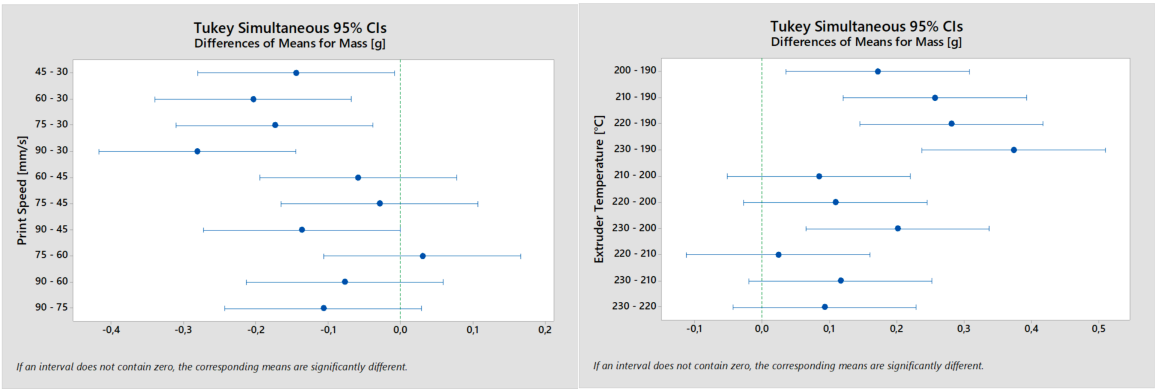
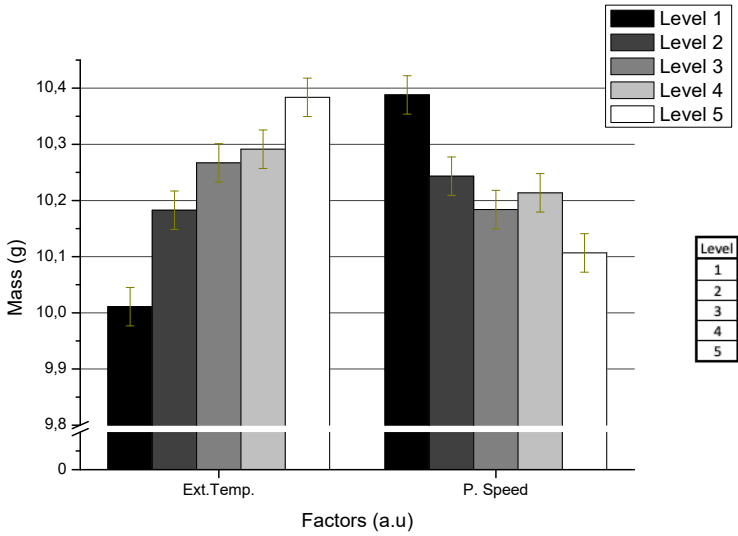


Figure 80 - Tukey Pairwise comparisons on the influence of Print speed (left) and Extruder temperature (right) with 95% confidence.



Level	Extruder Temp. [°C]	Print Speed [mm/s]
1	190	30
2	200	45
3	210	60
4	220	75
5	230	90

Figure 81 - Tensile test specimens - Plotting of the means and standard error for the mass according to the different levels of extruder temperature (left) and printing speed (right).

As for the predictive model, equations 4.9, 4.10 and 4.11 were obtained, with the output being the surface from Figure 82. As for the error yielded by the obtained model, the values were calculated to be as low as 0.50%, thus allowing the model to be validated.

$$m_T\,(v) = \alpha * v^{\beta} = 11.156 * v^{-0.022} \quad (4.9)$$

$$m_T\,(T) = \gamma * T^{\xi} = 3.987 * T^{0.1762} \quad (4.10)$$

$$m_T\,(v,t) = \mu * \left[\alpha * v^{\beta}\right] * \left[\gamma * T^{\xi}\right] = 0.098 * \left[\alpha * v^{\beta}\right] * \left[\gamma * T^{\xi}\right] \quad (4.11)$$

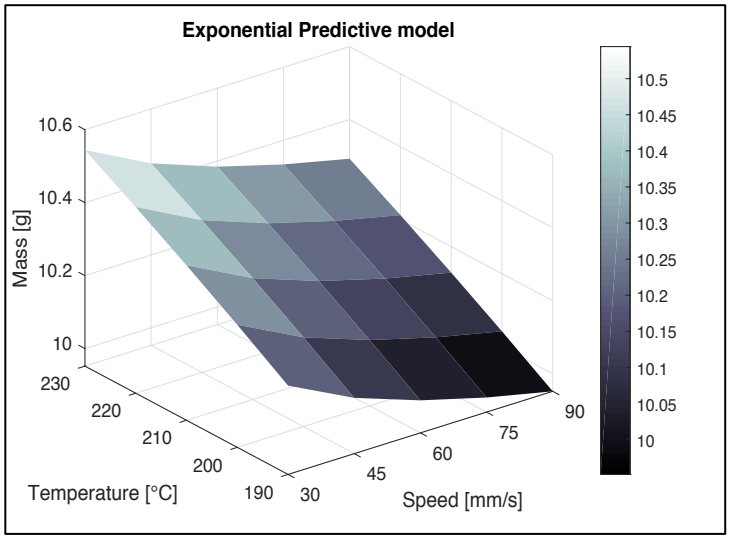


Figure 82 - Tensile - Predictive model for the mass with print speed and extruder temperature as inputs. Based off exponential regressions obtained through experimental results.

The subtraction of surfaces allowed for a good understanding of how small the error between each of the models actually was, and it can be observed in Figure 83.

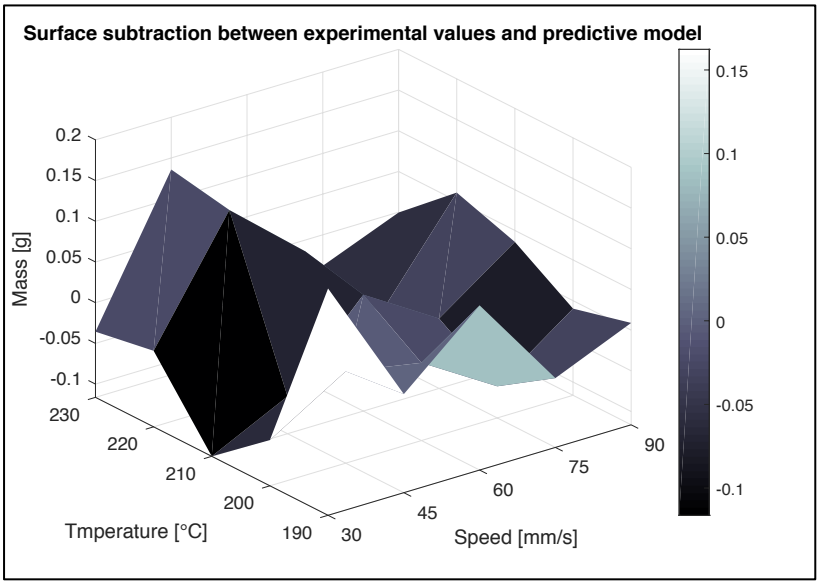


Figure 83 - Tensile - Subtraction of the experimental and the predictive model.

4.1.4 Flexural test specimens

Table 18 - Flexural test specimens -Mean values of the mass of the test specimens for each of the used conditions.

Condition	V_{print} [mm/s]	T_{print} [°C]	Mass [g]	± S.Dev [g]
CV1_T1	30	190	3.922	0.060
CV1_T2	30	200	3.963	0.078
CV1_T3	30	210	3.960	0.025
CV1_T4	30	220	4.035	0.044
CV1_T5	30	230	4.067	0.028
CV2_T1	45	190	3.890	0.013
CV2_T2	45	200	3.962	0.028
CV2_T3	45	210	4.003	0.046
CV2_T4	45	220	4.013	0.033
CV2_T5	45	230	4.042	0.032
CV3_T1	60	190	3.907	0.054
CV3_T2	60	200	3.940	0.035
CV3_T3	60	210	4.017	0.058
CV3_T4	60	220	4.025	0.083
CV3_T5	60	230	4.048	0.068
CV4_T1	75	190	3.860	0.048
CV4_T2	75	200	3.913	0.044
CV4_T3	75	210	3.962	0.028
CV4_T4	75	220	4.012	0.045
CV4_T5	75	230	4.030	0.035
CV5_T1	90	190	3.845	0.056
CV5_T2	90	200	3.877	0.014
CV5_T3	90	210	3.947	0.021
CV5_T4	90	220	3.962	0.006
CV5_T5	90	230	3.995	0.000

Following the same procedures as for the remaining test specimens, in this case the same tendency as in 4.1.2 and 4.1.3 was observed regarding the way that the process parameters at hand influence the mass of the produced components. The highest value for the mass was obtained at condition CV1_T5, visible in Table

18, which corresponded to the highest extruder temperature and print speeds. By observing Figure 84 it was made simpler to observe the increase in mass coupled with increased in extruder temperature, as well as the decrease of the mass as the print speeds were gradually increased.

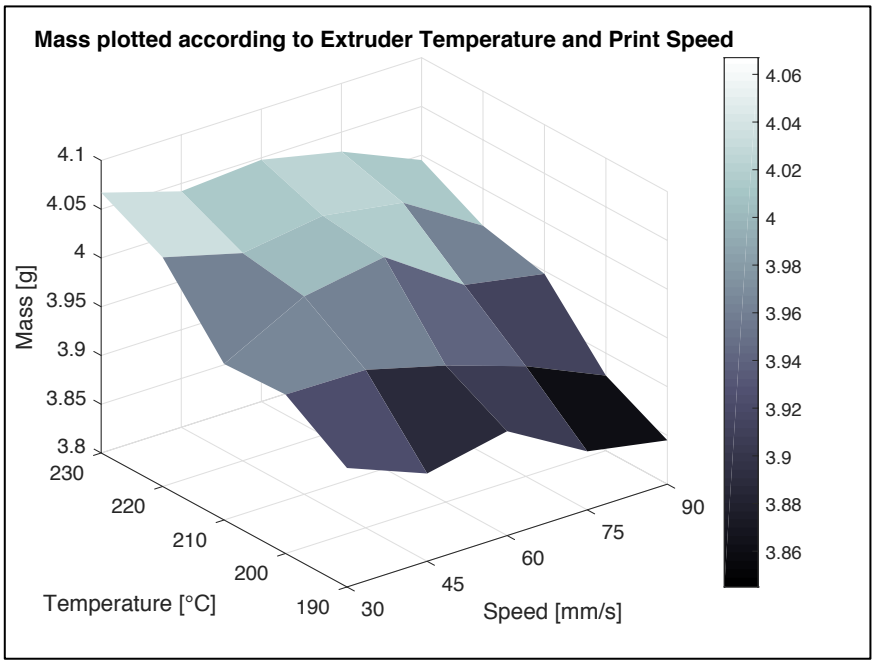


Figure 84 - Influence of the Extruder temperature and Print speed in the mass of flexural test specimens.

Print Speed [mm/s]	N	Mean	Grouping		
30	15	3,98933	A		
60	15	3,98733	A		
45	15	3,98200	A		
75	15	3,95533	A	B	
90	15	3,92500		B	

Means that do not share a letter are significantly different.

Extruder Temperature [°C]	N	Mean	Grouping			
230	15	4,03633	A			
220	15	4,00933	A	B		
210	15	3,97767		B		
200	15	3,93100			C	
190	15	3,88467				D

Means that do not share a letter are significantly different.

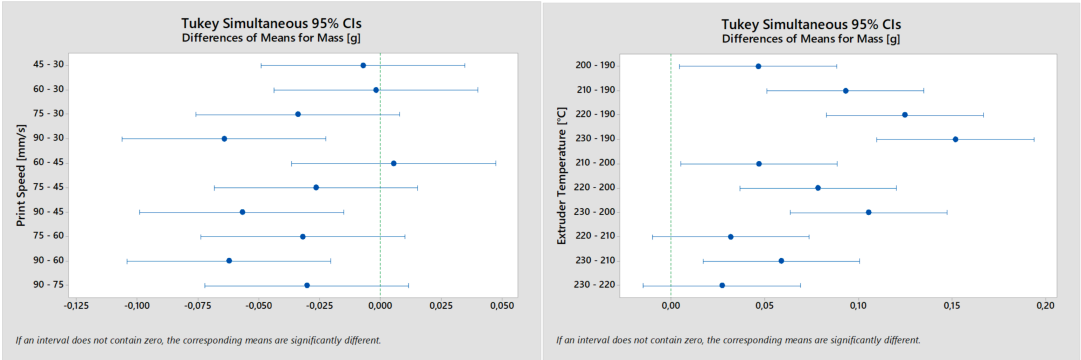
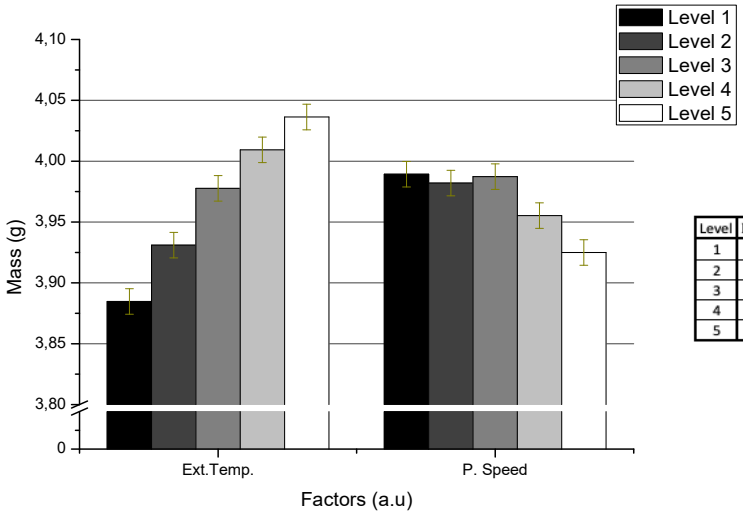


Figure 85 - Flexural - Tukey Pairwise comparisons on the influence of Print speed (left) and Extruder temperature (right) with 95% confidence.

As it can be seen in Figure 85, the results from the statistical analysis were similar in the way that it was possible to separate the lowest print speeds from the higher values, as well as the lower extruder temperatures from the higher values. Print speeds of 30-60 mm/s yielded very similar results for the mass and, afterwards, a significant decrease in mass could be observed as the print speed was increased until 90 mm/s. The fact that, in this case, the increase in print speed was not as prominent in terms of how it affected the mass as in the case of tensile test specimens further helps support the claim that the higher speeds might not have been obtained due to the smaller dimensions and inertial effects of the extruder module.



Level	Extruder Temp. [°C]	Print Speed [mm/s]
1	190	30
2	200	45
3	210	60
4	220	75
5	230	90

Figure 86 - Flexural test specimens - Plotting of the means and standard error for the mass according to the different levels of extruder temperature (left) and printing speed (right).

On the other hand, the influence of the extruder temperature follows the same pattern, visible in Figure 86, as in the other test specimens, which makes it safe to state that extruder temperature, as it was increased, yielded components with higher mass. This effect might have been due to the increase in fluidity of the material due to the higher processing temperatures, fact which enabled for more material to be extruded and oozed for the same amounts of torque being pushed by the stepper motors.

In the same fashion, the predictive model was obtained by exponential regression of the values of mass using extruder temperature and print speed as inputs, with the following equations having been used:

$$m_T(v) = \alpha * v^{\beta} = 4.1825 * v^{-0.013} \quad (4.12)$$

$$m_T(T) = \gamma * T^{\xi} = 1.3443 * T^{0.2025} \quad (4.13)$$

$$m_T(v,t) = \mu * \left[\alpha * v^{\beta}\right] * \left[\gamma * T^{\xi}\right] = 0.252 * \left[\alpha * v^{\beta}\right] * \left[\gamma * T^{\xi}\right] \quad (4.14)$$

The graphical output of the obtained surface can be seen in Figure 87 and the subtraction of the experimental and exponential surfaces can be observed in Figure 88, with the associated error to be estimated around 0.39%, thus making the model a good approximation to the obtained results in terms of mass.

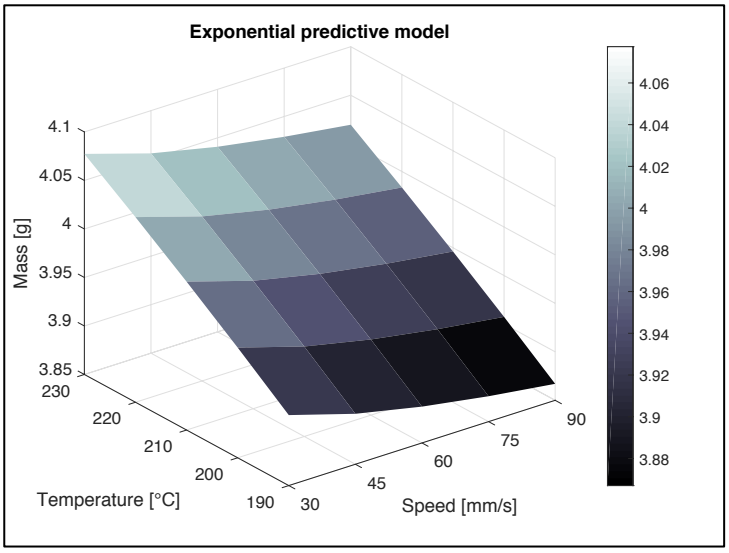


Figure 87 - Flexural - Predictive model for the mass with print speed and extruder temperature as inputs. Based off exponential regressions obtained through experimental results.

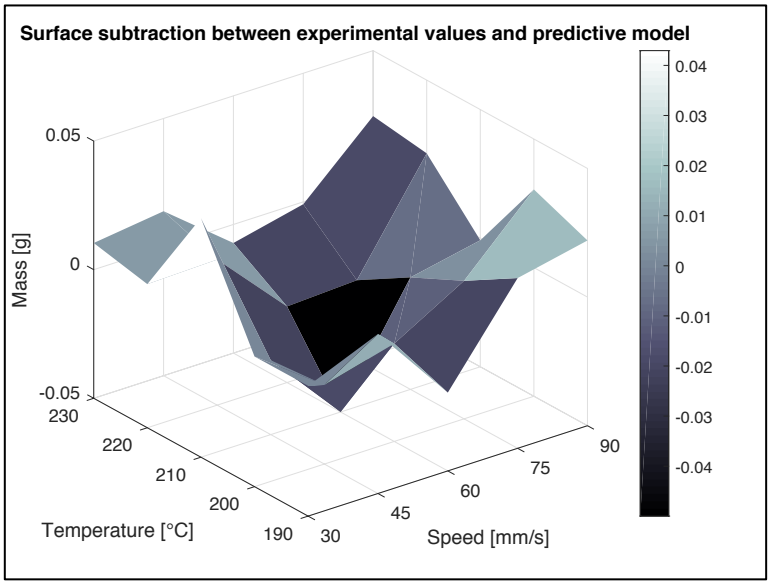


Figure 88 - Flexural - Subtraction of the experimental and the predictive model.

4.1.5 Generic predictive model

The obtained models in 4.1.1, 4.1.2, 4.1.3 and 4.1.4 were all able to predict the mass for each of the respectively used component to create them. As such, in order to obtain a model that could allow for the prediction of a wide range of components, an attempt was made to develop the information from the separate models.

Firstly, it was relevant to understand that the predictive models for the mass of short compression test specimens were not considered for this stage, seen as though this model did not behave accordingly to the remaining models and the literature.

Hence, taking into consideration that mass is a function of the material density and component volume, as well as that the density was the same for all the components seen as though the material was not altered, it was decided that component volume should be introduced to the model as an input variable. In order to do so, expressions 4.8, 4.11 and 4.14 were divided by the volume of their respective components. The rational procedure can be observed in equations 4.15 to 4.19.

$$m = V * \rho \tag{4.15}$$

$$\rho = constant \tag{4.16}$$

$$m_{T_{LC}}(V, v, t) = V * \mu * \left[v^{\beta}\right] * \left[T^{\xi}\right] = V * 4.21 * 10^{-4} * [v^{-0.014}] * [T^{0.2137}] \tag{4.17}$$

$$m_{T_F}(V, v, t) = V * \mu * \left[v^{\beta}\right] * \left[T^{\xi}\right] = V * 4.43 * 10^{-4} * [v^{-0.013}] * [T^{0.2025}] \tag{4.18}$$

$$m_{T_T}(V, v, t) = V * \mu * \left[v^{\beta}\right] * \left[T^{\xi}\right] = V * 5.24 * 10^{-4} * [v^{-0.022}] * [T^{0.1762}] \tag{4.19}$$

By calculating the error that each generalized model (expressions 4.17 to 4.19) yielded in same fashion as for the previous cases, it was possible to obtain Table 19 and observe that the smallest error originated from the coefficients from the flexural model.

Table 19 - Estimated errors for each of the components using coefficients from different models. (LC - Long Compression; F - Flexural; T - Tensile).

Coefficients from model	Prevision of component	Estimated error
LC	LC	0.49%
LC	F	0.64%
LC	T	1.39%
F	LC	0.64%
F	F	0.40%
F	T	0.98%
T	LC	1.40%
T	F	0.86%
T	T	0.52%

As such, due to the small error associated to the coefficients for the flexural model, as well as the similarity between the models for each of the different test specimens, the decision to include these in the predictive model for the mass was made, with the final expression being shown below. The volume is to be input in mm^3, print speed in mm/s, extruder temperature in ^{o}C and the output of the mass in g.

$$m_T(V, v, t) = V * 4.43 * 10^{-4} * [v^{-0.013}] * [T^{0.2025}] \tag{4.20}$$

4.2 Dimension

During the experimental phase, it was noted that, often, parts of the components with the same theoretical dimensions as the ones shown in Figure 89 were different from each other. In order to ascertain whether this phenomenon did in fact occur, that is, if the overall geometry of the test specimens influenced the dimensional accuracy of the process, a variance analysis on the parameters "*yy*" and "*zz*" was done, with the influencing factors being print speed, extruder temperature and, most importantly, the type of test specimens.

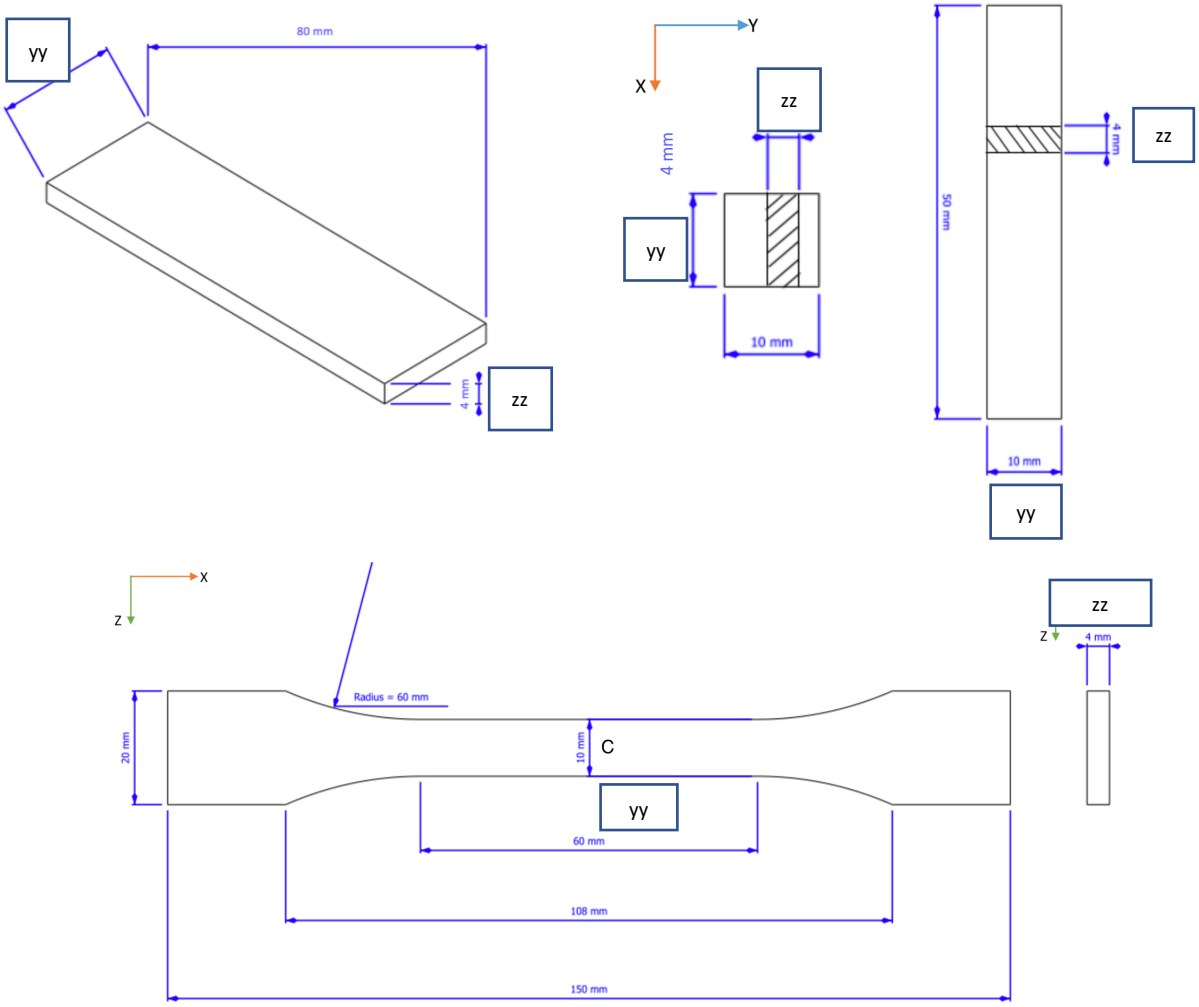


Figure 89 - Technical drawings of the test specimens according to the specified standards, with the dimensions under study (yy and zz) identified at the respective places.

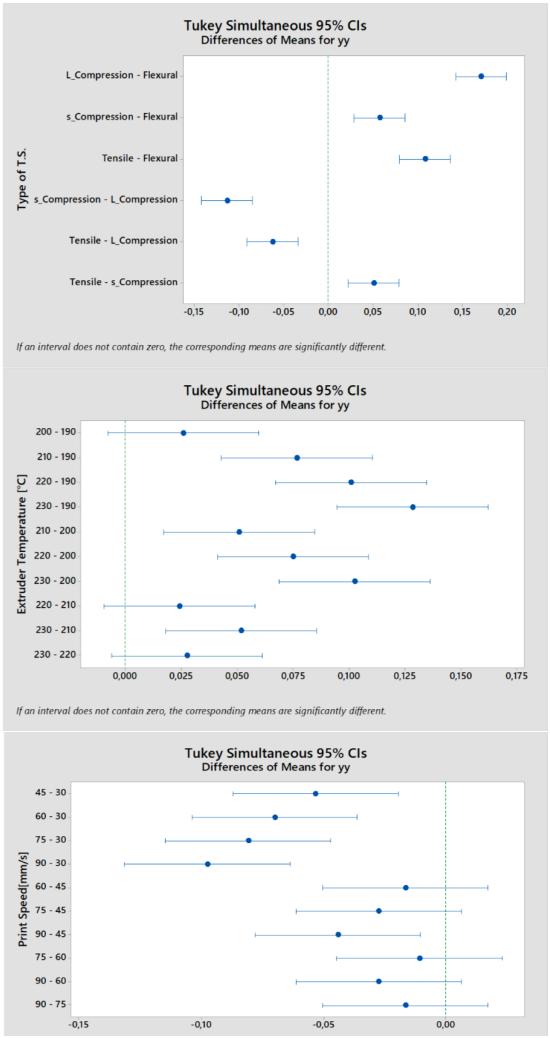
Analysis and comparison of the dimensional accuracy could only be done for dimensions that were the same across all test specimens, hence only dimensions regarding the movement of the machine in the Y and Z-axis were studied, seen as though there was not any feature with the same size for all of the test specimens regarding the X-axis. By observing Figure 89 it becomes clear that all of the different components had the same height, 4mm, which allowed this be one of the evaluated dimensions (named *zz* for convention). As for the dimension named *yy*, it was observed that all the test specimens had a region with a width of 10mm across the Y axis, hence the naming convention of *yy*.

Having defined all the parameters to be analysed, in order to perform the ANOVA analysis, the remaining step was to define the influencing parameters and their different levels, as is shown in Table 20.

Table 20 - Influencing factors under study and their different levels.

V_{print} [mm/s]	T_{print} [°C]	Type of test specimen
30 (V1)	190 (T1)	S_Compression (TT1)
45 (V2)	200 (T2)	L_Compression (TT2)
60 (V3)	210 (T3)	Tensile (TT3)
75 (V4)	220 (T4)	Flexural (TT4)
90 (V5)	230 (T5)	---

After this, the ANOVA analysis was performed, along with a Tukey pairwise comparison for both *yy* and *zz* and the influence print speed, extruder temperature and type of test specimen had on each of them. First analysing the influence that these factors had on the *yy* parameter, with the Tukey analysis visible in Figure 90, it was shown that all three of them exerted a relevant influence on the value of this dimension due their *p-value* being well below 0.05 for all cases. As for the *zz* parameter, with the Tukey analysis visible in Figure 91, only the extruder temperature and type of test specimen were considered as significant, with the print speed having a *p-value* of 0.176.



Type of T.S.	N	Mean	Grouping
L_Compression	75	10,1480	A
Tensile	75	10,0853	B
s_Compression	75	10,0347	C
Flexural	75	9,9773	D

Means that do not share a letter are significantly different.

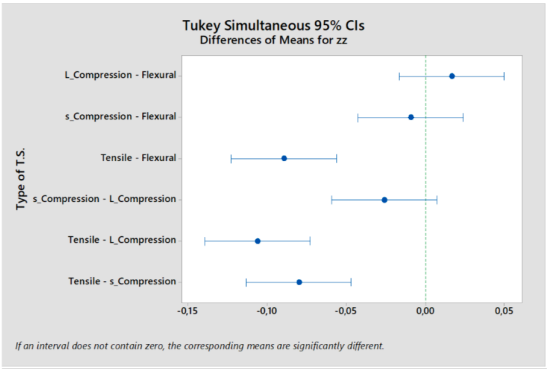
Extruder Temperature [°C]	N	Mean	Grouping
230	60	10,1233	A
220	60	10,0958	A B
210	60	10,0717	B
200	60	10,0208	C
190	60	9,9950	C

Means that do not share a letter are significantly different.

Print Speed[mm/s]	N	Mean	Grouping
30	60	10,1217	A
45	60	10,0683	B
60	60	10,0517	B C
75	60	10,0408	B C
90	60	10,0242	C

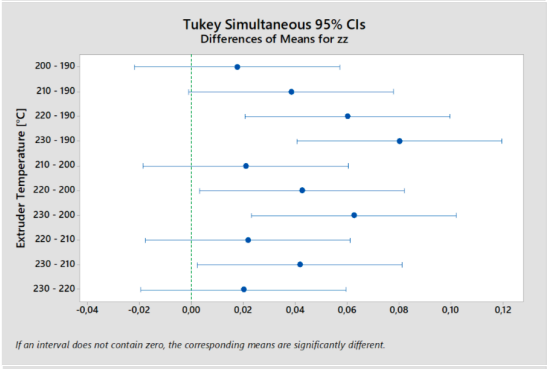
Means that do not share a letter are significantly different.

Figure 90 - Tuckey pairwise comparison regarding the yy dimension.



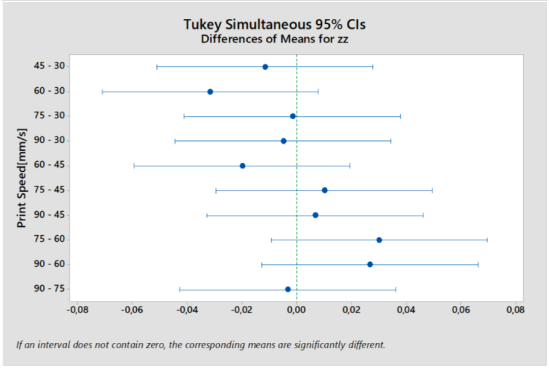
Type of T.S.	N	Mean	Grouping
L_Compression	75	4,22133	A
Flexural	75	4,20467	A
s_Compression	75	4,19533	A
Tensile	75	4,11533	B

Means that do not share a letter are significantly different.



Extruder Temperature [°C]	N	Mean	Grouping
230	60	4,22500	A
220	60	4,20500	A B
210	60	4,18333	B C
200	60	4,16250	C
190	60	4,14500	C

Means that do not share a letter are significantly different.



Print Speed[mm/s]	N	Mean	Grouping
30	60	4,19417	A
75	60	4,19250	A
90	60	4,18917	A
45	60	4,18250	A
60	60	4,16250	A

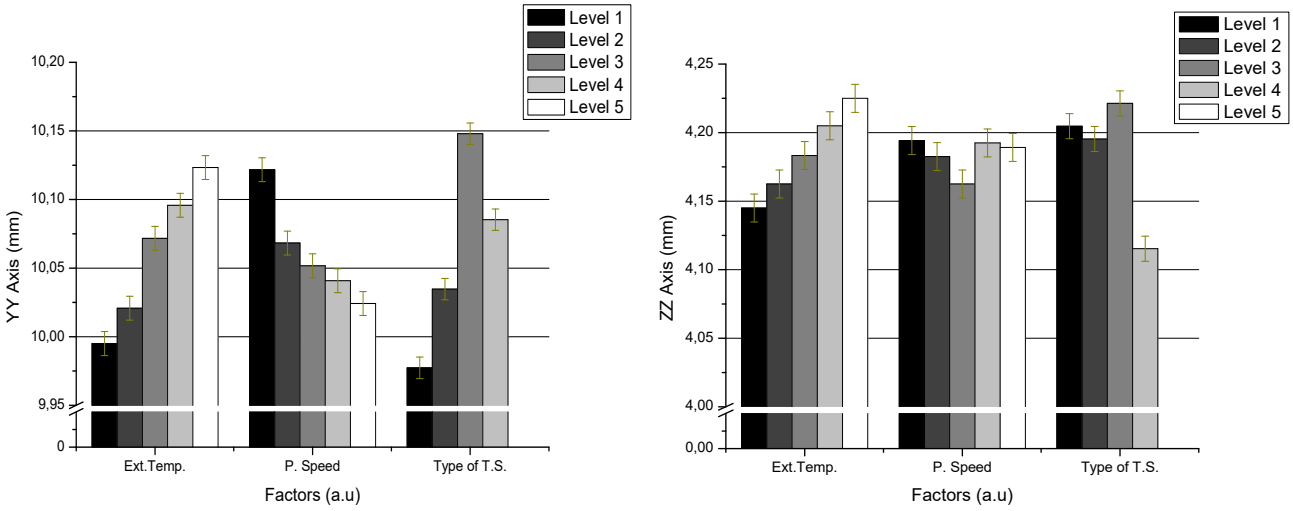
Means that do not share a letter are significantly different.

Figure 91 - Tuckey pairwise comparison regarding the zz dimension.

This discrepancy in terms of the print speed affecting only the dimensions with respect to the Y-axis and not the ones respecting the Z-axis can be explained by the fact that, when defining the print speed in the *slicing software*, only the movements in the X and Y-axis are affected, with the Z-axis movements being performed at a different speed and with no extrusion being done during said movements.

As for the influence of the extruder temperature, it was observed that, for both *yy* and *zz*, higher temperatures yielded higher values for these dimensions, which is according to what was mentioned in the previous section for the increase of the mass, due to phenomena of over-extrusion. Additionally, seen as though higher temperatures at the nozzle mean that there might have been a significant thermal expansion of this component, the orifice from which the filament was extruded was closer to the build surface. This led to the raster being over-pressed against the surface and filament being pushed aside as the nozzle deposited the material, which translated to a coarser surface finish, susceptible of higher dimensional errors.

The way print speed affected the *yy* dimension was so that the higher the printing speed yielded the smaller value, which can be explained by the fact that there was significantly less time for the filament to be deposited and solidify as the printing speeds were increased.



Level	Extruder Temp. [°C]	Print Speed [mm/s]	Type of T.S.
1	190	30	S_Compression
2	200	45	L_Compression
3	210	60	Tensile
4	220	75	Flexural
5	230	90	---

Figure 92 - Plotting of the means and standard error for the yy (left) and zz (right) according to the different levels.

Lastly, it was noted that the type of test specimen did in fact influence the values of *yy* and *zz*. However, as it can be easily observed in Figure 92, the relation between geometry and dimension was distinct when observing *yy* or observing *zz*. For the first case, there were significant differences for each of the different test specimens, which might indicate that the geometry being built does influence the dimensional accuracy of the Y-axis, whereas for *zz* only the flexural test specimens yielded a significantly different value for *zz*, which if the results for the flexural test specimens were considered as outliers, might indicate that the dimensional accuracy was not influenced by the geometry of the component being built.

4.3 Mechanical properties

For analysis purposes, all stress-strain curves can be observed in Appendix D. All test trials were performed at the "Laboratório de Caracterização Mecânica, Secção de Tecnologia Mecânica e Gestão Industrial do Departamento de Eng. Mecânica do Instituto Superior Técnico".

4.3.1 Compression

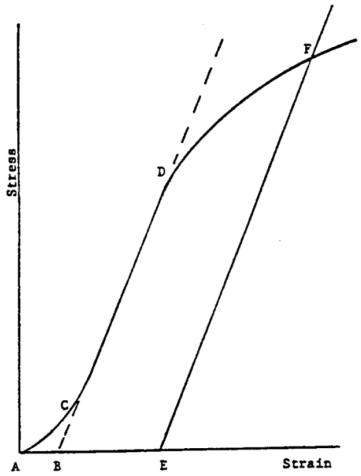


Figure 93 - Representation of the non-linear region (Hookean behaviour) in AC, and the corresponding linear aproximation in EF. Adapted from ASTM D 638-03.

After the trials were executed, the data was processed according to the guidance from the ISO 604 standard. During this procedure, it was noticed that the stress-strain curves of the test specimens were showing indications of a non-linear segment during the first instances (such as the one from Figure 93) due to a period were the test plates of the UTS machine were accommodating to some of the existing imperfections of the test specimens, as it can be observed in Figure 94.

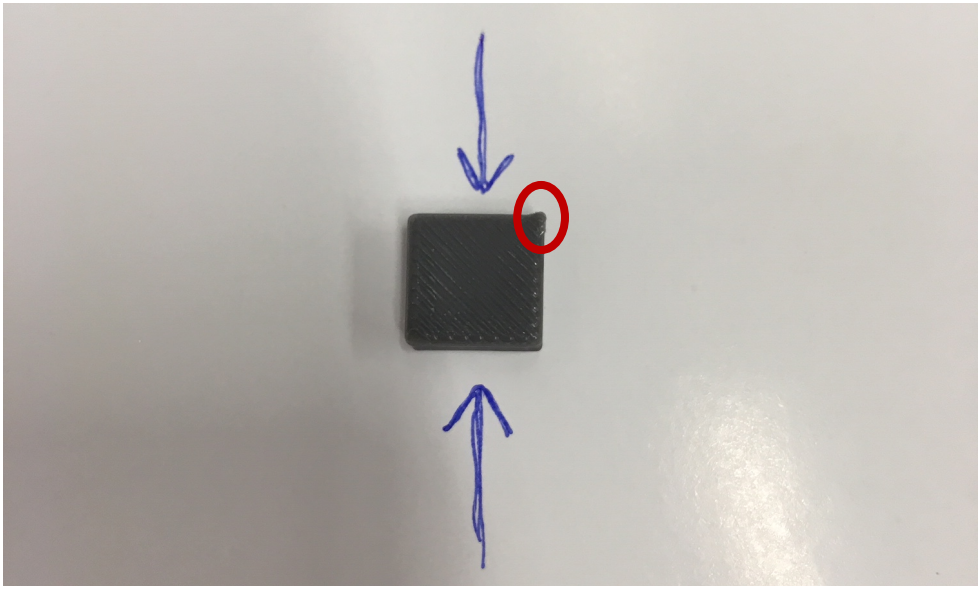


Figure 94 - Type B (Short compression test specimen) with the imperfections that caused the non-linear behaviour during the initial instances of the test specimen.

As such, in order to properly evaluate the mechanical results, a linear regression was made for each of the test specimens, followed by a correction of the stress-strain curves.

In addition, the type A test specimens, destined to determine the values of the compression module, showed very low reproducibility of results due to the fact that their slenderness, combined with some imperfections similar to the ones from the type B test specimens, led to random misalignments and overall instability during the test trials, as it can be observed in Figure 95.

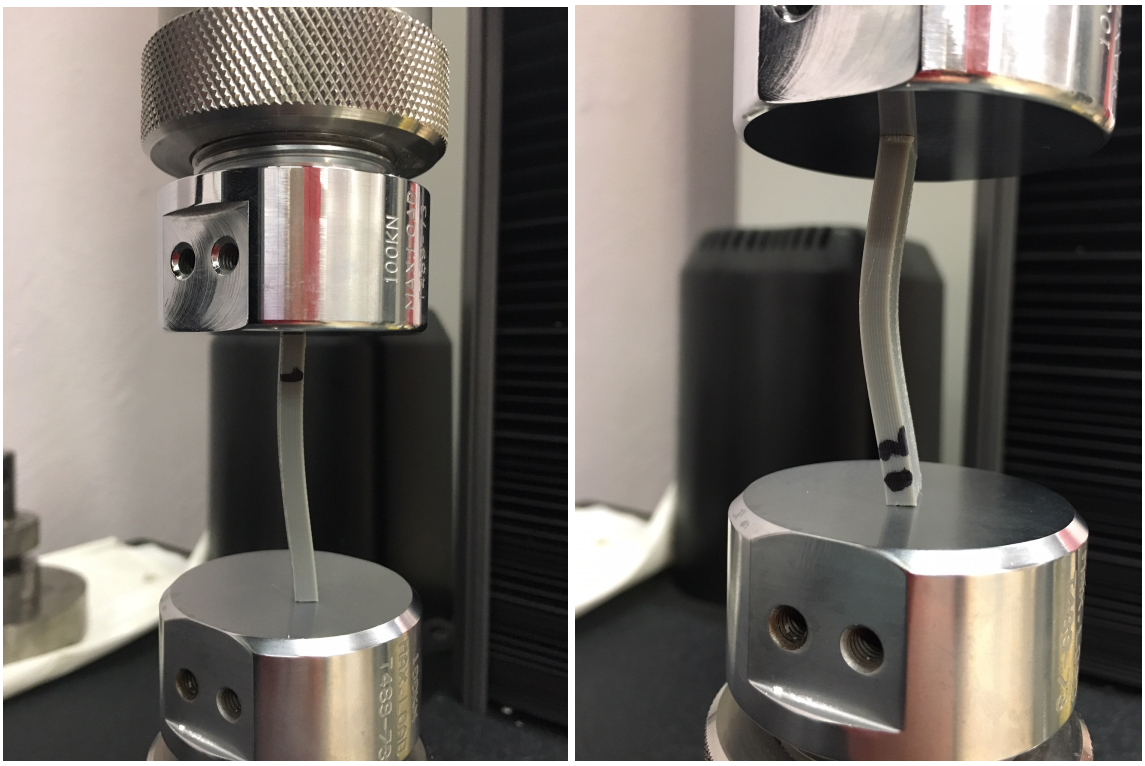


Figure 95 - Misalignment phenomenons that occured during the trials of the type A test specimens, causing for reproducibility issues.

In order to obtain more accurate values for the compressive module, seen as though the type A test specimens became unstable after certain stages of the test trial, the data treatment and analysis was made considering only values of compressive extension corresponding to a maximum displacement of 0,8mm, value after which the instability and misalignment issues became too severe for most of the cases.

In Table 21 it is possible to observe the average values for the compressive yield strength, yield strain and modulus for each of the different conditions of the experiment.

Table 21 - Summary of the average compressive mechanical properties.

Condition	Ec [GPa]	E ± SDev [GPa]	σ_{yield} [MPa]	σ ± SDev [MPa]	ε_{yield} [mm/mm]	ε ± SDev [mm/mm]
CV1_T1	1.59	0.46	82.61	1.09	0.0435	0.0036
CV1_T2	1.57	0.22	87.20	2.58	0.0467	0.0078
CV1_T3	1.76	0.24	89.02	2.01	0.0521	0.0113
CV1_T4	1.51	0.16	89.21	2.54	0.0525	0.0113
CV1_T5	1.58	0.23	89.03	1.55	0.0504	0.0086
CV2_T1	1.37	0.05	84.93	2.08	0.0436	0.0008
CV2_T2	1.55	0.16	81.30	0.43	0.0816	0.0557
CV2_T3	1.49	0.16	82.16	3.28	0.0547	0.0149
CV2_T4	1.43	0.06	83.18	2.82	0.0540	0.0159
CV2_T5	1.72	0.32	80.73	2.84	0.0621	0.0248
CV3_T1	1.60	0.12	87.94	3.55	0.0492	0.0074
CV3_T2	1.68	0.03	84.49	2.65	0.0633	0.0240
CV3_T3	1.58	0.09	88.31	2.40	0.0551	0.0167
CV3_T4	1.40	0.39	89.44	2.20	0.0503	0.0017
CV3_T5	1.62	0.13	90.65	2.93	0.0578	0.0151
CV4_T1	1.75	0.17	86.91	1.97	0.0519	0.0063
CV4_T2	1.77	0.04	87.60	2.21	0.0535	0.0086
CV4_T3	1.67	0.14	87.88	0.95	0.0609	0.0134
CV4_T4	1.67	0.18	88.90	1.41	0.0569	0.0099
CV4_T5	1.53	0.06	88.27	0.77	0.0540	0.0077
CV5_T1	1.34	0.35	85.34	1.28	0.0496	0.0029
CV5_T2	1.50	0.01	84.92	0.81	0.0508	0.0077
CV5_T3	1.54	0.08	86.14	0.52	0.0532	0.0062
CV5_T4	1.32	0.19	87.02	0.71	0.0590	0.0132
CV5_T5	1.56	0.04	88.13	0.66	0.0602	0.0145

By analysing the values on the table, it is possible to observe that the highest values of yield stress, strain and compressive modulus were respectively obtained in conditions CV3_T5, CV2_T2 and CV4_T2 with values of 90.75 MPa, 0.0816 mm/mm and 1.77 GPa. As for the lowest values, these were obtained at CV2_T5, CV1_T1 and CV5_T4, with respective values of 80.73 MPa, 0.0435 mm/mm and 1.32 GPa.

Afterwards, in the same fashion as for the analysis of the mass, transforming the information into the format of surface representations, such as the ones in Figure 96, allowed for a few observations to be made.

Firstly, it was noted that the compressive modulus was maintained throughout all of the different levels of the considered factors, with minor variations having occurred in a somewhat random manner. The compressive yield strength showed a tendency to increase as the extruder temperature was gradually increased, whereas the print speed showed a more stationary influence on this property, despite the fact that for print speeds of 45mm/s there was a significantly lower value range, when compared to the remaining levels of print speeds. As such, considering that this might have been an outlier case, then it could be observed that print speed did not greatly affect the compressive yield strength. As for the yield strain, it was observed that neither extruder temperature nor print speed showed significant influence on this parameter, with the values being similar throughout all levels of the experiment except for the CV2_T2 condition, that showed a spike when compared to the remaining situations.

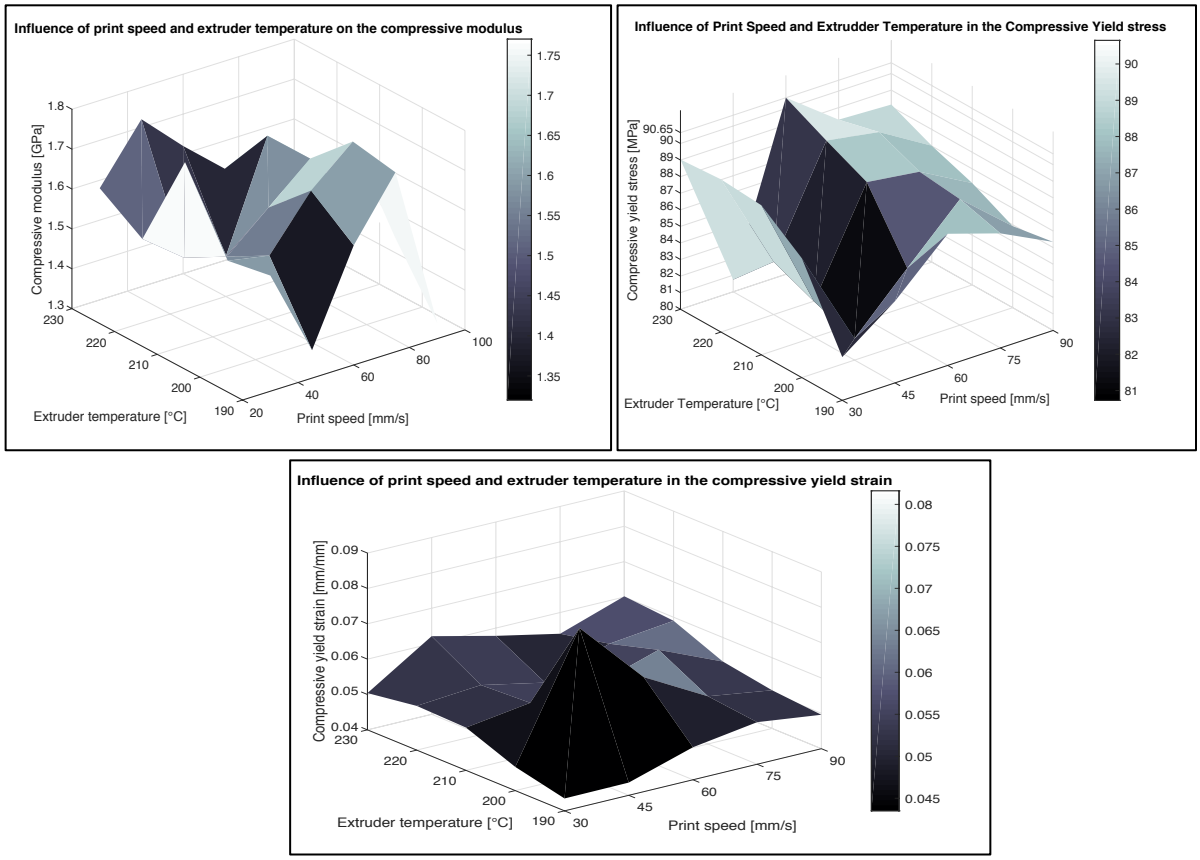


Figure 96 - Influence of print speed and extruder temperature on the compressive modulus (left), yield stress (right) and strain (bottom).

By resorting to an ANOVA analysis, it was possible to observe that compressive modulus was, in fact, slightly influenced by print speed due to its *p-value* being 0.019 (lower than 0.05), whereas there was no significant contribution by the extruder temperature, with a *p-value* of 0.173. It should be noted, though, that the values of the compressive module were obtained by analysing the Type A test specimens and, as it was stated at the beginning of the compressive properties analysis, the trials for these test specimens were marked by the occurrence of buckling and instability phenomena. As such, it was possible that the obtained results for the compressive modulus might have differed between themselves more due to these occurrences than the process parameter variation per se.

As for the compressive yield strength, it was observed that this property was influenced by both parameters, with the obtained *p-value* being well below 0.05 for print speed and 0.017 for extruder temperature. Regarding the compressive yield strain, it was noted that only the extruder temperature yielded a somewhat significant contribute on this property's values, with its *p-value* being 0.038 and. The print speed did not yield any significant contribute, with a *p-value* of 0.123.

In order to better ascertain the differences between the different values for each of the parameters' influence, a Tukey pairwise comparison was complementary performed for each of the properties.

Vprint [mm/s]	N	Mean	Grouping	
75	15	1,67600	A	
30	15	1,60067	A	B
60	15	1,57733	A	B
45	14	1,49914	A	B
90	15	1,45267		B

Tprint [°C]	N	Mean	Grouping
200	15	1,61467	A
210	15	1,60733	A
230	14	1,58914	A
190	15	1,52800	A
220	15	1,46667	A

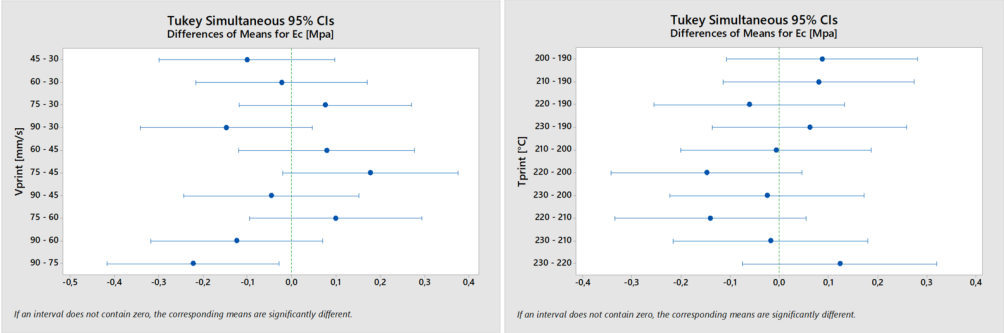


Figure 97 - Tuckey pairwise comparison regarding the compressive modulus.

By observing Figure 97, the claim that the compressive modulus' values were distributed in a random manner was corroborated, with no pattern being observed in terms of how the increase in print speed or extruder temperature altered the corresponding compressive modulus value. This would make sense, seen as though this property is majorly, a function of the material itself and, most importantly, the internal structure of the test specimens, which could alter their mechanical behaviour.

It was observed that the maximum difference between values was 0.22GPa, occurring between the print speeds of 75mm/s and 90mm/s. Although there was no information provided by the manufacturer regarding the compressive properties of this specific PLA, a comparison to the values from Table 4 (referring to monolithic PLA samples) shows that the compressive modulus was around half of these, which had a range of 3.3-3.6 GPa. In Figure 98, it is again possible to observe the absence of any noticeable patterns for each of the parameters.

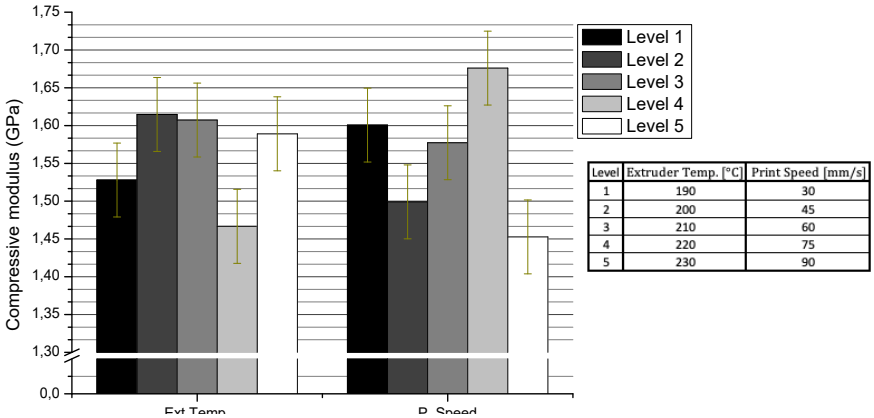


Figure 98 - Plotting of the means and standard error for the compressive modulus according to the different levels.

Focusing on the compressive yield strength, it can be seen in Figure 99 that print speed, in fact, yielded extremely similar values of compressive yield strength aside from the level of 45 mm/s. In order to confirm whether this parameter was non-influent on the compressive yield strength, it would be required to repeat the test trials with new test specimens, printed in the same conditions.

Vprint [mm/s]	N	Mean	Grouping	
60	15	88,1654	A	
75	15	87,9127	A	
30	15	87,4139	A	
90	15	86,3107	A	
45	15	82,4587		B

Tprint [°C]	N	Mean	Grouping	
220	15	87,5498	A	
230	15	87,3643	A	B
210	15	86,7012	A	B
190	15	85,5464	A	B
200	15	85,0998		B

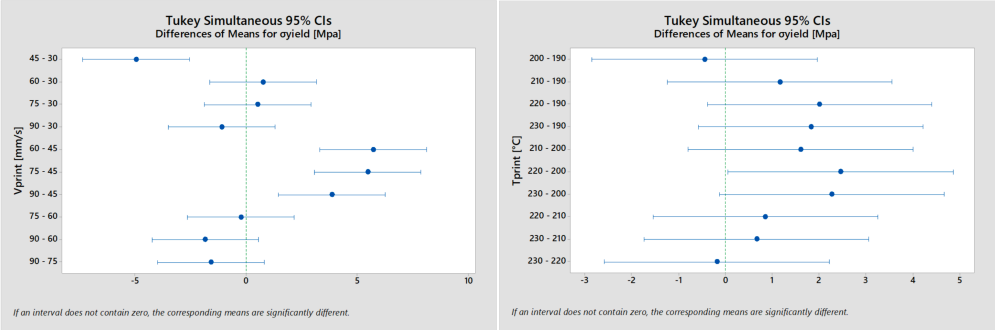
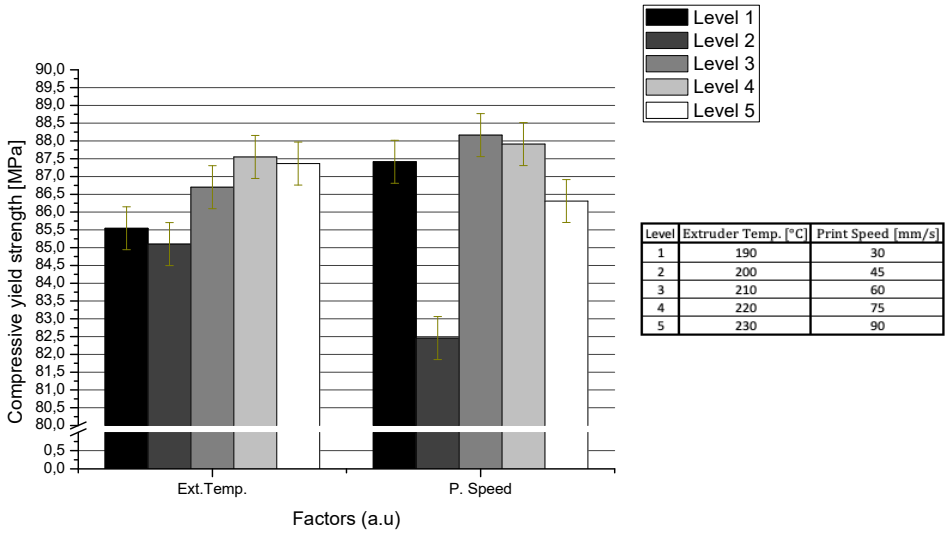


Figure 99 - Tuckey pairwise comparison regarding the compressive yield stress.

As for the effect of extruder temperature, this comparison helped establish that extruder temperature did influence the compressive yield strength, in such a way that higher extruder temperatures yielded higher yield strengths, with the results becoming fairly similar between themselves as the temperature range of 210-230°C was used. In Figure 100 it is possible to observe this behaviour in a bar chart, which allows for a separate analysis for each of the parameters.



Level	Extruder Temp. [°C]	Print Speed [mm/s]
1	190	30
2	200	45
3	210	60
4	220	75
5	230	90

Figure 100 - Plotting of the means and standard error for the compressive yield stress according to the different levels.

It should be noted that, although all of what was stated regarding both of these parameters' influence was true, the differences between opposite extremes for each case are extremely small, with the maximum difference being around 5,7MPa. As such, for solicitations where compressive yield strength would be one of the required specifications for a given component, then the opted parameter levels for extruder temperature and print speed should be 220°C and 60mm/s respectively. However, if time were to be one of the specified demands, it would be possible to utilise a higher print speed without a significant compromise on the compressive yield strength of the component.

Lastly, moving onward to the compressive strain, by performing the same analysis, as shown in Figure 101, it was observed that, although there are some differences for the value of compressive strain as the extruder temperature was altered, these were highly similar among themselves for all levels of both parameters, which could be confirmed by observing Figure 102.

Vprint [mm/s]	N	Mean	Grouping
45	15	0,0592067	A
75	15	0,0554333	A
60	15	0,0551067	A
90	15	0,0545733	A
30	15	0,0490133	A

Tprint [°C]	N	Mean	Grouping	
200	15	0,0591667	A	
230	15	0,0569067	A	B
210	15	0,0551933	A	B
220	15	0,0545267	A	B
190	15	0,0475400		B

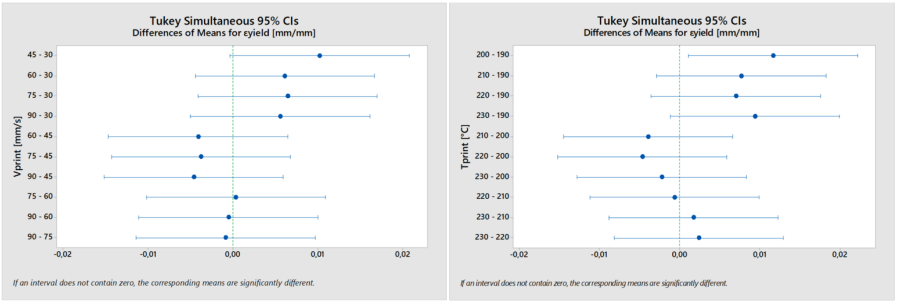
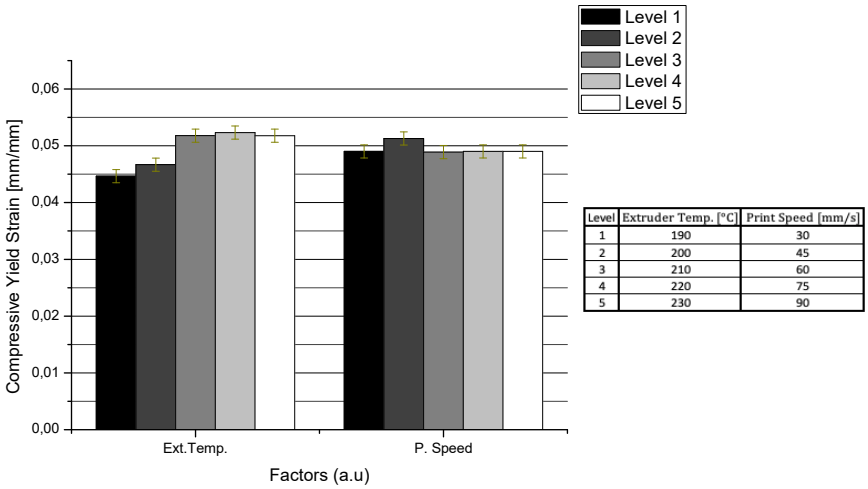


Figure 101 - Tuckey pairwise comparison regarding the compressive yield strain.



Level	Extruder Temp. [°C]	Print Speed [mm/s]
1	190	30
2	200	45
3	210	60
4	220	75
5	230	90

Figure 102 - Plotting of the means and standard error for the compressive yield strain according to the different levels.

Considering the intent of creating a predictive model for the compressive mechanical properties, the same procedure as for the mass was adopted, with the output being given by the equations 4.21 to 4.29.

$$\mathrm{E_c}\,(v) = \alpha * v^{\beta} = 1.5807 * v^{-0.0004} \quad (4.21)$$

$$\mathrm{E_c}\,(T) = \gamma * T^{\xi} = 1.9504 * T^{-0.005} \quad (4.22)$$

$$\mathrm{E_c}\,(v,t) = \mu * \left[\alpha * v^{\beta}\right] * \left[\gamma * T^{\xi}\right] = 0.5095 * \left[\alpha * v^{\beta}\right] * \left[\gamma * T^{\xi}\right] \quad (4.23)$$

$$\sigma_{c_{yield}}\,(v) = \alpha * v^{\beta} = 85.024 * v^{0.0003} \quad (4.24)$$

$$\sigma_{c_{yield}}\,(T) = \gamma * T^{\xi} = 74.688 * T^{0.0007} \quad (4.25)$$

$$\sigma_{c_{yield}}\,(v,t) = \mu * \left[\alpha * v^{\beta}\right] * \left[\gamma * T^{\xi}\right] = 0.0137 * \left[\alpha * v^{\beta}\right] * \left[\gamma * T^{\xi}\right] \quad (4.26)$$

$$\varepsilon_{c_{yield}}\,(v) = \alpha * v^{\beta} = 0.0501 * v^{0.0012} \quad (4.27)$$

$$\varepsilon_{c_{yield}}\,(T) = \gamma * T^{\xi} = 0.0282 * T^{0.0031} \quad (4.28)$$

$$\varepsilon_{c_{yield}}\,(v,t) = \mu * \left[\alpha * v^{\beta}\right] * \left[\gamma * T^{\xi}\right] = 36.85 * \left[\alpha * v^{\beta}\right] * \left[\gamma * T^{\xi}\right] \quad (4.29)$$

The output of the equations 4.23, 4.26 and 4.29 for the compressive modulus, yield strength and strain, respectively, yielded errors of around 6.39%, 2.59% and 8.73% and can be observed in Figure 103, with the surface subtraction for error representation in Figure 104. The fact that the values for the error were not possible to be further lowered was due to the outlier conditions, which were considered during the creation of the models.

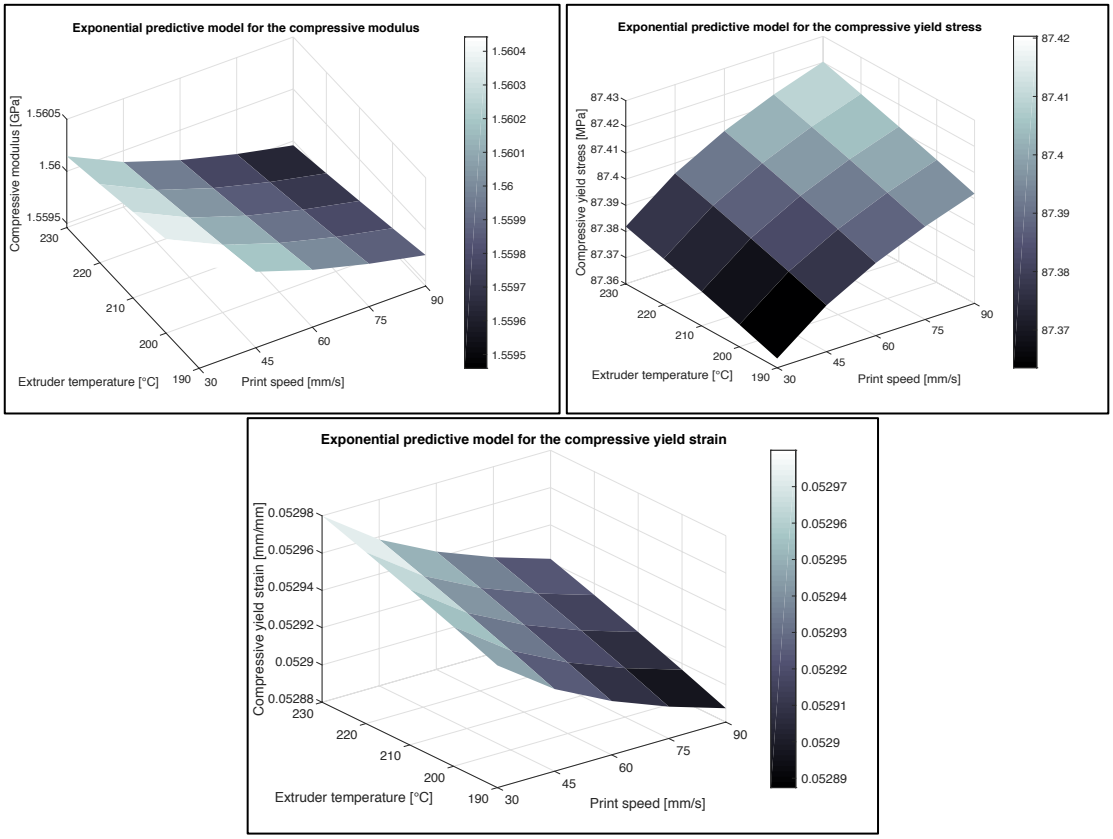


Figure 103 - Predictive model for the compressive modulus (left), yield strength (right) and strain (bottom) with print speed and extruder temperature as inputs. Based off exponential regressions obtained through experimental results.

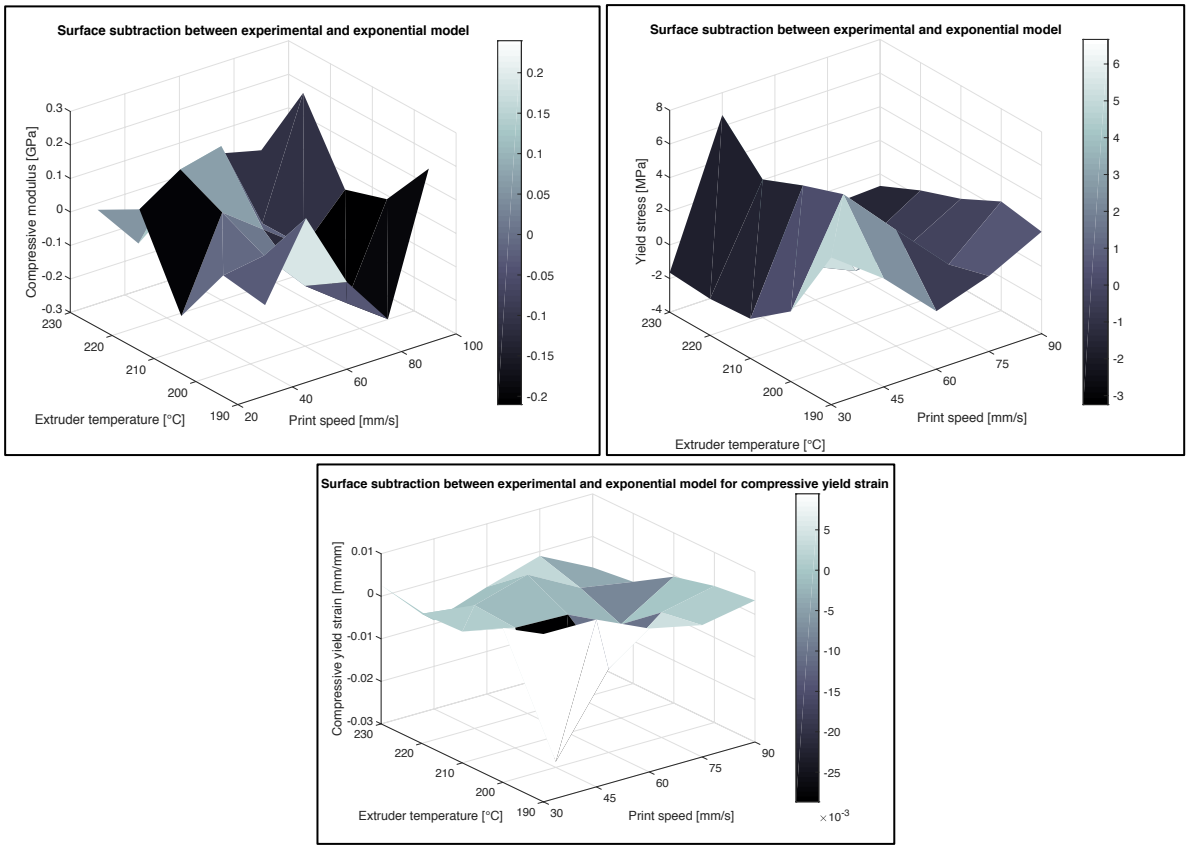


Figure 104 - Subtraction of the experimental and the predictive models for the compressive modulus (left), yield strenght (right) and strain (bottom).

4.3.2 Tensile

After the execution of the trials and analysis of the output data according to the ISO 527 standard, it was possible to obtain the values for tensile modulus, yield stress and strain, shown in Table 22.

Table 22 - Summary of the average tensile mechanical properties.

Condition	E [GPa]	E ± SDev [GPa]	σ_{yield} [MPa]	σ ± SDev [MPa]	ε_{yield} [mm/mm]	ε ± SDev [mm/mm]
CV1_T1	3.38	0.09	50.03	0.81	0.0200	0.0003
CV1_T2	3.35	0.05	51.99	0.66	0.0201	0.0002
CV1_T3	3.39	0.18	51.71	2.39	0.0193	0.0012
CV1_T4	3.39	0.17	51.43	0.81	0.0197	0.0004
CV1_T5	3.28	0.09	51.10	1.90	0.0197	0.0003
CV2_T1	3.09	0.17	46.51	1.75	0.0198	0.0001
CV2_T2	3.34	0.24	48.61	2.49	0.0200	0.0001
CV2_T3	3.09	0.20	49.30	1.52	0.0204	0.0004
CV2_T4	3.41	0.41	49.18	3.55	0.0197	0.0004
CV2_T5	3.12	0.03	48.44	0.33	0.0200	0.0003
CV3_T1	3.18	0.11	46.72	2.65	0.0203	0.0003
CV3_T2	3.10	0.07	47.35	0.54	0.0204	0.0006
CV3_T3	2.89	0.02	48.78	2.23	0.0210	0.0003
CV3_T4	3.05	0.13	48.69	2.25	0.0207	0.0006
CV3_T5	3.05	0.06	47.87	1.05	0.0206	0.0007
CV4_T1	3.20	0.08	47.47	0.80	0.0195	0.0006
CV4_T2	3.21	0.08	48.93	0.28	0.0198	0.0002
CV4_T3	3.03	0.08	49.14	2.75	0.0206	0.0003
CV4_T4	3.16	0.12	49.80	2.51	0.0202	0.0003
CV4_T5	2.99	0.13	47.74	0.76	0.0201	0.0002
CV5_T1	2.93	0.11	43.65	0.84	0.0198	0.0003
CV5_T2	3.01	0.06	46.44	1.03	0.0202	0.0002
CV5_T3	3.11	0.13	47.47	2.03	0.0201	0.0001
CV5_T4	3.18	0.06	49.12	1.19	0.0202	0.0002
CV5_T5	3.11	0.05	49.44	0.36	0.0202	0.0001

Quickly analysing the values on the table, it was possible to observe that the tensile modulus was fairly similar throughout all the different considered conditions, which implies this property was influenced by neither print speed nor extruder temperature. This would make sense, seen as though this is a function of the material itself. The same could be observed regarding the tensile yield strain, whereas the tensile yield stress was more affected throughout the different stages and conditions of the experiment, albeit in a small scale. As the print speed was increased, a decrease in tensile yield stress could be noted and in the case of extruder temperature, as this value was increased, so did the tensile yield stress increase as well, again, in a nearly unnoticeable manner.

The highest values of tensile modulus, yield stress and strain were respectively obtained in conditions CV2_T4, CV1_T2 and CV3_T3, with values of 3.41GPa, 51.99MPa and 0.0210 mm/mm. As for the lowest values, these were obtained at CV3_T3, CV5_T1 and CV1_T3, with respective values of 2.89GPa 43.65MPa and 0.0193mm/mm.

With the intent to better understand the influence of the parameters print speed and extruder temperature on these properties, the surfaces from Figure 105 were obtained.

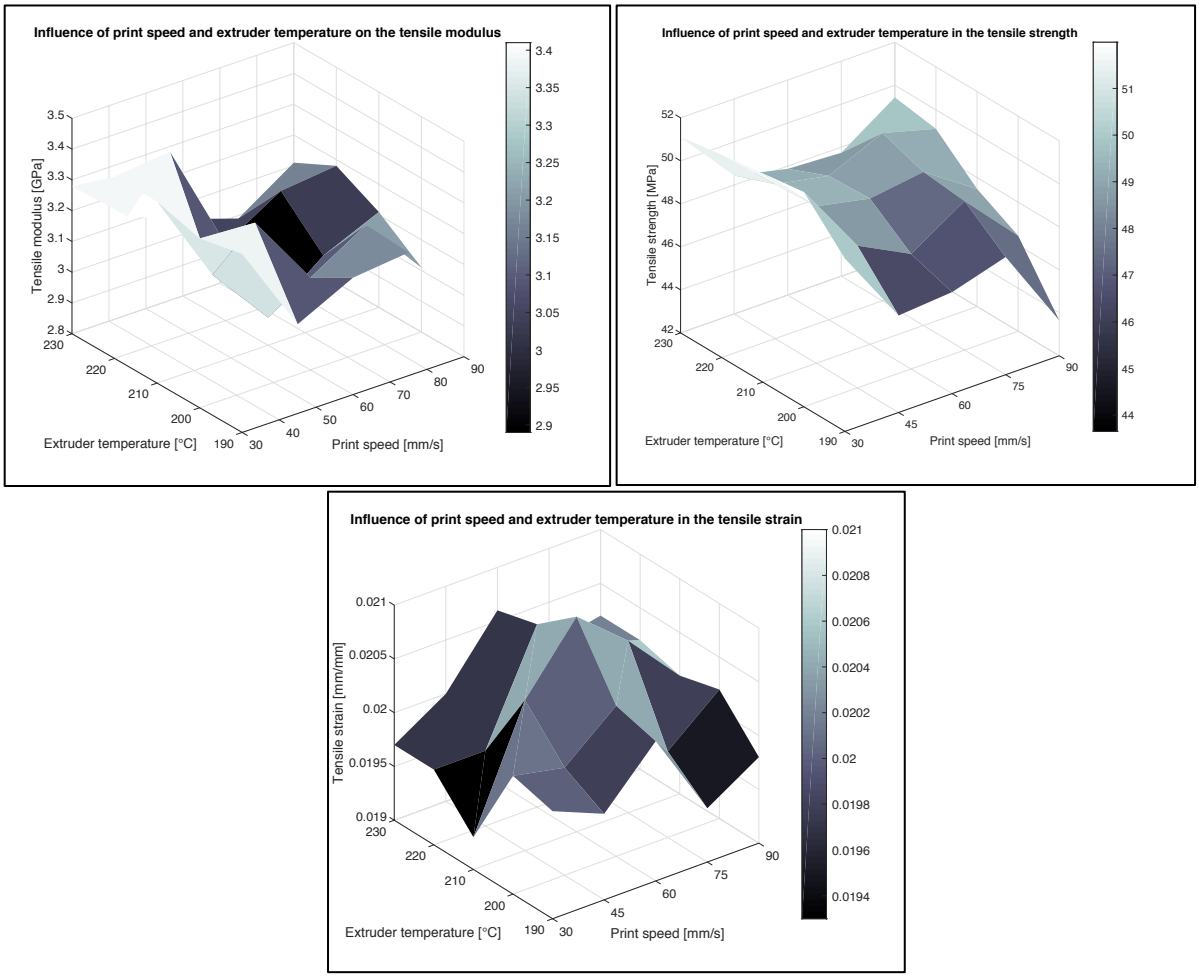


Figure 105 - Influence of print speed and extruder temperature on the tensile modulus (left), yield stress (right) and yield strain (bottom).

Analysing the surface for the influence on the tensile modulus, it could be observed that print speed was the most significant parameter for this property and that extruder temperature did not portray any meaningful influence. It was possible to confirm these claims by resorting to an ANOVA analysis and obtaining a *p-value* of 0.176 for the extruder temperature (non-influencing parameter) and well below 0.05 for the print speed. As for the values themselves, despite existing some variation from 2.89 to 3.41 GPa, these were according to the results obtained by others, such as Lanzotti et al. (2015), Tymrak, Kreiger and Pearce (2014) and, interestingly, the values for the tensile modulus are, at times, higher than this specific PLA variant producer's claims. This phenomenon could be related to the fact that, although the raster orientation was $\pm 45°$, the perimeter was deposited according to the solicitation orientation, which might have led to higher tensile resistance, confirming what was stated in 2.5.2, coupled with a constant deformative behaviour.

Similarly, when observing the influence on tensile yield stress it can be seen that the influence of both parameters was similar, both with *p-values* below 0.05, with the extruder temperature becoming an influencing factor as well, as expected. In this case, despite the tensile yield stress being lower than that of the producer's

specified values (77MPa), the results fall into accordance to the above-mentioned literature as well.

Regarding the print speed influence itself on the tensile modulus and yield stress, the fact that this parameter's increase meant a subsequent decrease on these properties' value, albeit small, could be related to the existence of larger gaps between rasters and overall porosity, as it was mentioned in 2.5.9. Consequentially, larger gaps in the test specimens' structure led to lower bonding between deposited filament, thus reducing the tensile yield stress and modulus.

As for the influence on the tensile yield strain, similar to what happened on the compressive test specimens, neither of the parameters presented significant influence, with the values being extremely similar throughout all levels of the experiment, ranging from 0.0193mm/mm to 0.0210 mm/mm. The reduced ductile behaviour can inclusively be observed on the test specimens after fracture, with an example shown in Figure 106. The remaining photographs of all the tensile test specimens are visible in Appendix E.

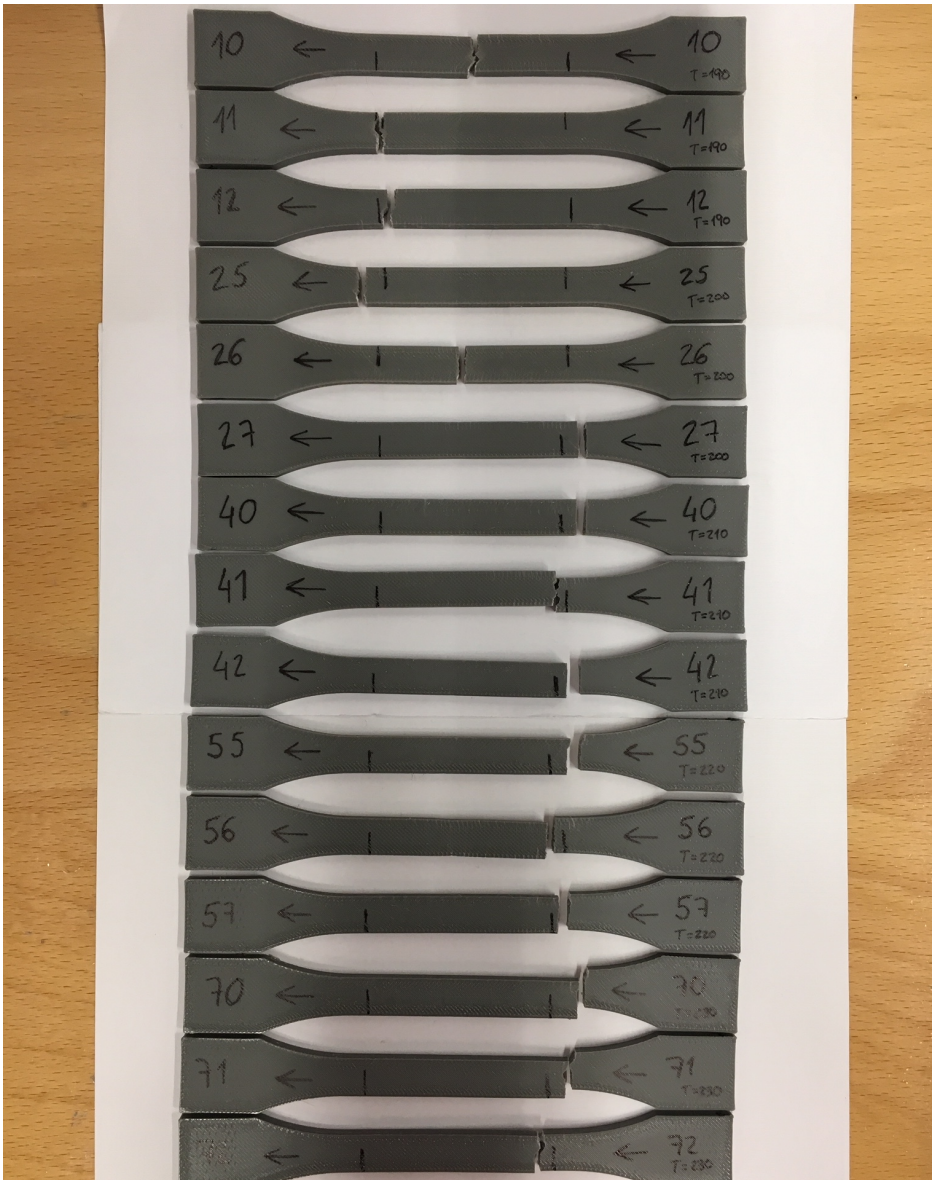
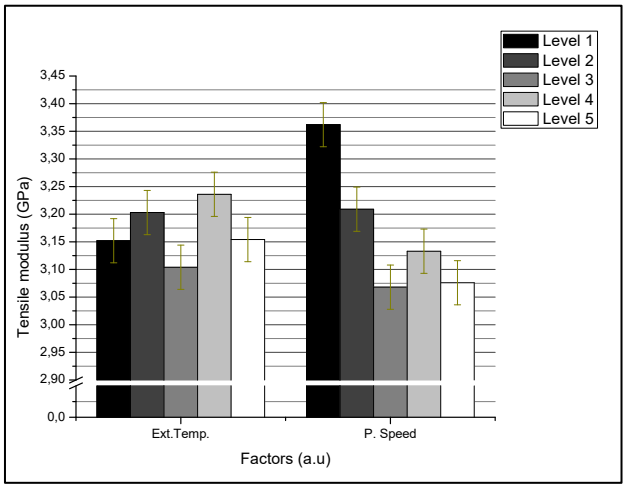
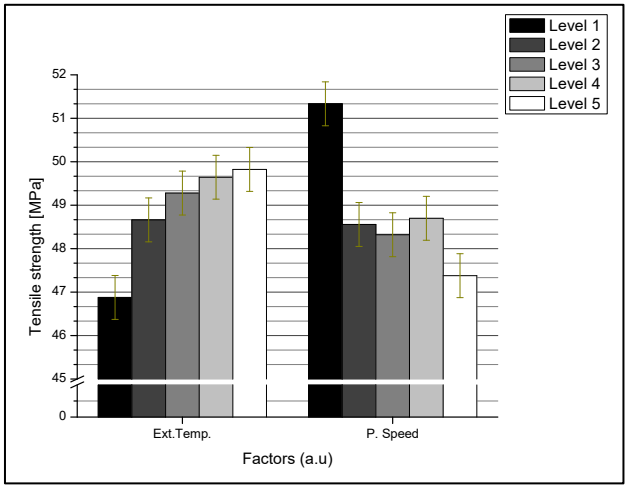


Figure 106 - Test specimens with print speeds of 75mm/s and extruder temperatures from 190-230°C.

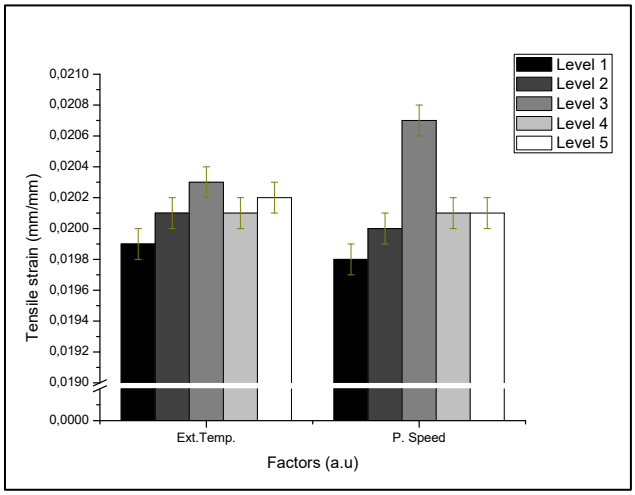
In Figure 107 it is possible to observe the plotting of the means for each of the tensile properties over the various parameter levels.



Level	Extruder Temp. [°C]	Print Speed [mm/s]
1	190	30
2	200	45
3	210	60
4	220	75
5	230	90



Level	Extruder Temp. [°C]	Print Speed [mm/s]
1	190	30
2	200	45
3	210	60
4	220	75
5	230	90



Level	Extruder Temp. [°C]	Print Speed [mm/s]
1	190	30
2	200	45
3	210	60
4	220	75
5	230	90

Figure 107 - Plotting of the means for the tensile modulus, yield stress and strain.

Afterwards, the predictive models were obtained in the following manner:

$$\mathrm{E}\,(v) = \alpha * v^{\beta} = 3.4241 * v^{-0.001} \quad (4.27)$$

$$\mathrm{E}\,(T) = \gamma * T^{\xi} = 3.13 * T^{0.0005} \quad (4.28)$$

$$\mathrm{E}\,(v,t) = \mu * \left[\alpha * v^{\beta}\right] * \left[\gamma * T^{\xi}\right] = 0.292 * \left[\alpha * v^{\beta}\right] * \left[\gamma * T^{\xi}\right] \quad (4.29)$$

$$\sigma_{yield}\,(v) = \alpha * v^{\beta} = 51.871 * v^{-0.001} \quad (4.30)$$

$$\sigma_{yield}\,(T) = \gamma * T^{\xi} = 36.556 * T^{0.0014} \quad (4.31)$$

$$\sigma_{yield}\,(v,t) = \mu * \left[\alpha * v^{\beta}\right] * \left[\gamma * T^{\xi}\right] = 0.02563 * \left[\alpha * v^{\beta}\right] * \left[\gamma * T^{\xi}\right] \quad (4.32)$$

$$\varepsilon_{yield}\,(v) = \alpha * v^{\beta} = 0.0198 * v^{0.002} \quad (4.33)$$

$$\varepsilon_{yield}\,(T) = \gamma * T^{\xi} = 0.0186 * T^{0.0004} \quad (4.34)$$

$$\varepsilon_{yield}\,(v,t) = \mu * \left[\alpha * v^{\beta}\right] * \left[\gamma * T^{\xi}\right] = 54.42 * \left[\alpha * v^{\beta}\right] * \left[\gamma * T^{\xi}\right] \quad (4.35)$$

The output from equations 4.29, 4.32 and 4.35 can be observed in Figure 108 and each model presented errors of 3.74%, 2.82% and 1.49%, respectively, with the subtraction surfaces visible in Figure 109.

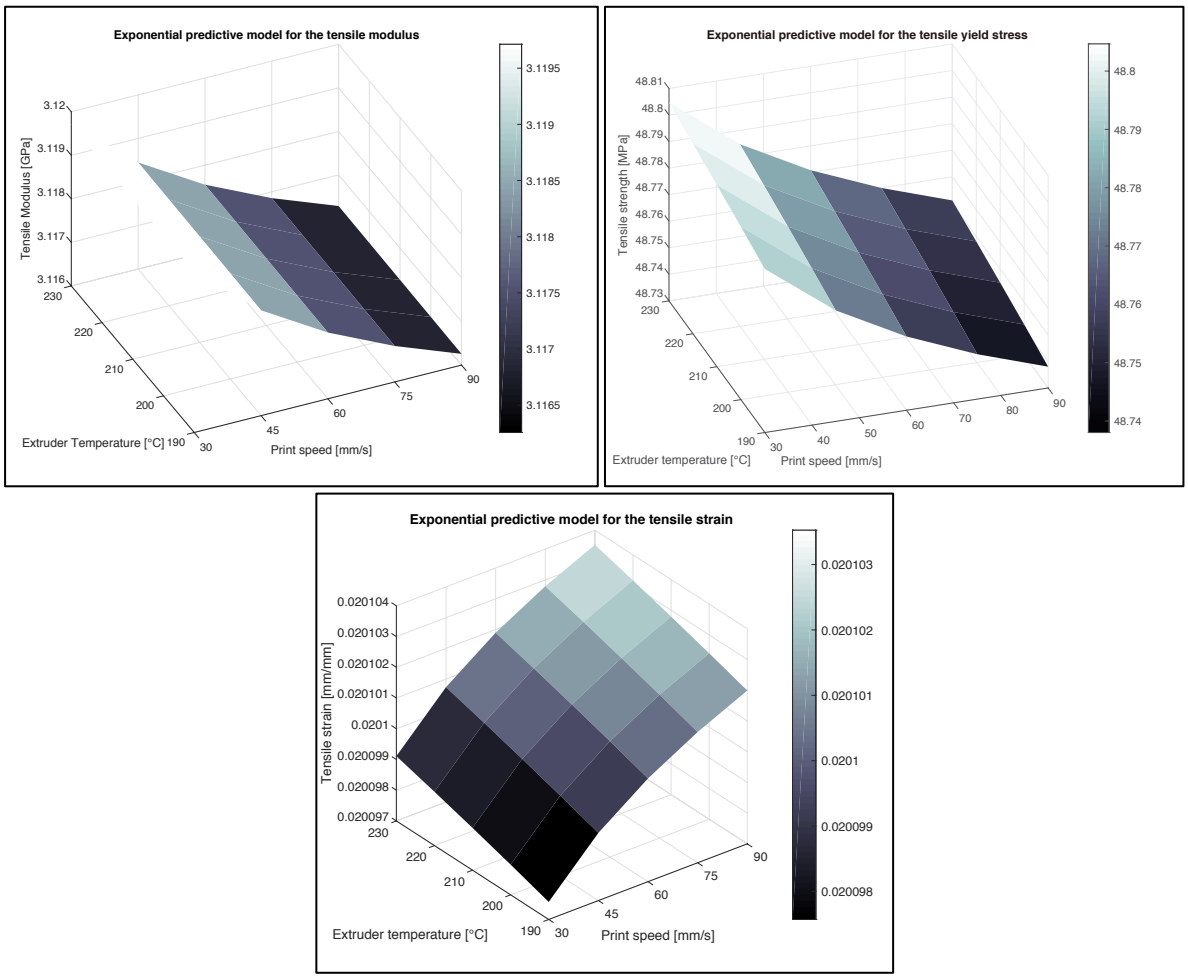


Figure 108 - Predictive model for the tensile modulus (left), yield stress (right) and strain (bottom) with print speed and extruder temperature as inputs. Based off exponential regressions obtained through experimental results.

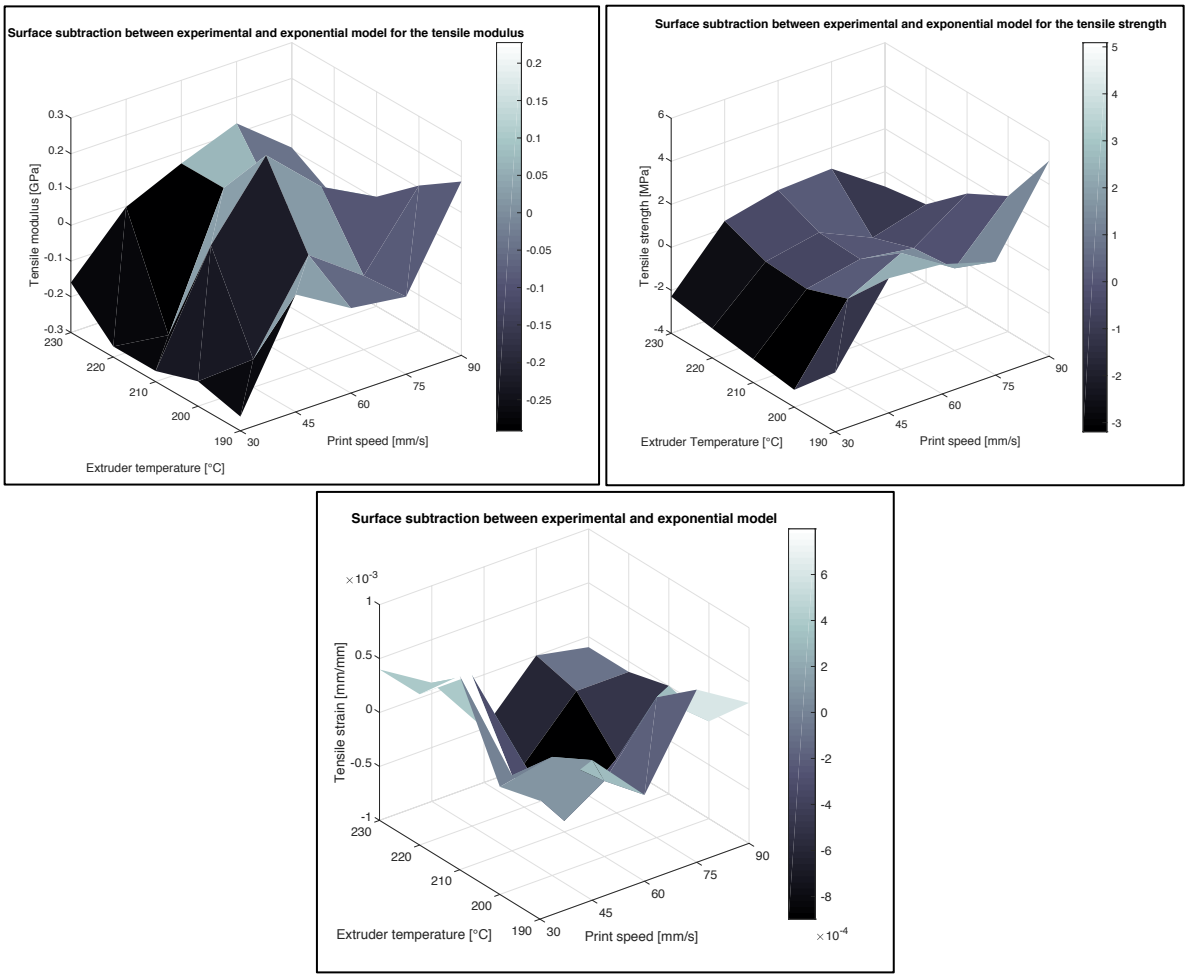


Figure 109 - Subtraction of the experimental and the predictive models for the tensile modulus (left), yield stress (right) and strain (bottom).

4.3.3 Flexural

After the execution of the trials and analysis of the output data according to the ISO 178 standard, it was possible to obtain the values for flexural modulus, maximum stress and strain, as shown in Table 23.

Table 23 - Summary of the average flexural mechanical properties.

Condition	E [GPa]	E ± SDev [GPa]	σ_{max} [MPa]	σ ± SDev [MPa]	ε_{max} [mm/mm]	ε ± SDev [mm/mm]
CV1_T1	2.75	0.16	78.83	0.53	0.0473	0.0046
CV1_T2	2.66	0.15	79.85	3.04	0.0441	0.0017
CV1_T3	2.65	0.18	80.86	1.68	0.0435	0.0008
CV1_T4	2.65	0.13	78.70	1.74	0.0435	0.0003
CV1_T5	2.44	0.10	79.52	3.42	0.0436	0.0006
CV2_T1	2.29	0.23	69.95	3.46	0.0434	0.0005
CV2_T2	2.48	0.10	75.03	1.14	0.0452	0.0017
CV2_T3	2.62	0.25	79.32	1.17	0.0434	0.0021
CV2_T4	2.62	0.21	82.03	2.14	0.0445	0.0010
CV2_T5	2.47	0.13	81.78	1.61	0.0469	0.0034
CV3_T1	2.59	0.09	76.01	0.86	0.0449	0.0003
CV3_T2	2.67	0.18	80.03	1.99	0.0444	0.0013
CV3_T3	2.73	0.19	82.06	0.92	0.0456	0.0011
CV3_T4	2.71	0.14	82.46	3.51	0.0454	0.0022
CV3_T5	2.66	0.02	82.48	2.48	0.0464	0.0013
CV4_T1	2.67	0.10	75.60	1.40	0.0450	0.0010
CV4_T2	2.57	0.25	77.61	3.51	0.0468	0.0036
CV4_T3	2.72	0.19	80.14	3.15	0.0469	0.0022
CV4_T4	2.59	0.11	79.75	2.00	0.0456	0.0005
CV4_T5	2.58	0.19	80.13	3.67	0.0461	0.0016
CV5_T1	2.47	0.15	72.27	1.83	0.0442	0.0011
CV5_T2	2.62	0.06	75.06	1.47	0.0430	0.0016
CV5_T3	2.69	0.26	76.10	3.64	0.0447	0.0014
CV5_T4	2.65	0.19	76.98	3.50	0.0453	0.0019
CV5_T5	2.65	0.29	79.45	2.96	0.0452	0.0002

Observing the values in the table, it can be observed that the maximum values for the flexural modulus, maximum stress and strain were 2.75, 82.48 and 0.0473 for the respective conditions of CV1_T1, CV3_T5 and CV1_T1. As for the minimum values, these were 2.44, 69.95 and 0.0430 for the conditions CV1_T5, CV2_T1 and CV5_T2, respectively.

Observation of the values, coupled with the representations from Figure 111, allows for a few aspects to be outlined. The flexural modulus did not show any tendency to increase or decrease with the process parameter variations, experiencing only a minor increasing variation as the print speed was incremented. The maximum flexural stress appeared to be more significantly influence by parameter variation, with higher print speeds yielding lower values and higher extruder temperatures yielding higher flexural resistance. Lastly, the maximum strain was not affected by any of the process parameters, with very small variations occurring in a somewhat random manner.

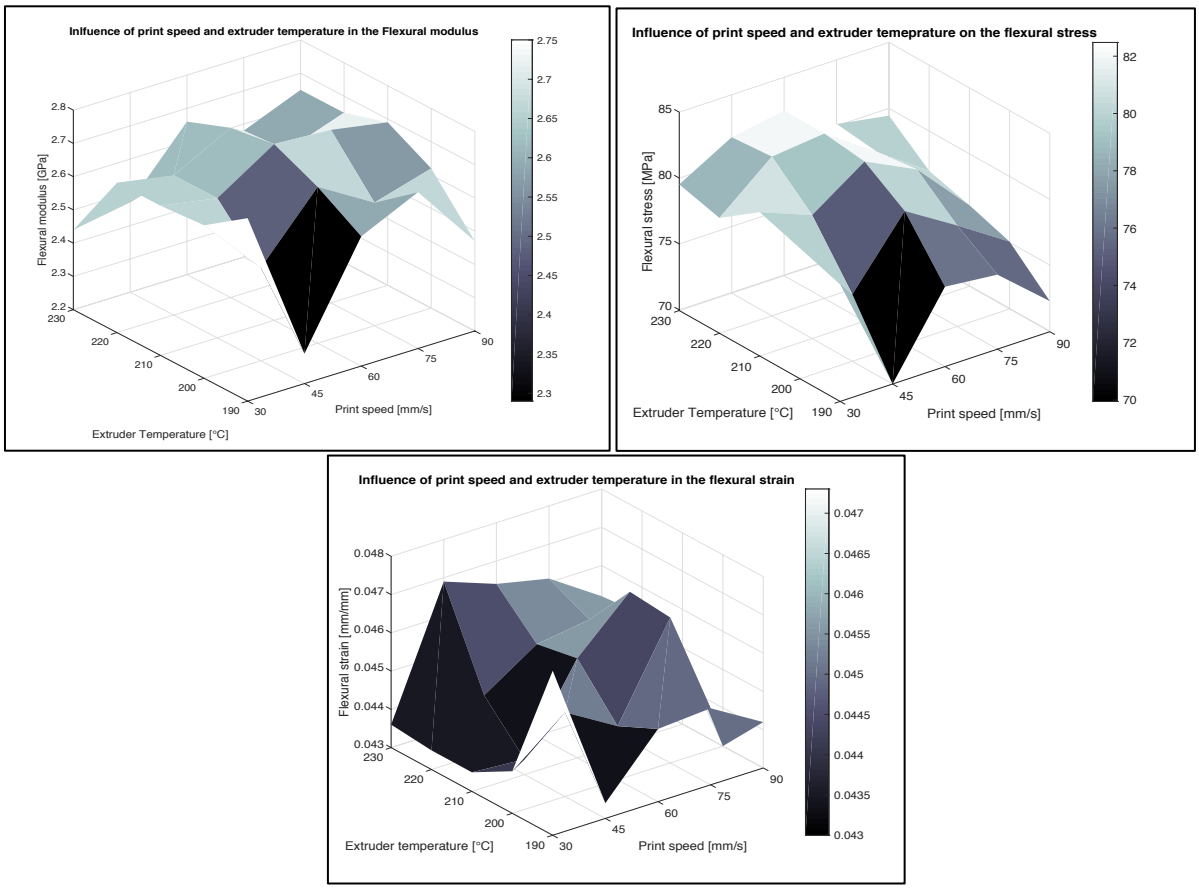


Figure 111 - Influence of print speed and extruder temperature on the flexural modulus (left), maximum stress (right) and maximum strain (bottom).

By resorting to an ANOVA analysis and Tukey comparison for each of these properties it was possible to confirm the afore-mentioned claims regarding the existence of parametrical influence, with print speed and extruder temperature having *p-values* of 0.064 and 0.194 for the flexural modulus, 0.000 for maximum stress and 0.110 and 0.649 for the maximum strain.

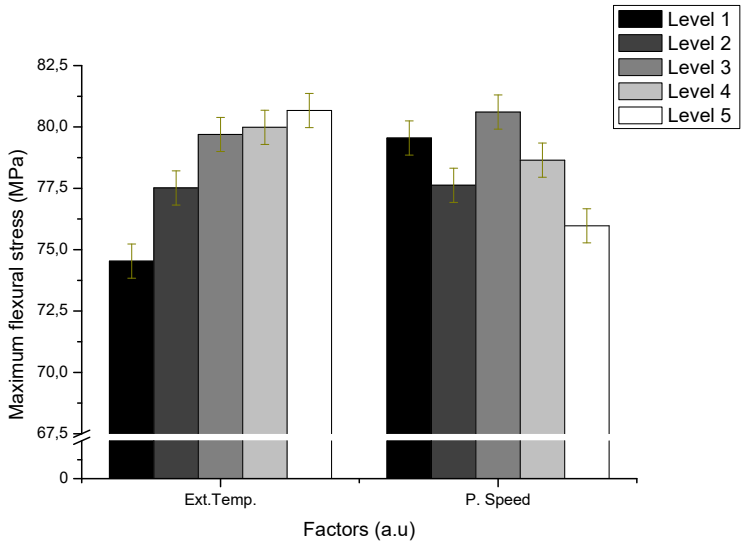
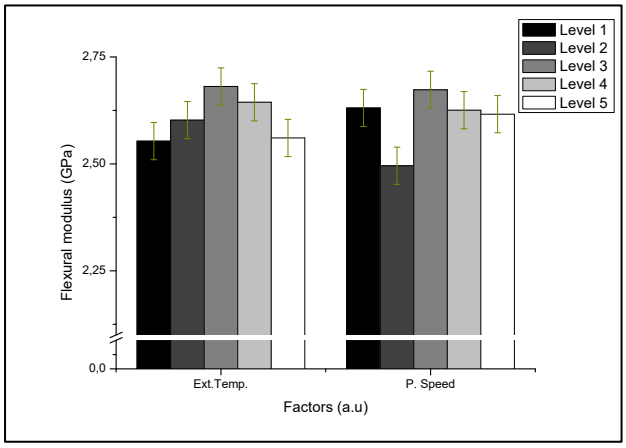


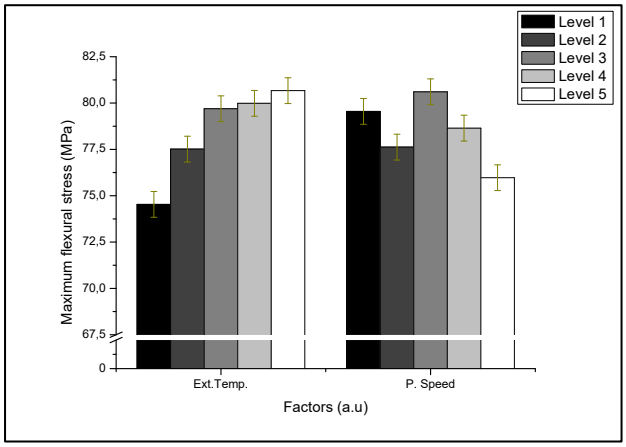
Figure 110 - Plotting of the means for the maximum flexural stress according to the different levels of print speed and extruder temperature.

Focusing on the maximum flexural stress, by observing Figure 110, it can be seen that, as the extruder temperature was set higher, so did the value for this property increase, which could be attributed to the larger amounts of thermal mass deposited, contributing to raster diffusion and bonding. Contrarily, as the print speed was increased the maximum flexural stress decreased, which would make sense, considering the increasing sparseness of the deposited raster and consequent lower bonding areas, similar to what happened in the other test specimens.

On the other hand, observing Figure 112, it can be confirmed that no patterns or significant influence where exerted by print speed and extruder temperature on the flexural modulus or maximum flexural strain. The flexural modulus itself would insert itself as more dependent on the material and imperfections resulting from the process itself than the process parameters, whereas the strain values were all extremely similar among themselves, indicating that this was a property dependant on the material's characteristics.



Level	Extruder Temp. [°C]	Print Speed [mm/s]
1	190	30
2	200	45
3	210	60
4	220	75
5	230	90



Level	Extruder Temp. [°C]	Print Speed [mm/s]
1	190	30
2	200	45
3	210	60
4	220	75
5	230	90

Figure 112 - Plotting of the means for the flexural modulus and maximum flexural strain.

Afterwards, the predictive models were obtained in the following manner:

$$\mathrm{E_f}(v) = \alpha * v^{\beta} = 2.5748 * v^{0.0001} \quad (4.27)$$

$$\mathrm{E_f}(T) = \gamma * T^{\xi} = 2.563 * T^{0.00006} \quad (4.28)$$

$$\mathrm{E_f}(v,t) = \mu * \left[\alpha * v^{\beta}\right] * \left[\gamma * T^{\xi}\right] = 0.40 * \left[\alpha * v^{\beta}\right] * \left[\gamma * T^{\xi}\right] \quad (4.29)$$

$$\sigma_{max}(v) = \alpha * v^{\beta} = 81.135 * v^{-0.0006} \quad (4.30)$$

$$\sigma_{max}(T) = \gamma * T^{\xi} = 52.753 * T^{0.0019} \quad (4.31)$$

$$\sigma_{max}(v,t) = \mu * \left[\alpha * v^{\beta}\right] * \left[\gamma * T^{\xi}\right] = 0.01842 * \left[\alpha * v^{\beta}\right] * \left[\gamma * T^{\xi}\right] \quad (4.32)$$

$$\varepsilon_{max}(v) = \alpha * v^{\beta} = 0.0443 * v^{0.0002} \quad (4.33)$$

$$\varepsilon_{max}(T) = \gamma * T^{\xi} = 0.0417 * T^{0.0004} \quad (4.34)$$

$$\varepsilon_{max}(v,t) = \mu * \left[\alpha * v^{\beta}\right] * \left[\gamma * T^{\xi}\right] = 24.30 * \left[\alpha * v^{\beta}\right] * \left[\gamma * T^{\xi}\right] \quad (4.35)$$

The output from equations 4, 4.32 and 4.35 can be observed in Figure 113 and each model presented errors of 2.99%, 3.12% and 2.26%, respectively, with the subtraction surfaces visible in Figure 114.

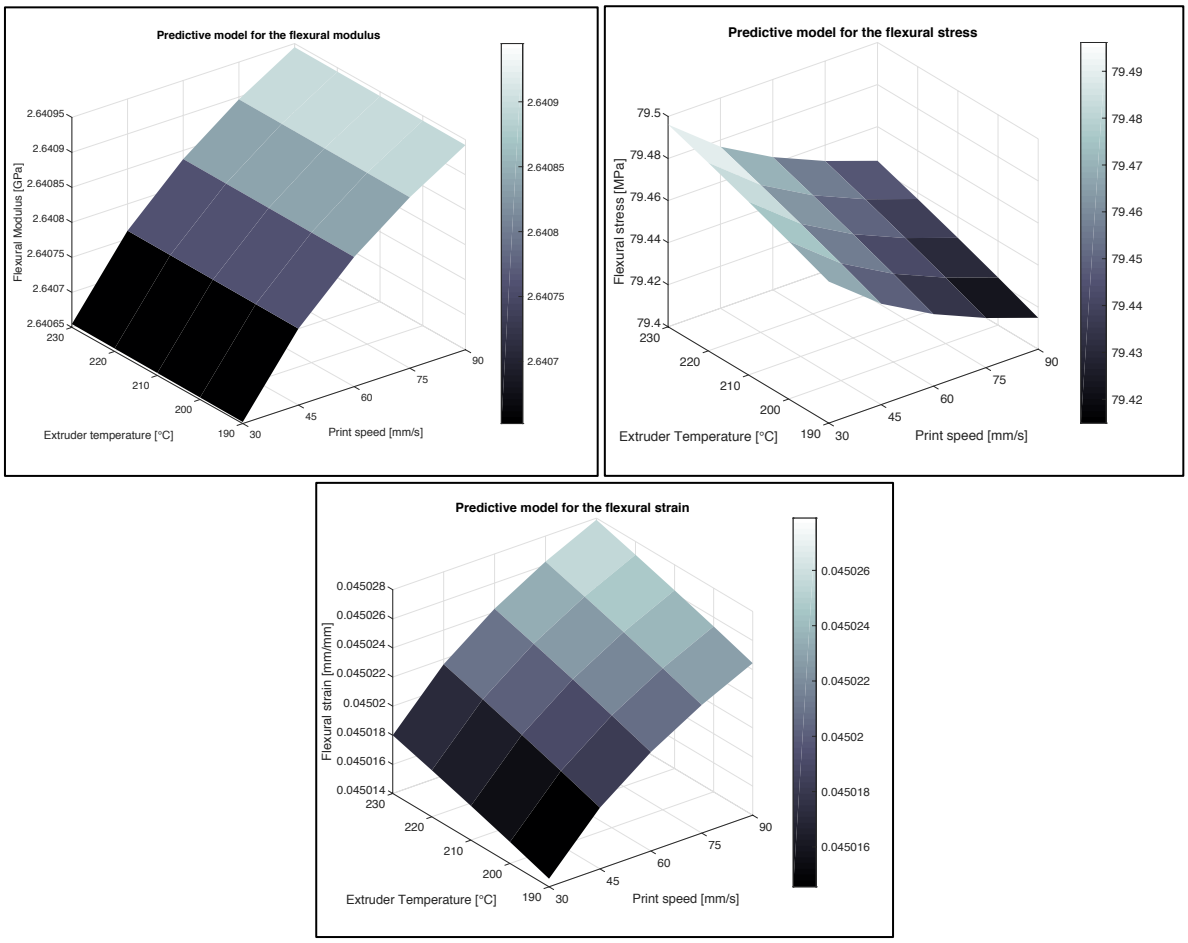


Figure 113 - Predictive model for the flexural modulus (left), maximum flexural stress (right) and maximum flexural strain (bottom) with print speed and extruder temperature as inputs. Based off exponential regressions obtained through experimental results.

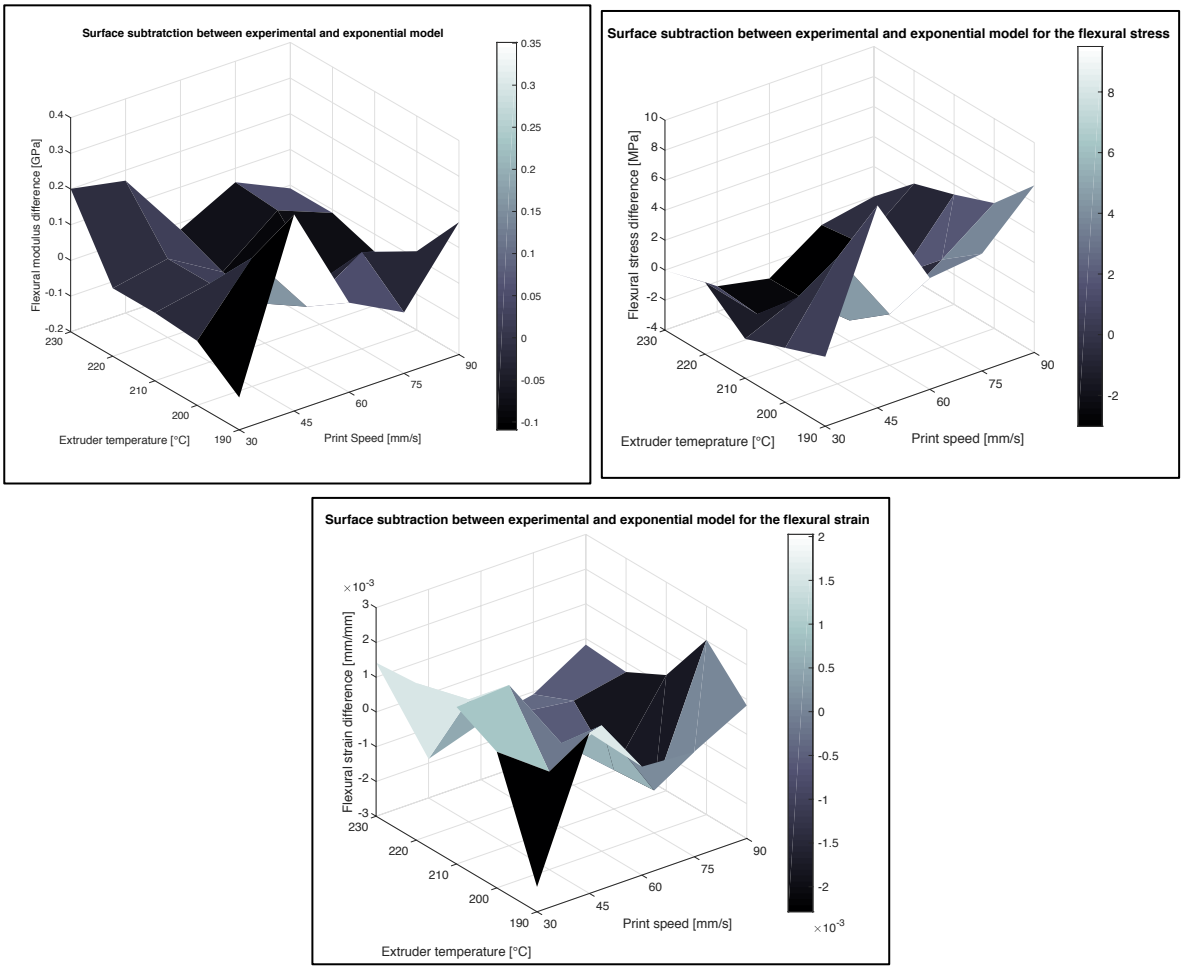


Figure 114 - Subtraction of the experimental and the predictive models for the flexural modulus (left), maximum flexural stress (right) and maximum flexural strain (bottom)

5. Conclusions

The proposal of performing research work on a topic as relevant and intricate as 3D printing, coupled with the preparation and realisation of an extensive experimental analysis allowed for some important bullet points to be outlined.

First off, given the extensive amount of research that was required to obtain an adequate knowledge level on the topic of *desktop* FFF additive manufacturing, it was possible to better understand how the many existing parameters that are involved in this process influence the produced components' characteristics. Although this is a process that allows for an unexperienced user to quickly become mildly proficient, certain parameters such as layer height, extrusion temperature, print speed, nozzle diameter and many others, present a certain level of co-dependency between themselves. This led to the necessity of obtaining a deep and well-structured understanding of their influences on the final components' properties, so as to be able to define optimum baselines for their manipulation depending on the desired outcomes, and, subsequentially, reduce the amount of failed prints and waste production. By performing a thorough study on the many research attempts performed by others, as well as partaking in exploratory production stages that involved the construction, instrumentation and calibration of 3D printing devices, it was possible to obtain said proficiency and understanding of the process and its parameters.

Additionally, given the main objective of evaluating a myriad of parameter variations and documenting the outcome, it was possible to define the importance of experiment design for the proper realisation of such an endeavour. By following structured guidelines set prior to the initial stages of the experimental work, as well as known experimental design methods, such as the full-factorial method, it was possible to obtain vast amounts of information on the topic at hand in a structured and easily processable manner, which was essential to the final stages of this work, consisting of the proper weighing and documentation of the influence of the process parameters, followed by the creation of predictive models that could be implemented in future applications such as simulation *software* for the FFF method.

As for the influence of the process parameters itself, it was possible to document relevant information regarding the mass, dimensional accuracy and mechanical properties of the components and, at the same time, further confirming previous findings regarding some of the process parameters.

Beginning by the influence on the mass, it was shown that both extruder temperature and print speed portrayed a significant role on this subject. Extruder temperature increase was shown to proportionally influence the mass in a crescent trajectory, whereas when the print speed was increased, the amount of deposited material tended to decrease. Additionally, it was possible to observe the importance of well-defined processing temperature intervals, typically provided by the feedstock material's producer, in regard to the overall consistency of material extrusion and oozing phenomena alike. Equally important, the experimental results outlined the influence that print speed may have when coupled with machine limitations such as the acceleration rate that can be outputted by the driving motors on the extruder module.

Moving onwards to the influence of these process parameters on the dimensional repeatability of the process itself, it was possible to confirm that extrusion temperature highly influences the accuracy of features on all construction

axis (X, Y and Z) in a way that higher temperatures, yielded consecutively higher dimensional inaccuracies. As well as that, it was also shown that, due to thermal expansion of the nozzle, tailored calibration of the nozzle-table clearance should be performed whenever the extrusion and, presumably, surface temperatures are required to be altered, so as to avoid the appearance of poorer surface roughness and improper dimensional tolerances caused by dragging effects. Lastly, it was shown that higher print speeds can lead to certain features in the *Oxy* plane becoming smaller than expected due to the less amount of deposited material, as shown for the mass analysis at higher print speeds.

As for the influence on the mechanical properties, it was possible to infer certain aspects regarding the extruder temperature and print speed by analysing the mechanical trials' output. It is important to note that, as shown in previous research work done by others, the mechanical properties of these additive manufacturing components are seldomly comparable to their monolithic counterparts in terms of magnitude. Nonetheless, it was observed that by altering extruder temperature and print speed it was possible to enhance certain mechanical properties, even if only marginally.

In regard to the tensile and compressive properties, it was shown that compressive and tensile yield stress are indeed dependent on the extruder temperature, becoming higher as the temperature is increased. However, the effects of this parameter variation were not as accentuated as in other studies, where it was shown that extrusion temperature largely improved the bonding between different rasters and, subsequentially, improved the tensile and compressive resistance as well. This observation can be justified by the small increases in temperature that were implemented, coupled with the fact that, out of 5 different levels for extrusion temperature (190°C to 230°C, with a 10°C increment), only one of the temperatures (230°C) was outside of the optimum processing window that was recommended by the manufacturer. In comparison to the manufacturer claims, the obtained tensile resistance was around 50% of the theoretical value, but still according to other experimental results.

As for the tensile and compressive modulus, it was shown that the determining factor was, for the most part, the considered print speed, so that higher print speeds yielded lower values of tensile and compressive modulus. This could be justified by the fact that the observed values were obtained by testing components that were built resorting to FFF, a process whose components typically present small imperfections such as voids between different rasters. These imperfections led to different behaviours according to the level of print speed that was defined, originating less ductile components as this parameter was gradually increased.

On the other hand, it was observed that, out of the analysed flexural properties, only the maximum flexural strain was affected by the process parameters, with higher extruder temperatures favouring higher flexural resistance and higher print speeds fragilizing the test specimens due to lower flexural resistance values.

Lastly, it was possible to produce relevant predictive models for the mass, tensile, compressive and flexural properties, based on the empirical evidence that was gathered throughout the experience. The models themselves were obtained by resorting to exponential regressions and minimisation of the corresponding errors when compared to the experimental values, with the output being valid for

situations where only print speed and extruder temperature were altered. In the case of the model for the mass, it was possible to create a model that would be able to predict the mass of any given component as long as its volume, extruder temperature and print speed are provided as inputs, all of which are always previously known before moving on to the printing stage.

In conclusion, *desktop* FFF additive manufacturing allows any user to build certain components using a wide range of parameter variations. Considering that the requirements may change with the purposed application, so should the parameters be altered according to what is pretended. In the case of extruder temperature and print speed, if the tensile yield stress and overall mechanical resistance are high-demanding specifications, then the recommended values for each parameter would be situated around 200-220°C and 30mm/s, respectively. However, for components of larger dimensions and lower demands in terms of dimensional accuracy and resistance, then higher print speeds of around 60mm/s would be advised, with a note that higher print speeds could also be used if the device at hand is capable of actually outputting them.

5.1 Future works

Due to the large amounts of information and procedures involved in the making of this work, some verifications and results were outlined as future works.

First off, a new experiment design focused on assessing the dimensional accuracy and repeatability of *desktop* FFF printers would be relevant, considering the observations that were made regarding these aspects. As well as this, due to the lack of information regarding the influence of component and feature geometry on the dimensional accuracy of the process, a study focused solely on these aspects could yield interesting results.

Additionally, after having evaluated the influence of print speed and extruder temperature on the mass, dimensions and mechanical properties of AM PLA components, it would be relevant to evaluate new parameter variation in further stages. This would enable for the creation of new predictive models for the remaining process parameters and complement this study. A suggestion would be to initially define fixed values for print speed and extruder temperature at 30mm/s and 210°C, respectively, and implementing a variation of layer height for five different stages (0.12-0.28mm with 0.04mm increments. Afterwards, a posterior and final stage could be defined by fixing a layer height value as well and implementing a variation of nozzle diameter for three commonly used diameters: 0.3, 0.4 and 0.5mm.

On a small note, it should be considered that the small variations observed in the mechanical properties throughout this dissertation, when in comparison to the revised literature, might have been due to the material itself, which could be confirmed in a posterior stage by using a different feedstock material to ascertain the veracity of this observation.

Lastly, it would be seen as fit to design experiments solely focused on improving the predictive models' capability by employed different model generation techniques such as neural networks, due to their efficacy in predicting values for values that are highly dependent on a wide range of parameters, as are mass and mechanical properties on process parameters such as print speed, layer height, extruder temperature, raster orientation, among many others.

6. References

3DNatives. 2017. https://www.3dnatives.com/en/wp-content/uploads/sites/2/FDM-3D-printer.jpg.

Ahn, Sung-Hoon, Michael Montero, Dan Odell, Shad Roundy, and Paul K. Wright. 2002. "Anisotropic material properties of fused deposition modeling ABS". *Rapid Prototyping Journal* 8, no. 4: 248-57. doi:10.1108/13552540210441166. https://www.emeraldinsight.com/doi/abs/10.1108/13552540210441166.

Akhoundi, B., and A. H. Behravesh. 2019. "Effect of Filling Pattern on the Tensile and Flexural Mechanical Properties of FDM 3D Printed Products". *Experimental Mechanics*. 10.1007/s11340-018-00467-y. https://doi.org/10.1007/s11340-018-00467-y.

Akhoundi, Behnam, Amir Hossein Behravesh, and Arvin Bagheri Saed. 2019. "Improving mechanical properties of continuous fiber-reinforced thermoplastic composites produced by FDM 3D printer". *Journal of Reinforced Plastics and Composites* 38, no. 3: 99-116. 10.1177/0731684418807300. https://journals.sagepub.com/doi/abs/10.1177/0731684418807300.

Alafaghani, Ala'aldin, and Ala Qattawi. 2018. "Investigating the effect of fused deposition modeling processing parameters using Taguchi design of experiment method". *Journal of Manufacturing Processes* 36: 164-74. https://doi.org/10.1016/j.jmapro.2018.09.025. http://www.sciencedirect.com/science/article/pii/S1526612518314026.

Alafaghani, Ala'aldin, Ala Qattawi, Buraaq Alrawi, and Arturo Guzman. 2017. "Experimental Optimization of Fused Deposition Modelling Processing Parameters: A Design-for-Manufacturing Approach". *Procedia Manufacturing* 10: 791-803. https://doi.org/10.1016/j.promfg.2017.07.079. http://www.sciencedirect.com/science/article/pii/S2351978917302615.

Åström, Karl Johan, and Tore Hägglund. 1995. *PID controllers: theory, design, and tuning*. Vol. 2: Instrument society of America Research Triangle Park, NC.

Baich, L., and G. Manogharan. 2015. "Study of infill print parameters on mechanical strength and production cost-time of 3D printed ABS parts". *Int. J. Rapid Manuf.* 5: 209-18.

Baumann, Felix, Halil Bugdayci, Jonas Grunert, Fabian Keller, and Dieter Roller. 2016. "Influence of slicing tools on quality of 3D printed parts". *Computer-Aided Design and Applications* 13, no. 1: 14-31. 10.1080/16864360.2015.1059184. https://doi.org/10.1080/16864360.2015.1059184.

Bentley, Robin E. 1998. *Handbook of Temperature Measurement Vol. 3: The Theory and Practice of Thermoelectric Thermometry*. Vol. 3: Springer Science & Business Media.

Bertoldi, M., M. A. Yardimci, C. M. Pistor, S. I. Guceri, and G. Sala. 1998. "Mechanical characterization of parts processed via fused deposition". *Proc. Solid Freeform Fabrication Symposium*: 557-65.

CESEduPack. 2019. CES EduPack.

Chacón, J. M., M. A. Caminero, E. García-Plaza, and P. J. Núñez. 2017. "Additive manufacturing of PLA structures using fused deposition modelling: Effect of process parameters on mechanical properties and their optimal selection".

Materials & Design 124: 143-57. https://doi.org/10.1016/j.matdes.2017.03.065. http://www.sciencedirect.com/science/article/pii/S0264127517303143.

Christiyan, K. G. Jaya, U. Chandrasekhar, and K. Venkateswarlu. 2016. "A study on the influence of process parameters on the Mechanical Properties of 3D printed ABS composite". *IOP Conference Series: Materials Science and Engineering* 114: 012109. 10.1088/1757-899x/114/1/012109. http://dx.doi.org/10.1088/1757-899X/114/1/012109.

Compton, Brett G., and Jennifer A. Lewis. 2014. "3D-Printing of Lightweight Cellular Composites". *Advanced Materials* 26, no. 34: 5930-35. 10.1002/adma.201401804. https://onlinelibrary.wiley.com/doi/abs/10.1002/adma.201401804.

Coogan, Timothy J., and David Owen Kazmer. 2017. "Bond and part strength in fused deposition modeling". *Rapid Prototyping Journal* 23, no. 2: 414-22. doi:10.1108/RPJ-03-2016-0050. https://www.emeraldinsight.com/doi/abs/10.1108/RPJ-03-2016-0050.

Croccolo, Dario, Massimiliano De Agostinis, and Giorgio Olmi. 2013. "Experimental characterization and analytical modelling of the mechanical behaviour of fused deposition processed parts made of ABS-M30". *Computational Materials Science* 79: 506-18. https://doi.org/10.1016/j.commatsci.2013.06.041. http://www.sciencedirect.com/science/article/pii/S0927025613003741.

Dawoud, Michael, Iman Taha, and Samy J. Ebeid. 2016. "Mechanical behaviour of ABS: An experimental study using FDM and injection moulding techniques". *Journal of Manufacturing Processes* 21: 39-45. https://doi.org/10.1016/j.jmapro.2015.11.002. http://www.sciencedirect.com/science/article/pii/S1526612515001395.

DeloitteUniversityPress. 2018. Schematization of the essential steps in the production of AM components. Deloitte University Press: Delloitte.

Devicharan, R., and Raghav Garg. 2019. "Optimization of the Print Quality by Controlling the Process Parameters on 3D Printing Machine". In *3D Printing and Additive Manufacturing Technologies*, edited by L. Jyothish Kumar, Pulak M. Pandey and David Ian Wimpenny, 187-94. Singapore: Springer Singapore. 10.1007/978-981-13-0305-0_16. https://doi.org/10.1007/978-981-13-0305-0_16.

Durgun, Ismail, and Rukiye Ertan. 2014. "Experimental investigation of FDM process for improvement of mechanical properties and production cost". *Rapid Prototyping Journal* 20, no. 3: 228-35. doi:10.1108/RPJ-10-2012-0091. https://www.emeraldinsight.com/doi/abs/10.1108/RPJ-10-2012-0091.

Ebel, Enno, and Thorsten Sinnemann. 2014. "Fabrication of FDM 3D objects with ABS and PLA and determination of their mechanical properties". *RTejournal* 2014, no. 1. http://nbn-resolving.de/urn:nbn:de:0009-2-38722.

Fatimatuzahraa, A. W., B. Farahaina, and W. A. Y. Yusoff. 2011. "The effect of employing different raster orientations on the mechanical properties and microstructure of Fused Deposition Modeling parts". Paper presented in 2011 IEEE Symposium on Business, Engineering and Industrial Applications (ISBEIA), 25-28 Sept. 2011. 10.1109/ISBEIA.2011.6088811.

Gibson, Ian, David W. Rosen, and Brent Stucker. 2009. *Additive Manufacturing Technologies: Rapid Prototyping to Direct Digital Manufacturing*. Springer Publishing Company, Incorporated.

Gleadall, Andrew, Dafydd Visscher, Jing Yang, Daniel Thomas, and Joel Segal. 2018. "Review of additive manufactured tissue engineering scaffolds: relationship between geometry and performance". *Burns & Trauma* 6, no. 1: 19. 10.1186/s41038-018-0121-4. https://doi.org/10.1186/s41038-018-0121-4.

Gonick, Melanie. 2018. http://news.mit.edu/2017/3-d-graphene-strongest-lightest-materials-0106.

Gorski, F. 2014. "Impact strength of ABS parts manufactured using fused deposition modeling technology". *Archives of Mechanical Technology and Materials* 34, no. 1: 1-12.

Górski, F., R. Wichniarek, W. Kuczko, and J. Andrzejewski. 2015a. "Experimental determination of critical orientation of ABS parts manufactured using fused deposition modelling technology". *J. Mach. Eng.* 15: 121-32.

Górski, Filip, Radosław Wichniarek, Wiesław Kuczko, Przemysław Zawadzki, and Paweł Buń. 2015b. "STRENGTH OF ABS PARTS PRODUCED BY FUSED DEPOSITION MODELLING TECHNOLOGY – A CRITICAL ORIENTATION PROBLEM". *Advances in Science and Technology Research Journal* 9, no. 26: 12-19. 10.12913/22998624/2359. http://dx.doi.org/10.12913/22998624/2359.

Jabbari, Esmaiel, and Nikolaos A. Peppas. 1994. "Polymer-Polymer Interdiffusion and Adhesion". *Journal of Macromolecular Science, Part C* 34, no. 2: 205-41. 10.1080/15321799408009635. https://doi.org/10.1080/15321799408009635.

Jamalabad, Vikram R., Ahmad Safari, Mukesh K. Agarwala, Noshir A. Langrana, Stephen C. Danforth, and Philip J. Whalen. 1996. "Structural quality of parts processed by fused deposition". *Rapid Prototyping Journal* 2, no. 4: 4-19. 10.1108/13552549610732034. https://doi.org/10.1108/13552549610732034.

Jones, Rhys, Patrick Haufe, Edward Sells, Pejman Iravani, Vik Olliver, Chris Palmer, and Adrian Bowyer. 2011. "RepRap – the replicating rapid prototyper". *Robotica* 29, no. 1: 177-91. 10.1017/S026357471000069X. https://www.cambridge.org/core/article/reprap-the-replicating-rapid-prototyper/5979FD7B0C066CBCE43EEAD869E871AA.

Kim, Kwang-Seop, Jung-Chul Heo, and Kyung-Woong Kim. 2010. "Effects of Temperature on the Microscale Adhesion Behavior of Thermoplastic Polymer Film". *Tribology Letters* 38, no. 2: 97-106. 10.1007/s11249-010-9578-4. https://doi.org/10.1007/s11249-010-9578-4.

Lanzotti, Antonio, Marzio Grasso, Gabriele Staiano, and Massimo Martorelli. 2015. "The impact of process parameters on mechanical properties of parts fabricated in PLA with an open-source 3-D printer". *Rapid Prototyping Journal* 21, no. 5: 604-17. doi:10.1108/RPJ-09-2014-0135. https://www.emeraldinsight.com/doi/abs/10.1108/RPJ-09-2014-0135.

Lee, B. H., J. Abdullah, and Z. A. Khan. 2005. "Optimization of rapid prototyping parameters for production of flexible ABS object". *Journal of Materials Processing Technology* 169, no. 1: 54-61.

https://doi.org/10.1016/j.jmatprotec.2005.02.259. http://www.sciencedirect.com/science/article/pii/S0924013605003717.

Letcher, Todd, Behzad Rankouhi, and Sina Javadpour. 2015. *Experimental Study of Mechanical Properties of Additively Manufactured ABS Plastic as a Function of Layer Parameters*. 10.1115/IMECE2015-52634.

Li, Hongbin, Taiyong Wang, Jian Sun, and Zhiqiang Yu. 2018. "The effect of process parameters in fused deposition modelling on bonding degree and mechanical properties". *Rapid Prototyping Journal* 24, no. 1: 80-92. doi:10.1108/RPJ-06-2016-0090. https://www.emeraldinsight.com/doi/abs/10.1108/RPJ-06-2016-0090.

Liu, Xinhua, Mingshan Zhang, Shengpeng Li, Lei Si, Junquan Peng, and Yuan Hu. 2017. "Mechanical property parametric appraisal of fused deposition modeling parts based on the gray Taguchi method". *The International Journal of Advanced Manufacturing Technology* 89, no. 5: 2387-97. 10.1007/s00170-016-9263-3. https://doi.org/10.1007/s00170-016-9263-3.

Lubombo, Christian, and Michel A. Huneault. 2018. "Effect of infill patterns on the mechanical performance of lightweight 3D-printed cellular PLA parts". *Materials Today Communications* 17: 214-28. https://doi.org/10.1016/j.mtcomm.2018.09.017. http://www.sciencedirect.com/science/article/pii/S2352492818301600.

Makerbot. 2015. "Composite materials".

MakerBot Industries, LLC. 2019. Thingiverse.

"Material Profiles". In. 2014. *Materials and Design (Third Edition)*, edited by Michael Ashby and Kara Johnson, 240-307. Butterworth-Heinemann. https://doi.org/10.1016/B978-0-08-098205-2.00019-6. http://www.sciencedirect.com/science/article/pii/B9780080982052000196.

Miguel, Fernandez-Vicente, Calle Wilson, Ferrandiz Santiago, and Conejero Andres. 2016. "Effect of Infill Parameters on Tensile Mechanical Behavior in Desktop 3D Printing". *3D Printing and Additive Manufacturing* 3, no. 3: 183-92. 10.1089/3dp.2015.0036. https://www.liebertpub.com/doi/abs/10.1089/3dp.2015.0036.

Nancharaiah, T %J Int J Emerg Technol. 2011. "Optimization of process parameters in FDM process using design of experiments". 2, no. 1: 100-02.

Netto, Aurélio da Costa Sabino, Leonardo Santana, Igor Pereira, Rodrigo Acácio Paggi, and Diovani Castoldi Lencina. 2017. "AVALIAÇÃO DE CORPOS DE PROVA PRODUZIDOS EM PLA POR MANUFATURA ADITIVA POR EXTRUSÃO E MOLDAGEM POR INJEÇÃO". Paper presented in 13o Congresso Ibero-americano de Engenharia Mecânica, Lisboa, Portugal.

Ning, Fuda, Weilong Cong, Yingbin Hu, and Hui Wang. 2017. "Additive manufacturing of carbon fiber-reinforced plastic composites using fused deposition modeling: Effects of process parameters on tensile properties". *Journal of Composite Materials* 51, no. 4: 451-62. 10.1177/0021998316646169. https://journals.sagepub.com/doi/abs/10.1177/0021998316646169.

Onwubolu, Godfrey C., and Farzad Rayegani. 2014. "Characterization and Optimization of Mechanical Properties of ABS Parts Manufactured by the Fused Deposition Modelling Process %J International Journal of

Manufacturing Engineering". 2014: 13. 10.1155/2014/598531. http://dx.doi.org/10.1155/2014/598531.

Pan, Ai Qiong, Zi Fan Huang, Rui Jie Guo, and Jun Liu. 2016. "Effect of FDM Process on Adhesive Strength of Polylactic Acid(PLA) Filament". *Key Engineering Materials* 667: 181-86. 10.4028/www.scientific.net/KEM.667.181. https://www.scientific.net/KEM.667.181.

Popescu, Diana, Aurelian Zapciu, Catalin Amza, Florin Baciu, and Rodica Marinescu. 2018. "FDM process parameters influence over the mechanical properties of polymer specimens: A review". *Polymer Testing* 69: 157-66. https://doi.org/10.1016/j.polymertesting.2018.05.020. http://www.sciencedirect.com/science/article/pii/S0142941818306093.

"Prusa Research Original Prusa i3 MK3". 2017. https://www.3dhubs.com/3d-printers/prusa-research-original-prusa-i3-mk3.

Rajpurohit, Shilpesh R., and Harshit K. Dave. 2018. "Effect of process parameters on tensile strength of FDM printed PLA part". *Rapid Prototyping Journal* 24, no. 8: 1317-24. doi:10.1108/RPJ-06-2017-0134. https://www.emeraldinsight.com/doi/abs/10.1108/RPJ-06-2017-0134.

Rankouhi, Behzad, Sina Javadpour, Fereidoon Delfanian, and Todd Letcher. 2016. *Failure Analysis and Mechanical Characterization of 3D Printed ABS With Respect to Layer Thickness and Orientation*. Vol. 16. 10.1007/s11668-016-0113-2.

Rayegani, Farzad, and Godfrey C. Onwubolu. 2014. "Fused deposition modelling (FDM) process parameter prediction and optimization using group method for data handling (GMDH) and differential evolution (DE)". *The International Journal of Advanced Manufacturing Technology* 73, no. 1: 509-19. 10.1007/s00170-014-5835-2. https://doi.org/10.1007/s00170-014-5835-2.

Relvas, Carlos Alberton Moura. 2018. *O mundo da Impressão 3D e o Fabrico Digital*. Edited by engebook. 07-2018 ed.

RepRap. 2018. "Prusa i3 Buyers Guide". https://www.reprap.org/wiki/Prusa_i3_Buyers_Guide#Sourcing_Your_Own_Parts.

Rodríguez, José F., James P. Thomas, and John E. Renaud. 2001. "Mechanical behavior of acrylonitrile butadiene styrene (ABS) fused deposition materials. Experimental investigation". *Rapid Prototyping Journal* 7, no. 3: 148-58. doi:10.1108/13552540110395547. https://www.emeraldinsight.com/doi/abs/10.1108/13552540110395547.

Santana, Leonardo, Jorge Lino Alves, Sabino Netto, Aurélio da Costa, and Claudia Merlini. 2018. "A comparative study between PETG and PLA for 3D Printing through thermal, chemical and mechanical characterization". *Matéria (Rio de Janeiro)* 23, no. 4.

Santana, Leonardo, Jorge Lino Alves, and Aurélio da Costa Sabino Netto. 2017. "A study of parametric calibration for low cost 3D printing: Seeking improvement in dimensional quality". *Materials & Design* 135: 159-72. https://doi.org/10.1016/j.matdes.2017.09.020. http://www.sciencedirect.com/science/article/pii/S0264127517308523.

Shojib Hossain, Mohammad, David Espalin, Jorge Ramos, Mireya Perez, and Ryan Wicker. 2014. "Improved Mechanical Properties of Fused Deposition Modeling-Manufactured Parts Through Build Parameter Modifications".

Journal of Manufacturing Science and Engineering 136, no. 6: 061002-02-12. 10.1115/1.4028538. http://dx.doi.org/10.1115/1.4028538.

Silva, Catarina Maia Moreira da. 2019. "3D printing of gyroid structures for superior structural behaviour". Master, Departamento de Engenharia Mecânica da Faculdade de Engenharia, Universidade do Porto.

Sood, A. K., R. K. Ohdar, and S. S. Mahapatra. 2012. "Experimental investigation and empirical modelling of FDM process for compressive strength improvement". *Journal of Advanced Research* 3, no. 1: 81-90. 10.1016/j.jare.2011.05.001. https://www.scopus.com/inward/record.uri?eid=2-s2.0-84855674497&doi=10.1016%2fj.jare.2011.05.001&partnerID=40&md5=3830bb3c9166c9cd1bd5d0007bbbca00.

Sood, Anoop Kumar, R. K. Ohdar, and S. S. Mahapatra. 2010. "Parametric appraisal of mechanical property of fused deposition modelling processed parts". *Materials & Design* 31, no. 1: 287-95. https://doi.org/10.1016/j.matdes.2009.06.016. http://www.sciencedirect.com/science/article/pii/S0261306909002945.

Spoerk, Martin, Joamin Gonzalez-Gutierrez, Janak Sapkota, Stephan Schuschnigg, and Clemens Holzer. 2018. "Effect of the printing bed temperature on the adhesion of parts produced by fused filament fabrication". *Plastics, Rubber and Composites* 47, no. 1: 17-24. 10.1080/14658011.2017.1399531. https://doi.org/10.1080/14658011.2017.1399531.

Sun, Q., G.M. Rizvi, C.T. Bellehumeur, and P. Gu. 2008. "Effect of processing conditions on the bonding quality of FDM polymer filaments". *Rapid Prototyping Journal* 14, no. 2: 72-80. doi:10.1108/13552540810862028. https://www.emeraldinsight.com/doi/abs/10.1108/13552540810862028.

Thrimurthulu, K., Pulak M. Pandey, and N. Venkata Reddy. 2004. "Optimum part deposition orientation in fused deposition modeling". *International Journal of Machine Tools and Manufacture* 44, no. 6: 585-94. https://doi.org/10.1016/j.ijmachtools.2003.12.004. http://www.sciencedirect.com/science/article/pii/S0890695503003262.

Torres, Jonathan, Matthew Cole, Allen Owji, Zachary DeMastry, and Ali P. Gordon. 2016. "An approach for mechanical property optimization of fused deposition modeling with polylactic acid via design of experiments". *Rapid Prototyping Journal* 22, no. 2: 387-404. doi:10.1108/RPJ-07-2014-0083. https://www.emeraldinsight.com/doi/abs/10.1108/RPJ-07-2014-0083.

Torres, Jonathan, José Cotelo, Justin Karl, and Ali P. Gordon. 2015. "Mechanical Property Optimization of FDM PLA in Shear with Multiple Objectives". *JOM* 67, no. 5: 1183-93. 10.1007/s11837-015-1367-y. https://doi.org/10.1007/s11837-015-1367-y.

Tymrak, B. M., M. Kreiger, and J. M. Pearce. 2014. "Mechanical properties of components fabricated with open-source 3-D printers under realistic environmental conditions". *Materials & Design* 58: 242-46. https://doi.org/10.1016/j.matdes.2014.02.038. http://www.sciencedirect.com/science/article/pii/S0261306914001538.

Udroiu, Razvan, Cristian Braga, and Anisor Nedelcu. 2019. *Evaluating the Quality Surface Performance of Additive Manufacturing Systems: Methodology and a Material Jetting Case Study*. Vol. 12. 10.3390/ma12060995.

Ultimaker. 2016. "Ultimaker 3". https://ultimaker.com/en/products/ultimaker-3.

Urbanic, R. J., and S. M. Saqib. 2019. "A manufacturing cost analysis framework to evaluate machining and fused filament fabrication additive manufacturing approaches". *The International Journal of Advanced Manufacturing Technology* 102, no. 9: 3091-108. 10.1007/s00170-019-03394-x. https://doi.org/10.1007/s00170-019-03394-x.

Volpato, Neri, Carlos Henrique Ahrens, André Luiz Jardini Munhoz, Carlos Costa, Jonas De Carvalho, Jorge dos Santos, Jorge Silva, José Foggiatto, and Milton Sergio Fernandes de Lima. 2017. *Manufatura Aditiva - Tecnologias e aplicações da impressão 3D*.

Vries, Caspar de. 2017. "Volkswagen Autoeuropa: Maximizing production efficiency with 3D printed tools, jigs, and fixtures". https://ultimaker.com/en/stories/43969-volkswagen-autoeuropa-maximizing-production-efficiency-with-3d-printed-tools-jigs-and-fixtures.

Wittbrodt, Ben, and Joshua M. Pearce. 2015. "The effects of PLA color on material properties of 3-D printed components". *Additive Manufacturing* 8: 110-16. https://doi.org/10.1016/j.addma.2015.09.006. http://www.sciencedirect.com/science/article/pii/S2214860415000494.

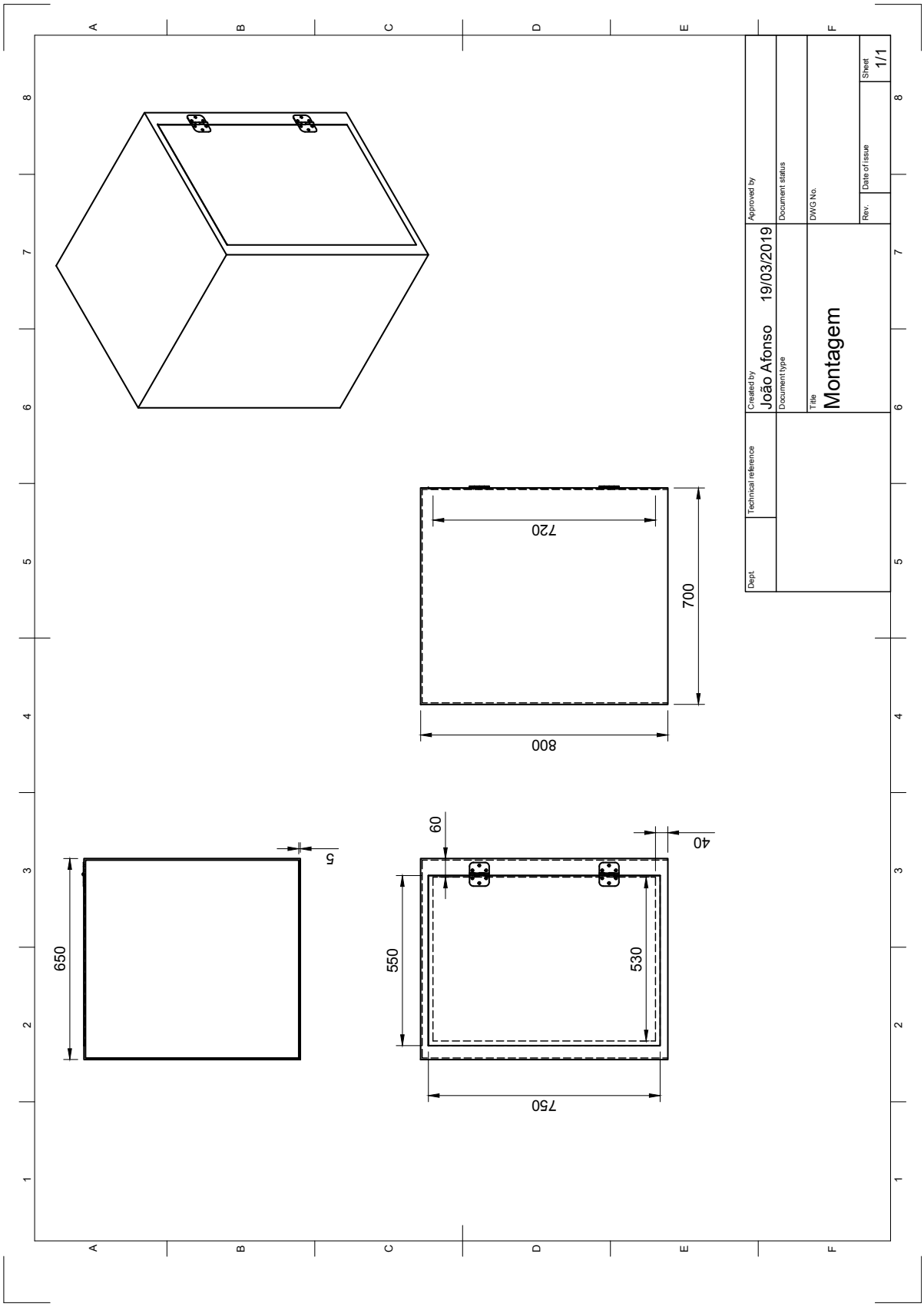
Wohlers, Terry, Ian Campbell, Olaf Diegel, and Joseph Kowen. 2019. *Wohlers Report 2018 - 3D Printing and Additive Manufacturing State of the Industry - Annual Worldwide Progress Report*.

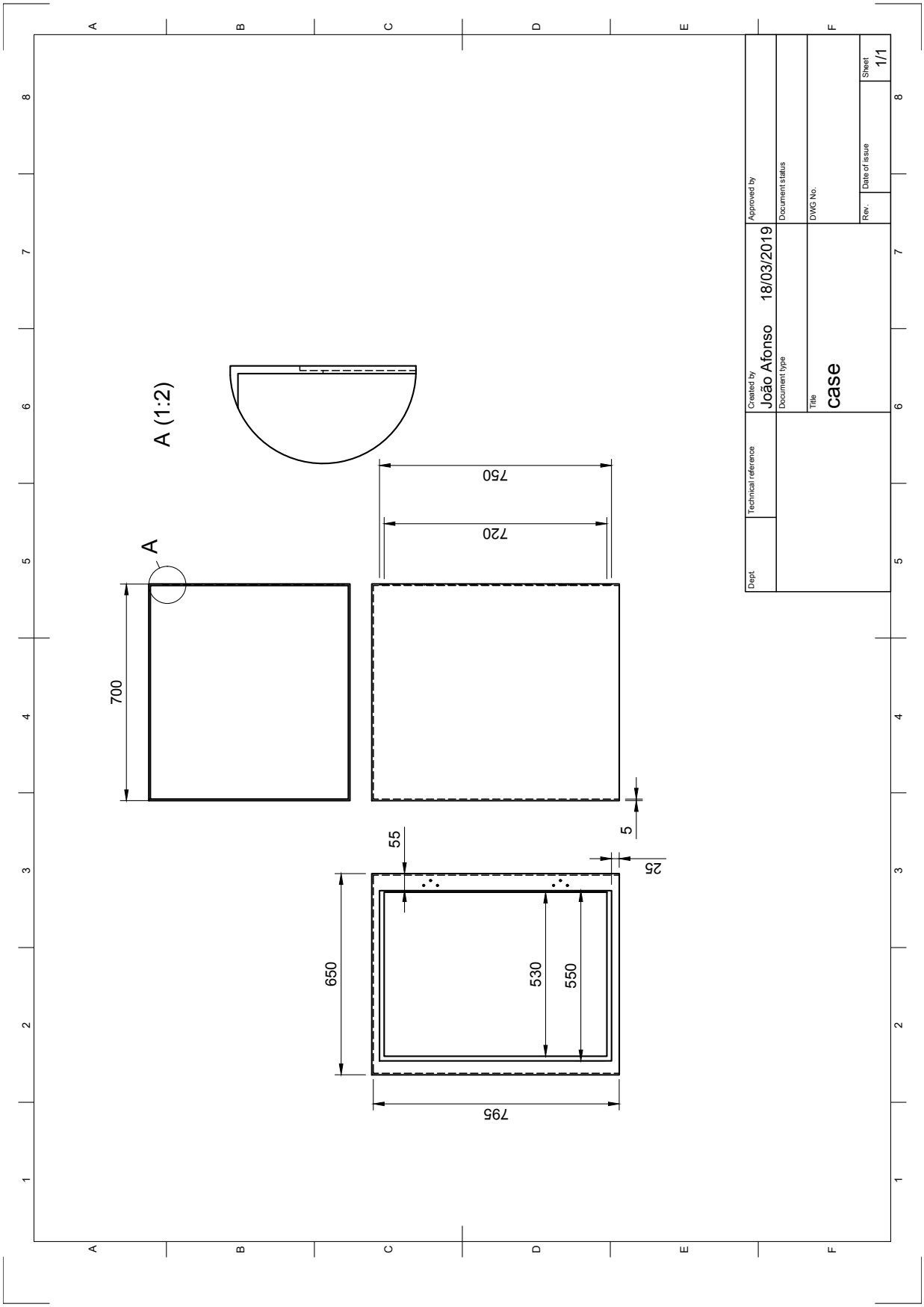
Wu, Wenzheng, Peng Geng, Guiwei Li, Di Zhao, Haibo Zhang, and Ji Zhao. 2015. "Influence of Layer Thickness and Raster Angle on the Mechanical Properties of 3D-Printed PEEK and a Comparative Mechanical Study between PEEK and ABS". *Materials* 8, no. 9: 5834-46. https://www.mdpi.com/1996-1944/8/9/5271.

Ziemian, Constance, Mala Sharma, and Sophia Ziemian. 2012. "Anisotropic Mechanical Properties of ABS Parts Fabricated by Fused Deposition Modelling".

7. Appendix

A – Enclosure




A (1:2)
A
750
720
700
5
55
25
650
530
550
795
Approved by
Document status
DWG No.
Rev.
Date of issue
Sheet
1/1
Created by
João Afonso
18/03/2019
Document type
Title
case
Technical reference
Dept.

B – Filament specification sheet

Technical Data Sheet

Product name: Premium PLA

Version: v3

Premium PLA is a high-end general purpose Poly-Lactic Acid type of 3D printer filament which is more purer and lesser modified than our EasyFil PLA for instance.
Premium PLA is a slightly harder PLA with an excellent thermal stability and a slightly faster crystallisation process of the 3D printed layers and is often used for large(r) scale prototyping on industrial-sized 3D printers. Therefore Premium PLA is available on large spool sizes.

Properties	Typical value	Test Method	Test condition
Physical			
Specific gravity	1.24 g/cc	ASTM D1505	-
Melt flow rate	6.0 g/10min	-	-
Water absorption	-	-	-
Moisture absorption	-	-	-
Mechanical			
Impact strength	6.0KJ/m²	-	-
Tensile strength	105 Mpa (MD)	ASTM D882	-
Tensile modulus	3145 Mpa (MD)	ASTM D882	-
Elongation at break	175% (MD)	ASTM D882	-
Flexural strength	± 54.4 Mpa	-	-
Flexural modulus	± 2364.3 Mpa	-	-
Hardness	-	-	-
Thermal			
Print temperature	± 190 - 225° C	-	-
Melting termperature	± 210 ± 10° C	-	-
Viscat softening temp.	± 62° C	ISO 306	-
Optical			
Haze	2.1%	ASTM D1003	-
Transmittance	-	-	-
Gloss	80	ASTM D1003	Gloss, 20°

Product details, certifications and compliance	
HS Code	39169090
REACH compliant	Yes
RoHS certified	Yes

Diameter	Tolerance	Roundness
1.75mm	± 0.05mm	≥ 95%
2.85mm	± 0.10mm	≥ 95%

Formfutura BV
Groenestraat 215
6531 HH Nijmegen
The Netherlands

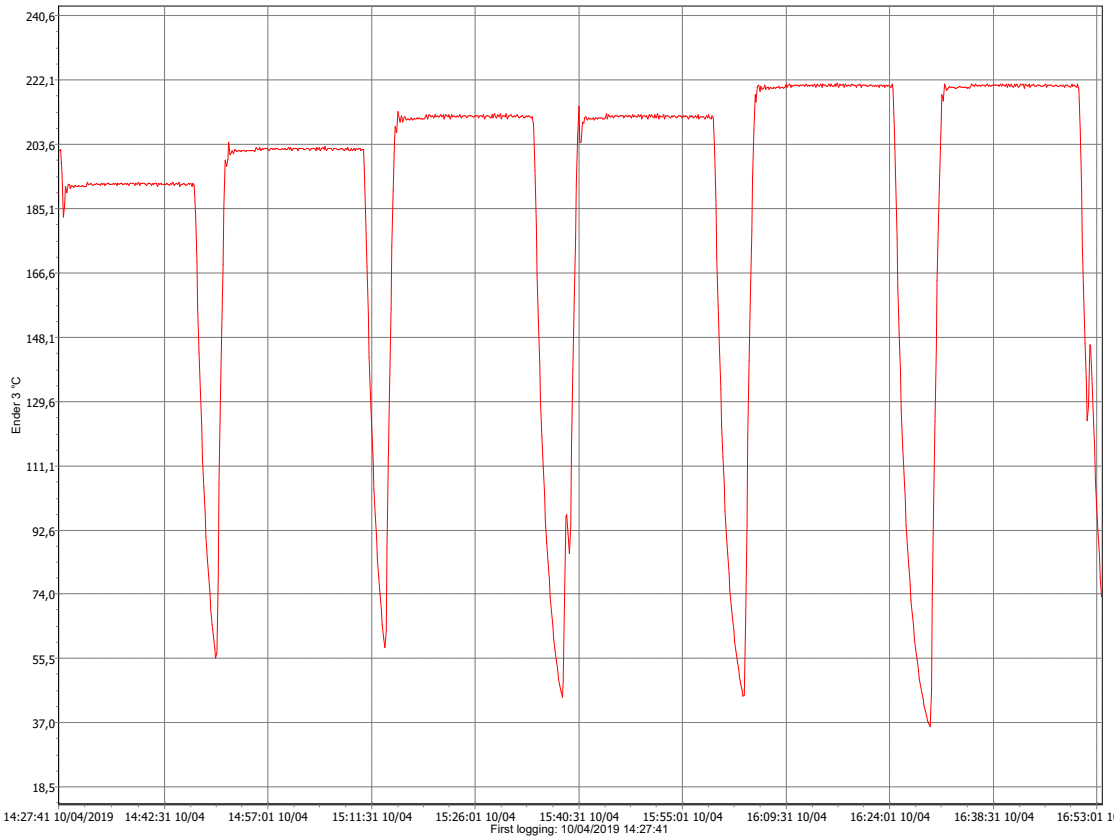
CoC: 69099502
VAT: NL857733709B01
EORI: NL857733709

Tel: +31 (0)85 002 0881
Email: info@formfutura.com
Website: www.formfutura.com

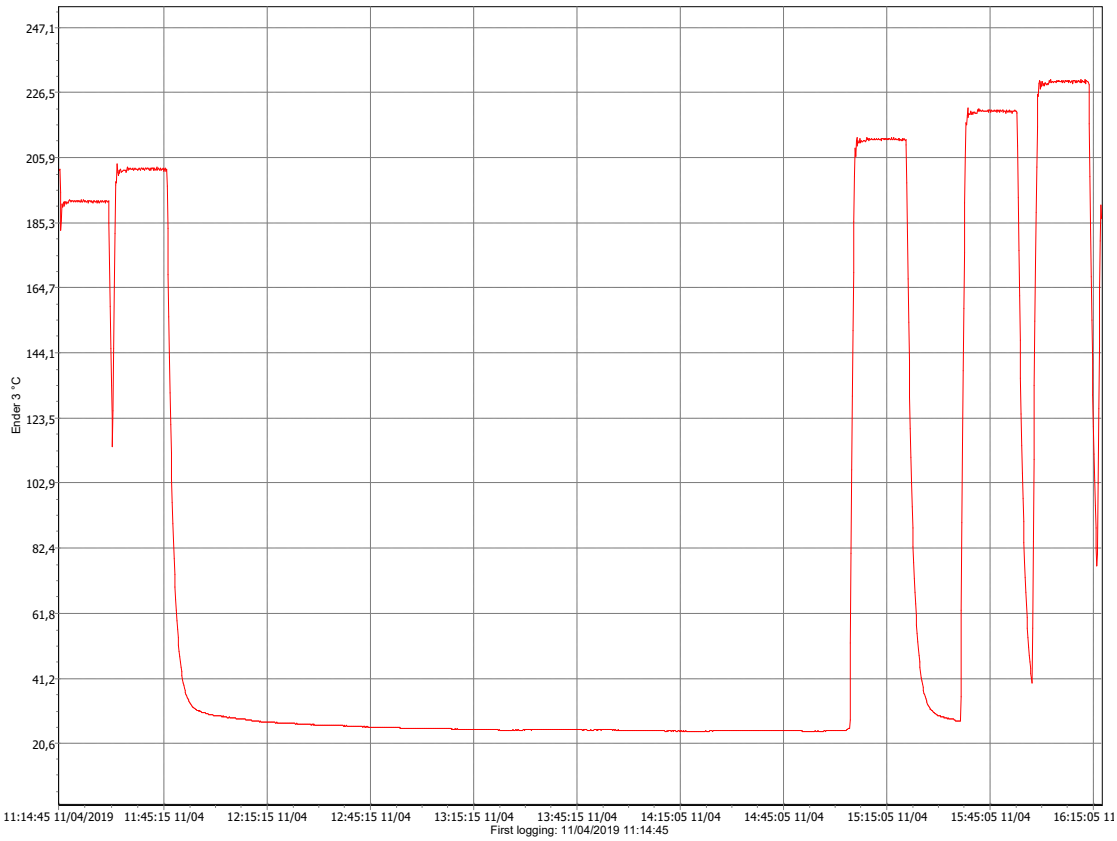
All information supplied by or on behalf of Formfutura in relation to its products, whether in the nature of data, recommendations or otherwise, is supported by research and, in good faith, believed reliable, but Formfutura assumes no liability and makes no warranties of any kind, express or implied, including, but not limited to, those of title, merchantability, fitness for a particular purpose or non-infringement or any warranty arising from a course of dealing, usage, or trade practice whatsoever in respect of application, processing or use made of the forementioned information or product. The user assumes all responsibility for the use of all information provided and shall verify quality and other properties or any consequence from the use of all such information. Typical values are indicative only and are not to be construed as being binding specifications.

C – Extruder temperature profiles

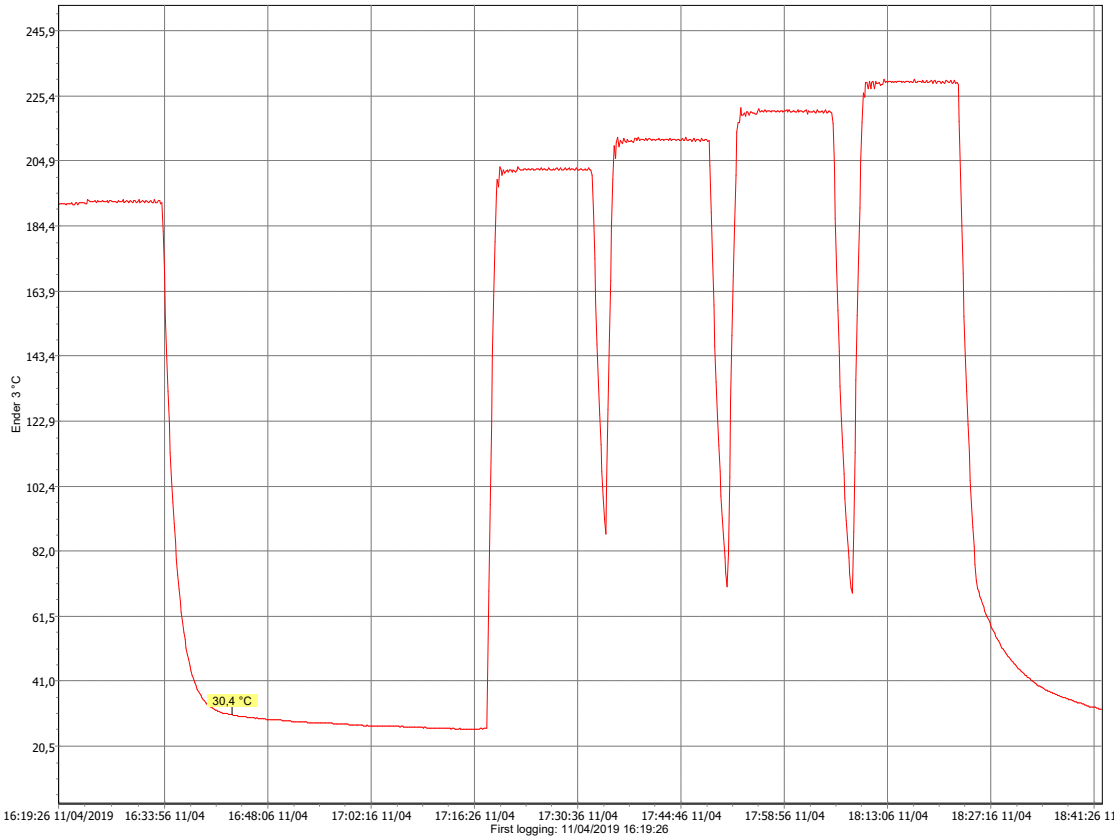
C1. L_Compression, $V_{Print} = 30mm/s$



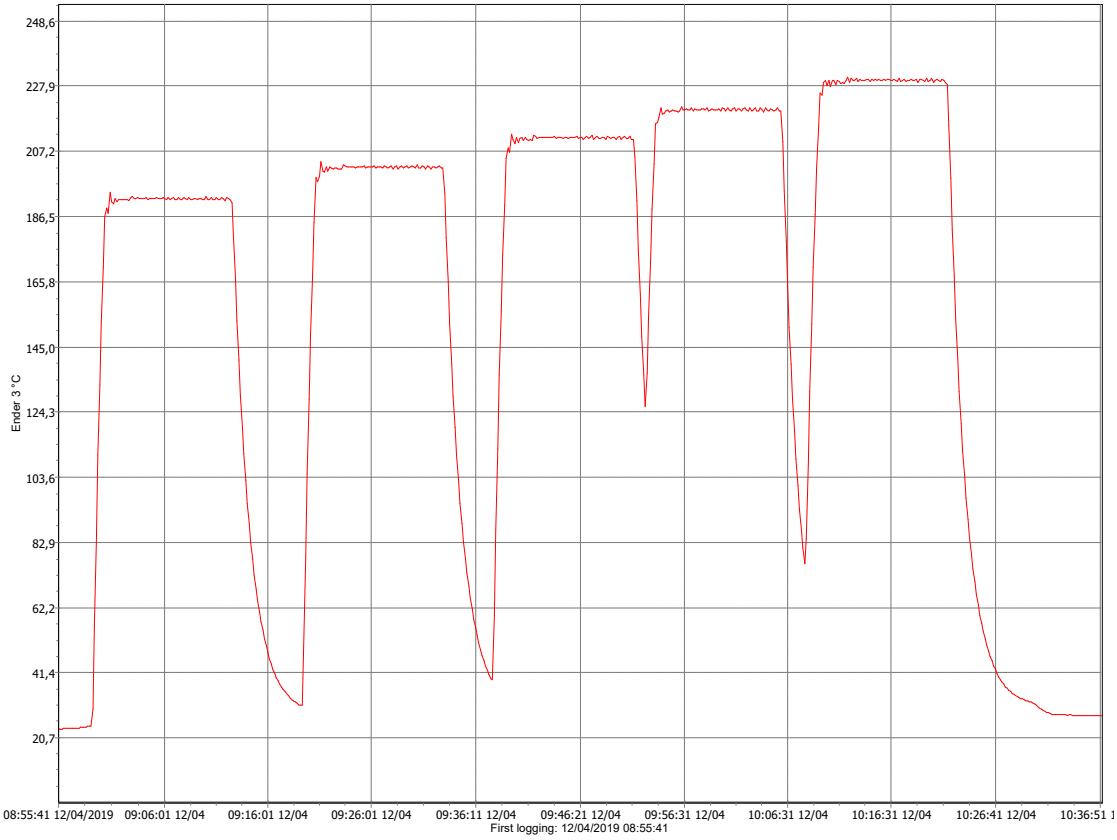
C2. L_Compression, $V_{Print} = 45mm/s$



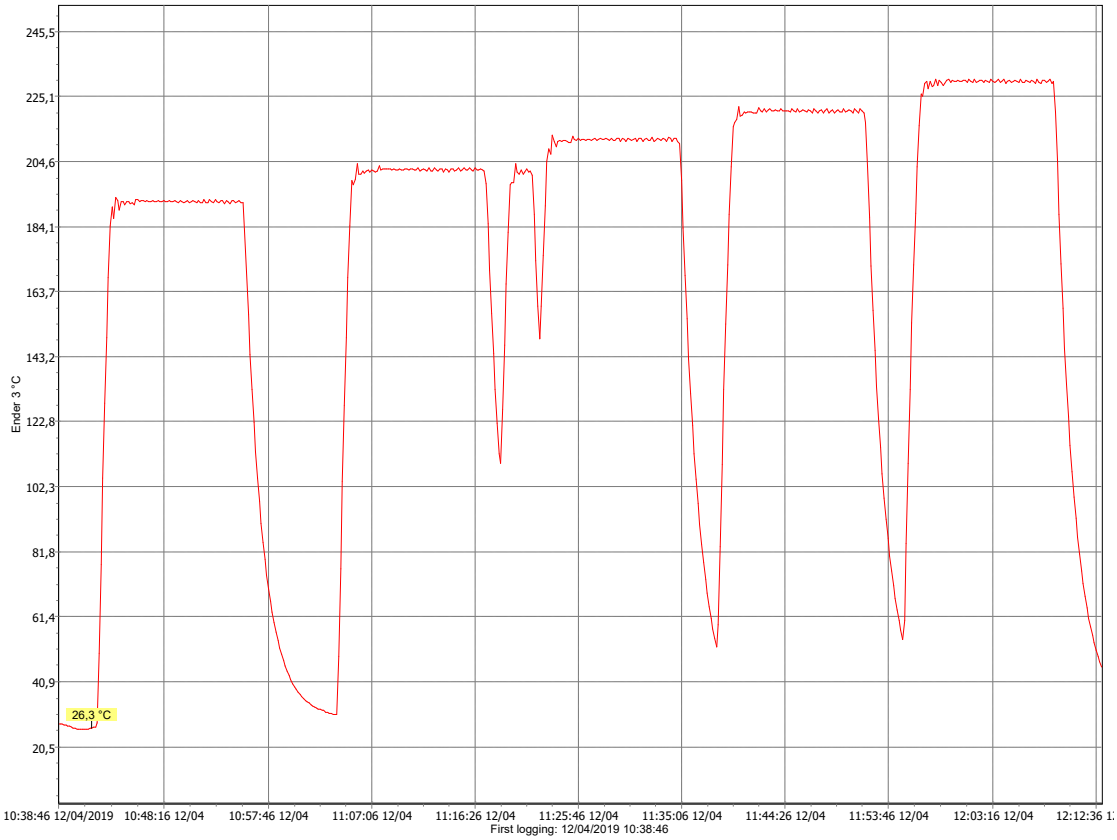
C3. L_Compression, $V_{Print} = 60mm/s$



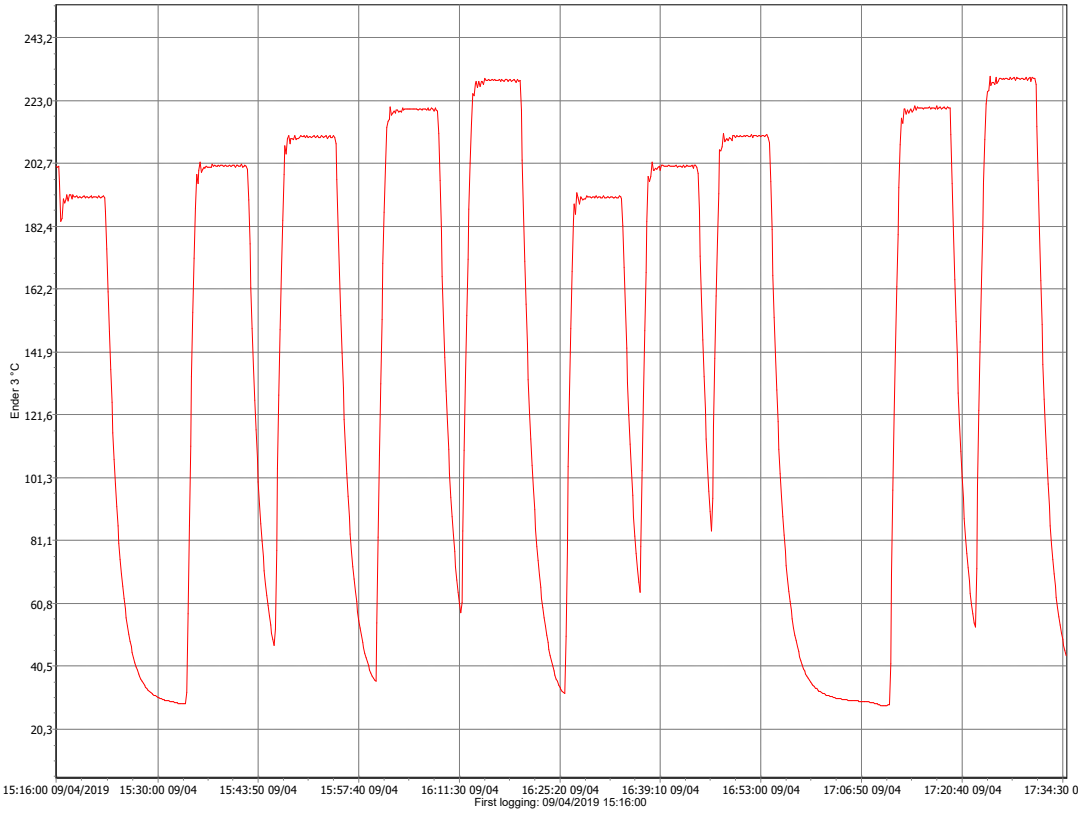
C4. L_Compression, $V_{Print} = 75mm/s$



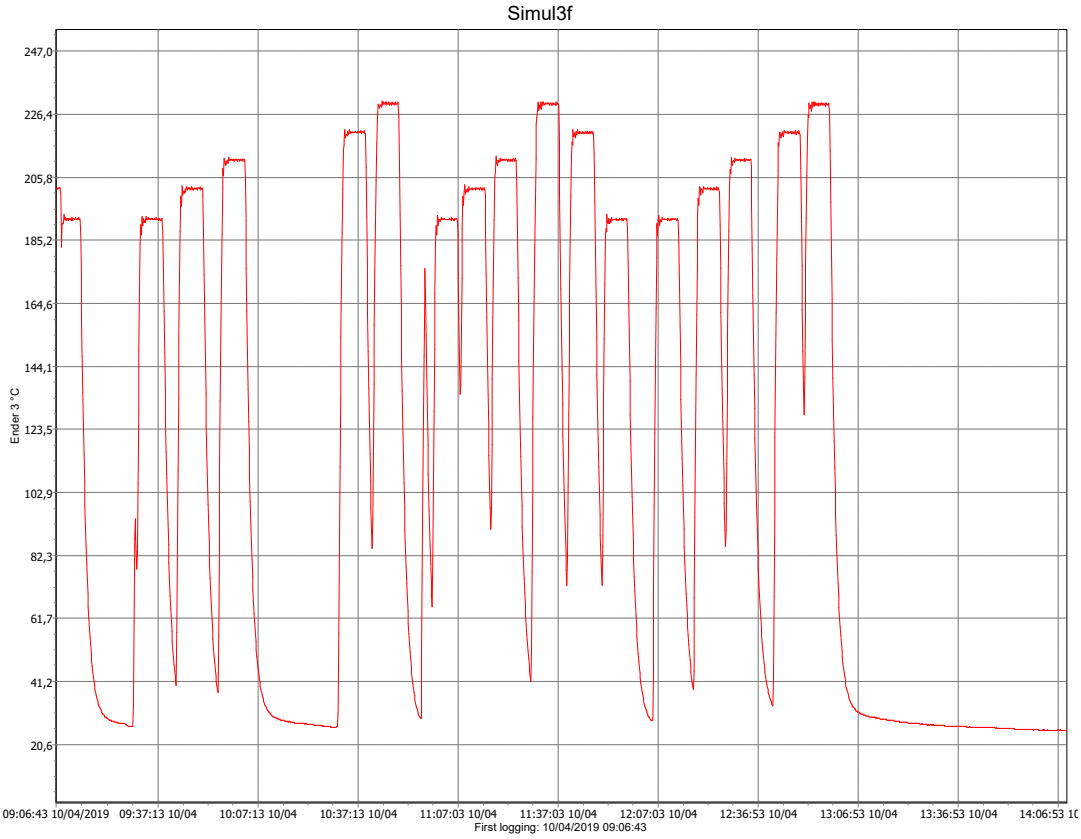
C5. L_Compression, V_{Print} = 90mm/s



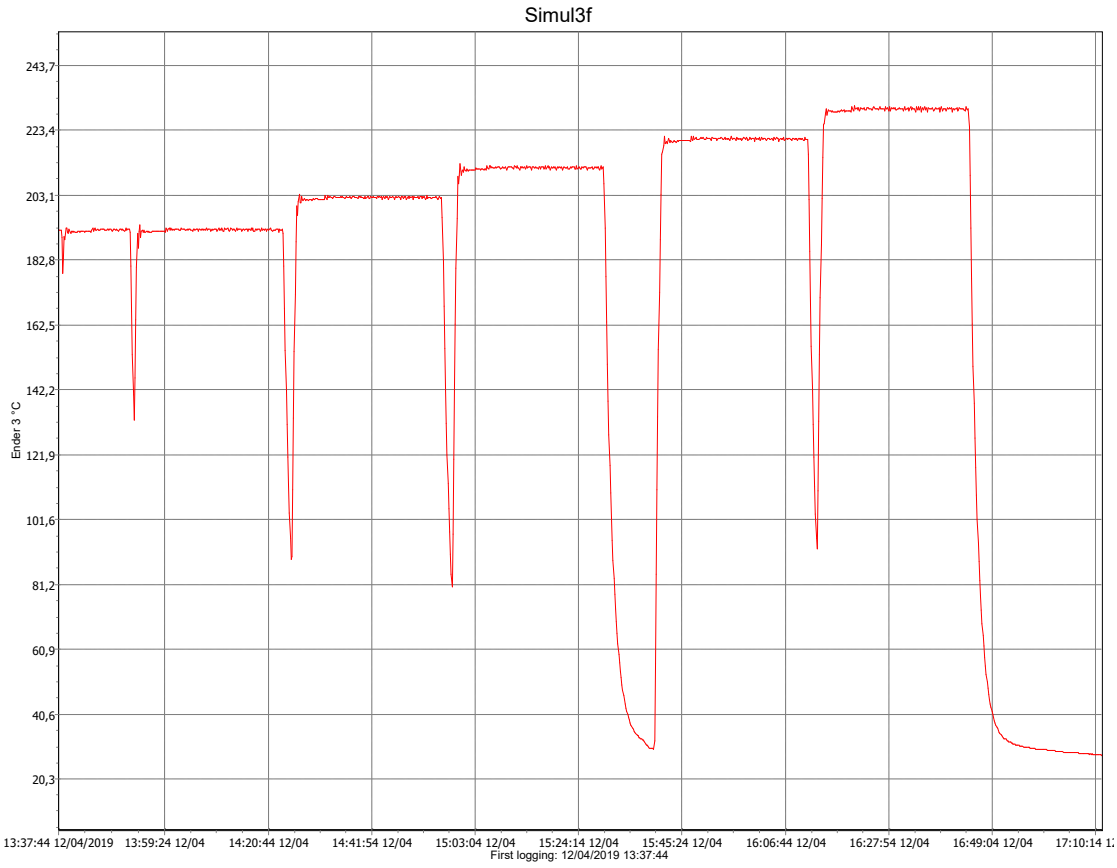
C6. S_Compression, V_{Print} = 30mm/s and V_{Print} = 45mm/s



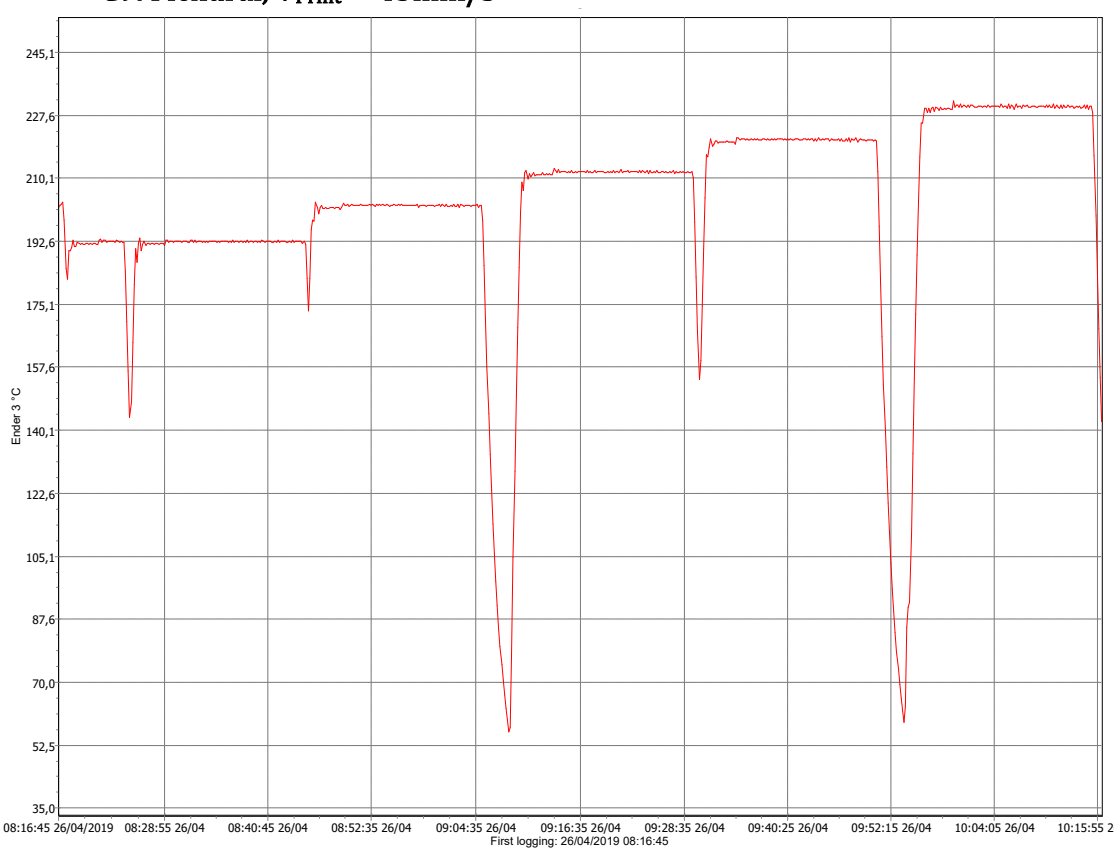
C7. S_Compression, V_{Print} = 60mm/s, V_{Print} = 75mm/s and V_{Print} = 90mm/s



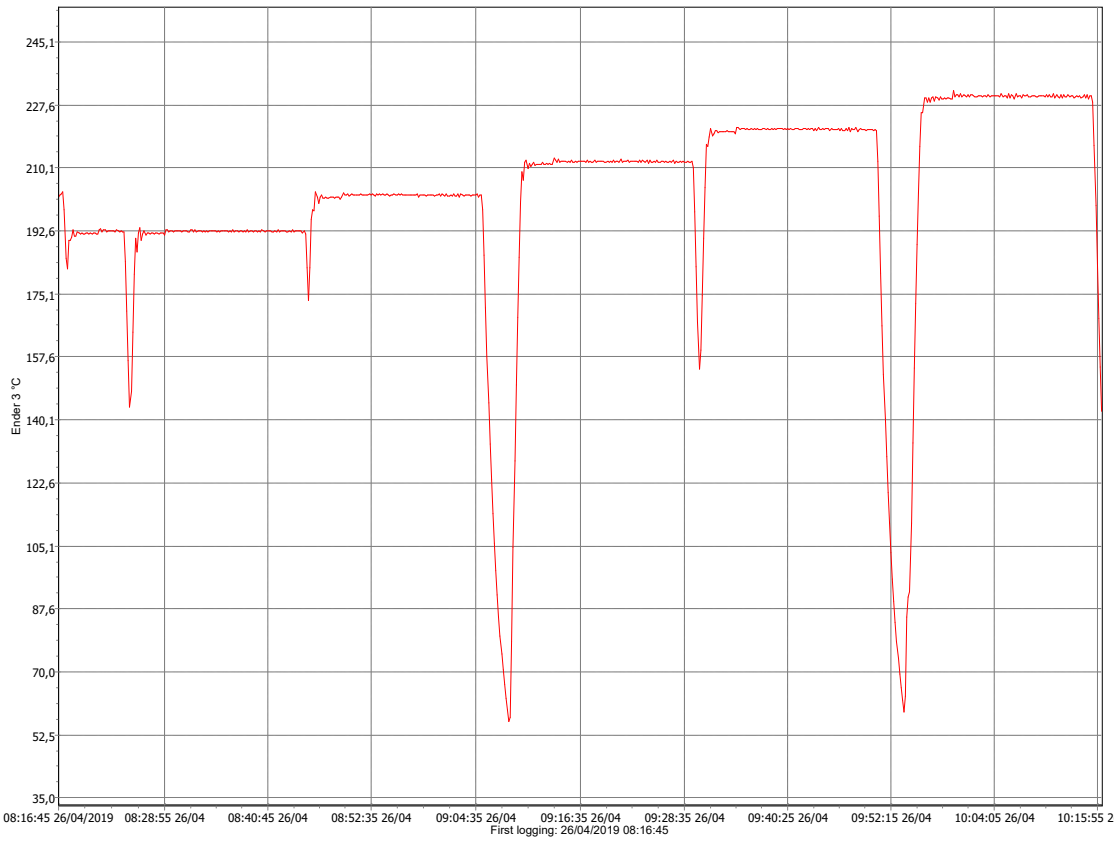
C8. Flexural, V_{Print} = 30mm/s



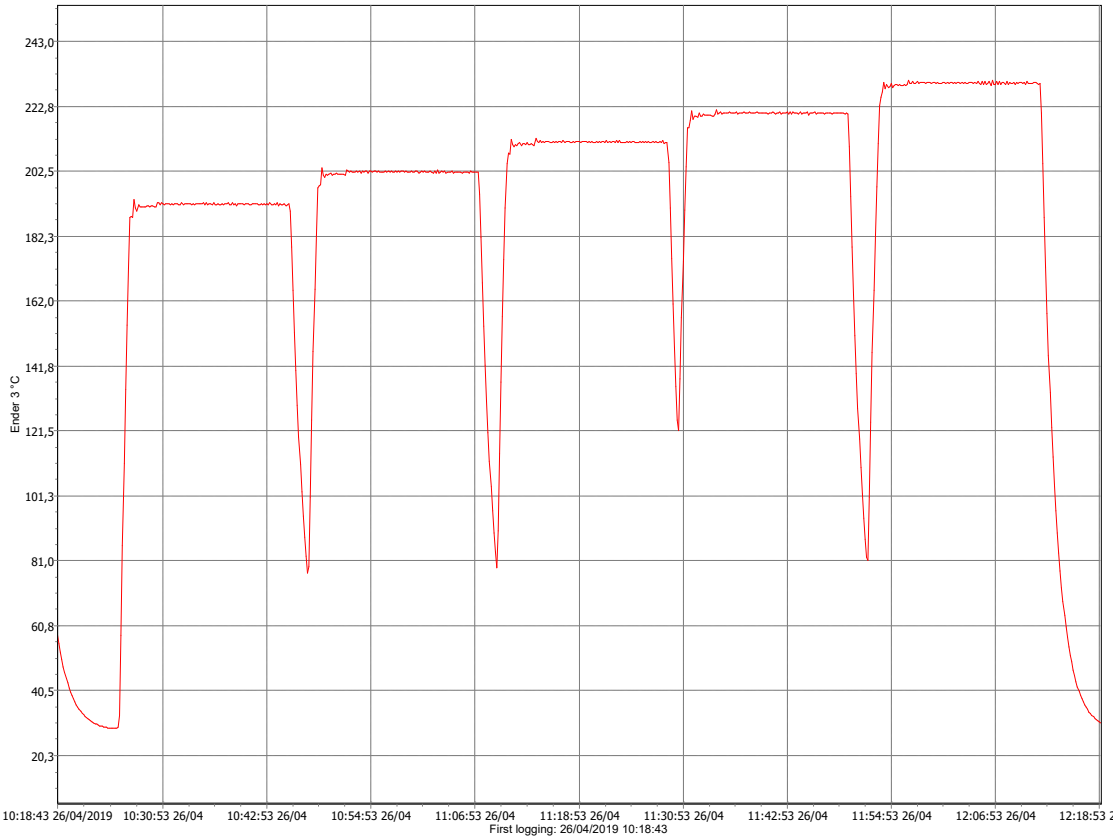
C9. Flexural, $V_{Print} = 45mm/s$



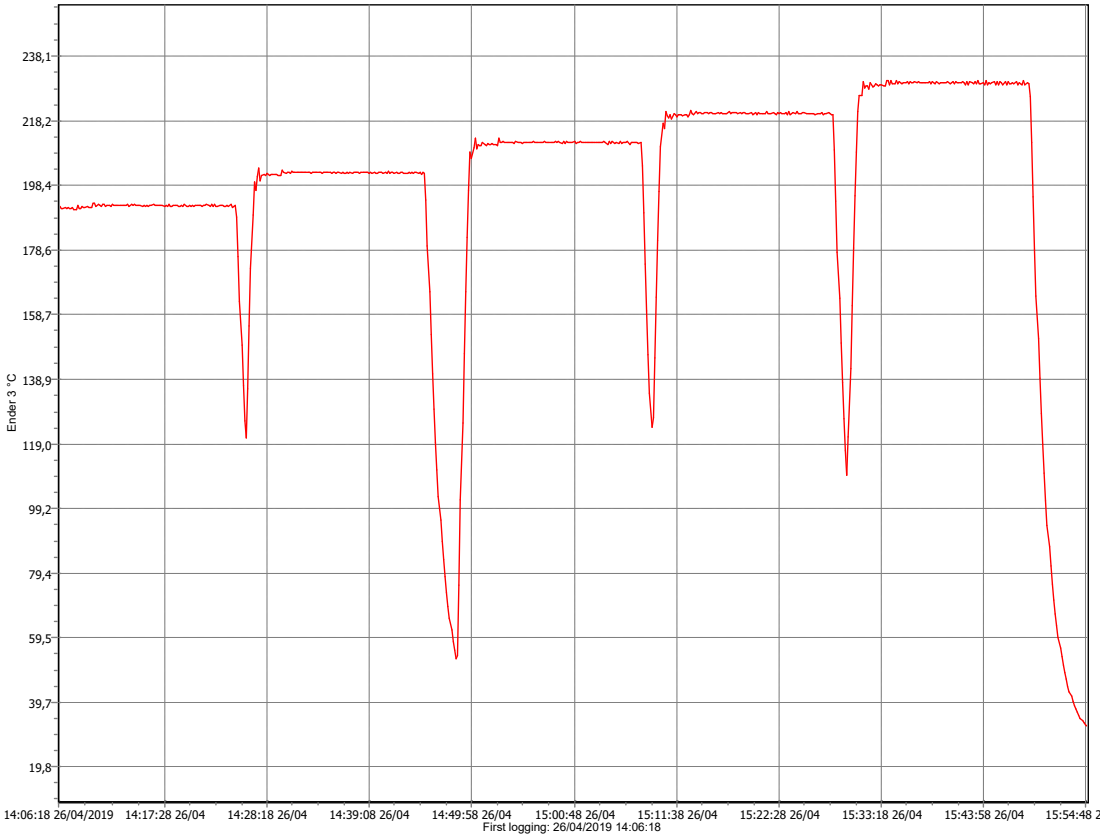
C10. Flexural, $V_{Print} = 60mm/s$



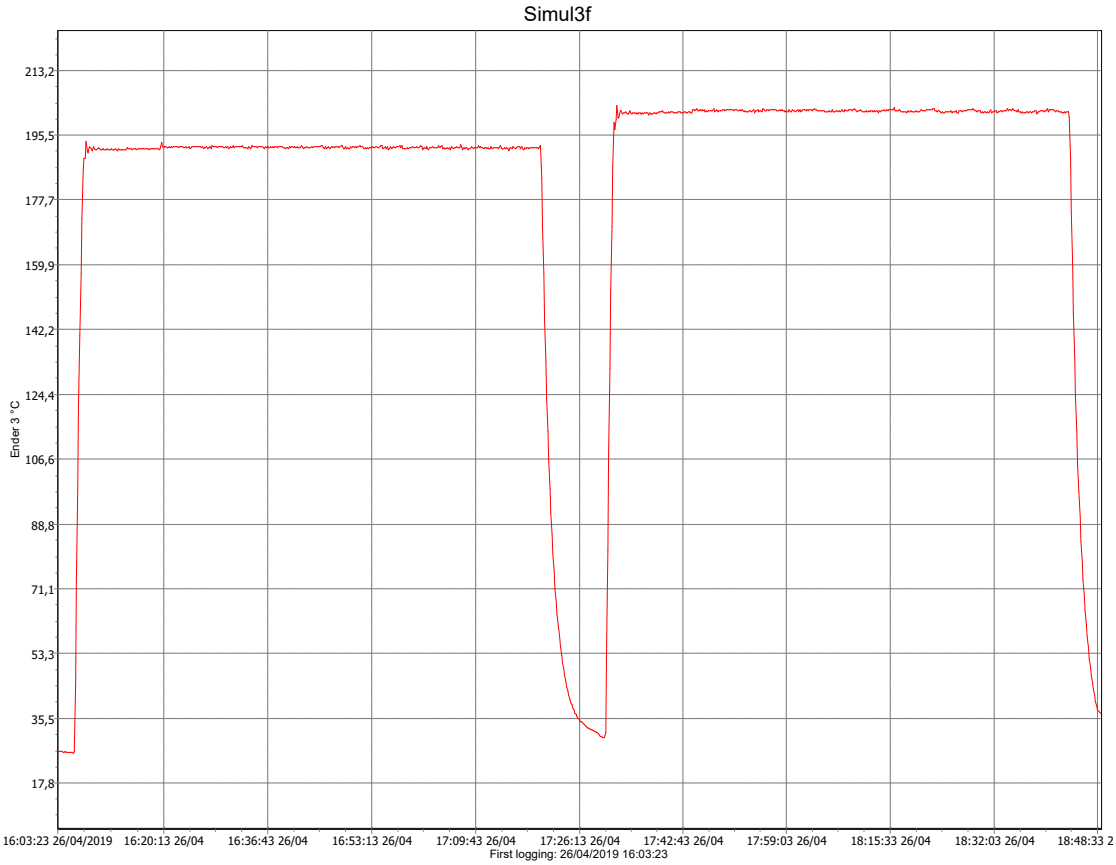
C11. Flexural, $V_{Print} = 75mm/s$

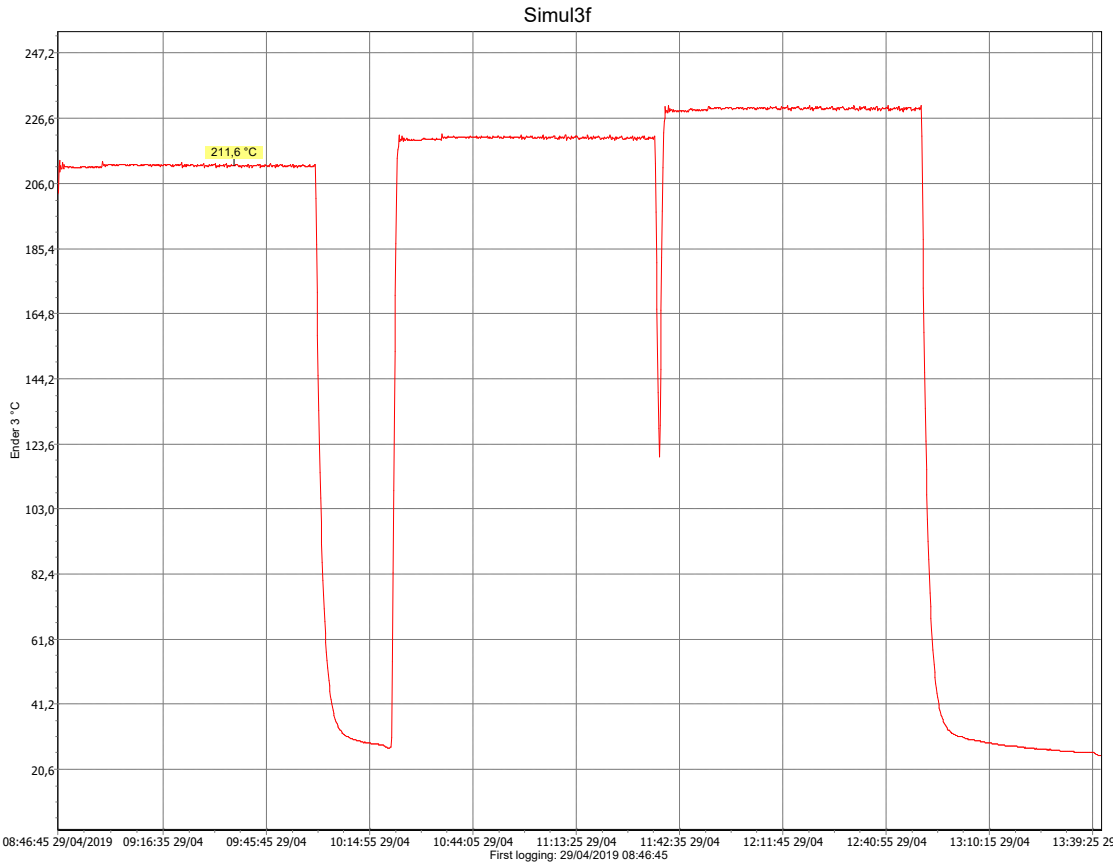


C12. Flexural, $V_{Print} = 90mm/s$

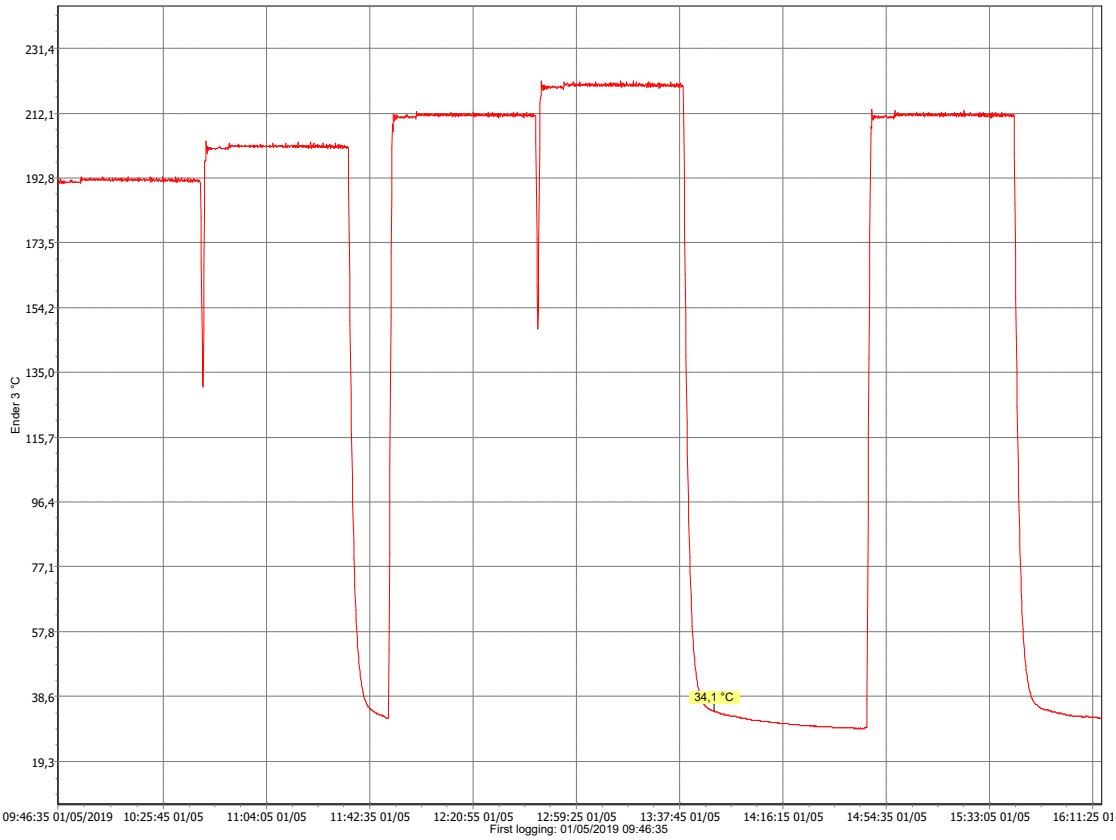


C13. Tensile, $V_{Print} = 30mm/s$

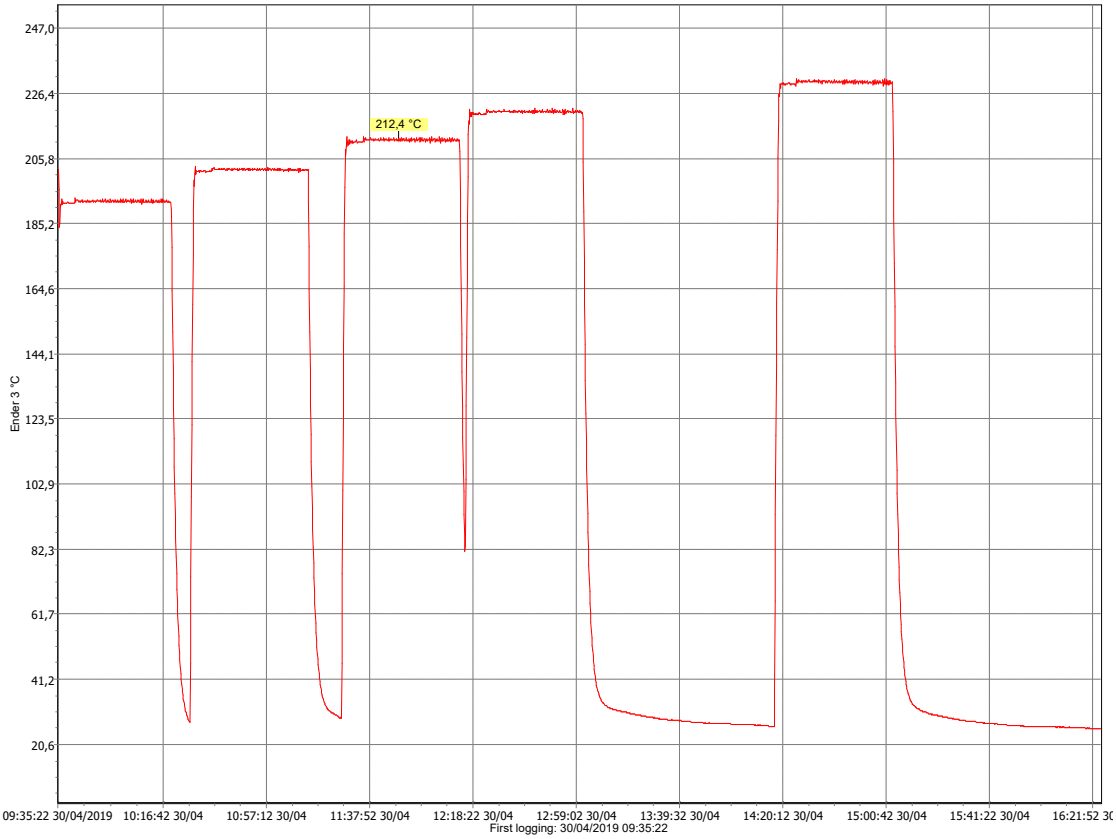




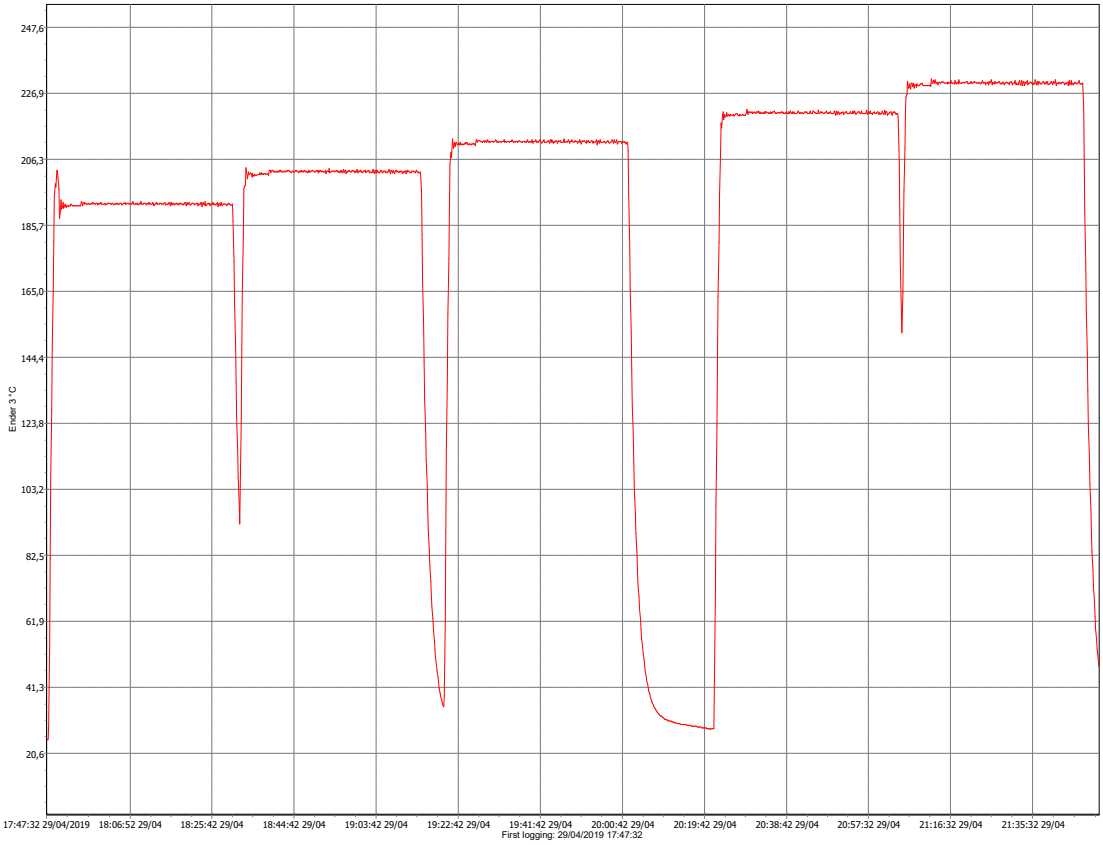
C14. Tensile, $V_{Print} = 45mm/s$



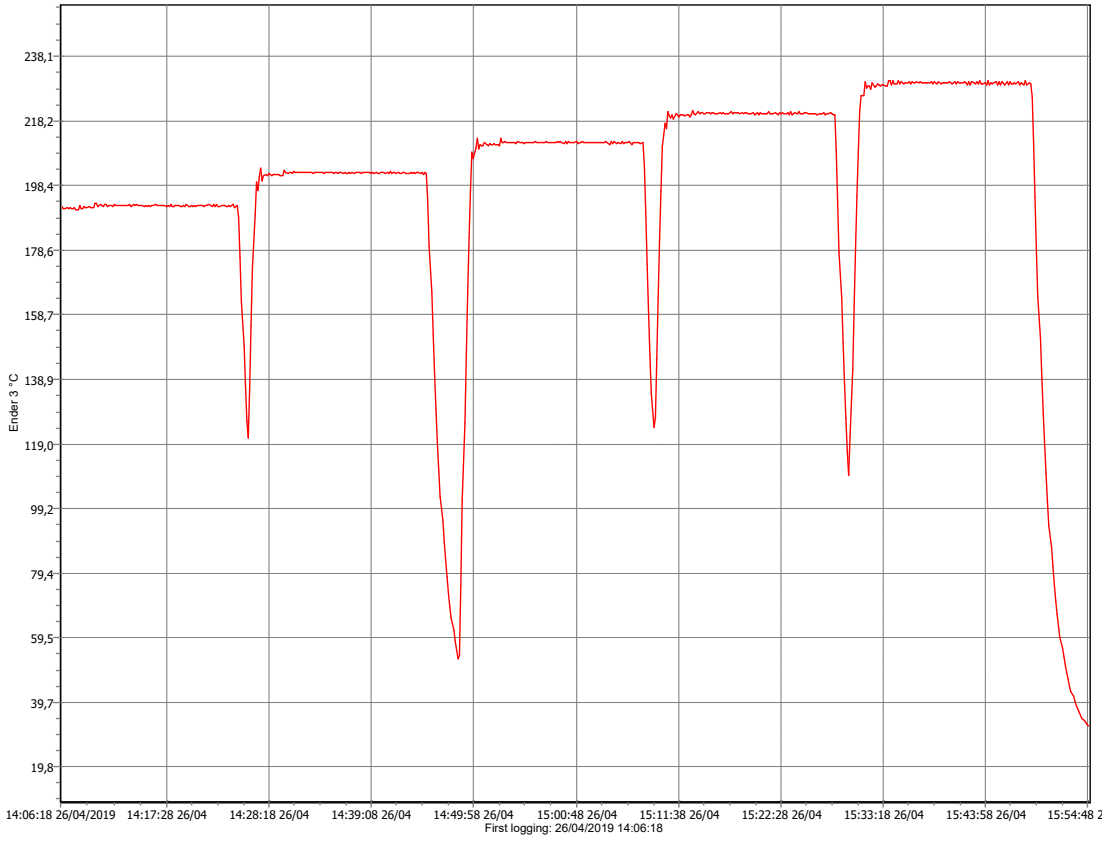
C15. Tensile, $V_{Print} = 60mm/s$



C16. Tensile, $V_{Print} = 75mm/s$

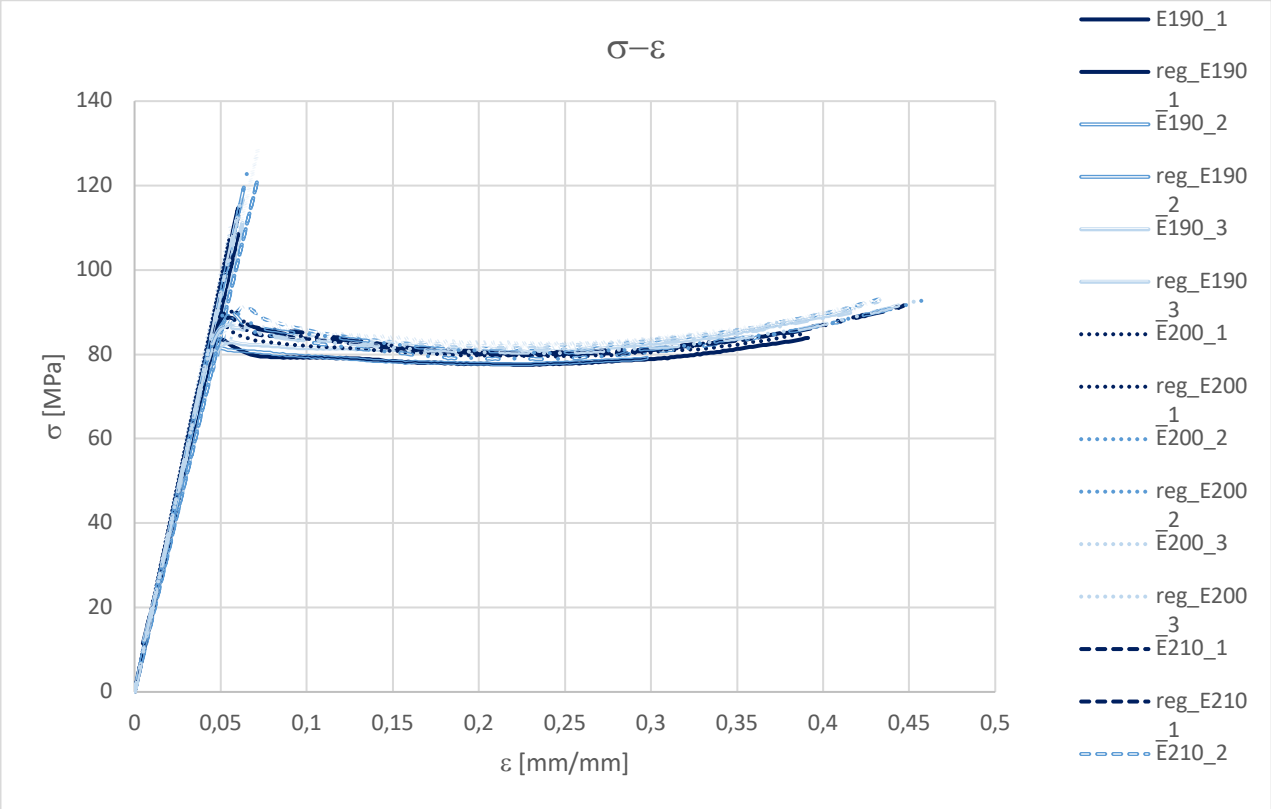


C17. Tensile, $V_{Print} = 90mm/s$

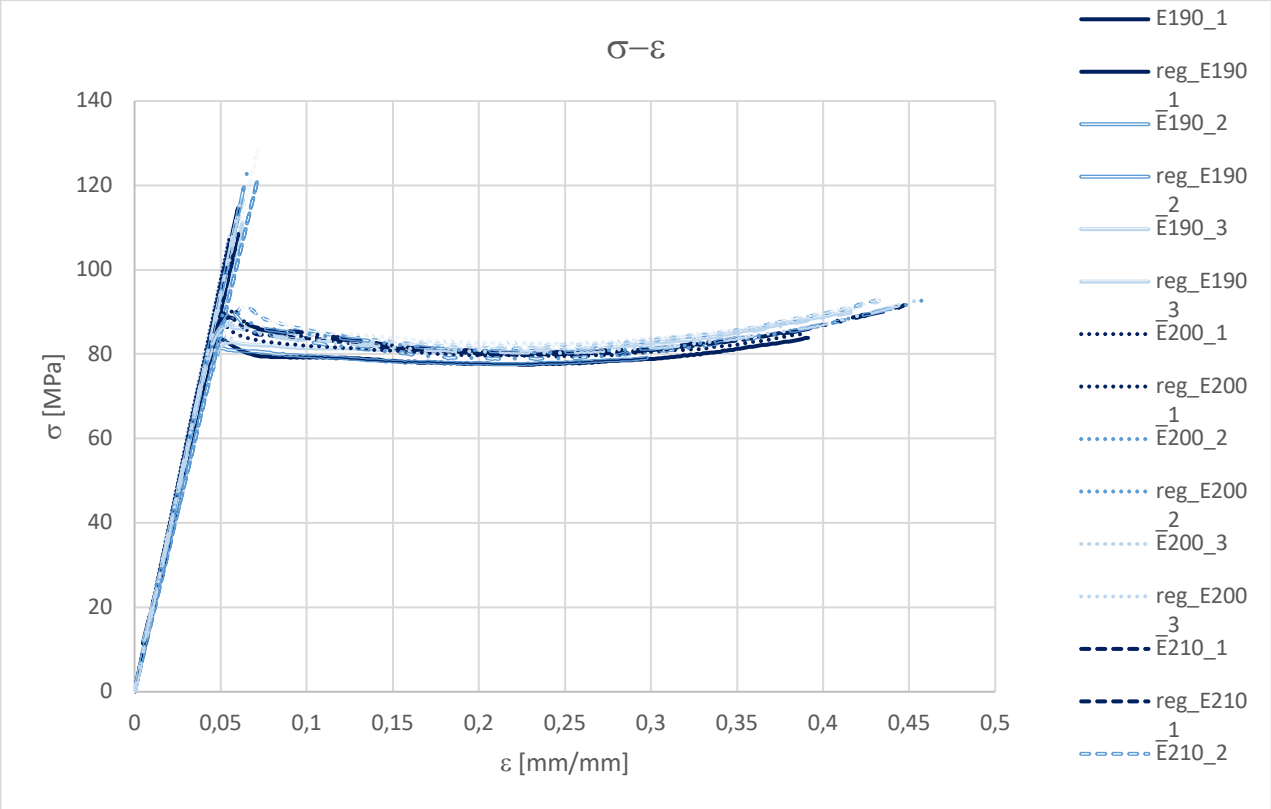


D – Stress-strain curves

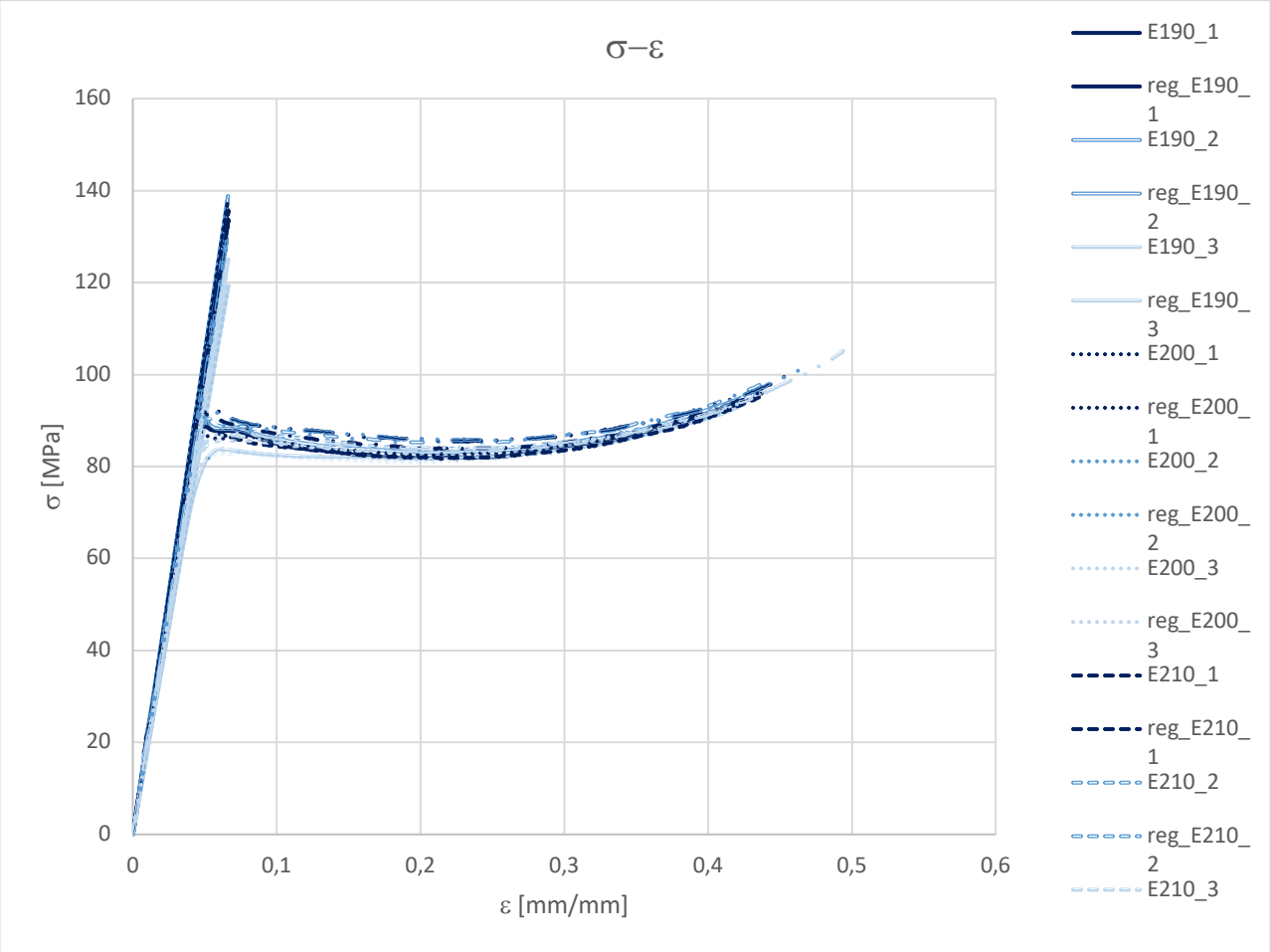
D1. Compression - V_{print}=30mm/s



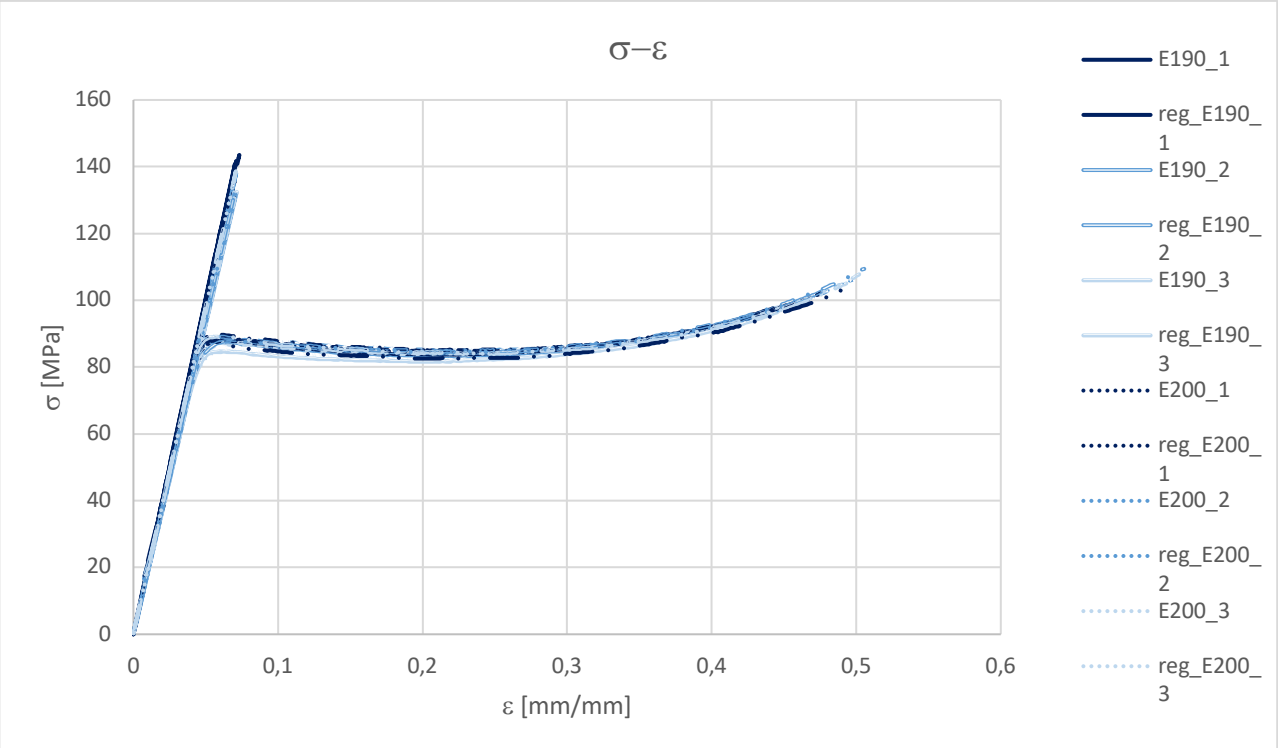
D2. Compression - V_{print}=45mm/s



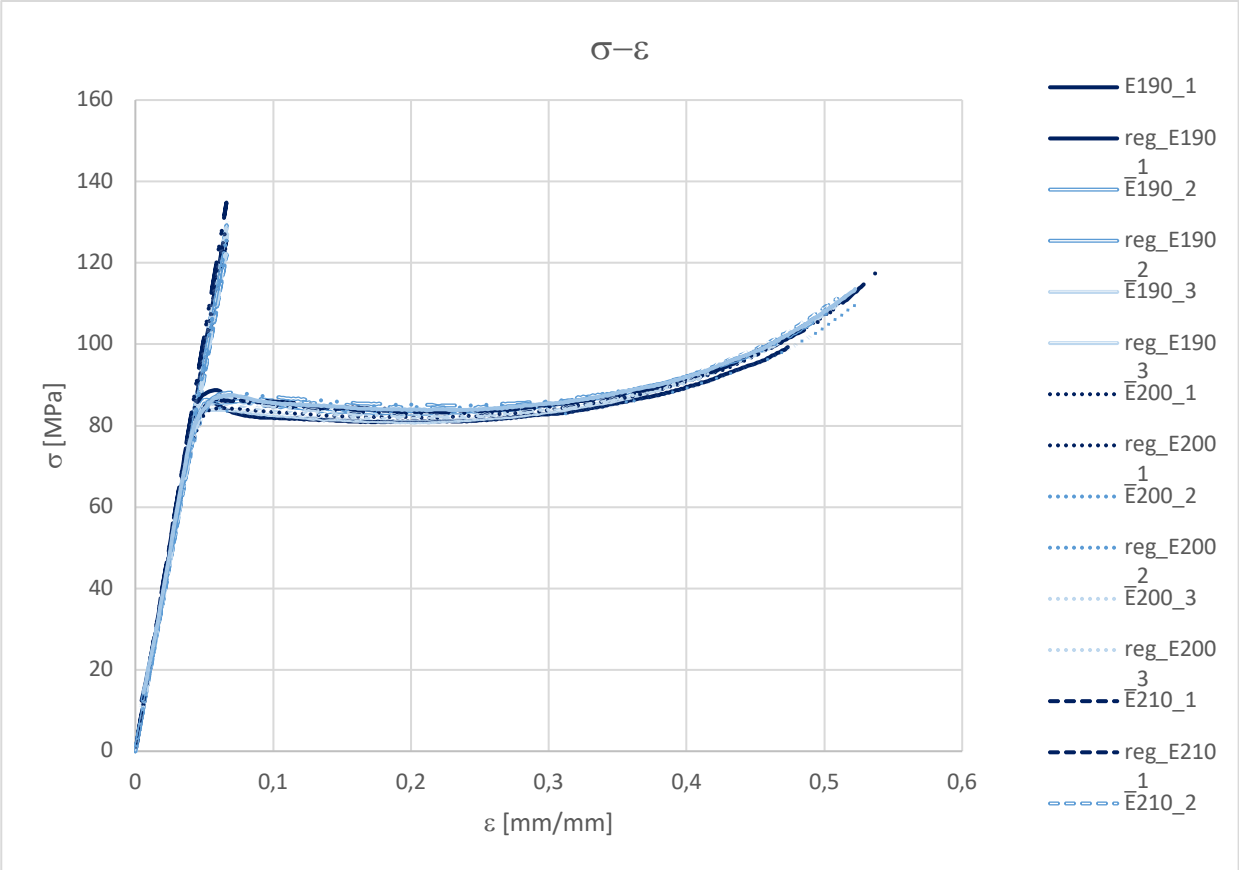
D3. Compression - V_{print}=60mm/s



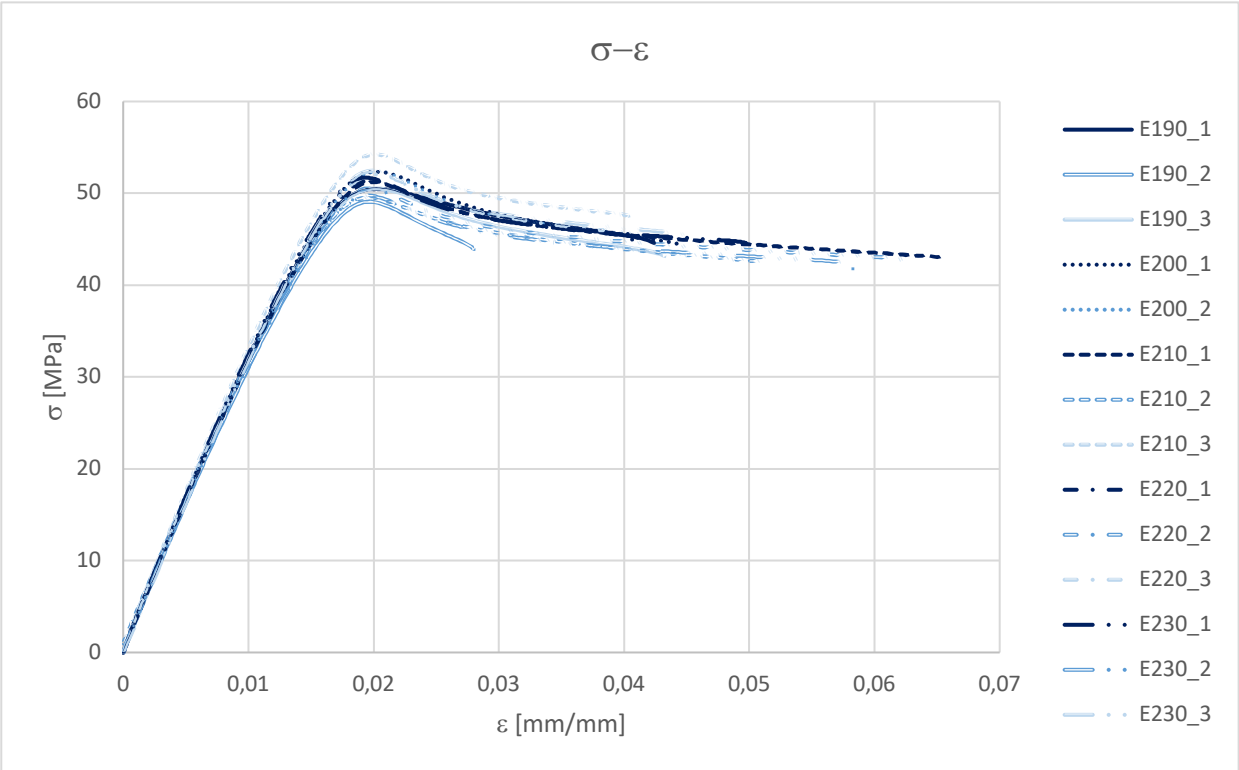
D4. Compression - V_{print}=75mm/s



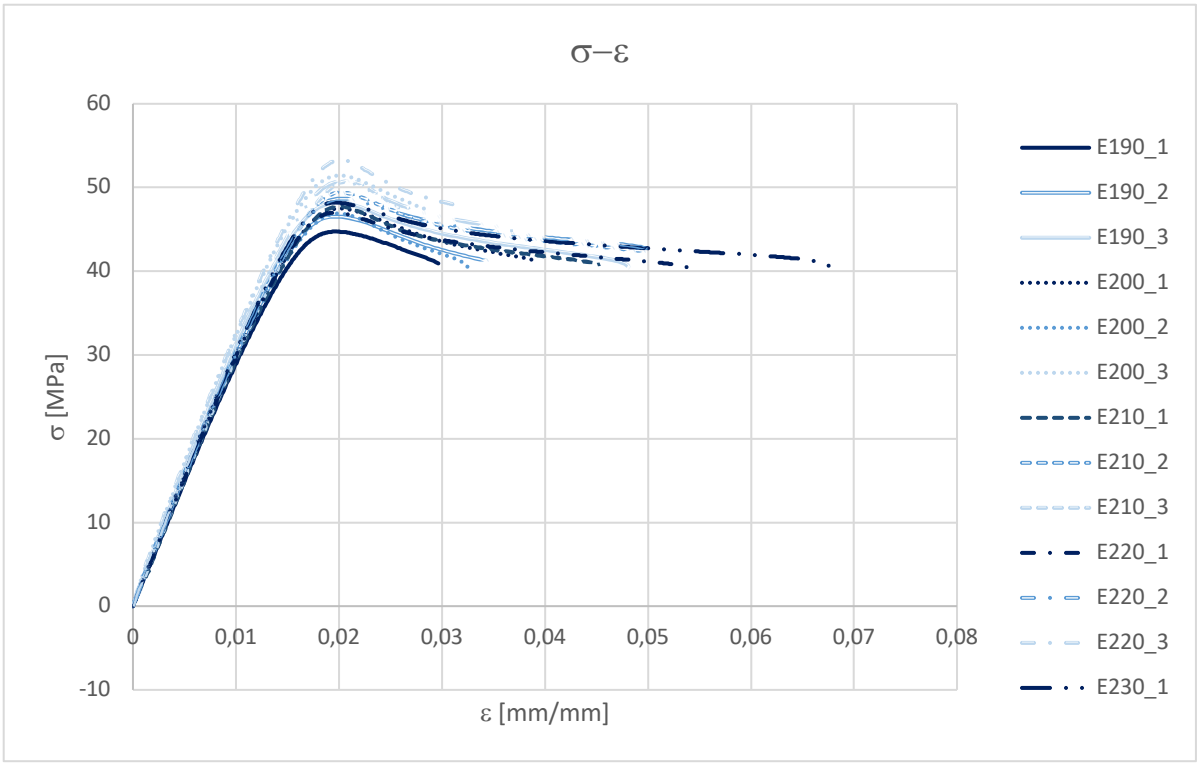
D5. Compression - V_{print}=90mm/s



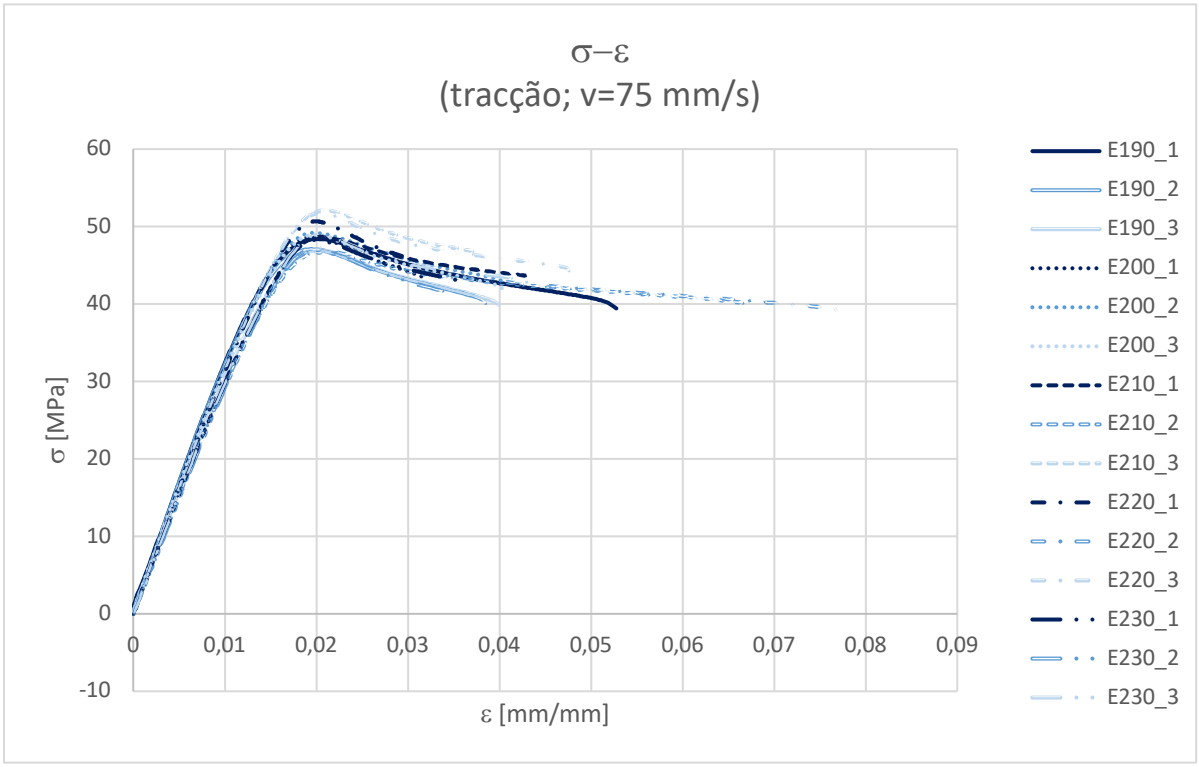
D6. Tensile - V_{print}=30mm/s



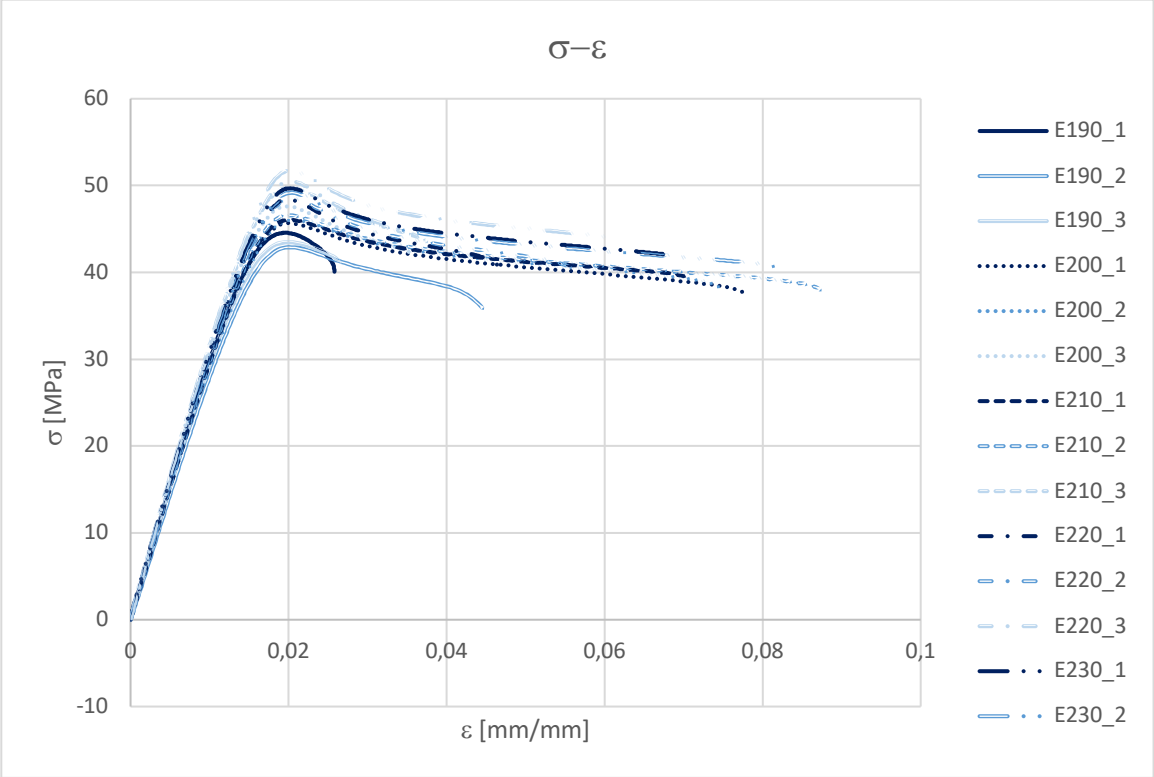
D7. Tensile - V_{print}=45mm/s



D8. Tensile - V_{print}=75mm/s

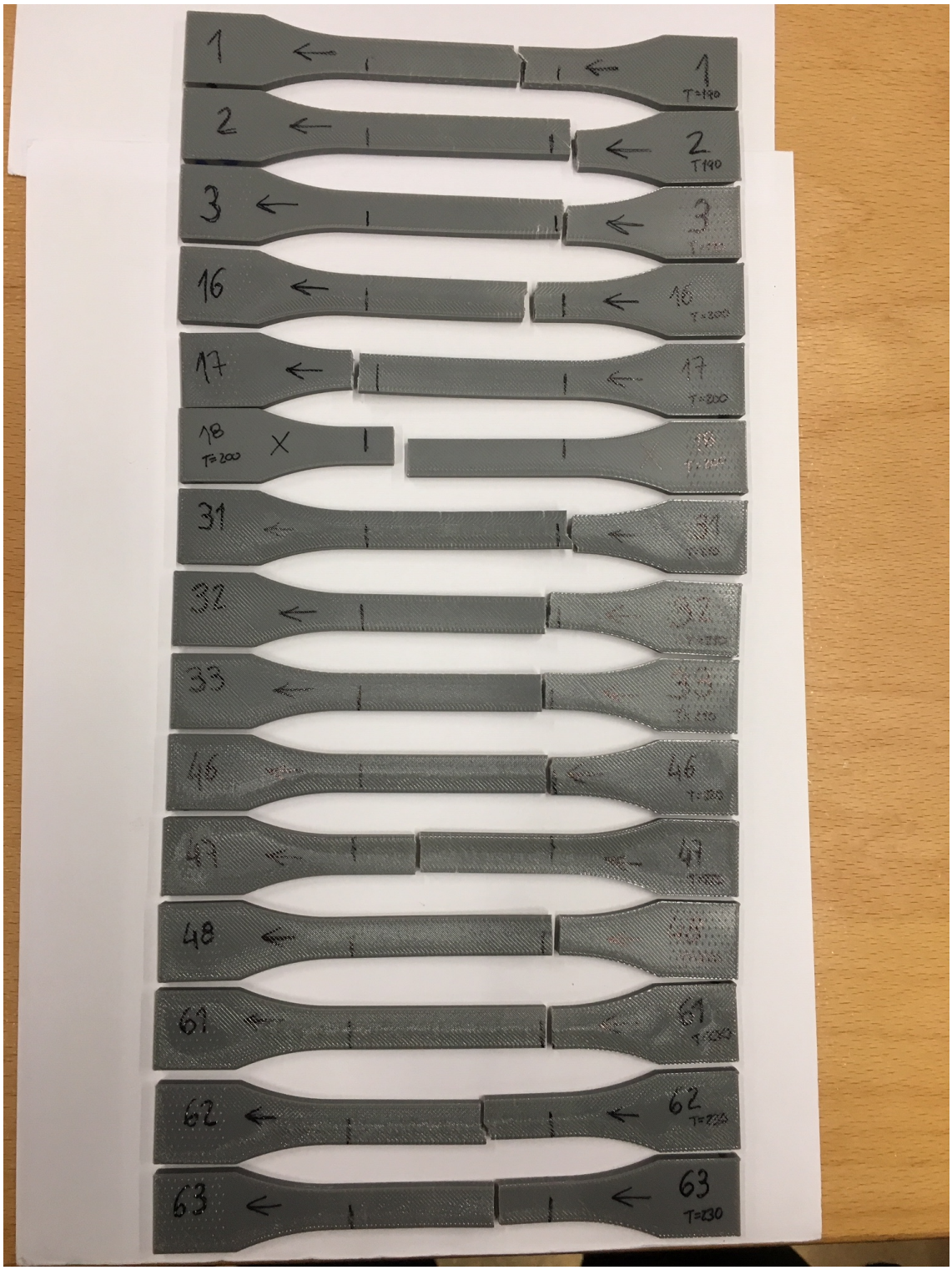


D9. Tensile - V_{print}=90mm/s

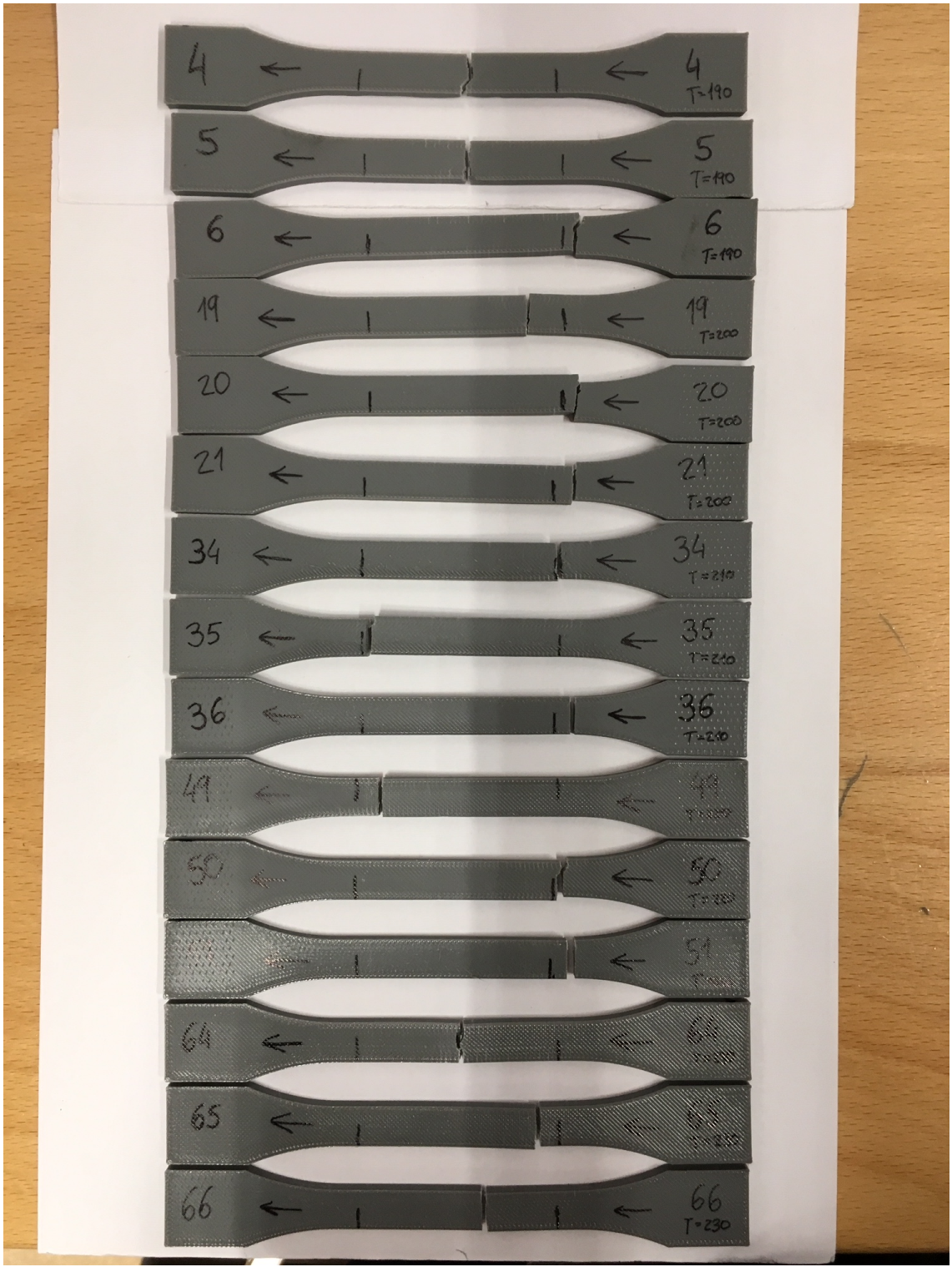


E – Photographs of the tensile test specimens after the test trials

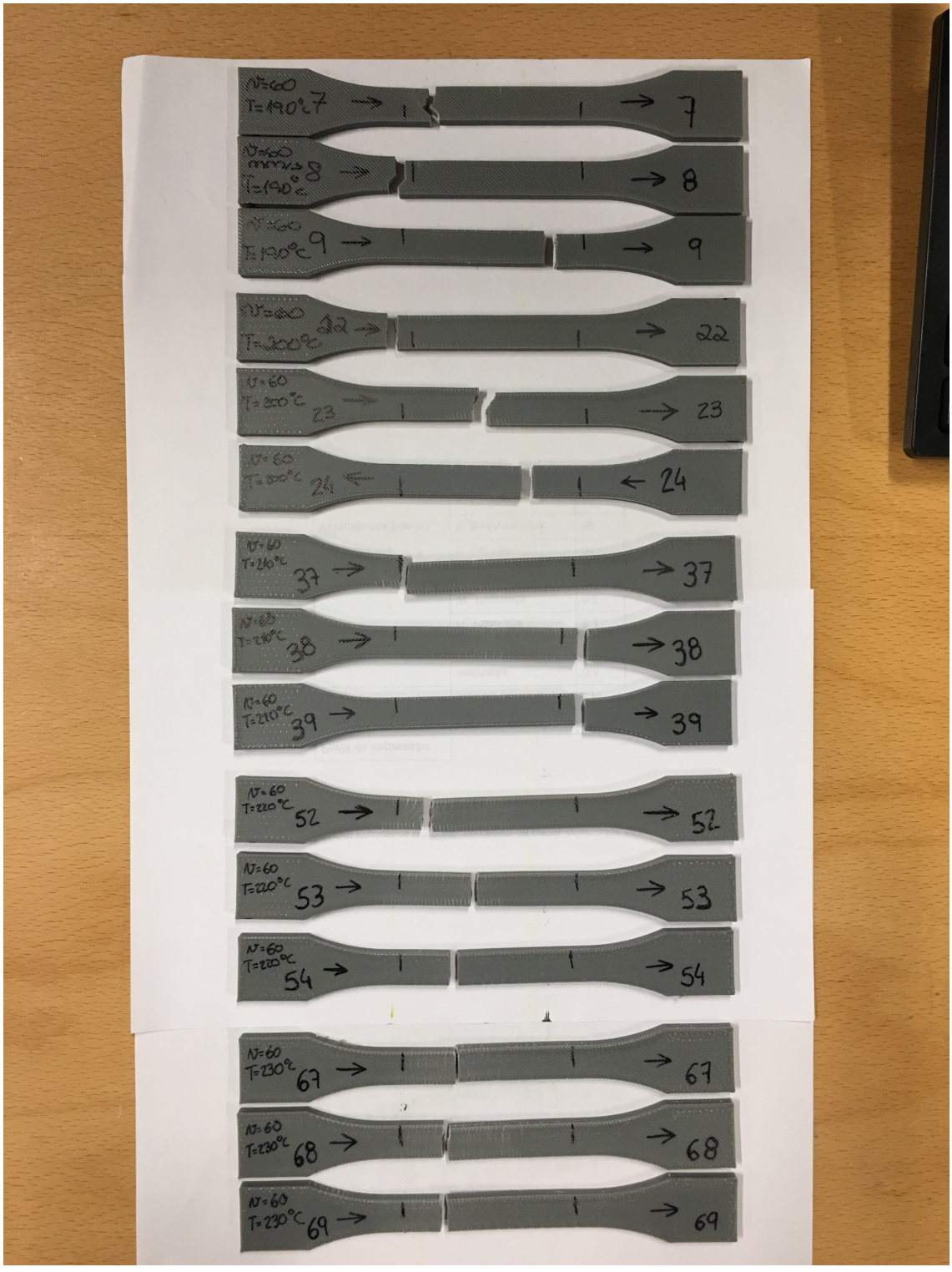
E1. Vprint=30mm/s



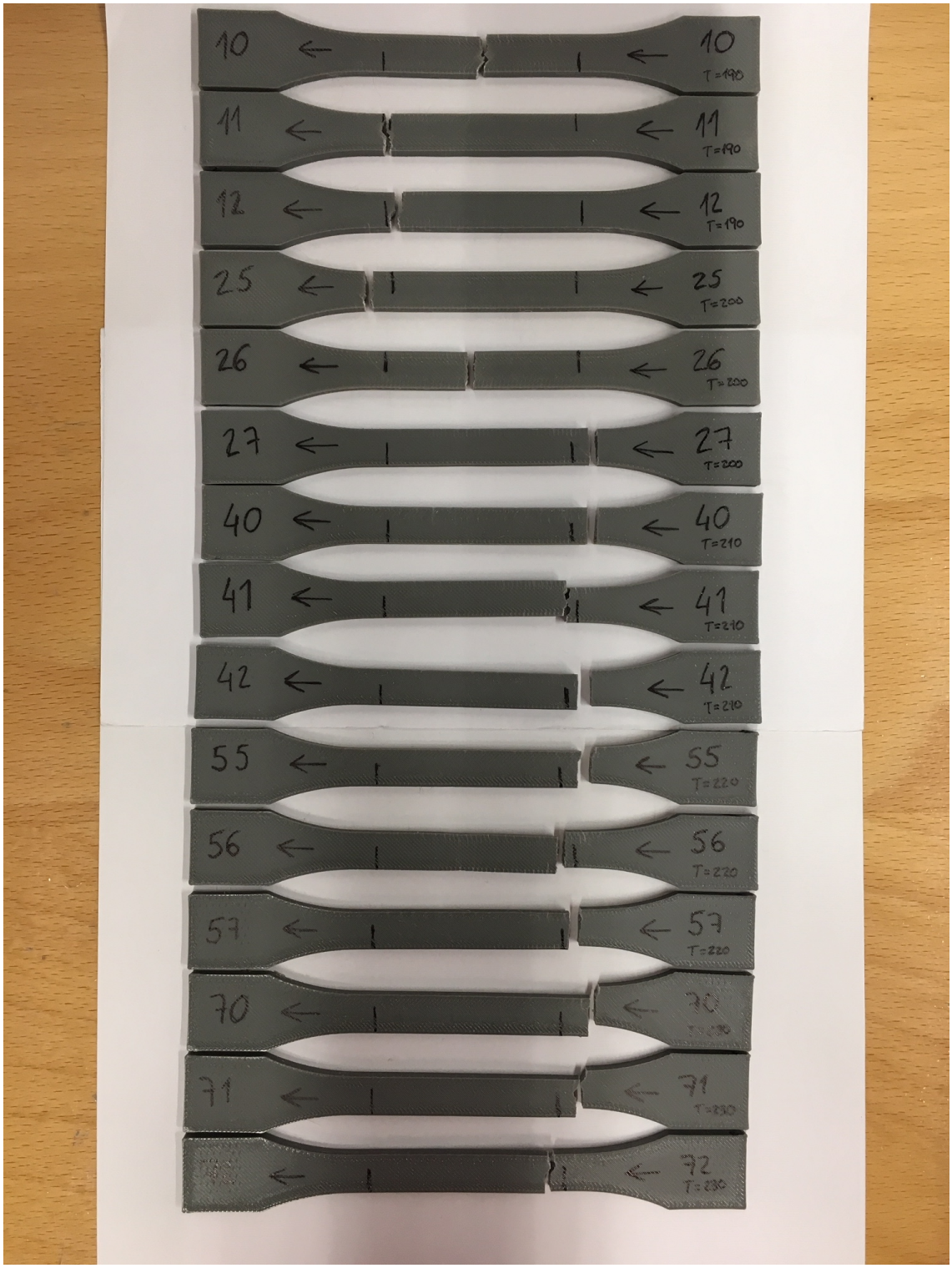
E2. Vprint=45mm/s



E3. Vprint=60mm/s



E4. Vprint=75mm/s



E5. Vprint=90mm/s

